UNIVERSITAT DE
BARCELONA

Roughness experiments of viscous fluid interfaces in disordered Hele-Shaw cells

Jordi Soriano i Fradera

Aquesta tesi doctoral està subjecta a la llicència **_Reconeixement 4.0. Espanya de Creative Commons_**.

Esta tesis doctoral está sujeta a la licencia **_Reconocimiento 4.0. España de Creative Commons_**.

This doctoral thesis is licensed under the **_Creative Commons Attribution 4.0. Spain License_**.

UNIVERSITAT DE BARCELONA

Departament d'Estructura i Constituents de la Matèria

Roughness experiments of viscous fluid interfaces in disordered Hele–Shaw cells

Jordi Soriano Fradera

Ph.D. thesis

Barcelona, February 2003

Universitat de Barcelona
Departament d'Estructura i Constituents de la Matèria
Programa de doctorat Física Avançada
Bienni 1997/99

Roughness experiments of viscous fluid interfaces in disordered Hele–Shaw cells

Memòria de la tesi presentada el febrer de 2003 per
Jordi Soriano Fradera
per optar al títol de Doctor en Física
dirigida pel Dr. Jordi Ortín Rull i la Dra. Aurora Hernández Machado

Jordi Ortín Rull i Aurora Hernández Machado

Als meus pares,
Ramon i Anna Maria

Agraïments

Primer de tot voldria agrair als meus directors de tesi, en Jordi Ortín i l'Aurora Hernández, el seu suport, ajuda i confiança durant tots aquests anys de la meva tesi no absents de dificultats. Tant amb en Jordi com amb l'Aurora he après moltes coses interessants al llarg d'aquest temps i he arribat a trobar fascinant i enriquidor un tema tant complex i extens com el del creixement d'interfícies rugoses en medis desordenats. A en Jordi Ortín voldria agrair-li especialment el fet que confiés en mi, allà cap a l'estiu de 1997, per a tirar endavant un projecte experimental nou i dificultós, del que a més no se'n tenia cap experiència prèvia dins del departament o en grups externs de col·laboradors. D'en Jordi especialment he après a tenir una enorme paciència en la batalla diària amb els experiments i a tenir molt clar que potser la millor virtut d'un bon experimental és a parts iguals la tossuderia i la imaginació. També he après a no desesperar-me i a intentar aprofitar qualsevol experiment, per horrorós que fos, per a extreure'n alguna informació útil.

També voldria agrair l'ajut inestimable d'en Jaume Casademunt. Primer, per motivar-me a fer una tesi doctoral quan el tenia de professor en el curs d'ampliació de física estadística; segon, per convèncem de parlar amb en Jordi Ortín en acabar la carrera; i tercer per la seva disponibilitat (fins i tot quan no tenia temps) per discutir física i donar-me ànims. També li voldria agrair el fet que em motivés a continuar en el món de la ciència i m'ajudés a trencar el gel amb el grup de biofísica a Bayreuth.

Un agraïment molt especial no podria faltar per a en Lluís Carrillo, que amb molta paciència i energia em va ajudar a arrencar com a físic experimental. Amb ell vaig compartir dos magnífics anys al laboratori i vam publicar un parell d'articles junts. A part d'en Lluís, també voldria agrair a en Eduard Obradó, l'Alfons González, el Francesc Magdaleno i el Jurgen Goicoechea la bona companyia, suport i magnífic bon humor durant els dos anys en que vam compartir despatx i hora del cafè. Sobre aquest últim punt voldria recuperar una frase d'en Lluís Carrillo: *potser les estones del cafè no ens van fer més savis, però sí més humans.*

Hi ha molta gent que d'alguna o altre forma han fet possible que aquesta tesi anés avançant al llargs dels anys. Primer voldria agrair als meus pares, el Ramon i l'Anna Maria, i als meus germans, el Xavier, l'Anna i el Marc, la paciència, comprensió i suport que han tingut durant tots aquests anys. També voldria agrair al meu pare les ajudes en AutoCad i que, a través de Volpack Packaging Machines, poguèssim instal·lar una còpia de l'AutoCad 13 i l'AutoCad 2000 per a fer el disseny de les plaques de desordre. Voldria agrair al personal del taller mecànic, en Javier Santana, el Manel Quevedo, el Francesc Suol i el Manuel Andrés, la seva ajuda, experiència i dedicació a l'hora de fer els diferents dissenys que hem tirat endavant els últims anys. A en Manel també li voldria agrair la seva amabilitat i tracte afable cada cop que hem necessitat alguna cosa; i a en Manu i en Javier, que sempre que ens ha fet falta ens han deixat alguna eina que no teníem o ens han regalat retalls de metall o plàstic per fer excel·lents espaiadors. Al personal de 2CI els hi voldria agrair la seva amabilitat i ajuda en la fabricació d'aquests circuits impresos tant estranys que són les nostres plaques de desordre. També voldria agrair a l'Albert Comerma l'excel·lent treball fet aquests últims dos anys en el laboratori i que m'ha facilitat molt la feina. També li voldria agrair la seva companyia i ajuda en moltes ocasions.

Als incansables treballadors de la Secretaria del Departament, Montse, Oriol i Rosa, els hi voldria agrair la seva ajuda constant en multitud d'aspectes, especialment en els últims mesos de la tesi, i la seva gran simpatia i bon humor.

A la Múriel Castro i al seu pare els hi voldria agrair la genial idea de fer servir pavonat d'òxid de coure per enfosquir el coure de les plaques amb desordre. A més, l'experiència de la Múriel com a restauradora d'obres d'art va ajudar-nos molt a millorar muntatges experimentals i a trobar el proveïdor adequat per a cada necessitat. També li voldria agrair la seva enorme simpatia i alegria, i les sempre benvingudes visites al laboratori. Uns agraïments especials els voldria dirigir a l'Enric Álvarez i la Mireia Torralba. Amb l'Enric he conviscut pràcticament quatre anys en el laboratori, ha estat el meu company d'habitació en multitud de congressos i escoles d'estiu i hem arribat a tenir una excel·lent amistat. La Mireia ha donat el toc femení al laboratori, i la seva alegria i simpatia natural han donat a la nostra *masmorra en les catacumbes* un ambient ideal de treball i relacions personals. A la Mireia voldria agrair-li especialment la seva saviesa literària, la inestimable companyia i suport en moments personals delicats i que ha fet que tinguem una excel·lent amistat, i els grans moments divertits que hem passat junts fent compres pel laboratori o en congressos.

A part de la gent que en major o menor mesura han contribuït en tirar endavant el projecte experimental, hi ha grans amics que amb la seva amistat incondicional han fet possible directa o indirectament tirar endavant aquest projecte, gaudir d'unes bones dosis de bon humor a les estones de dinar i a fer-me viure la vida intensament fora de la feina, cosa que quan les coses no van tant bé com un desitjaria es converteix en una tasca realment difícil. Voldria agrair primer de tot a aquestes magnífiques persones que són en Joan Simon, l'Àngels Aran, l'Albert Roura, la Marta Fonollosa, l'Ignasi Ariño, l'Olga Acosta, el Jordi Bosque, la María Jesús Sánchez, l'Alberto Roldán, la Lidia Aso, el Jesús Canales, l'Anna Marquès, el Xevi Noè, l'Alba Rodríguez, la Patricia Conde, el Dani Peralta, el Dani Arteaga, el David Gascón, l'Albert Comerma, la Muntsa Guilleumes, la Mari Sans, el Hao Qi, el Wolfgang Exl, l'Ivar Bratberg i la Kari Schjølberg. Amb la majoria d'ells he compartit vivències des de fa més de deu anys. A l'Àngels voldria agrair-li molt especialment el seu suport i ajuda en els moments més difícils tant científics com personals i per obligar-me a sortir mitja hora del laboratori totes les tardes. A tots ells els dec infinitat de petits grans moments i excel·lents estones de companyia.

Per la María Jesús voldria tenir un agraïment especial i afectuós. Amb ella vaig compartir quatre magnífics anys i m'ha animat i ajudat intensament en tot moment, molt sovint directament en el laboratori.

La Sandra Skowronek ha representat des de que la conec una forta injecció de moral, afecte i suport que tant importants són en els últims mesos de la tesi. La seva intel·ligència, gran cultura i esperit lluitador han estat una gran font d'ajuda en aquests últims mesos. *Eine herzliche Umarmung und einen großen Kuss aus Barcelona.*

Tampoc em voldria oblidar d'un altre grup d'amics amb els que també he passat unes grans estones en aquests anys: la Imma Abad, el Toni Ferrer, el Roger Serra, l'Anna Via, la Marta Rubio, el David Jiménez, la Ruth Cabero, el Xavi Martín, la Claudia Blanc i la Montse Puche.

També voldria tenir unes paraules per al magnífic grup d'amics que tenen la condició inicial a les classes d'anglès de l'Institut Nord-americà, ara fa cinc anys: en Pau Aliagas, un gran empresari sempre disposat a fer preguntes difícils de física; la Dolors Mejina, una excel·lent cirurgiana i futura mare; en Guillem Perea, un químic com n'hi ha pocs, contrincant a tennis dur de pelar i que em va donar una gran ajuda moral en moments delicats; l'Olga Álvarez, una excel·lent companyia i gran afeccionada al cinema; i la Cèlia Miguel, una gran persona sempre disposada a dir les coses com són i que sempre m'ha escoltat i ajudat en les situacions més difícils.

Hi han hagut una gran quantitat de persones que he conegut aquests anys com a companys de departament primer i bons amics després. A part de l'Enric i la Mireia no em voldria oblidar de l'Eduard Pauné, el Roger Folch, el Raúl Benítez, el Ricard

González, l'Andrea Rocco, l'Sten Ruediberg, el Toni Pons, el Sergio Alonso, l'Otger Campàs, la Maria Mañosas i el Xavi Illa. Amb la majoria d'ells he compartit molts congresssos arreu d'Europa i he passat divertits i inoblidables moments.

Tots els col·laboradors incansables amb els que he treballat durant aquests anys també es mereixen un reconeixement: el Miguel Ángel Rodríguez i el Jose Ramasco, a Santander, i l'Anna Lacasta i el Laureano Ramírez, a la UPC. A en Miguel i a en Jose els hi voldria agrair l'hospitalitat, companyia i tracte afable durant la meva estada al Instituto de Física de Cantabria al juliol de 1999. També els hi agraeixo les nombroses sortides turístiques i culturals que vam fer durant els caps de setmana de la meva estada. A en Jose també voldria agrair-li les moltes discussions que hem tingut per mail i per telèfon i que han permès que comprengués millor molts aspectes teòrics del món de les interfícies rugoses.

Un agraïment també per en Knut Jørgen, en Jean Schmittbuhl, l'Ivar Bratberg i la Kari Schjølberg, per la seva hospitalitat durant la meva estada a Oslo, el juny de 2001; i per en Po-Zeng Wong, l'Hao Qi i la família Newton per la seva hospitalitat i companyia durant la meva estada de tres mesos a Amherst, Massachusetts, l'últim trimestre de 1998.

Finalment, encara que sembli una mica ridícul, voldria dedicar unes paraules d'agraïment a tots aquells ciutadans anònims escampats per la ciutat de Barcelona i rodalies que fan la gloriosa tasca de vendre bens de consum, alguns d'ells fonamentals, d'altres totalment inútils per si sols, però que combinats han fet possible tirar endavant el projecte experimental. A més, l'experiència de comprar coses per un laboratori de física porta moltes vegades a situacions ben còmiques que serien la delícia d'una pel·lícula d'en Peter Sellers fent de científic boig. Un cop perds la vergonya i t'acostumes t'ho pots passar d'alló més bé. Les situacions curioses van des de la cara que posa la gent de l'autobús o el metro quan vas carregat amb un vidre que en aparença sembla destinat a una finestra peró que està misteriosament ple de forats. O la discussió en un estanc sobre la qualitat i les virtuts del millor paper de fumar del mercat, incloent un debat sobre la informació essencial del gruix del paper en micres, i que després d'una bona estona la senyoreta indignada descobreix que, per més que insisteixi ella, no te'l penses fumar sinó que el destinaràs a la fabricació d'excel·lents espaiadors. A vegades la gent pren la iniciativa i et sorprèn, com una senyoreta molt amable d'una tenda especialitzada en productes de cirurgia que, després d'observar sorpresa la quantitat de coses que li vaig demanar, va insistir en posar Dr. Frankenstein al nom de la factura en saber que volia tot alló per un laboratori de física. Fins i tot he hagut de fer de mainadera en alguna tenda per posar-me la venedora a la butxaca i tenir garantit un servei amable i pacient. I es que a vegades explicar en un merceria o, pitjor, en una farmàcia, l'experiment de Hele-Shaw que estàs muntant pot donar lloc a situacions d'alt risc. En fi, en tots aquests anys no he aconseguit encara que cap farmacèutica em cregui quan vull comprar xeringues, gomes i tubs de transfusió per injectar oli de silicona entre dos vidres.

Barcelona, 8 de novembre de 2002.

Contents

Part I

Resum en català

Capítol 1

Introducció, resum de resultats i conclusions

1.1 Introducció

El treball presentat en aquesta tesi va començar com una aportació experimental a les investigacions teòriques que Hernández–Machado i col·laboradors estaven realitzant. D'aquesta col·laboració inicial va esdevenir el nostre primer article [HMSL$^+$01]. Els resultats que vam obtenir ens van estimular a estudiar en profunditat diferents condicions experimentals en el límit que vam anomenar *soroll congelat dèbil*, i vam explorar la transició de soroll congelat *dèbil* a *fort*. Això va donar lloc a la nostra segona publicació [SOHM02b]. D'aquests resultats vam observar que, per a uns paràmetres experimentals adequats, l'escalament de les fluctuacions de la interfície canviaven de Family–Vicsek a escalament anòmal. Vam caracteritzar l'anomalia, el seu origen físic i les condicions experimentals en la qual apareixia. Això va proveir les nostres tercera [SRR$^+$02] i quarta [SOHM02a] publicacions. Finalment, per completitud, vam fer experiments a pressió constant i vam obtenir un resultats nous i substancialment diferents dels obtinguts a injecció constant. Aquests resultats es presenten en forma de *preprint* pendents de publicació [SOHM03].

En les següents seccions donarem una introducció general al problema de les interfícies rugoses i la seva descripció, i n'esmentarem alguns resultats teòrics i experimentals. Després descriurem breument el muntatge experimental i la seva caracterització. Finalment presentarem els resultats obtinguts, les conclusions i les perspectives futures.

1.1.1 Superfícies i interfícies rugoses en la natura

Qualsevol persona que obri els ulls i miri el món que l'envolta se n'adonarà que la nostra vida té lloc en un món de superfícies. Algunes d'elles es poden descriure a un primer cop d'ull com suaus, com ara una taula o un vidre d'una finestra. Altres es descriuen com rugoses, com ara un paper estripat o la forma de les muntanyes a l'horitzó. No obstant, els termes *suau* i *rugós* no estan sempre ben definits quan es parla de superfícies. Un astronauta veu La Terra com una suau bola blava, però La Terra no en té res de suau quan s'escala l'Himalàia. I una perla és una preciosa esfera de color blanc que recorda la superfície de la Lluna quan s'observa al microscopi. Així, l'aspecte de moltes superfícies depèn de quina sigui l'escala d'observació, i quina és l'aparença d'una superfície a diferents escales d'observació és el primer pas per a descriure les seves propietats. El segon pas seria entendre l'origen i la dinàmica del procés de rugositat.

Les superfícies o interfícies rugoses estan presents en molts processos naturals i tecnològics, i juguen un paper important en molts fenòmens d'interès científic i importància pràctica. Molts dels processos físics que condueixen a la formació de superfícies rugoses es donen en condicions lluny de l'equilibri. Alguns exemples són tant familiars com l'avanç d'una taca de cafè sobre unes estovalles, la forma d'estructures geològiques o l'avanç del foc en un incendi forestal. Altres exemples inclouen el creixement de colònies bacterianes [MM96; VCH90; BJCST95], el creixement o erosió de superfícies (com ara electrodeposició [HS01], abrasió [JZC96] o *molecular beam epitaxy* [YWL94]), fractura en sòlids [LS98; MSBV00], o el desplaçament immiscible de dos fluids en un medi desordenat [REDG89; Won94; ZMOW97]. Exemples d'alguns d'aquests casos es mostren en la Fig. 1.1.

Una característica general d'aquestes interfícies és que típicament presenten correlacions tipus llei de potències tant en l'espai com en el temps, pel que el seu estudi comparteix moltes característiques amb fenòmens crítics [BS95]. Per tant, una part rellevant de l'esforç fet per entendre aquests sistemes consisteix en extendre les nombroses tècniques teòriques que permeten descriure sistemes crítics al creixement d'interfícies fóra de l'equilibri. Una altra característica d'aquestes interfícies és que, excepte per casos particulars, no és possible relacionar fàcilment la dinàmica microscòpica del sistema amb la morfologia i propietats de la superfície rugosa generada. Per tant, les interfícies es descriuen mitjançant les seves propietats d'invariança d'escala i es caracteritzen mitjançant el que es coneix com a exponents d'escalament. En algunes situacions, sistemes que són diferents en la seva dinàmica interna es poden descriure amb els mateixos exponents d'escalament. En aquest cas diem que pertanyen a la mateixa classe d'universalitat.

Aquesta tesi s'emmarca en l'estudi d'interfícies fluides en medis desordenats. L'experiment típic consisteix en estudiar què s'esdevé quan un fluid entra en un medi porós que està inicialment ocupat per un altre. El primer s'anomena fluid invasor, mentre que el segon s'anomena fluid desplaçat o defensor. Quan els fluids són immiscibles es forma una interfície entre els dos. La morfologia del front canvia radicalment

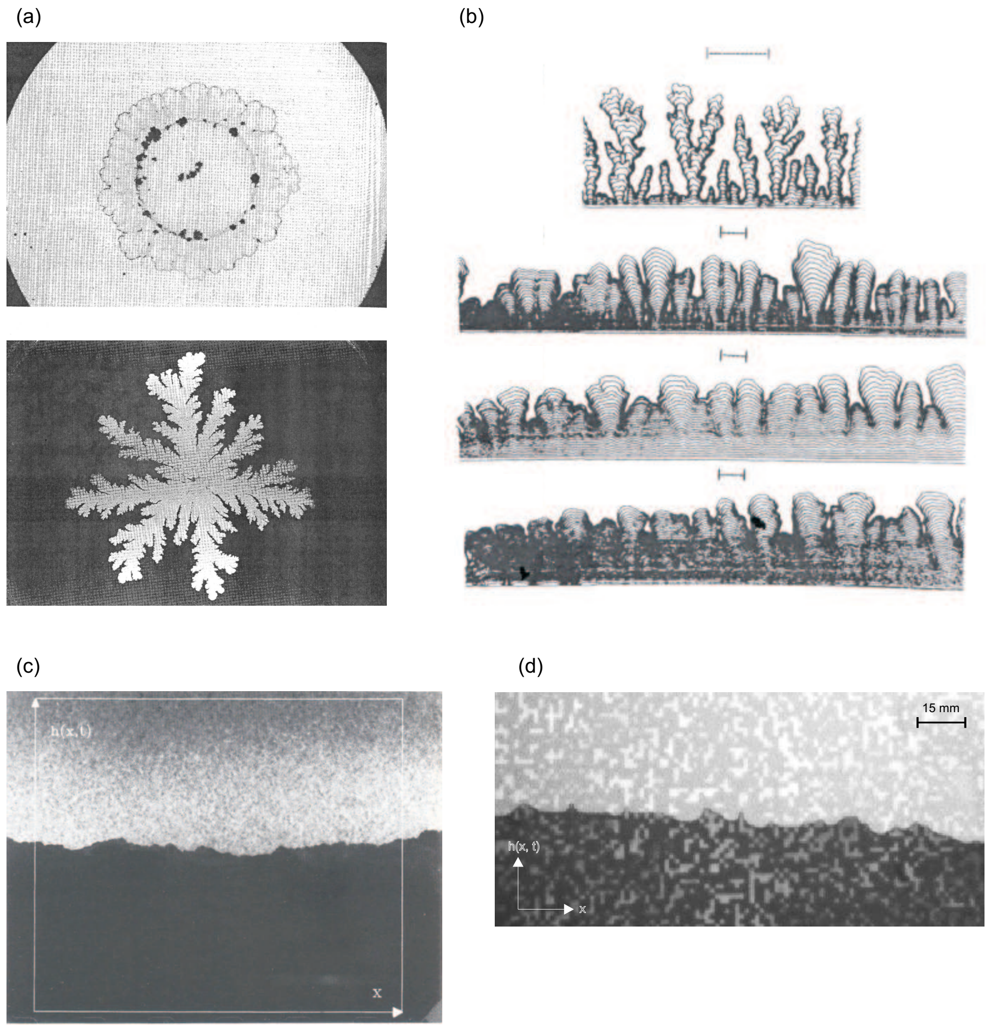

Figura 1.1: Diferents exemples d'interfícies. (a) Creixement de colònies bacterianes, on es poden observar estructures tant compactes (imatge superior, extreta de la Ref. [BJST$^+$94]) com ramificades (imatge inferior, extreta de la Ref. [MF90]). (b) Evolució temporal d'interfícies obtingudes en experiments d'electrodeposició química. Les interfícies passen de ser ramificades a compactes a mesura que s'augmenta el potencial (de [KZFW92]). (c) Front de paper cremat que avança en la direcció vertical (de [ZZAL92]). (d) Interfície fluida oli–aire que avança en un medi desordenat. La interfície representa un exemple típic del treball experimental presentat en aquesta tesi.

depenent de les propietats d'ambdós fluids, és a dir les viscositats respectives i l'efectivitat de cada un d'ells en el mullat del medi. Si el fluid invasor entra en el medi a injecció constant el procés s'anomena *forced fluid invasion*. Si el fluid invasor entra en el medi a pressió constant el procés s'anomena *forced imbibition* quan el fluid invasor mulla preferentment el medi, i *forced drainage* quan és el fluid desplaçat el que mulla preferentment el medi.

Es poden distingir dos tipus bàsics de comportament [Won94]:

i) El fluid invasor és menys viscós que el fluid resident. En aquest cas el fluid invasor pot penetrar al llarg de profunds camins, amb el que el front deixa de ser compacte per esdevenir discontinu. Aquest procés es coneix en general com a inestabilitat de Saffman–Taylor [ST58] o *viscous fingering*. Les estructures que s'observen depenen de quines siguin les propietats de mullat dels fluids presents en el medi [SWG$^+$86]. En molts casos, la dinàmica de la interfície s'esdevé en medis porosos de gran complexitat geomètrica i difícil caracterització [dG78; Sah95; Won98; Dul91] i dóna lloc a processos percolatius [BL77; WW83; MFJ85; RZ85; BFJ$^+$91; CRS94]. Aquest problema, a més, és de gran importància industrial degut a que està molt relacionat amb el problema de l'extracció de petroli [bPES81], pel que ha estat estudiat en multitud d'ocasions tant des dels punts de vista teòric i de simulació numèrica, com experimentals. Un altre procés molt interessant, caracteritzat per l'absència d'una tensió superficial, és el creixement limitat per difusió (*diffusion limited agregation*, DLA) [WS81; Pat84], en el qual la interfície ve caracteritzada per la formació de branques o estructures filamentoses.

ii) El fluid invasor és més viscós que el fluid resident. En aquest cas el front d'avanç de la interfície és compacte i no hi ha fluid atrapat (overhangs) o aquest és menyspreable, pel que la superfície rugosa que es forma és continua. Els casos més interessants d'aquest fenomen són els experiments coneguts en general com *desplaçament de fluids immiscibles en medis porosos*, on un fluid poc viscós, usualment aire, és desplaçat per un altre molt més viscós, com ara aigua, tinta, glicerol, o olis minerals, donant lloc a unes interfícies rugoses molt compactes. Els experiments clàssics són aquells realitzats en cel·les de Hele–Shaw plenes de boles de vidre [REDG89; HFV91; HKW92] i mullat de paper [BBC$^+$92; BBH$^+$92]. En aquest últim grup és habitual incloure els experiments coneguts com cremat de paper [ZZAL92; MMK$^+$97] i trencat de paper [KHW93]. Altres experiments que donen lloc a estructures compactes són els coneguts com fractura de materials fràgils [MHH92], com ara ciment [KYK97], granet [LS98] o fusta [MSLV98]. En tots aquests casos, encara que la física a darrera dels diferents processos sigui molt diferent, les interfícies que s'obtenen admeten la mateixa descripció matemàtica. A més, sistemes físics diferents pertanyen a la mateixa classe d'universalitat o es poden descriure amb els mateixos exponents crítics.

El desplaçament d'un fluid poc viscós per un altre de molt més viscós en un medi desordenat és on s'emmarca aquesta tesi. A continuació veurem com es descriu estadísticament una interfície rugosa i en veurem els resultats experimentals i teòrics més rellevants.

1.1.2 Fractals auto–similars i fractals auto–afins

Els fractals [Fed88; VSM94; KV94] es van començar a estudiar a finals del segle XIX. En principi eren una curiositat matemàtica, però a mesura que van passar els anys i va evolucionar la visió del món es va veure que hi havien una multitud d'estructures a la natura que satisfeien propietats fractals, tant a gran escala, com per exemple el creixement de muntanyes, com a petita escala, com és el cas del creixement de colònies bacterianes o la diposició de partícules sobre un substrat. La importància dels fractals en el creixement d'interfícies rugoses és que són l'eina fonamental que permet descriure-les matemàticament.

Els fractals auto–similars són aquells que son invariants sota una transformació isòtropa, és a dir mantenen la seva aparença sota una ampliació o reducció igual en totes les direccions. Exemples clàssics són el perfil de la costa de Noruega, una colònia bacteriana o una agrupació de núvols. El problema matemàtic d'aquestes estructures és que no en podem determinar la longitud o àrea que ocupen [Fed88], pel que es caracteritzen pel que es coneix com a dimensió fractal o dimensió de Hausdorf-Besicovitch. Els fractals auto–similars no tenen dimensió entera, al contrari del que passa amb les estructures simples. Així, la costa de Noruega té $D = 1.52$, entre una línia i una superfície, i s'ha mesurat $D = 1.82$ en invasio percolativa i $D = 1.71$ en processos tipus DLA en dues dimensions.

Els fractals auto-afins són estadísticament invariants sota una transformació anisòtropa (diferent en totes les direccions) [FV91]. Si una direcció canvia en un factor b, $x_1 \to bx_1$, aleshores les altres direccions s'han de reescalar un factor b^{α_i}, $x_i \to b^{\alpha_i} x_i$ per tal de preservar la invariança. Els exponents α_i es coneixen en general com a exponents de Hurst i donen una mesura del grau d'anisotropia. Un cas particularment rellevant per l'estudi de creixement d'interfícies rugoses és quan totes les direccions són equivalents excepte una, la direcció de creixement. Aleshores només hi ha un sol exponent de Hurst, i rep el nom d'exponent de rugositat. En el context de creixement d'interfícies rugoses, la situació més simple de fractal auto–afí és aquella en que la superfície es pot descriure com a una única funció univaluada que depèn només de la posició $h(x_1, x_2, ..., x_i)$ i compleix la condició $h(\vec{x}) = b^{-\alpha} h(\vec{x})$. Un exemple d'una superfície auto–afí es mostra en la Fig. 1.2(a).

1.1.3 Descripció estadística d'una interfície rugosa

Considerem una interfície o superfície de dimensió $d = 1$ (on $D = d+1$ és la dimensió del sistema físic) que evoluciona en el temps. Si la interfície admet una caracterització com a fractal auto–afí, es pot descriure per una funció univaluada $h(x,t)$ que dóna l'alçada dels punts de la interfície en la posició x i temps t (Fig. 1.2(b)). La condició d'univalualitat és essencial i no sempre es compleix estrictament, pel que es converteix en un problema freqüent el tractament de les possibles multivaluacions (*overhangs*), que normalment es soluciona prenent el valor més alt de h.

Per a caracteritzar completament una interfície rugosa de tamany lateral L es necessiten tres escales de longitud. Tal com es mostra en la Fig. 1.2(b), aquestes escales són: la posició mitjana de la interfície $\langle h \rangle$, la seva amplada mitjana w, que mesura les fluctuacions al voltant d'aquest valor mig, i una longitud de correlació $\xi(x)$ paral·lela a la superfície, que representa la distància sobre la que un punt de la interfície està correlacionat amb un altre. La quantitat w es pot entendre com una longitud de correlació en la direcció de creixement. Normalment estem interessats en estudiar les propietats estadístiques de la interfície mirant a diferents tamanys de finestra l. Així, donat un sistema de tamany lateral L, es defineix l'amplada mitjana de la interfície per a una finestra de tamany $l \leq L$ a temps t com

$$w(l,t) = \langle \frac{1}{N} \sum_{i=1}^{N} h(x_i,t)^2 - (\frac{1}{N} \sum_{i=1}^{N} h(x_i,t))^2 \rangle_j^{1/2}, \tag{1.1}$$

on $N = l/\Delta$, amb Δ l'interval de mostreig. $\langle \cdots \rangle_j$ indica un promig sobre la posició de la finestra j. En general és força habitual en la literatura referir-se a $w(l,t)$ com la *rugositat de la interfície*. Anomenarem rugositat global $w(L,t)$ a l'amplada mitjana calculada sobre el tamany del sistema L; i anomenarem rugositat local $w(l,t)$ a l'amplada mitjana calculada sobre una finestra de tamany $l < L$. El comportament de les escales globlals i locals pot ser molt diferent i donar lloc a classes d'universalitat diferenciades.

En una situació ideal, a $t = 0$ es té una interfície plana, $h(x,0) = 0$, i tots els punts de la interfície estan descorrelacionats, $\xi(t) = 0$. A mesura que la rugositat de la interfície augmenta en el temps, la longitud de correlació va creixent. Quan la longitud de correlació assoleix el tamany del sistema L, es diu que la interfície està saturada, i $w(L,t)$ es manté estadísticament invariant excepte petites fluctuacions. Una longitud de correlació que creix en el temps és imprescindible per a que tingui sentit descriure el creixement de la rugositat mitjançant un escalament dinàmic i es puguin descriure els diferents exponents d'escalament que descriuen el creixement de la interfície. Un d'aquests exponents, el que es coneix com a exponent dinàmic z, ens dóna informació de a quin ritme creixen les correlacions, $\xi(t) \sim t^{1/z}$.

En aquesta descripció L^z caracteritza el temps de saturació, $t_\times \sim L^z$, és a dir el temps en el qual la longitud de correlació assoleix el tamany del sistema L i l'amplada mitjana esdevé estacionària. L'escalament de la superfície, a saturació, amb el tamany del sistema es descriu mitjançant l'exponent de rugositat α. Finalment, el creixement de la rugositat abans de la saturació es caracteritza mitjantçant l'exponent de creixement β. Aquests tres exponents α, β, i z no són independents entre ells, sinó que verifiquen la relació d'escalament $\alpha = z\beta$.

A part de l'amplada mitjana, també és habitual estudiar el creixement de la

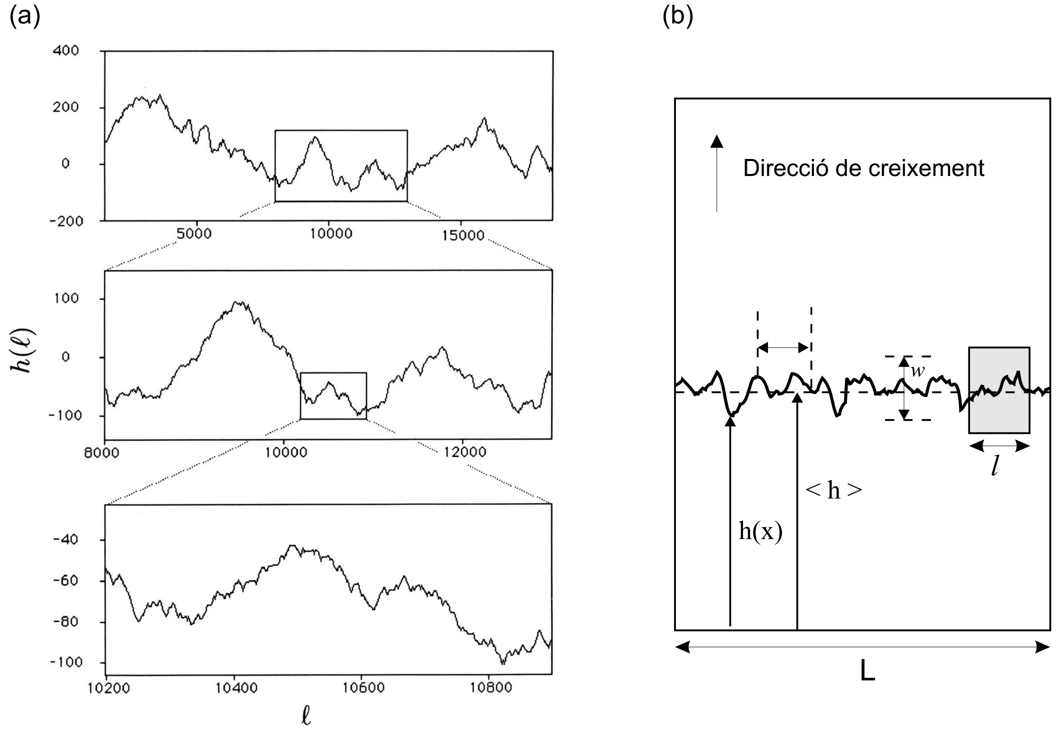

Figura 1.2: (a) Concepte geomètric d'auto–afinitat. La finestra ha de ser reescalada amb diferents factors en les direccions horitzontal i vertical per tal de mantenir la superfície invariant. (b) Representació esquemàtica de les escales característiques i les magnituds que es mesuren en una interfície auto–afí.

rugositat mitjançant altres quantitats. La més utilizada és la funció de correlació alçada–alçada generalitzada, $C(l,t)$, definida com

$$C(l,t) = \left[\langle (h(l+x,t) - h(x,t))^2 \rangle_x\right]^{1/2}. \tag{1.2}$$

Aquesta funció escala de la mateixa manera que $w(l,t)$ i permet obtenir els exponents d'escalament per un mètode alternatiu.

Tant l'amplada mitjana $w(l,t)$ com la funció de correlació alçada-alçada són funcions en l'espai real que permeten obtenir els diferent exponents d'escalament. No obstant, s'han desenvolupat eines que permeten fer la mateixa descripició en l'espai recíproc i que són especialment addients per a la determinació de l'exponent de rugositat α. L'eina més coneguda i emprada és l'espectre de potències $S(k,t)$, definit com

$$S(k,t) = \langle H(k,t) H(-k,t) \rangle, \tag{1.3}$$

on $\langle \ldots \rangle$ indica promig sobre configuracions de desordre, i

$$H(k,t) = \sum_x \left[h(x,t) - \langle h(x,t) \rangle_x\right] e^{ikx}. \tag{1.4}$$

1.1.4 Descripció genèrica de l'escalament de les interfícies rugoses

Considerant un sistema bidimensional ($d = 1$), en la descripció genèrica es proposa el següent escalament per a la rugositat global $w(L,t)$:

$$w(L,t) \sim \begin{cases} L^{\beta} & \text{si} \quad t \ll t_\times, \\ L^{\alpha} & \text{si} \quad t \gg t_\times, \end{cases} \tag{1.5}$$

on L és el tamany del sistema, $t_\times$ el temps de saturació i α l'exponent de rugositat global.

L'escalament de la funció de correlació alçada–alçada $C(l,t)$ i la rugositat local $w(l,t)$ es deriven, dins aquesta descripció global, a partir de la integral de l'espectre de potències per a cada cas particular [Ram02], el qual segueix el següent escalament:

$$S(k,t) = k^{-(2\alpha+1)}\, s\left(k\, t^{1/z}\right), \tag{1.6}$$

on

$$s(u) \sim \begin{cases} u^{2\alpha+1} & \text{si} \quad u \ll 1, \\ u^{2\theta} & \text{si} \quad u \gg 1, \end{cases} \tag{1.7}$$

on θ és un exponent introduït per conveniència que rep el nom d'*exponent d'anomalia* i que ve donat per $\theta = \alpha - \alpha_s$. El nou exponent α_s és l'*exponent de rugositat espectral* i pren diferents valors depenent dels diferents tipus d'escalament.

Per a les escales saturades, és a dir per $u \gg 1$ ($k \gg k_\times$), l'espectre de potències escala com $S(k,t) \sim t^{2\theta/z}\, k^{-2(\alpha_s+1)}$, i per temps després de saturació com $S(k,t) \sim k^{-2(\alpha_s+1)}$.

Depenent de quins siguin els valors de α i α_s tenim quatre tipus d'escalament diferents. Aquestes quatre possibilitats es poden resumir en el següent esquema:

$$\begin{cases} \text{Si} \quad \alpha_s < 1 \quad \Rightarrow \alpha_{loc} = \alpha_s \begin{cases} \alpha_s = \alpha & \Rightarrow \text{Escalament de Family–Vicsek,} \\ \alpha_s \neq \alpha & \Rightarrow \text{Escalament anòmal intrínsec.} \end{cases} \\ \text{Si} \quad \alpha_s > 1 \quad \Rightarrow \alpha_{loc} = 1 \begin{cases} \alpha_s = \alpha & \Rightarrow \text{Súper–rugositat,} \\ \alpha_s \neq \alpha & \Rightarrow \textit{Faceted interfaces.} \end{cases} \end{cases} \tag{1.8}$$

α_{loc} és l'exponent de rugositat local i es deriva a partir de l'escalament final de $C(l,t)$ per a cada cas particular, amb la hipòtesi que $C(l,t) \sim l^{\alpha_{loc}}$ per $t > t_\times$.

L'escalament de la rugositat local i l'espectre de potències per a cada cas particular els veurem a continuació.

1. **Escalament de Family–Vicsek ($\alpha_s < 1$, $\alpha_s = \alpha$).**

   Des d'un punt de vista històric va ser el primer escalament proposat, introduït per Family i Vicsek l'any 1985 [FV85]. Una important característica de l'escalament dinàmic de Family–Vicsek és que les escales globals (diferents tamanys del sistema L) i les escales locals (finestres de tamany $l < L$ dins el sistema) segueixen el mateix tipus d'escalament. Així, la rugositat local $w(l,t)$ estudiada en una finestra $l < L$ segueix l'escalament

   $$w(l,t) \sim \begin{cases} t^\beta & \text{si} \quad t \ll l^z, \\ l^\alpha & \text{si} \quad t \gg l^z. \end{cases} \tag{1.9}$$

   L'escalament dinàmic de Family–Vicsek per l'espectre de potències ve donat per:

   $$S(k,t) \sim \begin{cases} t^{(2\alpha+1)/z} & \text{per} \quad k \ll t^{-1/z}, \\ k^{-(2\alpha+1)} & \text{per} \quad k \gg t^{-1/z}. \end{cases} \tag{1.10}$$

   En saturació ($k\, t^{1/z} \gg 1$) l'espectre de potències escala com $S(k,t) \sim k^{-(2\alpha+1)}$. A més es té $\alpha_{loc} = \alpha_s$ i, per tant, $\theta = 0$.

   La Fig. 1.3 mostra esquemàticament el comportament de l'amplada mitjana i l'espectre de potències per a l'escalament de Family-Vicsek.

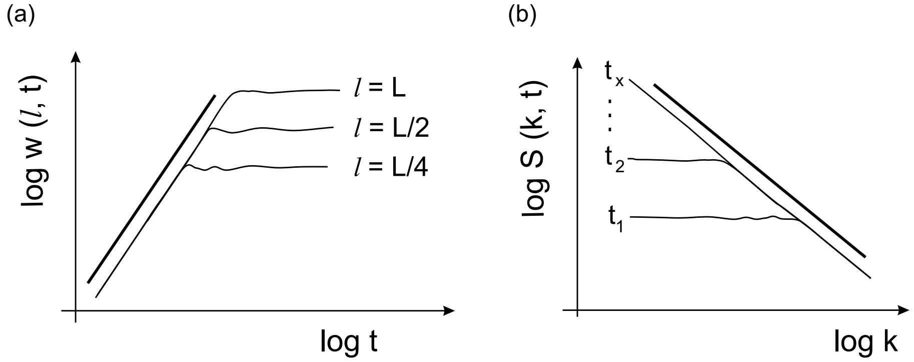

Figura 1.3: Representació esquemática de l'escalament de Family-Vicsek. (a) Determinació de l'exponent de creixement β mitjançant la representació de l'amplada mitjana en funció del temps. (b) Determinació de l'exponent de rugositat α mitjançant la representació de l'espectre de potències en funció del nombre d'ona k.

2. **Escalament anòmal intrínsec** ($\alpha_s < 1$, $\alpha_s \neq \alpha$).

L'escalament que s'obté per a $C(l,t)$ i $w(l,t)$ és [Ram02]:

$$w(l,t) \sim \begin{cases} t^{\beta} & \text{si} \quad t \ll t_l, \\ l^{\alpha_s}\, t^{\beta^*} & \text{si} \quad t_l < t < t_\times, \\ l^{\alpha_s}\, L^{(\alpha-\alpha_s)} & \text{si} \quad t_\times \ll t, \end{cases} \tag{1.11}$$

amb $\alpha_s = \alpha_{loc}$. L'exponent β^* és l'exponent de creixement local i mesura el creixement de la rugositat a escales petites.

Una de les implicacions de l'escalament anòmal intrínsec és que la rugositat local satura al mateix temps que la rugositat global, és a dir a temps $t_\times$, i *no* al temps local $t_l \sim l^z$ com passa en l'escalament de FV. L'escalament anòmal es pot identificar fàcilment si es representa l'amplada mitjana $w(l,t)$ en funció del temps per a diferents tamanys de finestra l. D'acord amb l'escalament donat per l'Eq. (1.11) les diferents corves presentaran un desplaçament vertical proporcional a l^{α_s}.

Per a l'espectre de potències $S(K,t)$ l'escalament que tenim és

$$S(k,t) \sim \begin{cases} t^{(2\alpha+1)/z} & \text{per} \quad k \ll t^{-1/z}, \\ k^{-(2\alpha_{loc}+1)} t^{2\theta/z} & \text{per} \quad k \gg t^{-1/z}, \end{cases} \tag{1.12}$$

amb $\theta = \alpha - \alpha_s$. Es tenen dues relacions d'escalament, $\alpha = z\beta$ i $\beta^* = (\alpha - \alpha_s)/z$.

Per a les escales saturades ($k \gg k_\times$), $S(k,t)$ escala com $S(k,t) \sim t^{2\theta/z}\, k^{-2(\alpha_s+1)}$. La depència $t^{2\theta/z}$ fa que en l'evolució temporal de l'espectre de potències aquests estiguin desplaçats verticalment. En la Fig. 1.4 es representa esquemàticament el comportament de $w(l,t)$ i $S(k,t)$ per a la rugositat anòmala intrínseca. Adonar-se que l'exponent β^* apareix progressivament, desplaçant l'exponent β a mesura que anem reduint el tamany de la finestra. Per a les escales més petites del sistema, tenim un únic exponent de creixement, β^*.

A part del comportament de $w(l,t)$ o $S(k,t)$, l'escalament anòmal intrínsec es pot detectar utilitzant altres eines, com són el comportament de les pendents locals [Lóp99], multiescalament [BV91; BBJ+92; Kru94] o la distribució estadística de diferències d'alçada [AMDAN02].

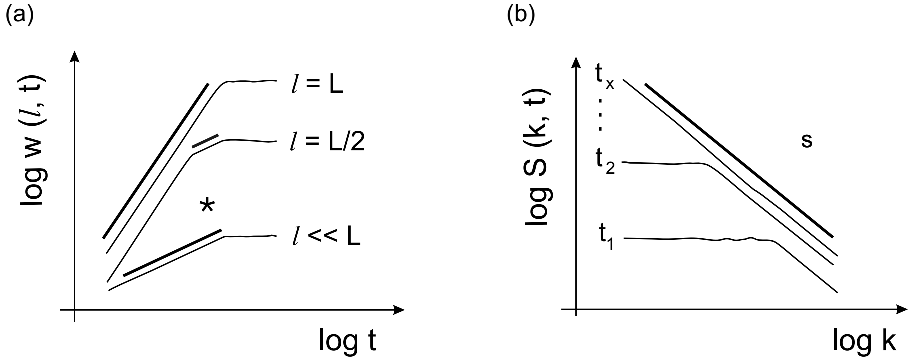

Figura 1.4: Representació esquemática de l'escalament anòmal intrínsec. (a) Rugositat local $w(l,t)$. (b) Espectre de potències $S(k,t)$.

3. **Súper–rugositat ($\alpha_s > 1$, $\alpha_s = \alpha$).**

L'escalament que s'obté per a $C(l,t)$ i $w(l,t)$ és [Ram02]:

$$w(l,t) \sim \begin{cases} t^{\beta} & \text{si} \quad t \ll t_l, \\ l\, t^{(\alpha-1)/z} & \text{si} \quad t_l < t < t_\times, \\ l\, L^{\alpha-1} & \text{si} \quad t_\times \ll t. \end{cases} \tag{1.13}$$

L'escalament de l'espectre de potències per a súper–rugositat és:

$$S(k,t) \sim \begin{cases} t^{(2\alpha+1)/z} & \text{per} \quad k \ll t^{-1/z}, \\ k^{-(2\alpha+1)} & \text{per} \quad k \gg t^{-1/z}. \end{cases} \tag{1.14}$$

En saturació, $S(k,t) \sim k^{-(2\alpha+1)}$, amb $\alpha > 1$. D'aquests escalaments es dedueix que $\alpha_{loc} = 1$ i que es compleixen les següents relacions d'escalament: $\alpha = z\beta$ i $\beta^* = (\alpha-1)/z$.

4. *Faceted interfaces ($\alpha_s > 1$, $\alpha_s \neq \alpha$).*

   L'escalament que s'obté per a $C(l,t)$ i $w(l,t)$ és [Ram02]:

   $$w(l,t) \sim \begin{cases} t^{\beta} & \text{si} \quad t \ll t_l, \\ l\, t^{(\alpha-1)/z} & \text{si} \quad t_l < t < t_\times, \\ l\, L^{\alpha-1} & \text{si} \quad t_\times \ll t. \end{cases} \tag{1.15}$$

   L'espectre de potències escala com

   $$S(k,t) \sim \begin{cases} t^{(2\alpha+1)/z} & \text{per} \quad k \ll t^{-1/z}, \\ k^{-(2\alpha+1)} & \text{per} \quad k \gg t^{-1/z}. \end{cases} \tag{1.16}$$

   En aquest cas $\alpha_{loc} = 1$ també. Observar que el fet que $\alpha \neq \alpha_s$ fa que aquest escalament tingui un comportament diferent del de súper–rugositat (on $\alpha \neq \alpha_s$). Un estudi acurat de totes les possibilitats de l'escalament de *faceted surfaces* es pot trobar a la Ref. [RLR00].

1.1.5 Alguns experiments de creixement d'interfícies en medis desordenats

Hi ha hagut molts experiments realitzats durant les últimes tres dècades relacionats amb el problema de creixement d'interfícies rugoses. En la majoria dels treballs experimentals s'han mesurat els exponents d'escalament α i β (així com també els exponents locals, α_{loc} i β^*, en cas d'haver-n'hi) i la seva dependència amb els paràmetres experimentals o propietats del material. La idea darrera de molts treballs experimentals ha estat la classificació dels diferents resultats en classes d'universalitat, el que permet en molts casos la descripció de diferents sistemes físics amb les mateixes equacions o models de creixement. Alguns exemples es mostren a continuació.

1. **Colònies bacterianes**.

   Vicsek i col·laboradors [VCH90] van estudiar colònies de *Escherichia coli* i *Bacilus subtilis* i van mesurar $\alpha = 0.78$. Matsushita i col·laboradors [MWR+98] van fer experiments també amb *Bacilus subtilis* i van estudiar diferents tipus d'estructures bacterianes, obtenint $\alpha = 0.78$ per a estructures tipus Eden i $\alpha = 0.50$ per a estructures tipus disc.

2. **Experiments de paper estripat, cremat i mullat**

   Kertész i col·laboradors [KHW93] van fer experiments de'estripat de paper i van obtenir valors de l'exponent de rugositat α en el rang $0.63 - 0.72$. Zhang i

Experiment	Exponents de rugositat	Exponents de creixement
Estripament [KHW93]	$\alpha = 0.63 - 0.72$	—
Cremat [ZZAL92]	$\alpha \simeq 0.70$	—
Cremat [MMK$^+$97]	$\alpha \simeq 0.48$	$\beta \simeq 0.32$
Cremat [BBC$^+$92]	$\alpha \simeq 63$	—
Cremat (3D) [BBH$^+$92]	$\alpha \simeq 0.5$	—
Cremat [HS95]	—	$\beta \simeq 0.56$
Cremat [KHO96]	$\alpha \simeq 0.67$	$\beta \simeq 0.24$
Mullat [ZMOW97]	$\alpha \simeq 0$ (paper isòtrop) $\alpha \simeq 0.47$ (paper anisòtrop)	— —
Mullat [BBOM00] (paper de filtre)	$\alpha = \alpha_{loc} = 0.73 - 0.75$	$\beta_L = 0.86$, $\beta_T = 0.47$
Mullat [BBOM00] (paper secant)	$\alpha = \alpha_{loc} = 0.63 - 0.64$	$\beta_L = 0.61$, $\beta_T = 0.35$

Taula 1.1: Resum dels exponents de rugositat i creixement per a experiments d'estripat, cremat i mullat de paper. β_L és l'exponent de creixement mesurat quan l'orientació del front és longitudinal a les fibres del paper, i β_T quan és transversal.

col·laboradors [ZZAL92] van fer experiments de cremat de paper i van obtenir $\alpha \simeq 0.70$. Experiments similars van ser fets per Maunuksela i col·laboradors [MMK$^+$97], obtenint $\alpha \simeq 0.48$ i $\beta \simeq 0.32$. Experiments de mullat de paper van ser fets per primera vegada per Buldyrev i col·laboradors [BBC$^+$92], obtenint $\alpha = 0.63$. Des d'aleshores molts altres experiments s'han fet, tant en 2D (fulls de paper) com en 3D (blocs de paper) i diferents exponents mesurats. Aquests resultats es presenten en la Taula 1.1.

3. **Fractura en materials fràgils**

   Experiments de fractura en materials fràgils (com ara fusta, porcelana o granet) han estat importants pel seu interès tecnològic i caracterització de materials. Una característica important és que molts dels experiments presenten escalament anòmal, i hi han evidències que semblen indicar que l'exponent de rugositat local és universal (independent del material i procés de fractura), en contrast amb l'exponent de rugositat global, que depèn del material sota estudi i l'orientació de la fractura respecte direccions privilegiades en el material.

   En fractures en 3D, Bouchaud i col·laboradors [BLP90] van investigar fractures en alumini i van trobar $\alpha_{loc} \simeq 0.8$. Måløy i col·laboradors [MHH92] van investigar diferents materials fràgils i van trobar petites diferències en els valors d'α_{loc} mesurats, amb un valor mitjà d'$\alpha_{loc} \simeq 0.87$. López i col·laboradors van proposar per primer cop en la referència [LS98] l'ús de l'escalament anòmal per a descriure experiments de fractura, i van fer experiments de fractura en blocs de granet, obtenint $\alpha \simeq 1.2$ i $\alpha_{loc} \simeq 0.79$. La descripció utilitzant escalament anòmal es va ampliar a fractura en fusta, i Morel i col·laboradors [MSLV98] van fer experiments amb diferents especimens, pi i picea, obtenint $\alpha = 1.35$ i $\alpha_{loc} = 0.88$ pel primer, i $\alpha = 1.60$ i $\alpha_{loc} \simeq 0.87$ pel segon.

En fractures en 2D, els valors obtinguts són similars als obtinguts en estripat de paper. Kim i col·laboradors [KYK97], per exemple, van obtenir $\alpha = 0.68$. Engøy i col·laboradors [EMHR94] van estudiar l'efecte de l'orientació de l'esquerda en fractura en fusta. Van observar un comportament diferent per fractures radials i tangencials, encara que en els dos casos el valor de l'exponent local era el mateix, $\alpha_{loc} = 0.68$. La morfologia de les interfícies per fractures radials era suau, en contrast amb les obtingudes en fractures tangencials i que venen caracteritzades per grans pendents.

4. **Experiments amb boles de vidre i fluxes viscosos**

Experiments d'interfícies fluides en cel·les de Hele–Shaw van ser el primer intent d'estudiar d'una manera controlada la dinàmica del desplaçament estable i immiscible d'un fluid en un medi desordenat. L'experiment típic consisteix en una cel·la de Hele–Shaw horitzontal feta de dues plaques de vidre separades una distància b. L'espai entre les plaques s'omple amb boles de vidre de diàmetre uniforme o aleatori, donant lloc a un medi poròs similar a aquells que es poden trobar en sistemes naturals. El fluid (aigua o glicerol) és injectat per un costat de la cel·la desplaçant aire. Les forces viscoses s'ajusten mitjançant la velocitat del fluid invasor, mentre que les forces capil·lars es modifiquen mitjançant la distribució de tamanys de les boles de vidre presents en el medi. Normalment el paràmetre de control en aquests experiments és el nombre de capil·laritat modificat, Ca' =Ca a^2/k, on Ca $= v\mu/\sigma$ és el nombre de capil·laritat ordinari, v la velocitat mitjana del fluid, μ la viscositat dinàmica, σ la tensió superficial fluid–aire, a el tamany característic dels porus i k la permeabilitat del medi. La Fig. 1.5(a) mostra un esquema del sistema experimental típic. La morfologia d'algunes interfícies experimentals es mostra en les Figs. 1.5(b) i 1.5(c).

El primer experiment d'interfícies fluides en cel·les de Hele–Shaw amb un desordre fet de boles de vidre va ser realitzat per Rubio i col·laboradors [REDG89].

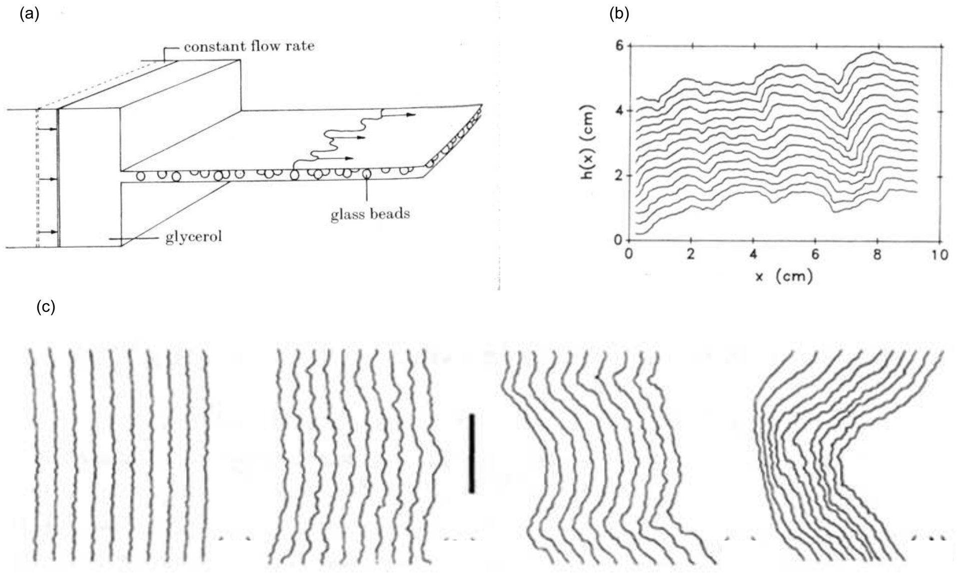

Figura 1.5: Experiments d'interfícies fluides en cel·les de Hele–Shaw plenes de boles de vidre. (a) Esquema d'un muntatge experimental típic (de la Ref. [BS95]). (b) Representació d'interfícies succesives amb Ca'$= 4.93 \times 10^{-3}$ (de la Ref. [REDG89]). (c) Seqüència d'interfícies amb creixent velocitat promig d'avanç d'esquerra a dreta (de la Ref. [HKW92]), i Ca' variant des de 1.18×10^{-2} fins 1.18×10^{-5}. La barra que representa l'escala equival a una longitud de 10 cm.

Van estudiar aigua desplaçant aire (Fig. 1.5(b)) i van mesurar $\alpha \simeq 0.73$, independent de Ca' (en el rang estudiat) i grandària de les boles de vidre. No obstant, una reanàlisi dels resultats fet per Horvátz i col·laboradors [HFV90] va donar $\alpha \simeq 0.91$, similar al valor d'$\alpha \simeq 0.88$ obtingut per ells mateixos en un experiment anàleg al de Rubio. Experiments fets amb glicerol enlloc d'aigua per Horvátz i col·laboradors [HFV91] van donar $\alpha \simeq 0.81$ per a escales de longitud petites, $\alpha \simeq 0.49$ per a escales de longitud grans, i $\beta \simeq 0.65$. L'últim experiment d'aquest tipus va ser realitzat per He i col·laboradors [HKW92], amb aigua desplaçant aire, i van investigar un ampli rang de Ca' (Fig. 1.5(c)). Van trobar grans fluctuacions de l'exponent de rugositat en Ca', i van mesurar valors d'α en el rang $0.65 - 0.91$. Encara que no van poder obtenir un escalament bó per a determinar l'exponent de creixement, van trobar que l'amplada global escalava amb Ca' amb un exponent -0.57. Un resum dels diferents resultats obtinguts en aquests experiments es msotra en la Taula 1.2.

En aquesta tesi es presenten resultats experimentals que hem obtingut en *forced fluid invasion* i *forced imbibition* en una cel·la de Hele–Shaw amb desordre.

Experiment amb boles de vidre	Exponent de rugositat	Exp. de creixement
aigua/aire [REDG89]	$\alpha \simeq 0.73$	—
(reanàlisi) [HFV90]	$\alpha \simeq 0.91$	—
aigua/aire [HFV90]	$\alpha \simeq 0.88$	—
glicerol/aire [HFV91]	$\alpha_1 \simeq 0.81$, $\alpha_2 \simeq 0.49$	$\beta \simeq 0.65$
aigua/aire [HKW92]	$\alpha \simeq 0.65$ (baix Ca')	—
	$\alpha \simeq 0.91$ (gran Ca')	—

Taula 1.2: Resum dels exponents de rugositat i creixement obtinguts per a experiments de *forced fluid invasion* en cel·les de Hele–Shaw plenes amb boles de vidre. Els subíndexs 1 i 2 fan referència a escales de longitud petites i grans respectivament.

1.1.6 Soroll congelat i no localitat

En els últims anys hi ha hagut un interès creixent cap a models de creixement que tenen en compte desordres *congelats*. Les fibres de paper en experiments de cremat de paper o els porus entre boles de vidre en experiments d'interfícies fluides en medis porosos en són dos exemples. Els models QEW [KL85; KLT91] i QKPZ [Par92] van ser introduïts per tal de descriure problemes amb soroll congelat. QEW va aparèixer per a modelitzar els experiments amb boles de vidre, i QKPZ per a descriure experiments de mullat de paper [BBC$^+$92; TL92] i que van donar lloc a una nova classe d'universalitat que es coneix com DPD (directed percolation depinning) [ABS94; ABMS95]. Aquests models van anar bé per descriure resultats experimentals amb dinàmica local. No obstant, hi ha sistemes físics que requereixen la introducció de lleis no locals, com és el cas d'interfícies fluides en medis desordenats (degut al transport de fluid [KM91; HKW92]) i creixement de colònies bacterianes (degut al paper dels nutrients i dels inhibidors [LJ98]). En aquestes situacions hi ha correlacions de llarg abast que no es poden caracteritzar utilitzant una descripció local, pel que es fa necessari la introducció de models no locals.

Recentment s'han proposat diferents models per a donar una descripció no local de la dinàmica d'interfícies fluides en medis desordenats, i s'han derivat diferents equacions no locals per a la interfície [GB98; DRE$^+$00; HMSL$^+$01; PC02]. Aquest models són consistents amb les equacions macroscòpiques del problema (llei de Darcy i condicions de contorn), i difereixen en la manera d'introduir el desordre en les equacions i en les propietats del desordre. Els diferents resultats que s'han obtingut per als exponents de rugositat α i de creixement β estan resumits en la Taula 1.3.

Primer autor	Exponents de rugositat	Exps. de creixement
Ganesan [GB98]	$\alpha = 3/4$ (velocitats baixes) $\alpha = 1/2$ (velocitats altes)	— —
Dubé [DRE$^+$99; DRE$^+$00]	$\alpha \simeq 1.25$	$\beta \simeq 0.3$
Hernández–Machado [HMSL$^+$01]	$\alpha_1 = 5/2$, $\alpha_2 = 1/2$	$\beta_1 = 5/6$, $\beta_2 = 1/2$
Pauné [PC02; Pau02]	$\alpha_1 \simeq 1.5$, $\alpha_2 \simeq 1.2$ (velocitats baixes)	$\beta \simeq 0.68$
	$\alpha_1 \simeq 1.5$, $\alpha_2 \simeq 0$ (velocitats altes)	$\beta \simeq 0.68$
	$\alpha = 3/2$ (desordre persistent)	$\beta = 1/2$

Taula 1.3: Resum dels exponents de rugositat i creixement corresponents a diferents models no locals. Els subíndexs 1 i 2 fan referència a escales de longitud petites i grans respectivament.

1.2 Resum dels resultats obtinguts

1.2.1 Muntatge experimental

Hem fet experiments de *forced fluid invasion* (injecció constant) i *forced imbibition* (pressió constant) en un cel·la de Hele–Shaw horitzontal de 190×550 mm^2 (Fig. 1.6). Hem utilitzat un oli de silicona amb viscositat cinemàtica $\nu = 50$ mm^2/s, densitat $\rho = 998$ kg/m^3 i tensió superficial oli–aire $\sigma = 20.7$ mN/m a 25 °C. Fluctuacions en l'espaiat entre plaques han estat introduïdes mitjançant un placa de fibra de vidre que conté una sèrie d'obstacles de coure de $d = 0.06$ mm d'alt. La separació entre la placa inferior i la superior defineix l'espaiat entre plaques b, el qual ha estat variat en el rang $b = 0.16 - 0.75$ mm. Tres configuracions de desordre s'han utilitzat: SQ, SQ-n i T.

L'oli és injectat a flux constant mitjançant una bomba d'injecció (pels experiments a velocitat constant) o una columna d'oli d'alçada adaptable (pels experiments a pressió constant). L'evolució de la interfície oli–aire es controla mitjançant dues càmeres CCD fixes i capturant cada una la meitat de la cel·la. Les imatges han estat preses amb una resolució espacial de 0.37 mm per pixel i un format de 768×574 pixels. Les interfícies es reconeixen amb una precisió d'1–pixel i els perfils resultants s'han analitzat per a obtenir les magnituds amb que s'han estudiat les propietats d'escalament de les fluctuacions interficials.

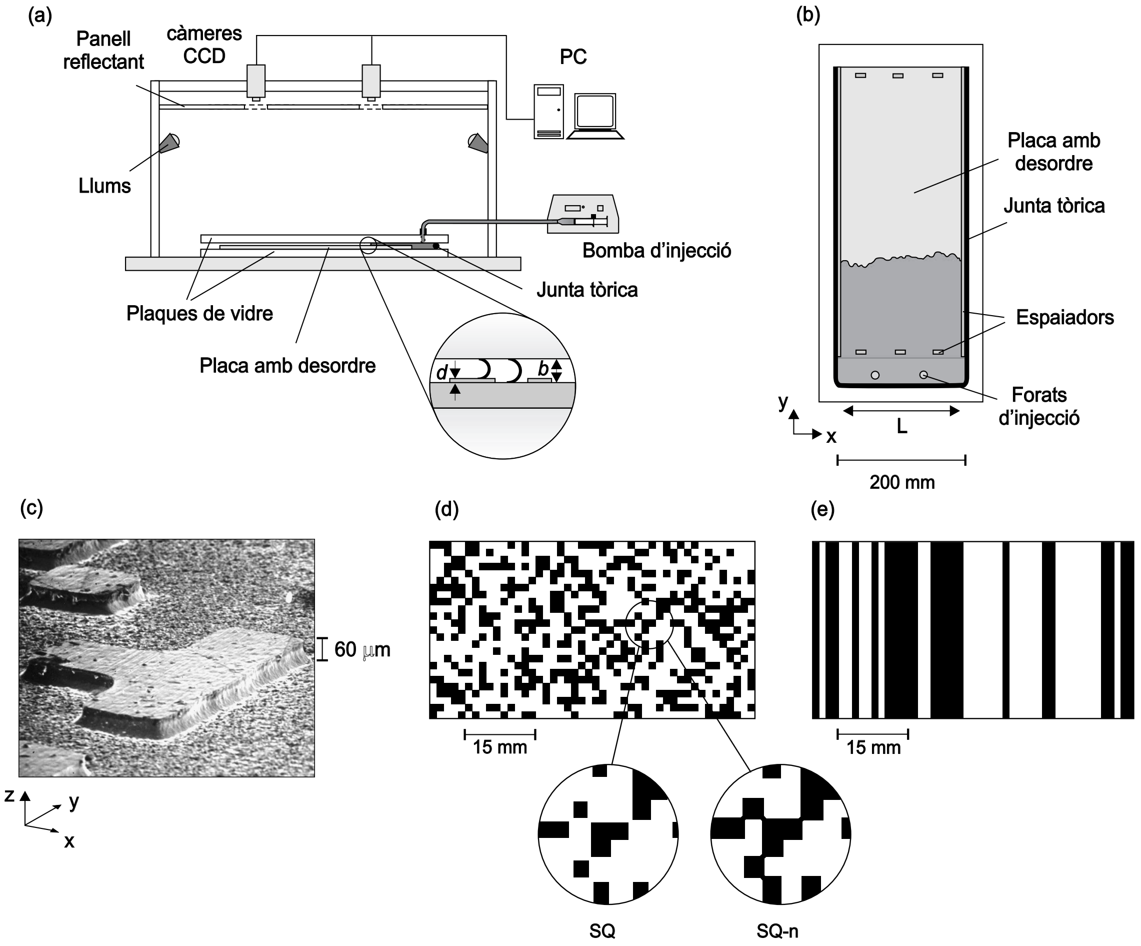

Figura 1.6: Esquema del muntatge experimental. a) Vista lateral, amb el detall del muntatge a injecció constant. b) Vista superior. c) Imatge SEM de les illes de coure en la placa de fibra de vidre. d) i e) Fragments de configuracions de desordre per d) quadrats (SQ) i e) pistes (T). Les illes de coure són les regions negres. Les ampliacions en d) mostren l'estructura detallada de la configuració de desordre per SQ i SQ-n.

1.2.2 Permeabilitat de la cel·la i nombre de capil·laritat modificat

Utilitzant un sistema de pressió constant i aplicant la llei de Darcy hem mesurat la permeabilitat de la cel·la, obtenint

$$k = \frac{b^2}{12}\left(1-(1-\Lambda^{1/2})\frac{d}{b}\right)^2, \qquad (1.17)$$

on b és l'espaiat entre plaques, $d = 0.06$ mm l'alçada dels obstacles de coure, i Λ un factor que conté la informació de les propietats del desordre. Hem obtingut $\Lambda = 1 - f = 0.65$ per T 1.50 i $\Lambda = 0.20$ per SQ 1.50. En el primer cas la relació

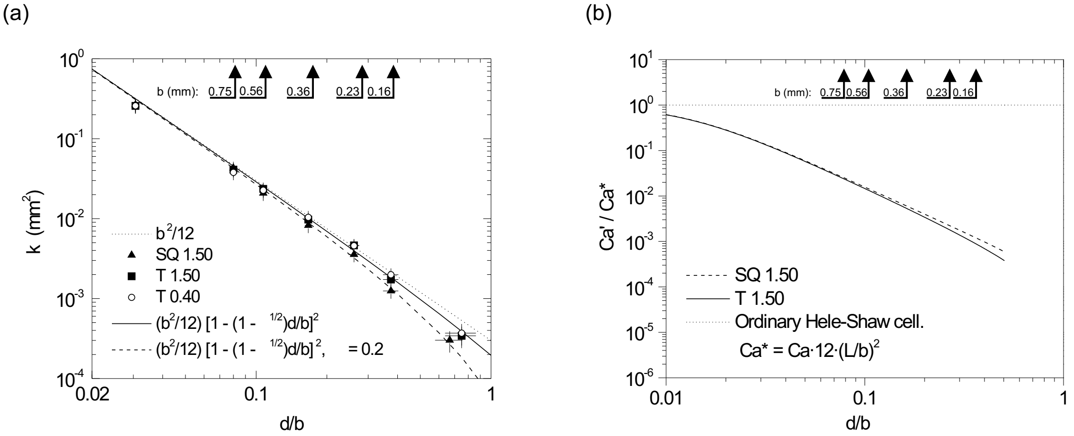

Figura 1.7: (a) Mesures de la permeabilitat, k, en funció de la intensitat del desordre, d/b, per $d = 0.06$ mm. La línia puntejada és la permeabilitat per a una cel·la de Hele–Shaw ordinària (sense desordre), i les línies discontinua i contínua són ajustos a les dades experimentals per configuracions de desordre SQ i T respectivament. (b) Quocient entre el nombre de capil·laritat modificat, Ca', i el nombre de capil·laritat modificat per a una cel·la de Hele–Shaw ordinària, Ca*, com a funció de la intensitat del desordre, d/b. Les línies discontinua i contínua corresponen a desordres SQ 1.50 i T 1.50. La línia puntejada representa el límit assimptòtic Ca'=Ca*. La fletxa indica els valors de d/b pels espaiats entre plaques utilitzats en els experiments.

és exacte. En el segon, el valor de Λ s'ha obtingut mitjançant un ajust de les dades experimentals.

Utilitzant la informació de la permeabilitat i avaluant el qüocient entre les forces viscoses i les forces capil·lars hem obtingut una expressió pel nombre de capil·laritat modificat,

$$\text{Ca'} = \text{Ca} \cdot \frac{12L}{b^2 \left(1 - (1 - \Lambda^{1/2})\dfrac{d}{b}\right)^2 \left(\dfrac{2}{b-d} - \dfrac{2}{b} + \dfrac{1}{L}\right)}, \tag{1.18}$$

on $\text{Ca} = v\mu/\sigma$ és el nombre de capil·laritat ordinari, v la velocitat mitjana de la interfície, μ la viscositat dinàmica i σ la tensió superficial oli–aire.

Les representacions gràfiques de la permeabilitat i el nombre de capil·laritat modificat per a diferents configuracions de desordre es presenten en les Figs. 1.7(a) i 1.7(b).

1.2.3 Resultats experimentals a injecció constant

Desordre congelat dèbil

Els resultats experimentals amb desordre congelat dèbil es caracteritzen per un escalament de les fluctuacions interficials que es descriu en el marc de l'escalament dinàmic de Family–Vicsek. Corresponen a paràmetres experimentals caracteritzats per grans velocitats de la interfície, un gran espaiat entre plaques o una petita longitud de persistència del desordre en la direcció de creixement.

Hem mesurat els exponents de creixement utilitzant diferents valors d'espaiat entre plaques, velocitats de la interfície i configuracions de desordre, i mesurat $\beta \simeq 0.50$. Aquest valor és quasi independent de la velocitat, l'espaiat entre plaques i la configuració de desordre, tal com es pot veure en les Figs. 1.8(a) i 1.8(b) que mostren corbes de $W(L,t)$ per desordre SQ 1.50 i T 1.50 per a diferents velocitats. L'exponent de rugositat, en canvi, és més sensible als paràmetres experimentals i dos règims, α_1 a escales petites i α_2, a escales grans han estat caracteritzats. Per a les configuracions de desordre estudiades, hem observat que en general α_1 augmenta amb la velocitat, mentre que α_2 decreix. Exemples d'espectre de potències per diferents velocitats es presenten en la Fig. 1.9(a) per SQ 1.50 i en la Fig. 1.9(b) per T 1.50. És remarcable observar que a mesura que la velocitat es fa cada cop més petita hi ha una convergència cap a un únic règim que s'extendria a totes les escales. També és interessant observar que, malgrat que els exponents de rugositat α_1 que es poden extreure de les pendents dels espectres són diferents per SQ 1.50 i T 1.50, a velocitats molt altes convergèixen cap a un mateix valor, al voltant d'$\alpha_1 \simeq 1.3$. La Taula 1.4 resumeix els resultats obtinguts en els exponents de rugositat.

Els dos règims α_1 i α_2 venen separats per un nombre d'ona de *crossover* k_c que

Desordre	Ca' baix ($\lesssim 3$)		Ca' moderat ($3 <$ Ca' < 10)		Ca' gran ($\gtrsim 10$)	
	α_1	α_2	α_1	α_2	α_1	α_2
SQ 1.50	0.6 – 0.9	–	$\simeq 1$	$\simeq 0.6$	$\simeq 1.3$	$\simeq 0$
SQ-n 1.50	0.6 – 0.9	–	$\simeq 0.9$	$\simeq 0.5$	$\simeq 1.3$	$\simeq 0$
T 0.40	Escalament anòmal		$\simeq 0.7$	$\simeq 0.5$	$\simeq 1.3$	$\simeq 0$
T 1.50	Escalament anòmal		$\simeq 0.5$	$\simeq 0.2$	$\simeq 1.3$	$\simeq 0$

Taula 1.4: Resum dels resultats de l'exponent de rugositat en el límit de desordre congelat dèbil.

divideix el règim en el qual les fluctuacions a grans escales de longitud (petites q) són escombrades pel camp de pressió viscosa, del règim en el qual les fluctuacions a petites escales de longitud (grans k) són escombrades per la tensió interficial en el pla de de la cel·la. Aquest nombre d'ona de *crossover* escala amb la velocitat com $k_c \sim v^{-\zeta}$, amb $\zeta = 0.47$, $\zeta = 0.28$ i $\zeta \simeq 0$ per desordres SQ, SQ-n i T respectivament. El fet que ζ tendeixi a zero a mesura que la longitud de persistència del desordre augmenta és degut a l'efecte estabilitzador de la tensió interficial en el pla de la cel·la, que és suprimit quan el desordre és totalment persistent en la direcció de creixement.

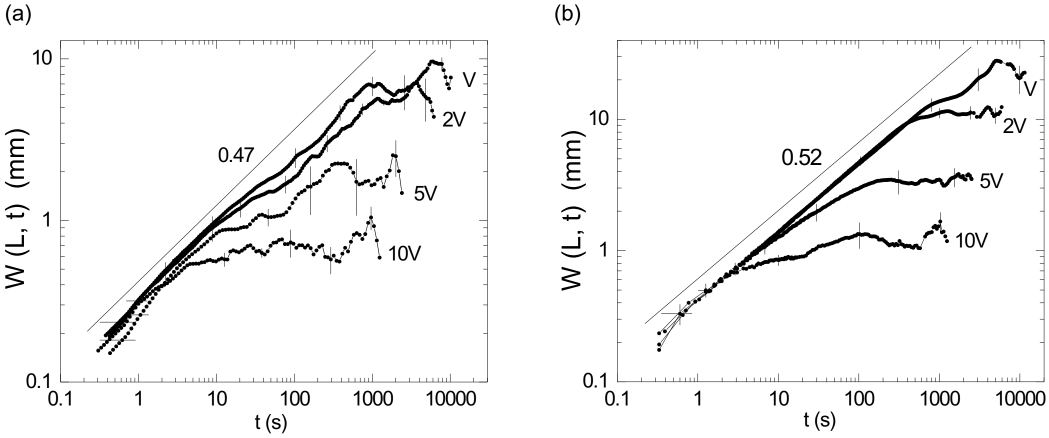

Figura 1.8: Dependència de l'exponent de creixement amb la velocitat mitjana de la interfície. (a) $W(L,t)$ per desordre SQ 1.50 i $b = 0.36$ mm. (b) $W(L,t)$ per desordre T 1.50 i $b = 0.36$ mm. $V = 0.04$ mm/s.

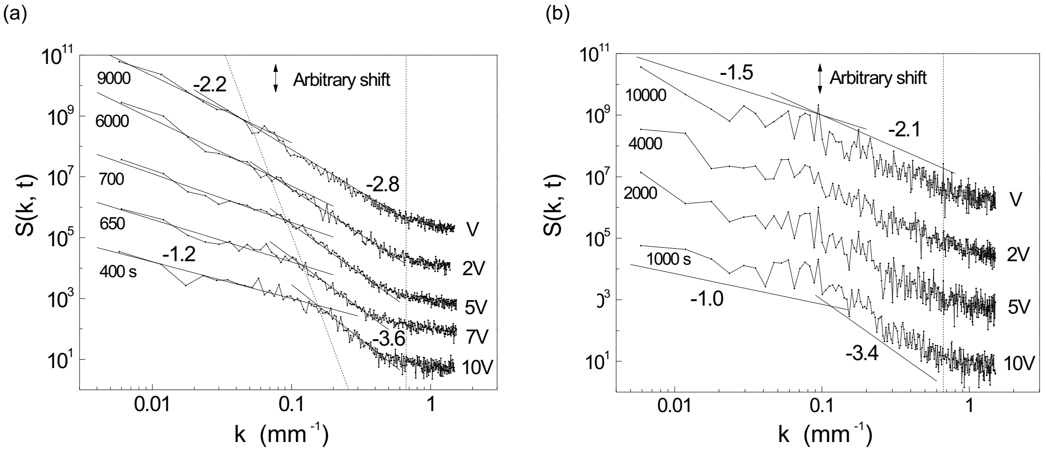

Figura 1.9: Dependència de l'exponent de rugositat amb la velocitat v. (a) $S(k,t)$ per desordre SQ 1.50 i $b = 0.36$ mm. (b) $S(k,t)$ per desordre T 1.50 i $b = 0.36$ mm. $V = 0.04$ mm/s.

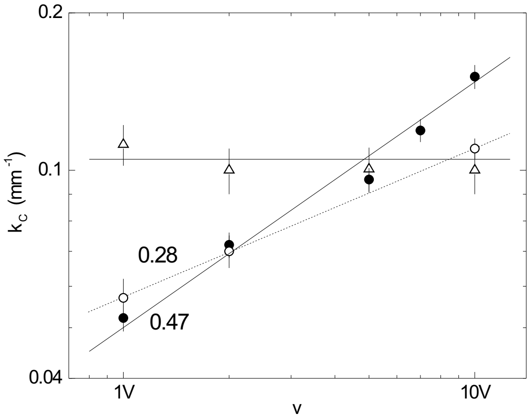

Figura 1.10: Dependència del nombre d'ona de crossover k_c amb la velocitat v per tres configuracions de desordre: SQ 1.50 (cercles negres), SQ-n 1.50 (cercles blancs) i T 1.50 (triangles). $b = 0.36$ mm i $V = 0.04$ mm/s.

En el límit de velocitats de la interfície molt grans l'exponent de rugositat α_1 i α_2 tendeixen assimptòticament a $\alpha_1 \simeq 1.3$ i $\alpha_2 \simeq 0$ respectivament, resultat que està d'acord amb resultats teòrics de models no–locals [DRE$^+$99; PC02].

Desordre congelat fort

Hem fet experiments variant l'espaiat entre plaques, la velocitat mitjana de la interfície i la configuració del desordre, i hem mesurat els exponents d'escalament. Els resultats obtinguts vénen caracteritzats pel fet de presentar escalament anòmal intrínsec.

Amb aquests experiments hem obtingut la primera evidència experimental d'escalament anòmal intrínsec en fluxes de Hele–Shaw. Tres condicions són necessàries per a observar escalament anòmal: i) un desordre suficientment persistent en la direcció de creixement, ii) forces capil·lars fortes (però no dominants), i iii) forces viscoses equilibrades amb les forces capil·lars. En aquestes condicions hem determinat els cinc exponents d'escalament que caracteritzen l'anomalia per diferents valors de l'espaiat entre plaques (intensitat de les forces capil·lars) i velocitats (intensitat de les forces viscoses). Les interfícies típiques que s'obtenen quan el desordre és persistent en la direcció de creixement venen caracteritzades per grans diferències d'alçada a les parets de les pistes (Fig. 1.11(a)), i el creixement d'aquestes diferències d'alçada és el responsable del diferent comportament de les escales globals i locals. Els exponents de creixement globals i locals β i β^* s'han obtingut a partir de l'estudi de les fluctuacions interficials com a funció del temps, $W(l = L, t)$ i $W(l = L/256, t)$ respectivament

(Fig. 1.11(b)). L'exponent de creixement local apareix progressivament a mesura que reduïm el tamany de la finestra desplaçant l'exponent β, d'acord amb l'ansatz de l'escalament anòmal. L'exponent de rugositat local α_{loc} ha estat mesurat mitjançant l'espectre de potències $S(k,t)$ (Fig. 1.12(a)). El col·lapse de l'espectre de potències (Fig. 1.12(b)) ha permès obtenir l'exponent de rugositat global α, l'exponent dinàmic z i ha permès un refinament de tot el conjunt d'exponents d'escalament.

Hem obtingut per $b = 0.36$ mm i $v = 0.08$ mm/s els següent conjunt d'exponents d'escalament:

$$\begin{aligned}&\beta = 0.50 \pm 0.04,\ \beta^* = 0.25 \pm 0.03,\\ &\alpha = 1.0 \pm 0.1,\ \alpha_{loc} = 0.5 \pm 0.1,\ z = 2.0 \pm 0.2.\end{aligned} \tag{1.19}$$

Aquests valors han estat confirmats utilitzant anàlisis alternatives, com ara la variació de les pendents locals, la presència de multi–escalament i la distribució estadística de diferències d'alçada.

Per a trobar l'origen físic de l'escalament anòmal hem fet experiments on només hi intervenen forces capil·lars, i trobat que la velocitat en una sola pista ve donada per la simple llei de relaxació $v = v_M\ t^{-1/2}$, amb v_M una certa velocitat màxima inicial. Una investigació detallada de la dinàmica de la interfície en les diferents pistes ha permès descriure l'escalament anòmal en termes de i) la diferent velocitat dels punts de la interfície que es mouen sobre pistes de coure (v_+) o sobre canals de fibra de vidre (v_-), que es pot expressar de forma compacta de la forma $v_\pm = v \pm (v_M - v)\ t^{-1/2}$; i ii)

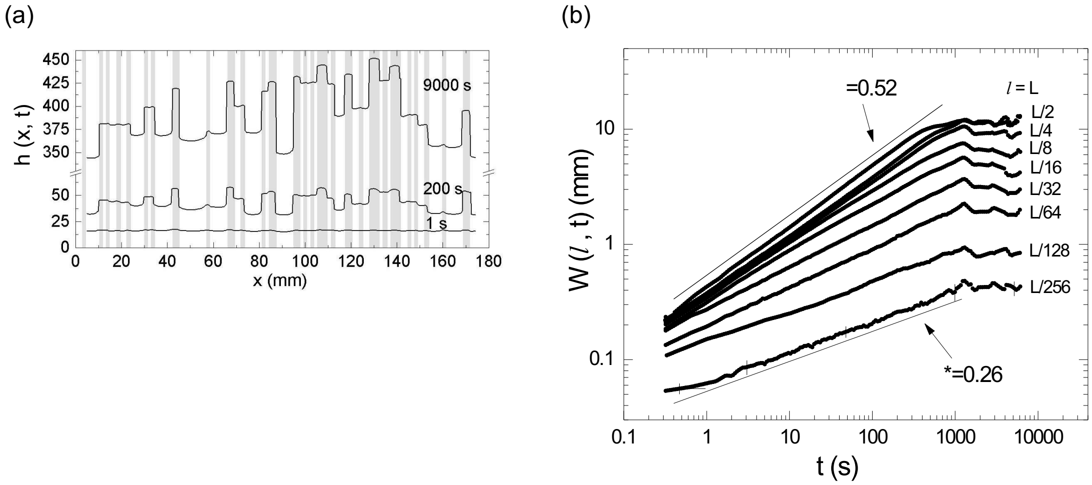

Figura 1.11: (a) Interfícies obtingudes en experiments amb desordre columnar. (b) Determinació experimental de β i β^*. El tamany de finestra l decreix de L a $L/256$. Els paràmetres experimentals són $b = 0.36$ mm i $v = 0.08$ mm/s.

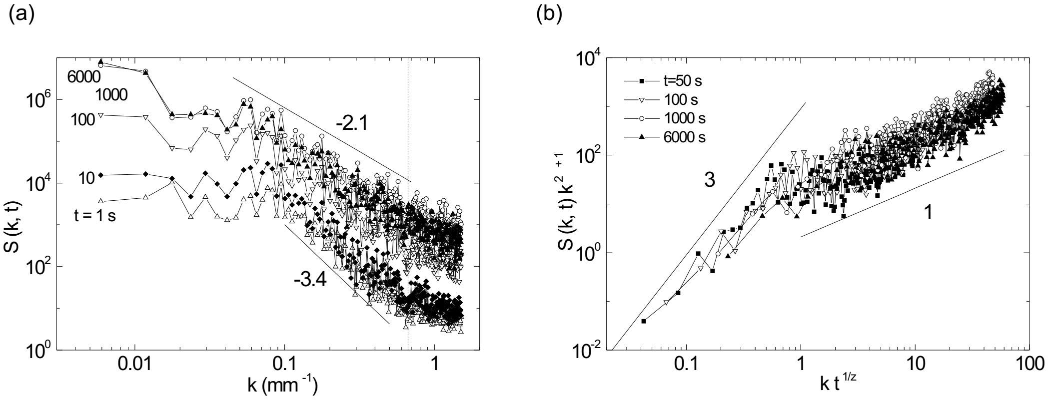

Figura 1.12: (a) Evolució temporal de l'espectre de potències pels mateixos experiments que en la Fig. 1.11(b). La línia vertical dóna el valor de k associat amb el tamany lateral de la pista de coure unitat. (b) Col·lapse de l'espectre de potències per $t > 10$ s.

l'acoblament en la dinàmica de la interfície entre pistes veïnes. Hem observat que un règim que es pugui descriure mitjançant un escalament dinàmic no es pot identificar quan una modulació regular de l'espaiat entre plaques és introduït o quan les forces capil·lars són dominants.

Per tal de conèixer el rang de validesa de l'anomalia hem explorat en profunditat com es veuen afectats els diferents exponents d'escalament segons quin sigui l'espaiat entre plaques, la velocitat de la interfície i la configuració del desordre. Tres diferents regions amb diferents tipus d'escalament s'han trobat:

1. Per forces capil·lars dominants hem obtingut que un règim d'escalament no pot ser caracteritzat degut a l'absència d'una longitud de correlació que creixi en la direcció x. El mateix resultat s'obté per forces capil·lars dèbils quan una modulació regular de l'espaiat entre plaques és introduït.

2. Per forces capil·lars fortes (però no dominants) i per velocitats per sota un valor llindar hem caracteritzat una regió on l'escalament és clarament anòmal. Encara que els exponents d'escalament depenen dels paràmetres experimentals, hem obtingut valors al voltant de $\beta = 0.50 \pm 0.04$, $\beta^{\star} = 0.25 \pm 0.03$, $\alpha = 1.0 \pm 0.1$, $\alpha_{loc} = 0.5 \pm 0.1$ i $z = 2.0 \pm 0.2$. Per velocitats per sobre un valor llindar l'escalament anòmal és inobservable, i una descripció mitjançant Family-Vicsek és més acurada.

3. Per forces capil·lars dèbils i per a qualsevol velocitat l'escalament de les fluctuacions interficials segueix Family-Vicsek.

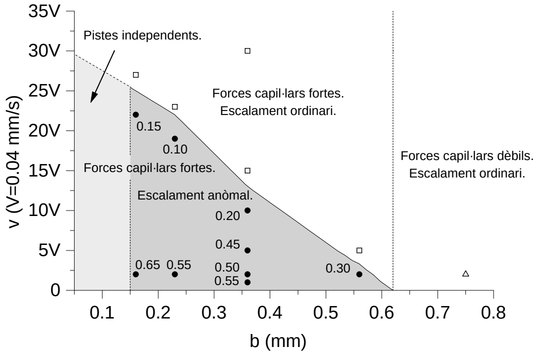

Figura 1.13: Diagrama de fases per a l'escalament anòmal. Els símbols indiquen els paràmetres explorats experimentalment. Els números adjacents als símbols en la regió d'escalament anòmal donen el valor de $2\theta/z$. La línia continua representa la corba $v = v_M(b)$.

Les diferents regions es poden representar en el diagrama de fases d'escalament anòmal que es mostra en la Fig. 1.13.

1.2.4 Resultats experimentals a pressió constant

En el sistema experimental hem reemplaçat la bomba d'injecció per un sistema de pressió constant consistent en una columna d'oli de silicona d'alçada H seleccionable (Fig. 1.14). Hem fet experiments explorant diferents alçades, amb un espaiat entre plaques fixat a $b = 0.36$ mm i un desordre SQ 1.50. Hem observat que la posició mitjana de la interfície, $\langle h\rangle(t) = \langle h(x,t)\rangle_x$, segueix la llei de Washburn $\langle h\rangle(t) \sim t^{1/2}$ (Fig. 1.15(a)). Per a un valor crític de l'alçada de la columna d'oli, $H_c \simeq -25$ mm, la interfície es troba a prop del punt d'ancoratge i la velocitat mitjana de la interfície és zero. Per a valors d'$H > H_c$ la interfície sempre avança. A prop d'H_c la interfície presenta ancoratge local i algunes regions de la interfíce avancen en forma d'allaus (Fig. 1.15(b)).

Hem mesurat els exponents de creixement β i rugositat α. Per $H = -17$ mm, a prop d'H_c, hem mesurat $\beta = 0.64 \pm 0.03$ (Fig. 1.16(a)). Aquest valor gran de l'exponent de creixement l'atribuïm a dos factors: i) la velocitat mitjana de la interfície decau en el temps segons la llei de Washburn, i ii) al ser la interfície moguda a pressió constant permet que el fluid disposi de tota la massa que requereixi per crèixer, en contrast amb els experiments a injecció constant, on hi ha un flux limitat de massa donat per la bomba d'injecció. L'exponent de rugositat a temps llargs dóna $\alpha = 0.7 \pm 0.1$ (Fig. 1.16(b)) i s'extèn a totes les escales, en contrast amb els experiments a injecció constant on apareixia clarament un punt de crossover k_c. A temps molts curts mesurem $\alpha = 1.1 \pm 0.1$, el qual és degut a l'alta velocitat de la interfície a temps curts. Estudiant la variació de l'esponent de rugositat en funció de diferents pressions aplicades (diferents H) hem vist que a mesura que ens acostem a H_c l'exponent de rugositat tendeix a un valor limit al voltant d'$\alpha = 0.6 - 0.7$. Aquest resultat, juntament amb $\beta \simeq 0.64$ suggereixen que en el punt crític podriem tenir una dinàmica local descrita per la classe d'universalitat DPD (o QKPZ), amb $\alpha = \beta = 0.63$.

1.3 Conclusions i perspectives futures

1.3.1 Conclusions

1. Hem desenvolupat una tècnica basada en la tecnologia de circuit imprès per a dissenyar un soroll congelat (*obstacles de coure*) d'alçada constant d i amb propietats estadístiques ben controlades. Tres tipus de configuracions de desordre, amb creixent longitud de persistència en la direcció de creixement, han estat investigades.

2. Hem dissenyat un sistema experimental per estudiar la dinàmica del desplaçament estable d'una interfície oli–aire en una cel·la de Hele–Shaw que conté un soroll congelat en la placa inferior. El procés de rugositat s'esdevé com a conseqüència de la competició entre les forces estabilitzadores del camp de pressió viscosa en el fluid i la tensió superficial en el pla de la cel·la, i les forces capil·lars desestabilitzadores degudes a la diferent corbatura del menisc en la direcció z com a conseqüència de la presència del desordre. Les forces capil·lars es controlen mitjançant l'espaiat entre plaques b, mentre que les forces viscoses es controlen mitjançant la velocitat externa v.

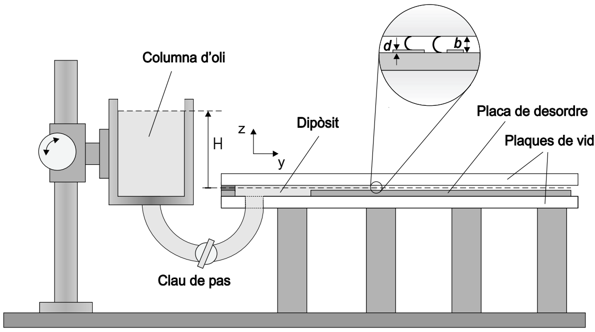

Figura 1.14: Detall del muntatge experimental a pressió constant.

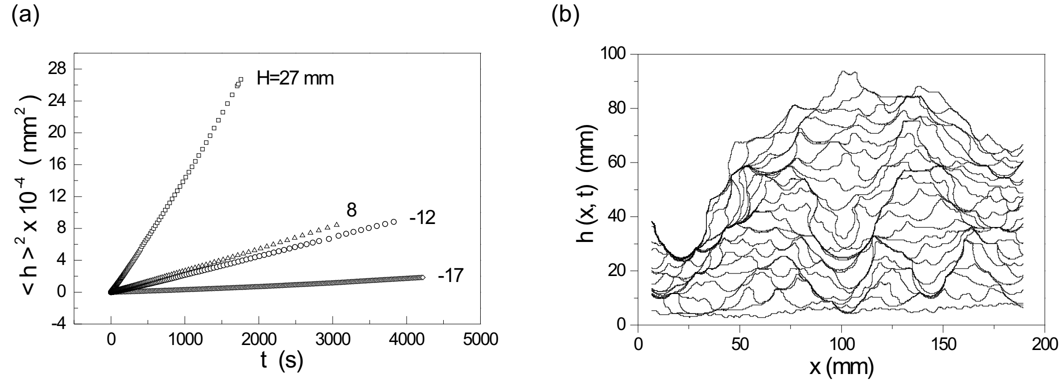

Figura 1.15: (a) Representació de $\langle h \rangle^2(t)$, que ha de seguir un comportament lineal si es compleix la llei de Washburn. (b) Evolució temporal d'interfícies per $H = -17$ mm. Les interfícies estan representades cada 120 s.

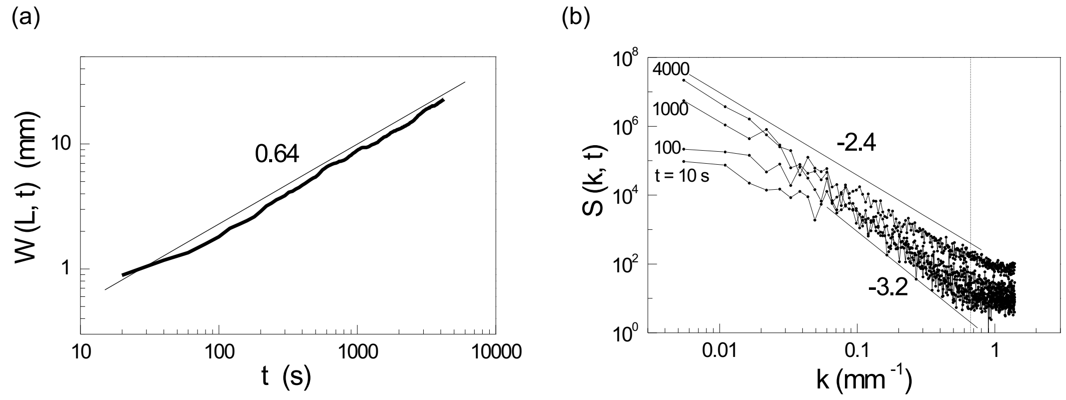

Figura 1.16: Resultats experimentals per als experiments a pressió constant. (a) Amplada mitjana en funció del temps. (b) Evolució temporal de l'espectre de potències. La línia vertical en (b) representa el valor de k associat a l'escala lateral del desordre.

3. Hem desenvolupat diferents eines informàtiques per tal de controlar el *hardware* d'adquisició d'imatges, seguir l'evolució de la interfície oli–aire, i processar les imatges adquirides i les dades obtingudes.

4. Hem fet experiments a injecció constant i a pressió constant. Pel primer cas la velocitat de la interfície es controla mitjançant una bomba d'injecció programable, mentre que en el segon cas la pressió constant es manté gràcies a una columna d'oli d'alçada regulable.

5. Hem caracteritzat la permeabilitat de la cel·la per diferents configuracions de desordre i per diferent grau de forces capil·lars. Per una gran separació entre plaques (forces capil·lars dèbils) recuperem la permeabilitat d'una cel·la de

Hele–Shaw ordinària, independentment de la configuració de desordre. Per una separació entre plaques petita, la permeabilitat és fortament depenent de la configuració de desordre. En aquest límit, quan el desordre consisteix en pistes de coure, hem derivat una expressió analítica per a la permeabilitat que està d'acord amb prediccions teòriques. Hem deduït també una expressió pel nombre de capil·laritat modificat, Ca', que mesura la força relativa de les forces viscoses respecte a les forces capil·lars en la cel·la amb desordre.

6. Hem fet experiments explorant diferents configuracions de desordre, separació entre plaques i velocitats d'injecció. Hem obtingut, per una banda, diferents exponents d'escalament quan la interfície és desplaçada a injecció constant que quan és desplaçada a pressió constant. Per altra banda, els exponents d'escalament depenen fortament de la intensitat del desordre, i dos grans famílies de resultats es poden caracteritzar, aquells amb soroll congelat *dèbil* i aquells amb soroll congelat *fort*.

7. Els resultats experimentals amb soroll congelat *dèbil* estan caracteritzats per uns exponents d'escalament de les fluctuacions interficials que són apropiadament descrits en el marc de l'escalament dinàmic de Family–Vicsek. Corresponen a paràmetres experimentals caracteritzats per velocitats de la interfície grans, separació entre plaques gran, o curta longitud de persistència del desordre en la direcció de creixement. En aquestes condicions hem mesurat $\beta \simeq 0.50$ gairebé independentment dels paràmetres experimentals. Els exponents de rugositat són sensibles als paràmetres experimentals i dos règims, α_1 a escales de longitud petites, i α_2 a escales de longitud grans, han estat caracteritzats. La longitud de *crossover* que separa els dos règims escala amb la velocitat com $\sim v^{-0.47}$. En el límit de velocitats de la interfície molt grans aquests exponents tendeixen assimptòticament a $\alpha_1 \simeq 1.3$ i $\alpha_2 \simeq 0$.

8. Els resultats experimentals amb desordre congelat *fort* estan caracteritzats per escalament anòmal intrínsec. Corresponen a paràmetres experimentals en els que el desordre és totalment persistent en la direcció de creixement (pistes), i les forces capil·lars i viscoses estan ben equilibrades. En aquestes condicions hem mesurat $\beta \simeq 0.50$, $\beta^* \simeq 0.25$, $\alpha \simeq 1.0$, $\alpha_{loc} \simeq 0.5$ i $z \simeq 2.0$. Un estudi acurat de la dinàmica de la interfície en les pistes ha permès fer una descripció de l'escalament anòmal en termes de i) la velocitat de la interfície en pistes de coure (v_+) i canals de fibra de vidre (v_-), que es pot expressar de forma compacta com $v_\pm = v \pm (v_M - v)\, t^{-1/2}$; i ii) l'acoblament en el moviment de la interfície

entre pistes veïnes. Un règim caracteritzat per un escalament dinàmic no es pot caracteritzar quan una modulació regular de l'espaiat entre plaques és introduït o quan les forces capil·lars esdevenen dominants. L'escalament anòmal desapareix per grans velocitats de la interfície (forces viscoses dominants), separació entre plaques gran (forces capil·lars dèbils) o quan la persistència del desordre en la direcció de creixement és reduïda.

9. La presència d'escalament anòmal ha estat confirmada, i els exponents d'escalament refinats, mitjançant anàlisis complementàries, que inclouen el creixement de les pendents mitjanes, multi–escalament i la distribució estadística de diferències d'alçada.
10. Hem fet experiments on les úniques forces que intervenen són les forces capil·lars (injecció aturada), i trobat que la velocitat en una sola pista ve donada per la llei de relaxació $v = v_M \; t^{-1/2}$, amb v_M una empenta inicial.
11. Hem desenvolupat experiments a pressió constant i explorat el règim de forces capil·lars dèbils. Hem mesurat que la velocitat mitjana de la interfície segueix la llei de Washburn, $v \sim t^{-1/2}$. Diferents règims s'han observat depenent de la pressió aplicada. Per a un valor crític de la pressió el sistema està a prop del punt d'ancoratge, i la velocitat mitjana de la interfície és zero. Per valors lleugerament superiors a aquest valor crític la interfície pot esdevenir localment ancorada, i en aquestes zones la interfície avança mitjançant allaus. En aquestes condicions hem obtingut uns exponents d'escalament $\beta \simeq 0.64$ i $\alpha \simeq 0.7$, que són diferents dels obtinguts prèviament a injecció constant.

1.3.2 Perspectives futures

1. **Confirmació experimental de l'escalament genèric.** L'escalament genèric proposat per Ramasco i col·laboradors en la Ref. [RLR00] descriu quatre tipus d'escalament dinàmic. Nosaltres hem observat experimentalment Family–Vicsek i escalament anòmal intrínsec. Seria interessant d'investigar altres tipus de desordre i condicions experimentals que ens permetessin obtenir súper-rugositat i *faceted surfaces.*
2. **Confirmació de prediccions teòriques de Pauné i Casademunt**. Resultats teòrics recents de rugositat en fluxos de Hele–Shaw amb una modulació de l'espaiat entre plaques, obtinguts per Pauné i col·laboradors [PC02; Pau02] donen unes prediccions pels exponents d'escalament β i α que en alguns casos

particulars estan d'acord amb els resultats experimentals. No obstant, les prediccions teòriques estan basades en el fet que les parets dels obstacles de coure són de pendent suau, és a dir $\nabla b \ll 1$. Es pot satisfer aquesta condició en el nostre cas a base de cobrir les nostres plaques de desordre amb una pel·lícula de plàstic, el que suavitzarà les parets dels obstacles de coure. En particular, Pauné i Casademunt van mostrar que per un soroll persistent (pistes) no hi ha observació d'escalament anòmal. Experiments que hem realitzat recentment (utilitzant les plaques habituals de desordre però cobrint-les amb una pel·lícula de plàstic) donen uns resultats que estan d'acord amb aquestes prediccions. Aquests experiments seran realitzats en el futur explorant diferents valors de l'espaiat entre plaques i velocitats d'avanç de la interfície.

3. **Investigacions a pressió constant**. El nostre muntatge experimental a pressió constant és molt convenient per a fer experiments de caracterització d'allaus i la transició d'ancoratge/desancoratge. No obstant, encara que hem començat a fer un estudi en aquests problemes, hem observat que aquests experiments són complexes i requereixen molt més temps, pel que es desenvoluparan en profunditat en els pròxims anys.

Altres experiments que es poden realitzar amb el nostre muntatge experimental són els següents.

1. **Mullat com a font del desordre**. Seria interessant realitzar experiments d'escalament anòmal on les forces capil·lars desestabilitzadores, enlloc de provenir de la diferent curvatura del menisc a sobre coure i fibra de vidre, provingués de diferents condicions de mullat. El muntatge experimental consistiria en una cel·la de Hele-Shaw ordinària on les plaques superior i inferior serien tractades per tal de tenir una distribució aleatòria de pistes, unes amb mullat perfecte i les altres sense.

2. **Pinçament**. Un fet interessant que hem observat en els experiments d'escalament anòmal es el problema del pinçament (*pinching*). Per a pistes de coure suficientment estretes hem observat que l'oli que hi avança pateix un pinçament per a una separació entre plaques suficientment petita. La nostra tècnica de generar un desordre columnar utilitzant la tècnica de circuit imprès més el nostre sistema experimental són ideals per a estudiar aquest problema en profunditat utilitzant pistes de diferent gruix i diferent espaiat entre plaques.

3. **Experiments amb fluids viscoelàstics**. Alguns problemes en biofísica es poden modelar com un flux d'un fluid viscoelàstic en una cel·la de Hele–Shaw amb desordre congelat. Un exemple podria ser el flux d'actina a través del citoesquelet d'una cèl·lula viva. El nostre sistema experimental és adequat per a desenvolupar aquesta mena d'investigacions.

Part II

Thesis

Chapter 1

Introduction

1.1 Presentation

The work presented in this thesis started as an experimental collaboration with the theoretical investigations that Hernández–Machado and coworkers were carrying out. This initial collaboration provided our first publication [HMSL^{+}01]. The results obtained stimulated us to investigate in deep different experimental conditions in the limit that we called *weak quenched disorder*, and explored the transition from *weak* to *strong quenched disorder*. This led to our second publication [SOHM02b]. From these experimental results we observed that, for a convenient set of experimental parameters, the scaling of the interfacial fluctuations changed from a Family–Vicsek description to anomalous scaling. We characterized the anomaly, its physical origin, and the experimental conditions in which it appeared. This provided our third [SRR^{+}02] and fourth [SOHM02a] publications. Finally, for completeness, we performed experiments at constant pressure and obtained different results from those reported at constant injection rate. These results are presented as a preprint pending for publication [SOHM03].

The outline of the thesis is as follows. In this Chapter we give a general introduction to the problem of rough interfaces and their description. Some experimental results performed in the last years are also presented, as well as some relevant theoretical results. In Chapter 2 we present our experimental setup. A summary of the experimental results is given in Chapter 3. Chapter 4 contains a copy of the publications and preprints where the experimental results of this thesis have been published. The final conclusions and future perspectives are given in Chapter 5. Appendices A and B contain a description and basic documentation of the different software tools that have been developed during these years for the experimental task, such as image and data analysis, design of the disorder medium, and the programming of the images acquisition hardware.

1.2 Rough surfaces and interfaces in nature

Any person that opens the eyes and takes a look to the world that surrounds him or her will realize that our life takes place in a world of surfaces. Some of them can be described at a first look as smooth, such as a desk or a window glass. And others as rough, such as a teared sheet of paper or the shape of a mountain in the horizon. However, the terms *smooth* and *rough* are not always well defined when talking about surfaces. An astronaut sees Earth as a smooth blue ball, but Earth appears to be anything than smooth when climbing the Himalaya. And a pearl is a beautiful white sphere that looks like the surface of the Moon when observed under the microscope. Thus, the appearance of many surfaces depend on the scale of observation, and how a surface looks like at different scales is the first step to describe its properties. The second step could be understanding the origin and the dynamics of the roughening process.

Rough surfaces or interfaces are present in several natural and technological processes, and play an important role in many phenomena of scientific interest and practical importance. Most of the physical processes that lead to the formation of rough interfaces take place under non–equilibrium conditions. Some examples are as familiar as the advance of spilled coffee over a tablecloth, the shape of a mountain, or the advance of a fire front in a forest. Other examples include the growth of bacterial colonies [MM96; VCH90; BJCST95], the growth or erosion of surfaces (such as electrodeposition [HS01], sputtering [JZC96] or molecular beam epitaxy [YWL94]), fracture in solids [LS98; MSBV00], or the immiscible fluid–fluid displacement in a disordered media [REDG89; Won94; ZMOW97]. Pictures of some of these examples are shown in Fig. 1.1.

A general feature of these interfaces is that they typically present power law correlations both in space and in time, so that their study shares many features with that of equilibrium critical phenomena [BS95]. Therefore a relevant part of the effort to understand these systems consists in extending the powerful theoretical tools which describe critical systems to non-equilibrium interfacial growth. Another feature of these interfaces is that, except for particular cases, it is not possible to relate easily the microscopic dynamics of the system with the morphology and properties of the rough interface generated. Thus, interfaces are described by means of their scale–

invariance properties, and characterized with what is called scaling exponents. In some situations, systems that are different in their internal dynamics can be described with the same scaling exponents. In this case we say that they belong to the same universality class.

The framework of this thesis is the study of fluid interfaces in a disordered medium. The typical experiment consists in studying the dynamics of a fluid that gets into

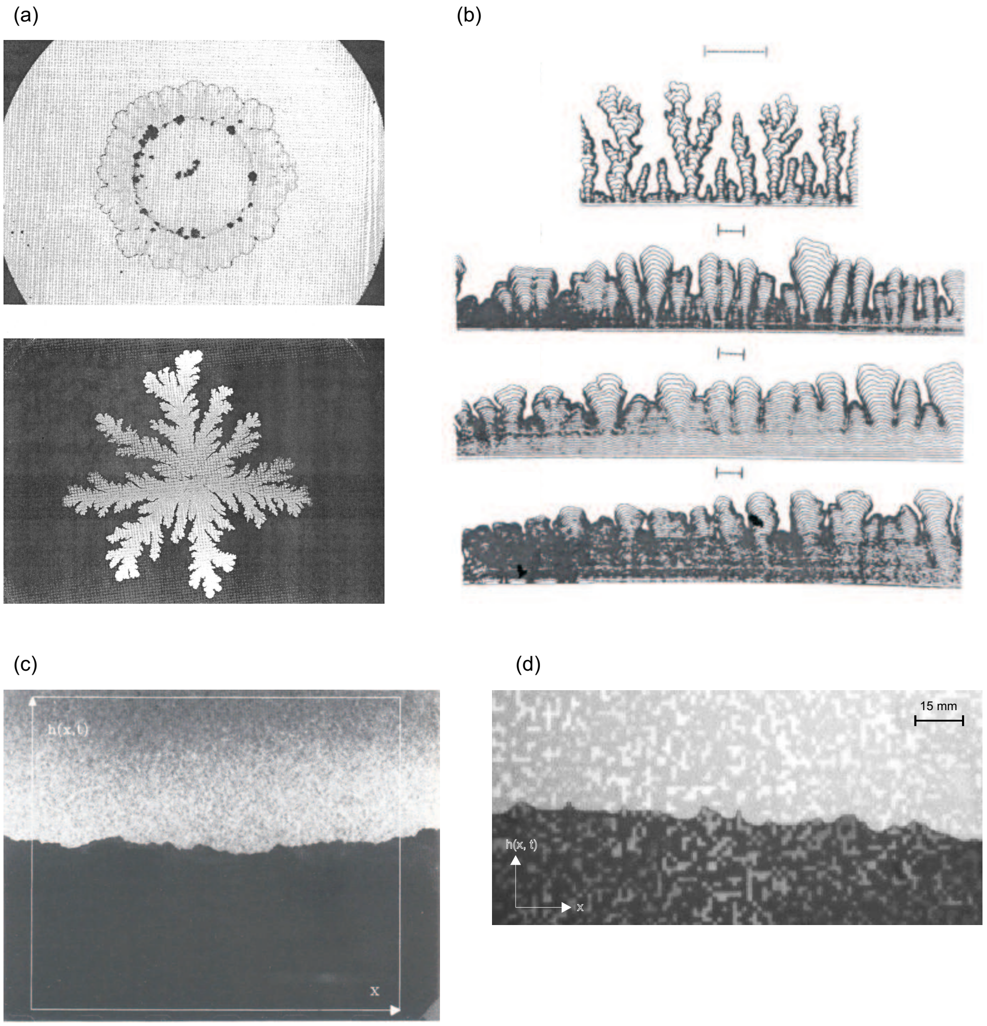

Figure 1.1: Different examples of interfaces. (a) Growth of bacterial colonies, where it is possible to observe both compact structures (top image, obtained from Ref. [BJST^{+}94]) and ramified structures (bottom image, obtained from Ref. [MF90]). (b) Temporal evolution of interfaces obtained from experiments on electrochemical deposition. The interfaces evolve from ramified to compact as the potential is increased (from [KZFW92]). (c) Front of burning paper advancing in the vertical direction (from [ZZAL92]). (d) Oil–air interface advancing in a disordered media. The latter is an example of the kind of experimental work carried out in this thesis.

a porous medium initially occupied by another fluid. The former is called invading fluid, while the latter receding or defending fluid. If the two fluids are immiscible there is an interface that separates them. The morphology of the front changes radically depending on the properties of both fluids, i.e. the respective viscosities and the effectiveness of each fluid wetting the medium. If the invading fluid is forced to get into the medium at constant injection rate the process is called *forced fluid invasion*. If the invading fluid is forced to get into the medium at constant pressure the process is called *forced imbibition* when the invading fluid wets preferentially the medium, and *forced drainage* when the receding fluid wets preferentially the medium.

Two basic kinds of behaviors can be observed [Won94]:

i) The invading fluid is less viscous than the receding fluid. In this case the invading fluid penetrates deep into the other fluid and the front adopts a finger–like configuration. This process is known as Saffman–Taylor instability [ST58] or *viscous fingering*. The structures that can be observed are strongly dependent on the wetting properties of the fluids present in the media [SWG$^+$86]. In many cases the dynamics of the interface takes place in porous media of strong complexity and difficult characterization [dG78; Won98; Sah95; Dul91], and gives rise to percolative processes [BL77; WW83; MFJ85; RZ85; BFJ$^+$91; CRS94]. In addition, this problem has received important attention and interest due to its relation with petroleum recovery [bPES81], and has been studied in depth from both theoretical and experimental points of view, as well as with numerical models. Another interesting process, characterized by the absence of an interfacial tension, is diffusion–limited aggregation, DLA [WS81; Pat84], and leads to the formation of branches or filaments.

ii) The invading fluid is more viscous than the receding fluid. In this case the front of advance of the interface is compact and there is no trapped fluid or it is negligible, and the rough surface that is formed is continuous. The most interesting examples of this phenomenon are the experiments known in general as *immiscible fluid displacement in porous media*, where a less viscous fluid, usually air, is displaced by a more viscous fluid, such as water, ink, glycerol, or mineral oils. The classical experiments are those performed in Hele–Shaw cells filled with glass beads [REDG89; HFV91; HKW92] and paper wetting [BBC$^+$92; BBH$^+$92]. In this last group it is usual to include the experiments known as paper burning [ZZAL92; MMK$^+$97] and paper rupturing [KHW93]. Other experiments that give rise to compact structures are fracture of brittle materials [MHH92], such as cement [KYK97], granite [LS98] or wood [MSLV98]. In all these cases, although the physics behind the different process are different, the interfaces obtained allow a similar mathematical description.

The displacement of a less viscous fluid by a more viscous one in a disordered medium is the framework of this thesis. We review in the next sections how a rough interface is statistically characterized. The generic dynamic scaling that describes them is presented. Two relevant particular cases for this thesis, Family–Vicsek and anomalous scaling, are described in more detail. The most important experimental results are also revised. Finally, we will introduce some theoretical aspects that are important for our experimental work.

1.3 Self–similar and self–affine fractals

Fractals [Fed88; VSM94; KV94] were studied at the first time by the end of 19th century. Initially a mathematical curiosity, as science evolved and changed the vision of the world, scientists realized that there were many structures in nature that satisfied fractal properties, both at large scales, such as the growth of mountains, and at small scales, such as the growth of bacterial colonies or the deposition of particles over a substrate. In the growth of rough interfaces, fractals are the fundamental tool to describe them from a mathematical point of view.

1.3.1 Self–similar fractals

A self–similar fractal is an object that is invariant under an isotropic transformation, i.e. it keeps its appearance under an enlargement or reduction equal in all directions. The Norwegian coast, a bacterial colony, or a group of clouds are examples in nature of self–similar fractals. The mathematical problem of these structures is that we cannot determine the length or the area that they occupy. Thus, if we consider for example a circle of perimeter $L_0 = 2\pi r$, where r is the radius of the circle, we can determine its length by simply covering the curve with segments of length δ. The number of segments $N(\delta)$ will tend asymptotically to L_0 as $\delta \to 0$. If we apply this method, known as *box counting* [Fed88] to the Norwegian coast, the method fails because $N(\delta)$ diverges when $\delta \to 0$. Thus, we cannot measure its length. However, we can give some parameter to characterize the fractal structure. This parameter is what is called fractal dimension or Hausdorf-Besicovitch dimension, D, in such a way that $N(\delta) \sim 1/\delta^D$.

Self–similar fractals do not have an integer dimension, contrary to simple structures (a point has $D = 0$, a line $D = 1$, a square $D = 2$, a cube $D = 3$, and so on). The Norwegian coast has $D = 1.52$, between a line and a surface.

The examples of rough interfaces shown in the point (i) of Sec. 1.2 are described by self–similar fractals, and the different structures observed are usually characterized by the fractal dimension D. To this respect, it has been measured $D = 1.82$ for some invasion percolation processes, and $D = 1.71$ in DLA (in two dimensions).

1.3.2 Self–affine fractals

A fractal is self–affine when it is invariant under an anisotropic transformation (different in all directions) [FV91]. If one direction is changed a factor b, $x_1 \rightarrow bx_1$, then the other directions must be rescaled a factor b^{α_i}, $x_i \rightarrow b^{\alpha_i} x_i$ in order to keep the structure invariant. The exponents α_i are known in general as Hurst exponents and give a measure of the degree of the anisotropy. A particular case that is especially relevant for the study of rough interfaces is when all directions are equivalent except one, the direction of growth. Then, there is only one Hurst exponent, and it is called roughness exponent.

In the context of growing interfaces, the simplest situation of self–affine fractal allows a description of the surface by means of a unique, single–valued function that depends only on the position $h(x_1, x_2, ..., x_i)$ and obeys the condition $h(\vec{x}) = b^{-\alpha} h(\vec{x})$. An example of a self–affine surface is shown in Fig. 1.2(a).

1.4 Statistical description of a rough interface

Let us consider a surface of dimension $d = 1$ (where $D = d + 1$ is the dimension of the physical system) that grows in time. If the interface allows a characterization as a self–affine fractal, it can be described by a single–valued function $h(x, t)$ that gives the height of the points of the interface at position x and time t (Fig. 1.2(b)). The condition of single–valuation is essential but not always strictly accomplished. Thus, it is frequent to deal with possible multivaluations in the system, known in general as *overhangs*. For self–affine interfaces, the problem of overhangs is usually solved taking the highest value of h in the surface.

In order to characterize completely a rough surface of lateral size L three length scales are necessary. As shown in Fig. 1.2(b), these scales are: the average position of the interface $\langle h \rangle$, its interfacial width w, which measures the *rms* fluctuations of the interface around its mean value, and a correlation length $\xi(x)$ parallel to the surface. This correlation length measures the distance at which a point of the interface is correlated with another. The quantity w can be understood as a correlation length in the direction of growth. Usually we are interested in the study of the statistical properties of the interface in systems of lateral size L and in subsystems or windows of lateral size l, with $l < L$. The interfacial *rms* width w for a region of lateral size l at time t is given by

$$w(l,t) = \langle \frac{1}{N}\sum_{i=1}^{N} h(x_i,t)^2 - (\frac{1}{N}\sum_{i=1}^{N} h(x_i,t))^2 \rangle_j^{1/2}, \tag{1.1}$$

where $N = l/\Delta$, with Δ the sampling interval. $\langle \cdots \rangle_j$ indicates an average over all origins of the window j. The quantity $w(l,t)$ is frequently referred in the literature as the *roughness* of the interface. We will call *global roughness* $w(L,t)$ the interfacial *rms* width calculated over the system size L; and *local roughness* $w(l,t)$ the interfacial *rms* width calculated over a window of lateral size $l < L$. As we will see later, the behavior of global and local scales can be different and give rise to different scaling behaviors and universality classes.

In an ideal situation the interface is flat at $t = 0$, $h(x,0) = 0$, and all points of the interface are uncorrelated, $\xi(t) = 0$. As the interface grows and becomes rough, the correlation length increases until it reaches the system size L, $\xi(t) \simeq L$. In this situation the interface is at saturation and $w(L,t)$ keeps statistically invariant except for small fluctuations. A growing correlation length is essential to

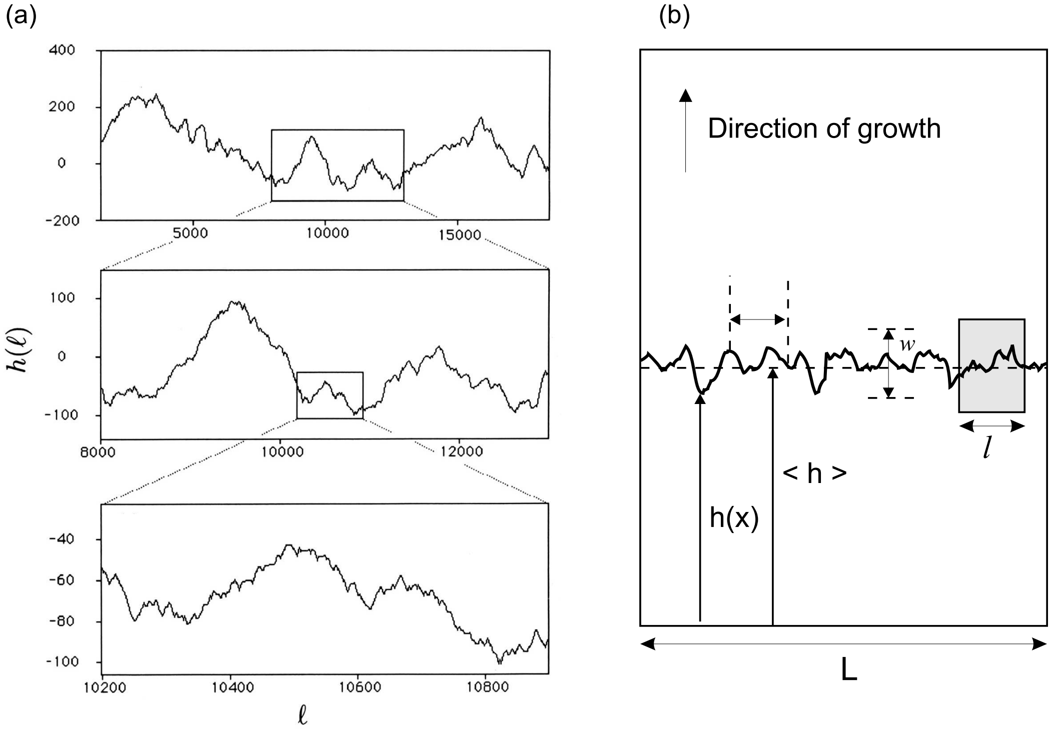

Figure 1.2: (a) Geometrical concept of self–affinity. The window must be rescaled with different factors in the horizontal and vertical direction to keep the surface invariant. (b) Schematic representation of the characteristic scales and magnitudes in a self–affine interface.

describe the growing properties of an interface by means of a dynamic scaling and the corresponding scaling exponents. In particular, one of these exponents is the dynamic exponent z, which provides information about how fast the correlations grow in the system, $\xi(t) \sim t^{1/z}$.

1.5 Family–Vicsek dynamic scaling

How can we characterize the dynamic behavior of a self–affine interface? How can we determine the scaling exponents?

To answer these questions, Family and Vicsek proposed in 1985 [FV85] a dynamic scaling for the global roughness $w(L,t)$. For a bi–dimensional system, this dynamic scaling reads

$$w(L,t) = L^{\alpha} f(L/t^{1/z}), \tag{1.2}$$

where z is the dynamic exponent and $f(u)$ the scaling function

$$f(u) \sim \begin{cases} \text{constant} & \text{if} \quad u \ll 1, \\ u^{-\alpha} & \text{if} \quad u \gg 1. \end{cases} \tag{1.3}$$

Thus, $w(L,t)$ scales as

$$w(L,t) \sim \begin{cases} t^{\beta} & \text{if} \quad t \ll L^{z}, \\ L^{\alpha} & \text{if} \quad t \gg L^{z}. \end{cases} \tag{1.4}$$

L^z characterizes the saturation time, $t_{\times} \sim L^z$, and is the time at which the correlation length has reached the system size L, $\xi(t_{\times}) = L$. α is the roughness exponent, and describes the scaling of the *rms* interfacial fluctuations with system size at saturation. β is the growth exponent and characterizes the growth of global roughness before saturation. These three exponents α, β, and z are not independent but verify the scaling relation $\alpha = z\beta$.

An important feature of the Family–Vicsek (FV) dynamic scaling is that the global scales (different systems of lateral size L) and the local scales (subsystems of lateral size $l < L$) follow the same scaling. Hence, for FV the local interfacial fluctuations verify:

$$w(l,t) \sim \begin{cases} t^{\beta} & \text{if} \quad t \ll l^{z}, \\ l^{\alpha} & \text{if} \quad t \gg l^{z}. \end{cases} \tag{1.5}$$

Fig. 1.3(a) shows schematically the behavior of the interfacial width according to the FV dynamic scaling.

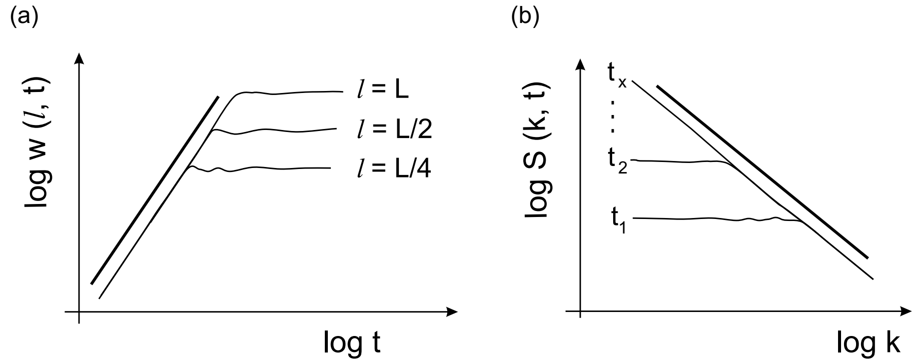

Figure 1.3: Schematic representation of the Family-Vicsek dynamic scaling. (a) Determination of the growth exponent β from the scaling of the interfacial width with time. (b) Determination of the roughness exponent α from the scaling of the power spectrum with the wavenumber k.

In addition to the interfacial width, it is common to study the interfacial growth by means of other quantities. The most frequently used is the generalized height–height correlation function, $C(l,t)$, defined as

$$C(l,t) = \left[\langle (h(l+x,t) - h(x,t))^2 \rangle_x\right]^{1/2}. \tag{1.6}$$

This function scales in the same way as $w(l,t)$ and provides an alternative method to obtain the scaling exponents.

Both the interfacial width, $w(l,t)$, and the height–height correlation function, $C(l,t)$, are functions in the real space that allow to obtain the different scaling exponents. However, different tools have been developed to perform the same description but in the reciprocal space, which is particularly convenient for the determination of the roughness exponent α. The most used is the power spectrum $S(k,t)$, defined as

$$S(k,t) = \langle H(k,t) H(-k,t) \rangle, \tag{1.7}$$

where the notation $\langle \ldots \rangle$ indicates average over disorder realizations, and

$$H(k,t) = \sum_x \left[h(x,t) - \langle h(x,t) \rangle_x\right] e^{ikx}. \tag{1.8}$$

For a bidimensional system the dynamic scaling of FV for the power spectrum reads:

$$S(k,t) = k^{-(2\alpha+1)}\, s_{FV}\left(k\, t^{1/z}\right), \tag{1.9}$$

where the scaling function s_{FV} is given by

$$s_{FV}(u) \sim \begin{cases} u^{2\alpha+1} & \text{for} \quad u \ll 1, \\ \text{constant} & \text{for} \quad u \gg 1. \end{cases} \tag{1.10}$$

At saturation ($k\,t^{1/z} \gg 1$) the power spectrum scales as $S(k,t) \sim k^{-(2\alpha+1)}$. An schematic representation of the power spectrum for the FV scaling is shown in Fig. 1.3(b).

The power spectrum is related with the global roughness $w(L,t)$ through the relation

$$w^2(L,t) = \left(\frac{\Delta}{L}\right)^2 \sum_k S(k,t), \tag{1.11}$$

where Δ is the sampling interval in the x direction. This expression is known as *Parseval identity*, and can also be written for $C(L,t)$, in the form [LRC97]:

$$C(L,t) = \int_{2\pi/l}^{\pi/a} \left[1 - \cos\left(kl\right)\right] \frac{S_{FV}\left(kt^{1/z}\right)}{k^{2\alpha+1}} dk. \tag{1.12}$$

In real space is not possible to measure roughness exponents $\alpha > 1$, except for the scaling of the global roughness as a function of different system sizes [LT93]. This limitation does not exist in the reciprocal space, and for this reason the power spectrum is one of the most reliable tools for the determination of roughness exponents [RH94; SVR95]. However, new investigations carried out in the last years have questioned the effectiveness of the power spectrum for the determination of the roughness exponents, in particular when there are small number of realizations. For this reason, other tools such as the Wavelet Transformation Method [SHN98] are receiving an increasing attention.

There are several growth models, as well as experiments, that follow the scaling ansatz of Family–Vicsek. All the models that can be described using the KPZ equation [KPZ86] or the EW equation [EW82] follow this dynamic scaling. As regards experiments, interfacial growth in burning fronts or bacterial colonies can be usually described using the Family–Vicsek scaling, as well as some experiments of fluid flow in disordered media and fracture of brittle materials.

1.6 Anomalous scaling

Since the introduction of the Family–Vicsek dynamic scaling, new experiments have shown that this scenario is limited. The most relevant experiments include fracture of granite blocks [LS98], fracture in wood [EMHR94; MSLV98; MSBV00], sputtering [JZC96], molecular beam epitaxy [YWL94], and electrodeposition [HS01]. In addition, there are growth models that cannot be completely characterized using the Family–Vicsek description, such as the Wolf–Villain model [SSW$^+$93], solid-on-solid models [Kru94], molecular beam epitaxy models [SLKG96; DSK96], random diffusion models [LR96], models with quenched noise [RH94; ABMS95] and

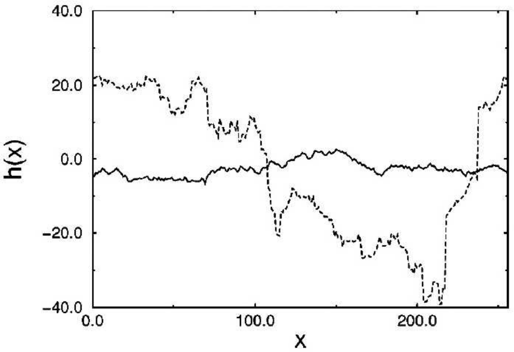

Figure 1.4: Example of two interfaces with the same local roughness exponent but different global one. The solid interface has $\alpha = \alpha_{loc} = 1/2$ and corresponds to the Edward–Wilkinson growth equation. The dashed interface has $\alpha = 3/4$ and $\alpha_{loc} = 1/2$, and corresponds to the random diffusion growth process, which exhibits anomalous scaling. (From Ref. [LS98].)

some nonlocal models [MCSDA98]. In order to fully describe the different dynamic behavior present in these experimental results and growth models, new scaling ansatzs were proposed, and are grouped in what is known as *anomalous scaling* [SSW$^+$93; Kru94; LR96; SLKG96; DSK96; LRC97; MCSDA98].

The origin of the anomaly comes from the different behavior of the interfacial fluctuations at global scales, i.e. with different system sizes L, and at local scales, i.e. with different window sizes $l < L$.

In the Family–Vicsek description, the scaling of the interfacial width is the same for both $w(L,t)$ and $w(l,t)$, i.e. global and local scales follow the same scaling. In anomalous scaling, however, the global roughness behaves as Family–Vicsek, while the local roughness follows a different scaling given by

$$w(l,t) \sim \begin{cases} t^{\beta} & \text{if} \quad t \ll l^z, \\ l^{\alpha_{loc}} t^{\beta^*} & \text{if} \quad l^z \ll t \ll L^z, \\ l^{\alpha_{loc}} L^{\alpha-\alpha_{loc}} & \text{if} \quad L^z \ll t, \end{cases} \tag{1.13}$$

where $\beta^* = (\alpha - \alpha_{loc})/z$ is the local growth exponent, and α_{loc} is the local, anomalous rough exponent. Thus, for anomalous scaling, two more exponents, β^* and α_{loc}, are necessary to characterize the scaling properties of the surface. To illustrate the different roughness exponents that we can find in a surface or interface, Fig. 1.4 shows two interfaces with the same local roughness exponent α_{loc} but different global one α.

In terms of the power spectrum, anomalous scaling is characterized by a new scaling function $s_A(u)$ in Eq. (1.9) given by

$$s_A(u) \sim \begin{cases} u^{2\alpha+1} & \text{for} \quad u \ll 1, \\ u^{2\theta} & \text{for} \quad u \gg 1. \end{cases} \tag{1.14}$$

For times $t \gg t_\times$ the power spectrum scales as $S(k,t) \sim k^{-(2\alpha_{loc}+1)} t^{2\theta/z}$ and not simply as $k^{-(2\alpha+1)}$, as for the ordinary, Family–Vicsek scaling.

Two kinds of anomalous scaling were initially described: *super-roughness* and *intrinsic anomalous scaling*. However, these forms of anomalous scaling were finally grouped in a generic form that included Family-Vicsek, super-roughness, intrinsic, and a new class known as *faceted surfaces* [RLR00; Ram02]. The name *generic* comes from the fact that the different kinds of scaling can be described by means of a generalized height–height correlation function [RLR00].

The generic form of the anomalous scaling is described next. We will focus on the intrinsic anomalous scaling because it will be the scaling ansatz adequate to describe an important part of the experimental results carried out in this thesis.

1.6.1 Global description

In the global description of the scaling of the interfacial fluctuations the global roughness $w(L,t)$ scales as

$$w(L,t) \sim \begin{cases} L^{\beta} & \text{if} \quad t \ll t_\times, \\ L^{\alpha} & \text{if} \quad t \gg t_\times, \end{cases} \tag{1.15}$$

where L is the system size, $t_\times$ the saturation time, β the global growth exponent, and α the global roughness exponent.

The scaling of the height–height correlation function (as well as the local roughness) can be derived, in the generic scaling ansatz, from the integral of the power spectrum for each particular case [Ram02]. For this reason the behavior of $w(l,t)$ will be presented for each particular case.

The generic scaling ansatz in terms of the power spectrum reads

$$S(k,t) = k^{-(2\alpha+1)}\, s\left(k\, t^{1/z}\right), \tag{1.16}$$

where

$$s(u) \sim \begin{cases} u^{2\alpha+1} & \text{if} \quad u \ll 1, \\ u^{2\theta} & \text{if} \quad u \gg 1, \end{cases} \tag{1.17}$$

where θ is an *anomalous* exponent introduced by convenience that measures the degree of the anomaly and is given by $\theta = \alpha - \alpha_s$. The new exponent α_s is the *spectral roughness exponent* and takes different values depending on the different types of scaling, as we will see below.

For the saturated scales, i.e. for $u \gg 1$ ($k \gg k_\times$), the power spectrum scales as $S(k,t) \sim t^{2\theta/z}\, k^{-2(\alpha_s+1)}$, and for times after saturation as $S(k,t) \sim k^{-2(\alpha_s+1)}$.

Depending on the values of α and α_s we have four different types of scaling. These four possibilities can be summarized in the following scheme:

$$\begin{cases} \text{If} \quad \alpha_s < 1 \quad \Rightarrow \alpha_{loc} = \alpha_s \begin{cases} \alpha_s = \alpha & \Rightarrow \text{Family–Vicsek scaling,} \\ \alpha_s \neq \alpha & \Rightarrow \text{Intrinsic anomalous scaling.} \end{cases} \\ \text{If} \quad \alpha_s > 1 \quad \Rightarrow \alpha_{loc} = 1 \begin{cases} \alpha_s = \alpha & \Rightarrow \text{Super–roughness,} \\ \alpha_s \neq \alpha & \Rightarrow \text{Faceted interfaces.} \end{cases} \end{cases} \tag{1.18}$$

The value of the local roughness exponent α_{loc} is derived from the final scaling form of $C(l,t)$ and for each particular case, with the assumption that $C(l,t) \sim l^{\alpha_{loc}}$ for $t > t_\times$.

1.6.2 Intrinsic anomalous scaling

Intrinsic anomalous scaling is present when $\alpha \neq \alpha_s < 1$. The scaling that one gets for $C(l,t)$ and $w(l,t)$ is then

$$w(l,t) \sim \begin{cases} t^\beta & \text{if} \quad t \ll t_l, \\ l^{\alpha_s}\, t^{(\alpha-\alpha_s)/z} & \text{if} \quad t_l < t < t_\times, \\ l^{\alpha_s}\, L^{(\alpha-\alpha_s)} & \text{if} \quad t_\times \ll t, \end{cases} \tag{1.19}$$

with $\alpha_s = \alpha_{loc}$.

One of the implications of the anomalous scaling is that the local roughness saturates at the same time as the global roughness, i.e. at time $t_\times$, and *not* at the local time $t_l \sim l^z$ as occurs in the FV scaling. Anomalous scaling can be easily identified by plotting the interfacial width $w(l,t)$ as a function of time for different window sizes l. According to Eq. (1.19) the different plots will show a vertical displacement proportional to l^{α_s}. An schematic representation of this behavior is presented in Fig. 1.5. It is interesting to note that the exponent β^* appears progressively, displacing the exponent β to shorter times as the window size is reduced. For the smallest window sizes, i. e. the smallest scales, we have a unique growth exponent β^*.

The scaling in terms of the power spectrum $S(k,t)$ reads

$$S(k,t) \sim \begin{cases} t^{(2\alpha+1)/z} & \text{for} \quad k \ll t^{-1/z}, \\ k^{-(2\alpha_s+1)} t^{2\theta/z} & \text{for} \quad k \gg t^{-1/z}, \end{cases} \tag{1.20}$$

with $\theta = \alpha - \alpha_s$.

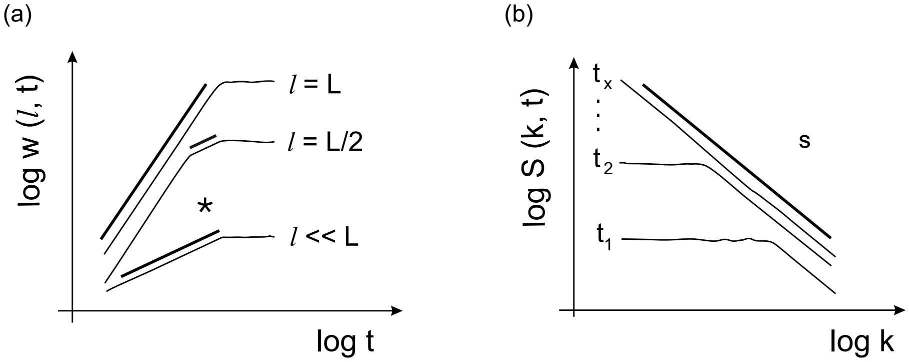

Figure 1.5: Schematic representation of the intrinsic anomalous scaling. (a) Local roughness $w(l,t)$. (b) Power spectrum $S(k,t)$.

The scaling relations that we have for intrinsic anomalous scaling are $\alpha = z\beta$ and $\beta^* = (\alpha - \alpha_s)/z$.

During growth and for the saturated scales ($k \gg k_\times$) the power spectrum scales as $S(k,t) \sim t^{2\theta/z}\, k^{-2(\alpha_s+1)}$. This temporal dependency is responsible for the vertical displacement of the power spectrum at different times. Figs. 1.5(a) and 1.5(b) show an schematic representation of the behavior of $w(l,t)$ and $S(k,t)$ for the intrinsic anomalous scaling.

The intrinsic anomalous scaling has been used to characterize, for example, the models of Random Diffusion Equation [LRC97] and linear MBE, as well as an important group of experiments, such as fracture in wood, sputtering, and MBE.

1.6.3 Super–roughness

An interface presents a super–rough behavior when $\alpha = \alpha_s > 1$. The scaling for $C(l,t)$ and $w(l,t)$ is then [Ram02]:

$$w(l,t) \sim \begin{cases} t^{\beta} & \text{if} \quad t \ll t_l, \\ l\, t^{(\alpha-1)/z} & \text{if} \quad t_l < t < t_\times, \\ l\, L^{\alpha-1} & \text{if} \quad t_\times \ll t. \end{cases} \tag{1.21}$$

The scaling of the power spectrum for super–roughness is given by:

$$S(k,t) \sim \begin{cases} t^{(2\alpha+1)/z} & \text{for} \quad k \ll t^{-1/z}, \\ k^{-(2\alpha+1)} & \text{for} \quad k \gg t^{-1/z}. \end{cases} \tag{1.22}$$

An important characteristic of super–roughness is that the plot of the power spectrum does not present any anomaly. It behaves as Family–Vicsek except for the fact that $\alpha > 1$. Hence, at saturation, $S(k,t) \sim k^{-(2\alpha+1)}$, with $\alpha > 1$. From these

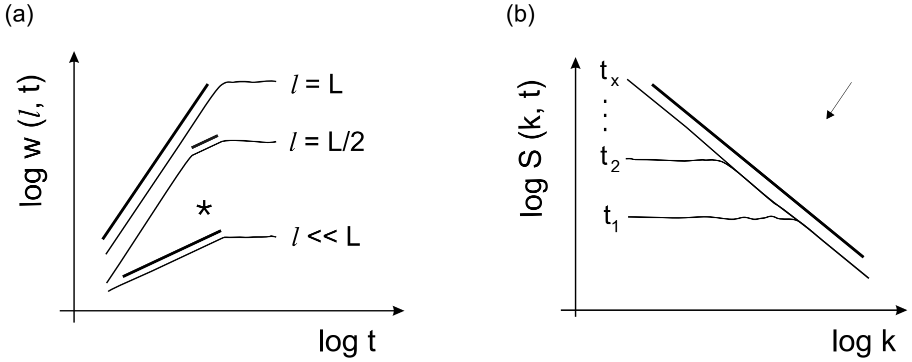

Figure 1.6: Super–roughness. (a) Local roughness $w(l,t)$. (b) Power spectrum $S(k,t)$.

scalings it can be derived that $\alpha_{loc} = 1$. In addition, we have the following scaling relations: $\alpha = z\beta$ and $\beta^* = (\alpha - 1)/z$.

Fig. 1.6 shows an example of the behavior of $w(l,t)$ and $S(k,t)$ for super–roughness.

The most important theoretical examples where an anomalous scaling due to super–roughness has been detected are the models of Molecular Beam Epitaxy [LRC97] and Quenched–EW [KL85; KLT91].

1.6.4 Faceted surfaces

This last case corresponds to $\alpha_s > 1$ and $\alpha \neq \alpha_s$. The scaling that one gets for $C(l,t)$ and $w(l,t)$ is:

$$w(l,t) \sim \begin{cases} t^{\beta} & \text{if} \quad t \ll t_l, \\ l\, t^{(\alpha-1)/z} & \text{if} \quad t_l < t < t_\times, \\ l\, L^{(\alpha-1)} & \text{if} \quad t_\times \ll t. \end{cases} \tag{1.23}$$

The power spectrum scales as

$$S(k,t) \sim \begin{cases} t^{(2\alpha+1)/z} & \text{for} \quad k \ll t^{-1/z}, \\ k^{-(2\alpha+1)} & \text{for} \quad k \gg t^{-1/z}. \end{cases} \tag{1.24}$$

In this case we get $\alpha_{loc} = 1$, as it was obtained for super–roughness. Notice that the fact that $\alpha \neq \alpha_s$ makes faceted surfaces different from super–roughness (where $\alpha = \alpha_s$). A detailed study of the different possibilities that can be observed for the faceted surfaces scaling can be found in Ref. [RLR00]. The Sneppen model (type A) for self–organized depining is the clearest example of interfaces that follow this scaling [RLR00]. The described interfaces are similar to a combination of triangles with the vertices in the direction of growth and with their sides strongly faceted, as it is shown in Fig. 1.7.

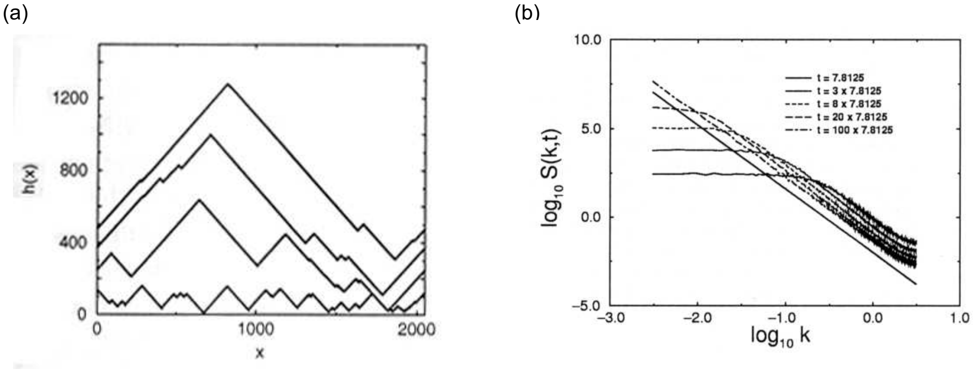

Figure 1.7: Faceted surfaces. (a) Interfaces obtained from the Sneppen A model at different times (from Ref. [Ram02]). (b) Power spectrum $S(k,t)$. The straight line has slope $-(2\alpha_s + 1) = -3.7$. (from Ref. [RLR00]).

1.7 Detection of anomalous scaling

Besides the behavior of the local roughness or the power spectrum, there are other ways to confirm the existence of anomalous scaling or to check the reliability of the scaling ansatzs and the measured scaling exponents. For this reason, we will present here on one hand how the magnitudes $w(l,t)$ and $S(k,t)$ can be rescaled, using convenient scaling functions, to confirm the measured scaling exponents or to refine their numerical value. On the other hand, we will study the behavior of local slopes, multiscaling, and the statistical distributions of height differences as other tools to detect anomalous scaling.

1.7.1 The collapse of $w(l,t)$ and $S(k,t)$

For the case of intrinsic anomalous scaling, we can define a new scaling function for the behavior of $w(l,t)$, in the form $w(l,t)/l^{\alpha} = g(l/t^{1/z})$. From Eq. (1.19), $g(u)$ scales as

$$g(u) \sim \begin{cases} u^{-(\alpha-\alpha_{loc})} & \text{if} \quad u \ll 1, \\ u^{-\alpha} & \text{if} \quad u \gg 1. \end{cases} \tag{1.25}$$

As $\alpha_{loc} = \alpha_s$ we have preferred to use α_{loc} in Eq. (1.25) in order to be consistent with the notation used in our publications [SRR$^+$02; SOHM02a]. This function is very useful to collapse the $w(l,t)$ plots obtained from experiments or numerical simulations and to check if the most appropriate scaling ansatz is Family–Vicsek or anomalous scaling. Notice that for Family–Vicsek the function $g(u)$ should display a plateau for $u \ll 1$ instead of a power law with slope $-\theta = -(\alpha - \alpha_{loc})$. The use of this function is a common procedure in the analysis of experiments of fracture with anomalous scaling [LS98; MSLV98]. An example of the use of this collapse in wood fracture is shown in Fig. 1.8.

The power spectrum for the case of anomalous scaling is given by $S(k,t) = k^{2\alpha+1} s_A(kt^{1/z})$, where $s_A(u)$ is the scaling function

$$s_A(u) \sim \begin{cases} u^{2\alpha+1} & \text{if} \quad u \ll 1, \\ u^{2(\alpha-\alpha_{loc})} & \text{if} \quad u \gg 1. \end{cases} \tag{1.26}$$

Thus, the power spectrum can be collapsed by plotting $s_A = S(k,t)k^{2\alpha+1}$ as a function of $kt^{1/z}$. Notice that for a Family–Vicsek structure factor the collapse will display a plateau for $u \gg 1$.

An example of the collapse of the power spectrum for the random diffusion model, which displays intrinsic anomalous scaling, is presented in Fig. 1.9.

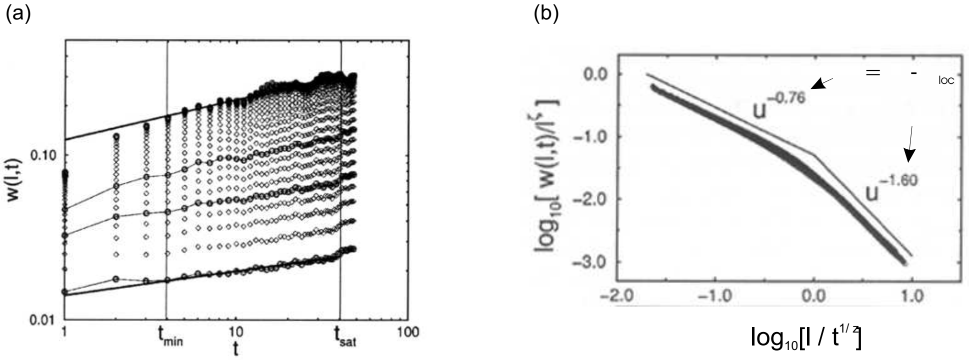

Figure 1.8: (a) $w(l,t)$ plots obtained from experimental data in wood fracture. (b) Collapse of $w(l,t)$ using the scaling function of Eq. (1.25). See Ref. [MSLV98] for details of the plots.

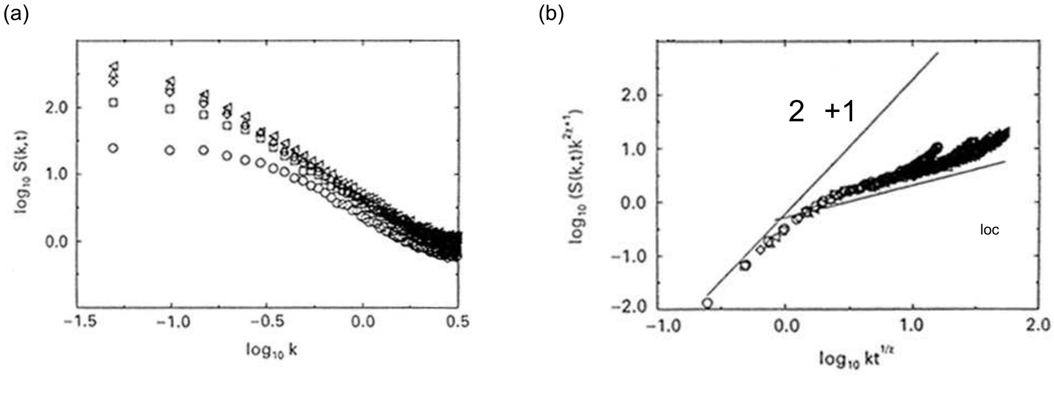

Figure 1.9: Collapse of the power spectrum $S(k,t)$ for numerical results on random diffusion model. (a) Temporal evolution of the power spectrum. (b) Collapse of $S(k,t)$ using the scaling function of Eq. (1.26). See Ref. [LRC97] for details.

1.7.2 Local slopes

Many growth process that can be found in the literature accept a description using continuous equations, such as the KPZ or linear MBE models. For these models, and for some situations, López [Lóp99] showed that it is possible to predict the scaling behavior of the growth process and to calculate the local, anomalous scaling exponents. Suppose that the growth model can be described with the following Langevin–type equation

$$\frac{\partial h}{\partial t} = \Phi\left(\nabla h\right) + \eta(\mathbf{x}, t), \tag{1.27}$$

where $h(\mathbf{x}, t)$ is the height of the interface at position $\mathbf{x}$ and time t, $\Phi\left(\nabla h\right)$ a functional that defines the growth model, and $\eta(\mathbf{x}, t)$ a noise term uncorrelated in both space and time. The local slopes $\rho(t) = [\overline{\langle (\nabla h)^2 \rangle_x}]^{1/2}$, where the brackets denote a spatial average along x and the overbar denotes average over disorder realizations, have a non–trivial dynamics when anomalous scaling is present. Thus, extracting the behavior of $\rho(t)$ provides information about the anomaly of a given growth process.

To obtain the behavior of $\rho(t)$ the procedure proposed in Ref. [Lóp99] is to apply the gradient operator ∇ to Eq. (1.27). We obtain then the equation of motion of the local derivative $\Upsilon\left(\mathbf{x}, t\right) = \nabla h$, of the form

$$\frac{\partial \Upsilon}{\partial t} = \frac{\partial \Phi}{\partial \Upsilon} \nabla \Upsilon + \nabla \eta(\mathbf{x}, t). \tag{1.28}$$

Finally, assuming that $\langle \Upsilon \rangle_x = 0$, $\rho(t)$ is the variance of Υ, which grows with time as $\rho(t) \sim t^{\kappa}$. The exponent κ is $\kappa > 0$ in the case of anomalous scaling and can be identified with the local growth exponent $\beta^{\star}$. For Family–Vicsek scaling, $\kappa < 0$.

As an example, for the growth models introduced before, KPZ follows Family–Vicsek scaling, while linear MBE follows superroughening. For $d = 1$, the above procedure gives $\kappa = -1/5$ for KPZ, and $\kappa = 1/8$ for linear MBE.

From an experimental point of view, the analysis through the mean local slopes provides an alternative way to detect anomalous scaling and to determine the local growth exponent β^{*}.

1.7.3 Multiscaling

Anomalous scaling arises from the different scaling of global and local scales, which are characterized for different roughness exponents, α and α_{loc}. This implies that the interface is not well described as a simple self–affine fractal with a unique roughness exponent. Generalizing this concept, one says that we have multiscaling (or multifractality) in a self–affine interface when the scaling properties of the interface are described by an infinite hierarchy of rough exponents [BV91; BBJ$^+$92; Kru94]. The usual procedure (but not the unique) to determine the series of Hurst exponents is to compute the qth–order correlation function, of the form $C_q(l) = \{(h(x+l,t) - h(x,t))^q\}^{1/q}$. This function scales as $C_q(l) \sim l^{\alpha_q}$, where α_q are local roughness exponents. The values of α_q are progressively smaller as q increases. An example of the behavior of $C_q(l)$ is presented in Fig. 1.10(a), which corresponds to a model proposed by Krug in Ref. [Kru94]. If the features present in the model that lead to multiscaling are eliminated, the scaling of $C_q(l)$ display the same exponent at all orders, as shown in Fig. 1.10(b).

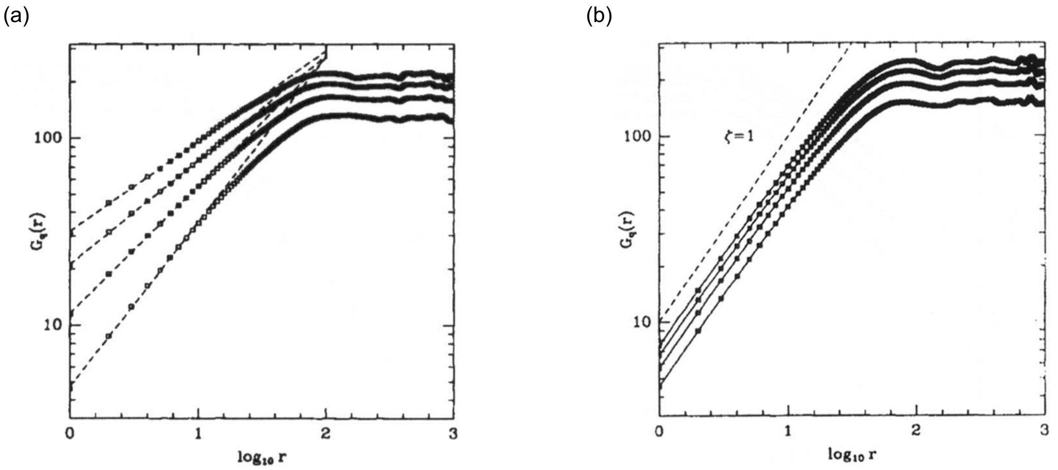

Figure 1.10: Example of the behavior of $C_q(l)$ in presence (a) and absence (b) of multiscaling. In both plots q varies from 1 (bottom curve) to 4 (top curve). Both figures have been obtained from Ref. [Kru94].

A self–affine surface with a correlation function that has multiscaling properties can be constructed, for example, by iteratively replacing the segment of the surface in the step i by a properly rescaled version of a preset initial configuration (Fig. 1.11). This technique was carried out by Barábasi *et al.* in Ref. [BV91], and provides an example of the morphology of the interfaces that present multiscaling.

The origin of multiscaling in many growth processes and models is a consequence of the statistical properties of the disorder. The KPZ equation with a Gaussian noise, for example, does not present multiscaling, i.e. has a unique value of α_q for all q. On the contrary, systems characterized by a quenched disorder spatially distributed following a power law are suspicious candidates of presenting multiscaling [BS95].

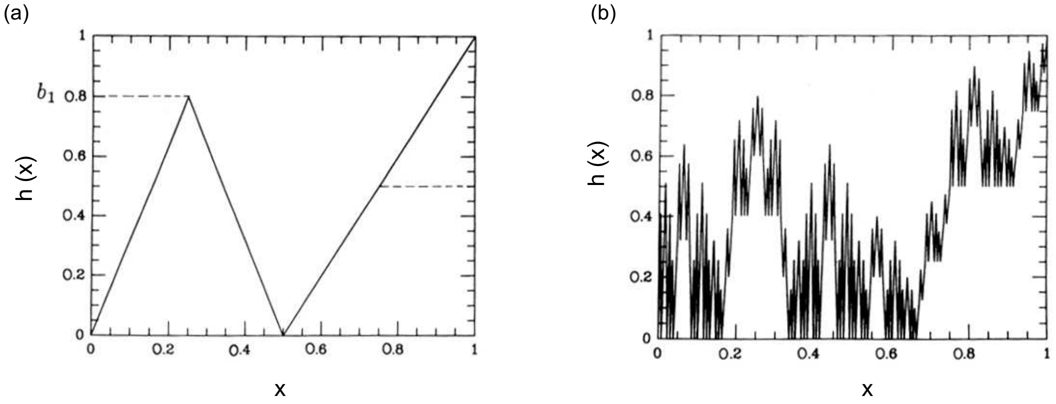

Figure 1.11: Construction of a surface with multiscaling properties. (a) Starting surface. (b) In each step the intervals obtained in the previous steps are replaced with a properly rescaled version of the initial configuration shown in (a). Both plots have been obtained from Ref. [BV91].

1.7.4 Statistical distribution of height differences

In a recent work Asikainen *et al.* [AMDAN02] showed that when the height differences Δh of the interface front $h(x,t)$ follow a Lévy distribution with well defined power law decay, $P(\Delta h) \sim (\Delta h)^{-\gamma}$, with $0 < \gamma < 2$, the interfacial growth presents multiscaling and thus anomalous scaling. For a model that follows ordinary scaling, such as the KPZ equation, the distribution of Δh is Gaussian.

The authors carried out numerical simulations with two models: invasion percolation with trapping (TIP) and no trapping (NTIP). The interfaces profile obtained from the numerical simulation were characterized by large height differences, and overhangs were overcome using the standard procedure of taking the highest value of $h(x)$. They calculated the generalized correlation functions in space and time, and observed that both displayed multiscaling and, thus, anomalous scaling. They observed that the distribution of height differences followed a Lévy distribution with exponent $\gamma = 2$. Using this value of γ they also got an analytical expression for the values of the local growth exponents β_q and the local roughness exponents α_q, suggesting that the former were given by $\beta_q = 1 - 1/q$ for $q > 1$, and the latter by $\alpha_q = 1/q$ for $q \geq 1$.

The interest of this work for our experimental investigations is that it gives an alternative way to check for anomalous scaling. In addition, the kind of interfaces obtained in our experiments of anomalous scaling are characterized by large jumps in the interface profile, similarly to the interfaces presented in the numerical simulations of the TIP and NTIP models.

1.8 Some experiments of growing interfaces in disordered media

There have been many experiments, developed along the last three decades, related to the problem of growth surfaces or interfaces. Since the appearance of the Family–Vicsek dynamic scaling, as well as many theoretical advances on the description of self–affine surfaces, there has been increasing interest to enrich the theoretical investigations with experimental work. And viceversa, new experimental results have led to the proposal of new theoretical models that extended the universality classes. In other cases, novel experimental results have forced to a revision of the scaling concepts for self–affine interfaces, which is the case of the experiments that led to the introduction of the anomalous scaling.

Some experiments consisted in the methodic observation and characterization of natural or familiar processes, such as the growth of bacterial colonies, or the wetting of a paper towel by coffee. Others were motivated by their relevant technological importance, such as epitaxial growth or sputtering; or for their industrial interest, such as fracture of brittle materials or fluid flow through porous media.

The usual analysis in most of the experimental work has been the study of the scaling exponents α, β (as well as the local ones, α_{loc} and β^*, if present) and their dependence with the experimental parameters or material properties. The idea behind most of the experimental work has been to classify the different results in universality classes, which allows the description of different physical systems with the same equations or growth models.

1.8.1 Bacterial colonies

The growth of bacterial colonies were studied by both biologists and physicists in order to understand the cooperative phenomena that leads to the complex structures observed experimentally. However, a unified description of the bacterial growth process is very complex due to the different variables one must take into account, such as substrate softness, nutrient concentration and distribution, inhibitors, or bacterial competition and growth. In general the structures that have been observed vary from ramified, DLA–like to different kinds of compact structures [MWR$^+$98; WRI$^+$98], as shown in the phase diagram of Fig. 1.12(a). In the case of compact structures, Vicsek *et al.* [VCH90] studied colonies of *Escherichia coli* and *Bacilus subtilis* (Fig. 1.12(b)) and reported a value for the roughness exponent of $\alpha = 0.78$. Matsushita *et al.* [MWR$^+$98] made experiments with *Bacilus subtilis* and studied the regions B and D

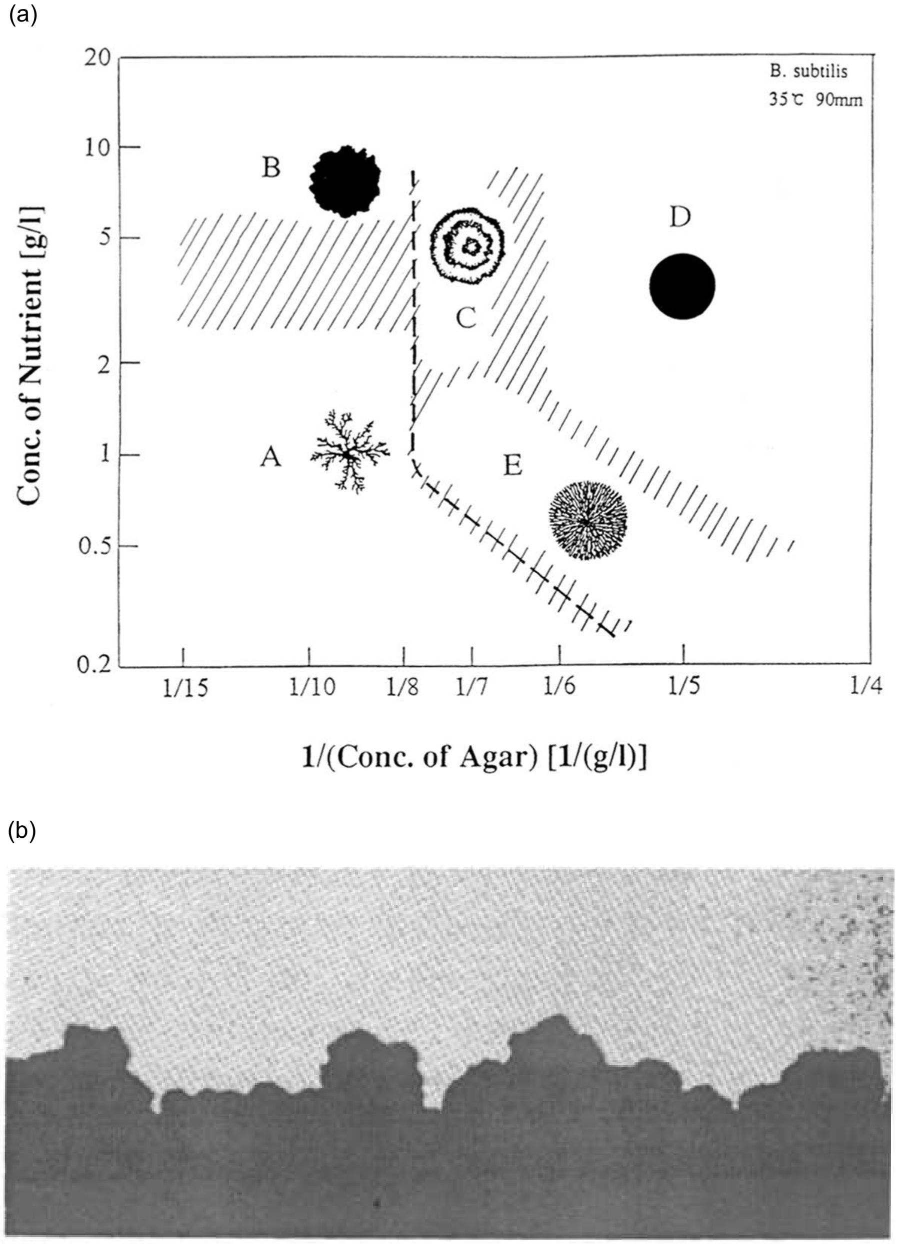

Figure 1.12: Experiments of bacterial colonies. (a) Different morphologies observed in the growth of *Bacilus Subtilis* ((from Ref. [WRI$^+$98]). A: DLA–like, B: Eden–like, C: concentric–ring–like, D:homogeneously spreading disk–like, and E: DBM–like. (b) Detail of the growth front, advancing from bottom to top (from Ref. [VCH90]).

of Fig. 1.12(a). They reported $\alpha = 0.78$ for the former and $\alpha = 0.50$ for the latter, and attributed the difference in the roughness exponents to the different microscopic growth mechanisms: cooperative movement with long range correlations in B, and individual movement in D.

1.8.2 Experiments with paper rupturing, burning, and wetting

Several experiments have been performed to describe interfacial growth using paper as disordered medium. Experiments with paper are usually cheap and easy to mount in a laboratory. Kertész *et al.* [KHW93] carried out experiments of paper rupturing (Fig. 1.13) and measured roughness exponents α in the range $0.63 - 0.72$. Zhang *et al.* [ZZAL92] studied interfacial growth in slow, flameless burning experiments with paper towels, and reported $\alpha \simeq 0.70$. Similar experiments were performed by Maunuksela *et al.* [MMK$^+$97] and reported $\alpha \simeq 0.48$ and $\beta \simeq 0.32$. They observed that the scaling exponents were dependent on the type of paper used, and described their experimental results in terms of the KPZ equation with thermal noise. Fig. 1.14 shows an sketch of their experimental setup and the morphology of the interfaces obtained.

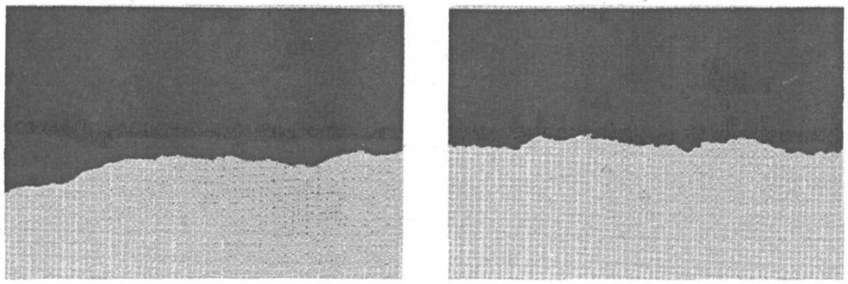

Figure 1.13: Examples of interfaces obtained from experiments of paper rupturing (from Ref. [KHW93]). The two images in correspond to the rupture line at two different magnifications.

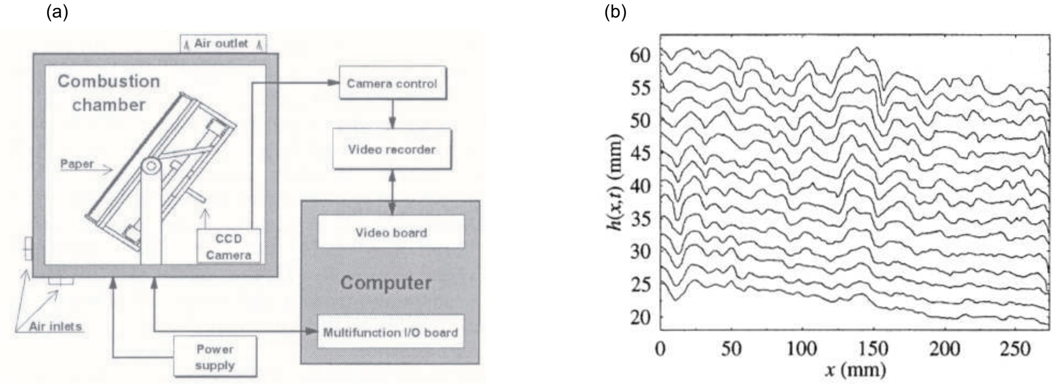

Figure 1.14: Paper burning experiments. (a) Sketch of the experimental setup. (b) Successive digitized burned front at intervals of 5 s. Both figures have been taken from Ref. [MMK$^+$97].

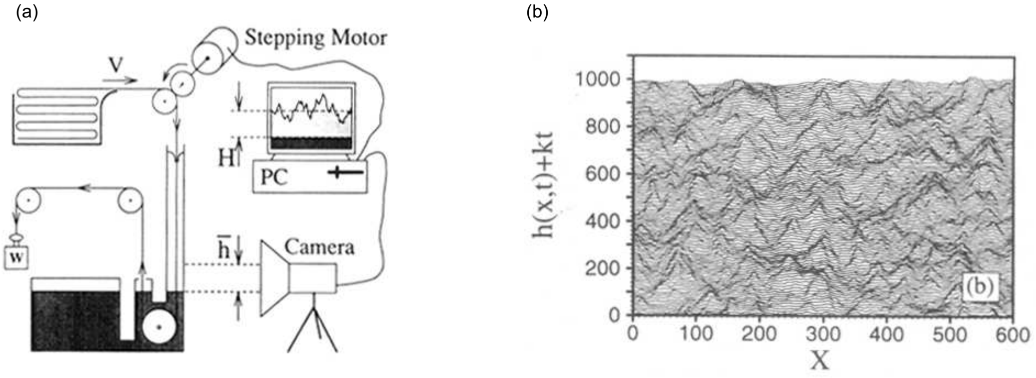

Figure 1.15: Imbibition experiment of water invading a paper towel. (a) Sketch of the experimental setup. The paper sheet is immersed at constant speed v into the container and the interface water/air is recorded using a video camera. (b) Sequence of digitized interfaces for $v = 1.32 \times 10^{-2}$ cm/s. Both figures have been taken from Ref. [HS95].

Experiments of wetting of paper were initially motivated to test the KPZ equation, but they gave rise to the DPD (and QKPZ) universality classes. The typical experiment consists on an imbibition process in which a paper towel is submerged into a container that contains a fluid, typically water, coffee, or ink. An sketch of one of the experimental setups used in this kind of experiments, as well as a sequence of the interfaces obtained, is shown in Fig. 1.15. Buldyrev *et al.* [BBC$^+$92] were the first to perform this kind of experiments. They reported $\alpha = 0.63$ and proposed the directed percolation depinning model (DPD), which has $\alpha = \beta = 0.63$, to describe their experimental results. Since their work, many authors have carried out similar experiments and reported experimental results with a wide variety of values of the scaling exponents, both in 2D (paper sheets) and 3D (paper blocks). These results are presented in Table 1.1. Recently, Balankin *et al.* [BBOM00] made accurate experiments on paper wetting and measured global and local exponents. They argued that the discrepancy between different experimental results could be attributed, on one hand, to the properties of the different paper materials and, on the other hand, to the interface front orientation with respect to the preferred direction of paper fibers.

1.8.3 Fracture of brittle materials

Experiments of fracture in brittle materials (such as wood, porcelain, or granite) have been important for their technological interest and material characterization. One of the motivations was to find a relation between the geometrical properties of the surface and the mechanical properties of the material. This would provide

Experiment	Roughness exponents	Growth exponents
Rupturing [KHW93]	$\alpha = 0.63 - 0.72$	—
Burning [ZZAL92]	$\alpha \simeq 0.70$	—
Burning [MMK$^+$97]	$\alpha \simeq 0.48$	$\beta \simeq 0.32$
Wetting [BBC$^+$92]	$\alpha \simeq 63$	—
Wetting (3D) [BBH$^+$92]	$\alpha \simeq 0.5$	—
Wetting [HS95]	—	$\beta \simeq 0.56$
Wetting [KHO96]	$\alpha \simeq 0.67$	$\beta \simeq 0.24$
Wetting [ZMOW97]	$\alpha \simeq 0$ (isotropic paper) $\alpha \simeq 0.47$ (anisotropic paper)	— —
Wetting [BBOM00] (filtro paper)	$\alpha = \alpha_{loc} = 0.73 - 0.75$	$\beta_L = 0.86$, $\beta_T = 0.47$
Wetting [BBOM00] (secant paper)	$\alpha = \alpha_{loc} = 0.63 - 0.64$	$\beta_L = 0.61$, $\beta_T = 0.35$

Table 1.1: Summary of the roughness and growth exponents for experiments with paper rupturing, burning, and wetting. β_L is the growth exponent measured when the orientation of the front is longitudinal to the fibers of the paper, and β_T when it is transverse.

a characterization of the material through the roughness exponent, in the line of the investigations carried out by Morel *et al.* [MSBV00; MBV00] An important characteristic of the experiments in fracture is that many of them display anomalous scaling. Most of the results were initially analyzed in the framework of Family–Vicsek dynamic scaling, but later it was clear that a description using anomalous scaling was much more complete. To this respect, there are many evidences that suggest that the local roughness exponents are universal (independent of the material and fracture process), as contrary to the global roughness, exponent that depends on the material under study and the orientation of the fracture with respect to the privileged directions in the material.

The universality of the local roughness exponents has been investigated by many authors, and a description of all the results obtained would require an extensive review. Some experimental examples are given next.

In 3D fractures, Bouchaud *et al.* [BLP90] investigated ductile cracks in aluminium and found $\alpha_{loc} \simeq 0.8$. Måløy *et al.* [MHH92] investigated many different brittle materials and found slight differences in the values of α_{loc}, with an average value of 0.87. López *et al.* proposed by the first time in Ref. [LS98] the use of the anomalous

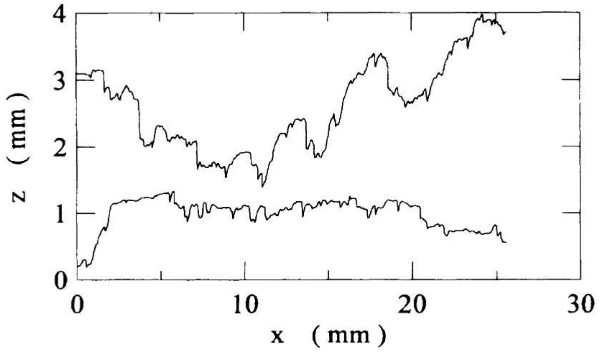

Figure 1.16: Example of interfaces in fracture in wood where radial and tangential fractures are studied. Top curve corresponds to tangential fracture, and the bottom to radial (from Ref. [EMHR94]).

scaling description for fracture of brittle materials, illustrated their hypothesis with experiments of fracture of a granite block, and obtained $\alpha \simeq 1.2$ and $\alpha_{loc} \simeq 0.79$. The anomalous scaling description was extended to fracture in wood, and Morel *et al.* [MSLV98] carried out experiments with different wood specimens, pine and spruce, obtaining $\alpha = 1.35$ and $\alpha_{loc} = 0.88$ for the former, and $\alpha = 1.60$ and $\alpha_{loc} \simeq 0.87$ for the latter.

In 2D fractures, the values reported are similar to those obtained for paper rupturing. Kim et al. [KYK97] for example reported $\alpha = 0.68$, in agreement with the values measured in paper rupturing. Engøy *et al* [EMHR94] studied the effect of the orientation of the crack in wood fracture. They observed a different behavior for tangential and radial fractures, but in both cases the local roughness exponent was the same, $\alpha_{loc} = 0.68$. The morphology of the interfaces for radial fractures were smooth, in contrast to the tangential fractures, which were characterized by large slopes (Fig. 1.16). To this respect, López *et al.* [LS98] suggested that the origin of anomalous scaling could come from the presence of these large slopes in the profile of the interfaces.

1.8.4 Experiments with glass beads

Experiments of fluid flow through porous media in Hele–Shaw geometry were the first attempt to study in a controlled way the dynamics of stable, immiscible fluid–fluid displacements. The typical experiment consists on a horizontal Hele–Shaw cell made of two glass plates separated a distance b. The gap between the two glass plates is filled with glass beads of uniform or random diameter, giving rise to a porous medium similar to those that can be found in natural systems. The fluid (water

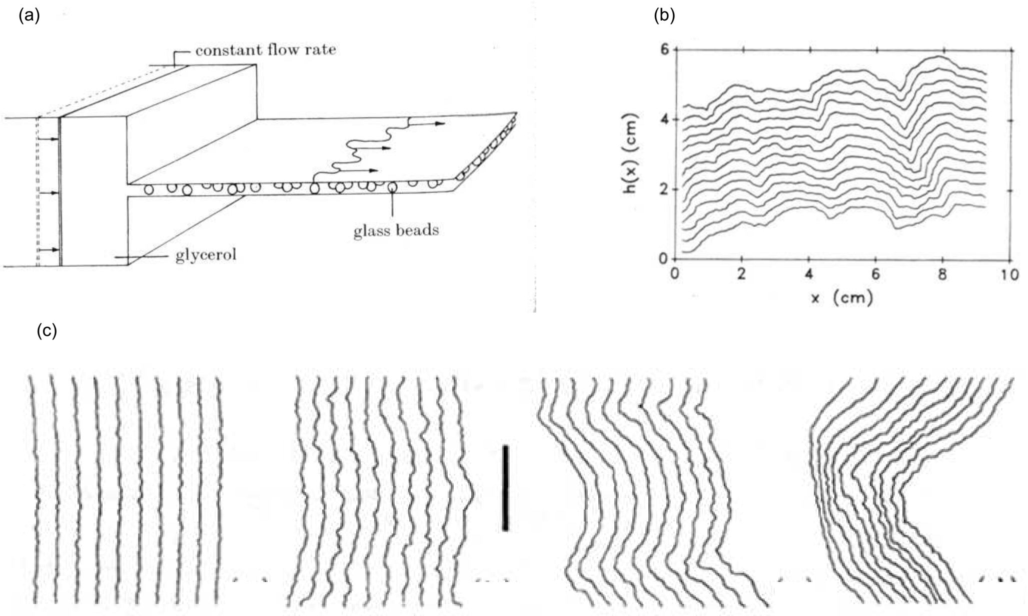

Figure 1.17: Experiments of fluid flow in a Hele–Shaw cell filled with glass beads. (a) Sketch of a typical experimental setup (from Ref. [BS95]). (b) Plot of successive interfaces at Ca'= 4.93×10^{-3} (from Ref. [REDG89]). (c) Sequences of interfaces with increasing driving velocity from left to right (from Ref. [HKW92]), and Ca' varying from 1.18×10^{-2} to 1.18×10^{-5}. The scale bar is 10 cm long.

or glycerol) is injected at one side of the cell and displaces air. The viscous forces are tuned by changing the driving velocity of the invading fluid, while the capillary forces are changed by modifying the distribution of sizes of the glass beads present in the medium. Usually the control parameter in these experiments is the modified capillary number, Ca' =Ca a^2/k, where Ca $= v\mu/\sigma$ is the ordinary capillary number, v the average fluid velocity, μ the dynamic viscosity, σ the surface tension fluid–air, a the characteristic size of the pores, and k the permeability of the medium. Fig. 1.17(a) shows an sketch of a typical experimental setup. The morphology of some experimental interfaces is shown in Figs. 1.17(b) and 1.17(c).

The first experiments of forced fluid invasion with a disorder medium made of glass beads were reported by Rubio *et al.* [REDG89]. They studied water displacing air (Fig. 1.17(b)) and measured $\alpha \simeq 0.73$, independent of Ca' (in the range studied) and bead size. However, a reanalysis of their data by Horvátz *et al.* [HFV90] gave $\alpha \simeq 0.91$, similar to the value $\alpha \simeq 0.88$ obtained by carrying themselves an experiment analogous to the one by Rubio *et al.*. Experiments performed using glycerol instead of water by Horvátz *et al.* [HFV91] gave $\alpha \simeq 0.81$ for short length scales, $\alpha \simeq 0.49$ for long length scales, and $\beta \simeq 0.65$. The last experiments of this kind were reported

Glass beads experiment	Roughness exponents	Growth exponents
water/air [REDG89]	$\alpha \simeq 0.73$	—
(reanalysis) [HFV90]	$\alpha \simeq 0.91$	—
water/air [HFV90]	$\alpha \simeq 0.88$	—
glycerol/air [HFV91]	$\alpha_1 \simeq 0.81$, $\alpha_2 \simeq 0.49$	$\beta \simeq 0.65$
water/air [HKW92]	$\alpha \simeq 0.65$ (low Ca')	—
	$\alpha \simeq 0.91$ (large Ca')	—

Table 1.2: Summary of the roughness and growth exponents for forced fluid invasion experiments in a Hele–Shaw cell filled with glass beads. The subscripts 1 and 2 refer to short and long length scales respectively.

by He *et al.* [HKW92], with water displacing air, who investigated a wide range of Ca' (Fig. 1.17(c)). They found large fluctuations of the roughness exponents on Ca', and measured values of α in the range $0.65 - 0.91$. Although they could not found a reliable scaling to obtain the growth exponent, they showed that the global width scaled with Ca' with an exponent -0.57. A summary of the different results obtained in these experiments is shown in Table 1.2.

The motivation to perform this kind of experiments was to check the KPZ universality class in fluid flow experiments, but clearly the results obtained are far from the expected exponents for KPZ ($\alpha = 1/2$, $\beta = 1/3$). He *et al.* [HKW92] pointed out that the discrepancy with KPZ is not surprising taking into account the nonlocal nature of the experiments, were the local capillary pressure in the pores competes with the nonlocal viscous pressure. Hence, nonlocal models had to be introduced to look for a complete description of the experiments. To this respect, Geromichalos *et al.* [GMH02] have recently performed experiments on spontaneous imbibition in roughened glass plates and measured two regimes for the roughness exponent, $\alpha_1 \simeq 0.81$ at short length scales and $\alpha_2 \simeq 0.58$ at long length scales. The first regime is interpreted as dominated by nonlocal effects due to the fact that the fluid required to advance in one place must be taken from the neighboring places. The authors argue that the nonlocality would be relevant at short length scales and, hence, the second regime would correspond to local dynamics according to the QKPZ universality class.

In this thesis we present the experimental results that we have obtained on forced fluid invasion and forced imbibition in a disordered Hele–Shaw cell.

1.9 Quenched disorder and nonlocality

In the last years there has been an increasing interest for growth models that take into account the *quenched* nature of the disorder. The paper fibers in experiments of burning fronts, or the pores between glass beads in experiments of fluid flow through model porous media, are some of the many experimental situations in which the properties of the disorder depend on its spatial distribution, $\eta = \eta(x, h)$. Certainly, the basic models based on continuous equations, such as EW or KPZ, are based on a *thermal* disorder term, $\eta = \eta(x, t)$, and they fail when trying to describe these kind of experiments. New models were introduced to fill this gap, and gave rise to the quenched EW (QEW) and the quenched KPZ (QKPZ) models. QEW was introduced to describe fluid flow into disordered media [KL85; KLT91] and provided growth and roughness exponents in the range $0.78 \leq \beta \leq 0.88$ and $1 \leq \alpha \leq 1.25$, depending on the different techniques used to treat the quenched noise. However, experiments on paper wetting and the models proposed to describe them (known as directed percolation depinning, DPD) [BBC$^+$92; TL92] showed that there was a universality class different from QEW. The scaling exponents reported for this new universality class were $\alpha = \beta \simeq 0.63$. To describe this new universality class a more general equation was introduced by adding the nonlinear term to QEW and gave rise to the QKPZ equation [Par92]. Amaral *et al.* [ABS94; ABMS95] demonstrated that in the pinning threshold QKPZ can be mapped into DPD. Hence, DPD and QKPZ belong to the same universality class.

These models were very successful to describe some experimental results with local dynamics. However, there are physical systems in which nonlocal laws must be introduced. This is the case for example of fluid flow in disordered media and of growth of bacterial colonies [LJ98]. In the first case the origin of the nonlocality is the fluid transport in the system [KM91; HKW92], and the role of nutrients and inhibitors in the second. In these situations there are long range effects that cannot be characterized using a local description. Thus, nonlocal models must be introduced.

Different models for a nonlocal description of fluid flow in disordered media have been proposed recently and different nonlocal interfacial equations derived [GB98; DRE$^+$00; HMSL$^+$01; PC02]. These models are consistent with the well known macroscopic equations of the problem (Darcy's law and interfacial boundary conditions). They differ in the way the disorder is included in the equations and in the disorder properties. Ganesan *et al.* [GB98] proposed a model for forced imbibition based in a random field Ising model. The permeability is taken spatially uniform and the disorder exhibits long range spatial correlations. Using a Flory–type scaling, the model predicts that the roughness exponent α depends on the capillary number Ca, with asymptotic values $\alpha = 3/4$ for the smallest drivings and $\alpha = 1/2$ for the largest drivings. Dubé *et al.* [DRE+99; DRE+00] considered a conserved Ginzburg-Landau model with the disorder introduced in a fluctuating chemical potential. They considered only the case of spontaneous imbibition, and by numerical integration they obtained $\alpha = 1.25$ and $\beta = 0.3$. Hernández–Machado *et al.* [HMSL+01] considered also a conserved Ginzburg-Landau model, but in this case the disorder was introduced in the mobility, without long range correlations. They studied the case of forced imbibition, and predicted two different scalings at short and long length scales, with exponents $\beta_1 = 5/6$, $\alpha_1 = 5/2$ in the former regime, and $\beta_2 = 1/2$, $\alpha_2 = 1/2$ in the latter. Finally, Pauné *et al.* [PC02; Pau02] proposed a Hele-Shaw model for forced fluid invasion with variable gap spacing. They made the assumption that Darcy's law can be applied locally and imposed incompressibility of the full 3D flow. The variable gap spacing was introduced in the mobility and in the boundary conditions on the interface. Numerical integration of the model gave $\beta \simeq 0.68$. Two regimes for the roughness exponent were reported, α_1 at short length scales and α_2 at long length scales, with $\alpha_1 \simeq 1.5$, $\alpha_2 \simeq 1.2$ for small drivings, and $\alpha_1 \simeq 1.5$, $\alpha_2 \simeq 0$ for large drivings. In addition, when the disorder was totally persistent in the direction of growth, the model could be solved exactly, and with $\alpha = 1.5$, $\beta = 0.5$.

The different results that contemplate these models are summarized in Table 1.3.

First author	Roughness exponents	Growth exponents
Ganesan [GB98]	$\alpha = 3/4$ (low drivings) $\alpha = 1/2$ (large drivings)	— —
Dubé [DRE+99; DRE+00]	$\alpha \simeq 1.25$	$\beta \simeq 0.3$
Hernández–Machado [HMSL+01]	$\alpha_1 = 5/2$, $\alpha_2 = 1/2$	$\beta_1 = 5/6$, $\beta_2 = 1/2$
Pauné [PC02; Pau02]	$\alpha_1 \simeq 1.5$, $\alpha_2 \simeq 1.2$ (low drivings)	$\beta \simeq 0.68$
	$\alpha_1 \simeq 1.5$, $\alpha_2 \simeq 0$ (large drivings)	$\beta \simeq 0.68$
	$\alpha = 3/2$ (persistent disorder)	$\beta = 1/2$

Table 1.3: Summary of the roughness and growth exponents from different nonlocal models. The subscripts 1 and 2 refer to short and long length scales respectively.

Chapter 2

Experimental Setup

In this chapter we provide all details concerning the experimental setup that have not been treated in full detail in the publications, such as the design and characterization of the disorder medium, image analysis, data treatment, permeability of the cell and modified capillary number.

2.1 Motivation of our experimental work

The motivation for developing our experimental work, which started at the end of 1997, was to look for an experimental setup to study interface dynamics with well controlled quenched disorder, and that could provide some novel experimental results for the increasing theoretical advances in nonlocal models. Many experiments of this kind that have been carried out in the past, such as the experiments with glass beads [REDG89; HFV91; HKW92], have had the problem that the statistical properties of the disorder could not be completely characterized. It was not possible –or very difficult– to i) determine the distribution of pore sizes, and ii) prepare a medium with a desired pores configuration. Our technique allows to design different disorder configurations and with desired statistical properties. Fig. 2.1 shows schematically the idea behind our experimental setup: a Hele–Shaw cell with a quenched disorder in the bottom plate.

2.2 The disorder pattern

Here we describe how the disorder was designed and manufactured, its statistical characterization, and some other aspects concerning the disorder plates.

2.2.1 Precedents

Along the last three decades many researches have extensively investigated flow through porous media using a wide range of experimental techniques, from direct observation or microscopy to X-ray tomography. However, most of the porous materials that we can find in nature are so complex that, when we try to analyze their structure or to describe the fluid dynamics inside them, the medium itself can be destroyed or no clear information can be extracted [Dul91; Won99]. For these reasons, the research in this field quickly evolved to the idea of designing experiments where the porous media could be created with some control of the pores structure and, most importantly, the fluid flow inside the pores could be described and studied.

One of the most interesting experiments in this way was performed by Lénormand and coworkers [BL77; LZS83; RZ85; LTZ88]. They made experiments in transparent etched networks and studied invasion percolation problems, fluid trapping and fluid dynamics at the scale of the pores. Figs. 2.2(a) and 2.2(b) show two examples of this kind of networks. Although these networks cannot represent the complexity of real porous media, such as 3D connectivity, variable wettability, adsorption, or arbitrary cross–section of the capillary tubes [Won99], they are an excellent tool to understand the rich variety of phenomenologies that have been observed in flows in real porous media, from two–phase flow [Dul91] to fractal structures [MFBJ88].

Apart from experimental investigations, this kind of networks have been used in 2D numerical simulations to describe fluid flow [KKT96; JSAAF$^+$97], percolation processes [LB80; RZ85; JSASS$^+$95], or permeability characterization [CCF$^+$90;

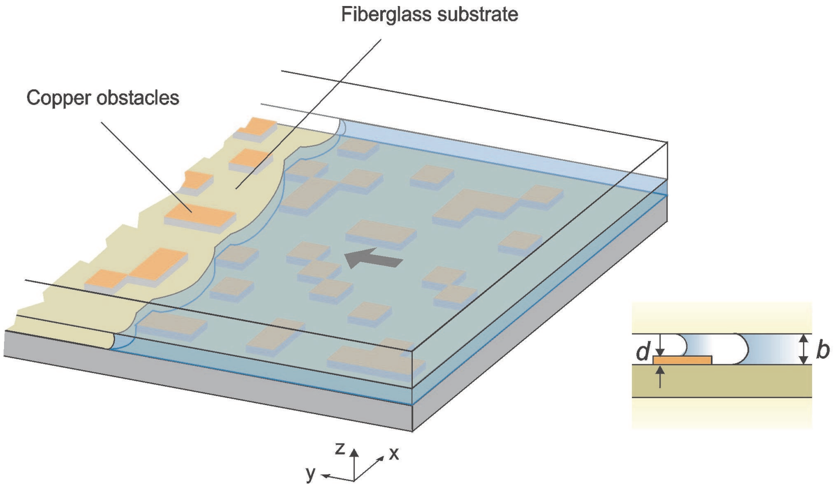

Figure 2.1: Schematic representation of our Hele–Shaw cell with quenched disorder in the bottom plate. d is the height of the copper obstacles, and b the gap spacing.

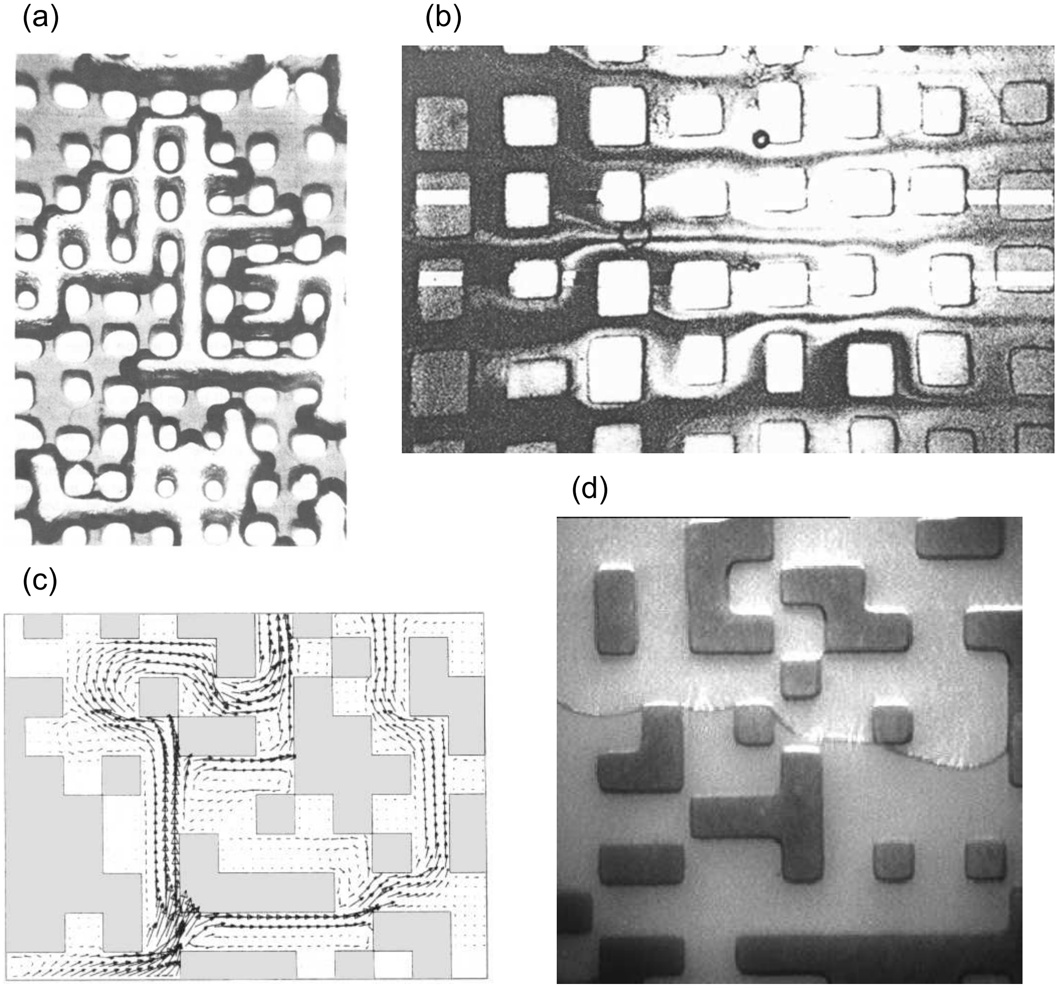

Figure 2.2: Examples of micromodels. (a) Distribution of oil and air in the pores of a resin etched micromodel [RZ85]. (b) Experiment of trace flow [Won99]. (c) 2D simulations of fluid flow, with the fluid moving from bottom to top [JSAAF+97].(d) Close-up view of the micromodel and the fluid flow in our Hele–Shaw cell. The oil is advancing from bottom to top [SOHM02b]. See references for extensive details.

SMB+93; KKT97]. Fig. 2.2(c) shows an example of simulations of fluid flow in a 2D network.

Instead of performing studies in detail of fluid flow at the scale of the pores, our objective in the design of our micromodels (Fig. 2.2(c)) was to look for a reliable, low cost technique to study roughening and pinning in a rectangular Hele–Shaw cell. Indeed, the problem of interfacial roughening with quenched disorder has received a lot of attention in the last years. Our experimental setup and technique, as well as our results, have been an important starting point for very interesting and fruitful investigations in the forthcoming years.

2.2.2 Design and manufacture

Basically, the disorder medium in our experiments is a printed circuit with a particular design. The disorder pattern consists on copper obstacles of a uniform height placed over a fiberglass substrate. How these copper obstacles are distributed over the substrate defines the type of disorder configuration used in our experiments. The maximum size of the plate that we could find in the industry and with a reasonable cost is $y \times x = 560 \times 350$ mm [1]

The disorder pattern is designed by computer using the program `PlatesDesign.exe` (Appendix A). We consider a square lattice where a is the lateral size of the unit cell. The nominal values of a used in the experiments are 0.40 mm and 1.50 mm. The ratio between occupied sites and the total sites of the lattice defines the *filling fraction* f. The occupied sites will be those filled with copper. The same value of f has been used in all the disorder patterns, $f = 0.35$. Three kinds of disorders have been used, and examples of the patterns are given in Fig. 2.3.

1. **SQ**. The sites of the lattice are randomly occupied until f reaches the preset value. We allow nearest neighbors connections only, leaving next-nearest neighbors separated a small distance.
2. **SQ-n**. The sites of the lattice are randomly occupied allowing both nearest and next-nearest neighbors connections.
3. **T**. The sites of the lattice are occupied forming parallel tracks, continuous in the y direction, and randomly distributed along x.

We have used frequently the same type of disorder configuration but with a different size of the unit cell. To distinguish them, the disorder configurations are named using the code that identifies the disorder configuration (SQ, SQ-n, or T) followed by the size of the unit cell in mm, which can be 1.50 or 0.40.

Once the design of the disorder is completed, the pattern is exported to AUTOCAD (version 13 or higher), which prepares the design in a proper format for manufacture. The process of manufacturing goes through the following steps (Fig. 2.4): i) Using photochemical techniques, the original design is projected over a fiberglass substrate that contains a layer of copper 70 μm high. This technique leaves a thin film over the regions that correspond to the unoccupied sites of the design. ii)

---

[1] The manufacturer is *2CI Catalana de Circuitos Impresos S.A. Ciutat de Granada 130, 1. E-08018 Barcelona*. The cost of three identical boards of 560 × 350 mm is about 350 euros. Three copper heights are available: 35, 70, and 110 μm (nominal values).

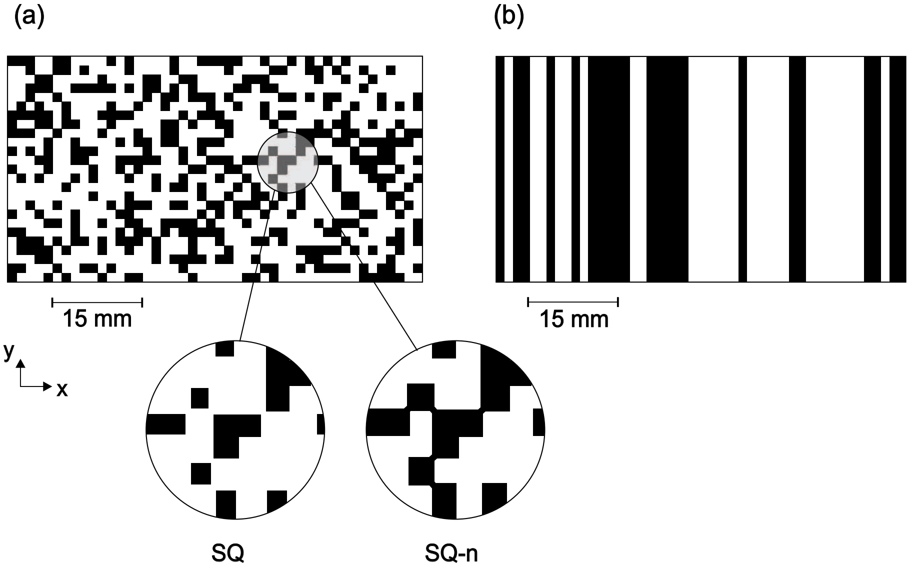

Figure 2.3: Partial views of the disorder patterns used in the experiments. Black regions are the occupied sites. (a) Squares (SQ and SQ-n). (b) Tracks (T). The blow-ups in (a) show the detailed configuration of the disorders SQ and SQ-n. The lateral size of the lattice unit cell is 1.50 mm.

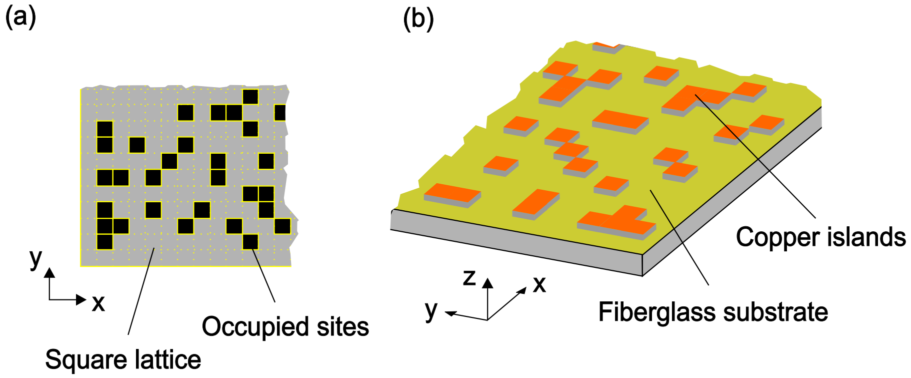

Figure 2.4: Schematic representation of (a) the original design and (b) the final plate.

The plate is immersed in a bath of Pb-Sn alloy. The alloy fixes only in the copper regions not covered by the thin film. iii) The thin film is removed. iv) The plate is immersed in an ammoniacal bath that removes the copper not covered with the alloy. v) Finally, the alloy previously fixed is removed. The plate that results from all these operations has copper islands in the occupied sites of the lattice and fiberglass substrate in the unoccupied sites.

The manufacturing process consists on a series of chemical processes, which causes that the final height and size of the copper obstacles is slightly reduced. We have

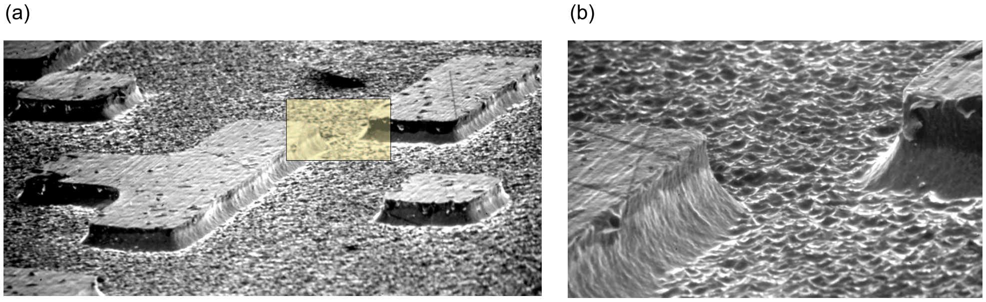

Figure 2.5: (a) SEM image of a region of a plate with disorder SQ 0.40. The height of the copper obstacles is 60 μm, and the actual lateral size of the unit cell 360 μm (instead of the nominal 400 μm). Notice that in the final plate there are no contacts between neighboring squares. (b) Detail of the edges of the copper obstacles.

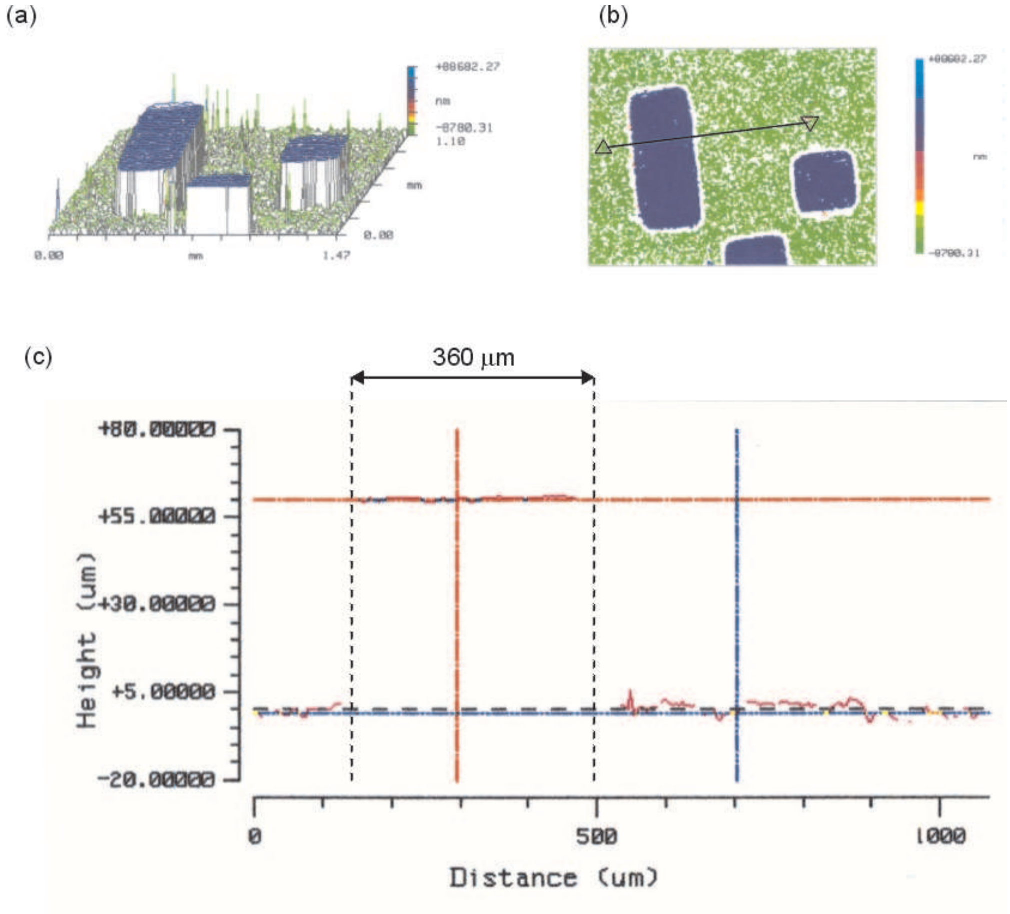

Figure 2.6: Determination of the real height and size of the copper obstacles using interferometric microscopy, for disorder SQ 0.40. (a) Side view of the sample. (b) Top view. (c) Measured height as a function of the distance along the direction indicated by the black line in (b).

measured the actual lateral size and height of the obstacles by analyzing samples of the plates using scanning electron microscopy (SEM) and interferometric microscopy. Fig. 2.5 shows a SEM image of a portion of a plate with disorder SQ 0.40. As can be observed, the edges of the copper obstacles are not completely sharp, presenting a slightly curved shape. The precise measure of the changes in height and size has been performed using the interferometric microscope. The results are presented in Fig. 2.6, which shows clearly these changes. The conclusion of this analysis is that the chemical process reduces the height of the copper islands in 10 μm (from the nominal value of 70 μm to 60 μm). The reduction in lateral size is not homogeneous, varying from 20 to 40 μm at each side. Fig. 2.6 shows the maximum reduction observed.

The manufacturer produces three copies of the same plate. The largest dimension of the plate is always kept as the growth direction, and we make specific cuts in the other direction to obtain plates of three different widths: 200, 100 and 50 mm. The cuts are made in appropriate locations to have three different realizations of the disorder for each width.

Out of the 560 mm in the direction of growth, 20 mm (at each side of the plate for SQ, and only at one side for T) has been used to allocate the *preparation region*, which is a set of transverse copper tracks designed to prepare an initially flat front. Photographs of a portion of two plates with different disorder configuration, SQ 1.50 and T 1.50, are shown in Fig. 2.7.

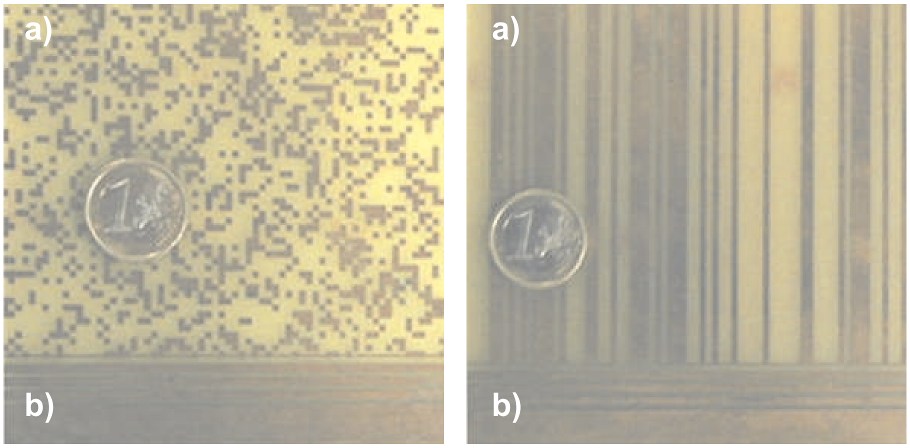

Figure 2.7: Partial views of two disorder plates, with configurations SQ 1.50 (left) and T 1.50 (right). (a) Disorder region. (b) Preparation region.

2.2.3 Statistical characterization of the disorder

The disorder is specifically designed to be uncorrelated in x for disorders T, and uncorrelated in both x and y for disorders SQ and SQ-n (over distances larger than one unit cell). We have characterized the disorder properties in two ways: i) the distribution of copper clusters, and ii) the so called *persistence length of the disorder*, $\widetilde{l}$, which gives an estimation of the average distance that the oil–air interface can cover advancing over a copper obstacle.

The statistical distribution of clusters, i.e. the distribution of sizes of copper islands is presented in the main plot of Fig. 2.8(a) for disorders SQ 1.50 (dark grey) and SQ-n 1.50 (light grey), and the nominal occupation $f = 0.35$. The interesting feature is that when we change from SQ to SQ-n the number of large islands increases appreciably, which means that, locally, the flow in the experiment can cover higher distances without stopping. The distribution function of the clusters can be fitted to a power law of the form $N\psi^{-a}$, where ψ is the cluster size. This fit allows characterizing the distribution of clusters with two parameters, N and a. It could be interesting to study in the future the different flow dynamics or interface profiles that can be obtained using different obstacles (e.g. circles instead of squares) but with the same distribution of sizes. For the results presented in Fig. 2.8 the values of N and a are $N = 790$, $a = 1.58$ for SQ 1.50, and $N = 700$, $a = 1.52$ for SQ-n 1.50.

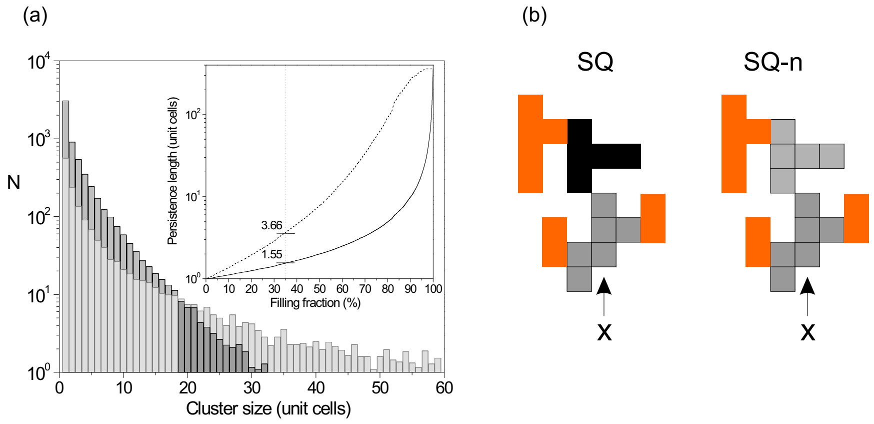

Figure 2.8: Statistical characterization of the disorder. (a) Main plot: Distribution of sizes of copper obstacles for SQ 1.50 (dark grey) and SQ-n 1.50 (light grey). Inset: Variation of the persistence length with the occupation fraction. (b) Definition of the persistence length $\widetilde{l}$. The grey sites are those in the interval $[x - \Delta x, x + \Delta x]$ that are connected, the black sites are those not connected, and the red sites are those outside the interval under analysis.

The persistence length $\widetilde{l}$ is defined as follows (Fig. 2.8(b)): i) We consider every site x of the lattice along the lateral direction, and measure the average length $l(x)$ of the cluster formed by the connected copper sites at $x-\Delta x$, x, and $x+\Delta x$, where Δx is the lattice spacing. (ii) We average $l(x)$ over the lateral direction in the interval $(0, L)$. Notice that by definition, $\widetilde{l} = H$ (the length of the cell) for disorder T.

The purpose of defining $\widetilde{l}$ is to quantify in some way the different behavior observed in the experiments with different disorders (SQ, SQ-n, and T), and to point out the importance of increasing the continuity of the disorder in the direction of growth.

In the inset of Fig. 2.8(b) we present the variation of $\widetilde{l}$ for different occupation fractions f, for SQ and SQ-n. Notice that for $f = 0.35$ the value of $\widetilde{l}$ almost doubles when we change from SQ to SQ-n.

2.2.4 The problem of the contrast in the images

One of the major problems found during the preparation of the experimental setup has been the brightness of the copper islands in the brand new plates. This caused that the oil–air interface that was advancing over the disorder could not be clearly identified. To avoid this problem it was necessary to look for a technique to accelerate the oxidization of the copper obstacles. Different techniques where tested, such as immersing the plates in baths of H_2O_2 or in solutions with low concentrations of NH_3. These techniques, however, damaged the plates, so it was necessary to look for another methods. The process that finally was applied consisted on coating the plate with a thin layer of a copper solution that accelerated the natural oxidization process of the copper and, in addition, protected the copper of further oxidization at the end. This technique is usually used by metal artisans and is known from ancient times, giving us excellent results. Fig. 2.9 gives an example of two identical plates before (left) and after (right) the oxidization protocol.

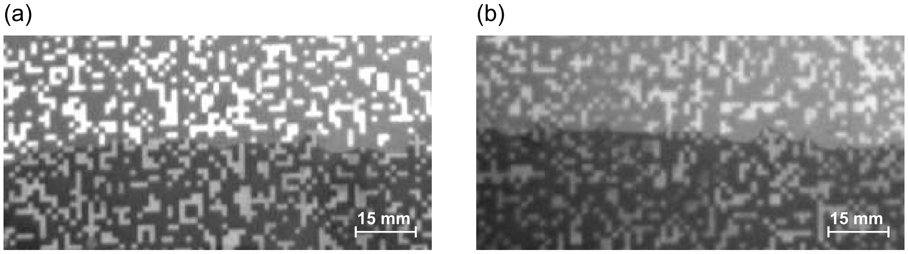

Figure 2.9: The problem of the contrast. (a) An oil–air interface over a brand new plate. (b) A similar interface after the oxidization protocol. The disorder configuration is SQ 0.40.

We performed identical experiments with and without the oxidization protocol and, apart from the poorest quality of the images corresponding to brand–new plates, no appreciable differences in the quantities measured could be observed.

2.2.5 Fluid characterization and contact angles

In all the experiments we have used the same fluid, silicone oil Rhodorsil 47V, with nominal kinematic viscosity $\nu = 50$ mm^2/s, density $\rho = 998$ kg/m^3, and surface tension oil–air $\sigma = 20.7$ mN/m at room temperature. We have routinely measured the viscosity of the fluid during the experiments using a Cannon-Fenske capillary viscometer, and measured an average kinematic viscosity $\nu = 48.31 \pm 0.02$ mm^2/s. at 22.8 °C (the average temperature of the fluid during the experiment), with a maximum fluctuation of about 3% respect to the average value. We have not observed any appreciable difference between two identical experiments performed at the highest (26.8 °C) or at the lowest (20.4 °C) temperature measured.

The oil wets three surfaces: the glass plate, the copper obstacles, and the fiberglass substrate. The oil wets with zero contact angle the glass plates, but this cannot be stated in general for the fiberglass plates and the copper deposits. Measurements of the contact angles using our own cameras have shown that the contact angle is zero or almost zero in the three surfaces. However, to make sure that the oil wets perfectly the surfaces that it is contact with, we have always left a thin layer of oil in the disorder plate and in the glasses. Careful repetition of identical experiments with and without the oil film have shown that there are no appreciable differences.

On the other hand, it is well known that the dynamic contact angle can change depending on the velocity of the interface [Dus79; Hof75]. This can affect the balance between the in–plane stabilizing capillary forces, the stabilizing viscous forces and the destabilizing capillary forces in the z direction. In our work we have not considered the effect of the dynamic contact angle. However, we have observed that in some conditions of very strong capillary forces the contact angle reverses when the oil gets in contact with the disorder. Close–up experiments of the dynamics at the scale of the disorder have shown that the light is reflected in different directions when the oil jumps from the fiberglass substrate to the copper obstacles. The interface acts as a convergent lens in the first case and as a divergent lens in the second. The sequence of images shown in Fig. 2.14 and Fig. 2.15, as well as the movies `MICRO001.AVI` and `MICRO018.AVI`, included in the accompanying CD, illustrate this observation.

2.3 Image analysis and data treatment

In this section we give further details that were not included in the publications. We will describe the technique to extract the interface profiles and the different data treatments applied.

2.3.1 Image analysis

The images are acquired using a VisualBasic application (see appendix B) that controls two JAI CV-M10BX progressive scan CCD cameras connected to a PCVision frame grabber. The images obtained from the experiments have a size of 768 × 574 pixels, with an spatial resolution of 0.37 mm/pixel. The cameras are mounted along the vertical direction and fixed (Fig. 2.10(a)), each camera capturing half the cell, with a slight overlap for the transition from one camera to the other. The process to extract the interface profile from the images is as follows (Fig. 2.10(b)): i) A base image which was taken before starting the experiment that contains only the disorder background and all possible undesired light inhomogeneities or reflections is subtracted from the original images. ii) The resulting images have a much more contrasted interface contour that it can be thresholded to get a neat black and white contour. iii) The contour is resolved using 1–pixel accuracy to get the final profile of the interface.

The oxidization protocol applied to the disorder plates improves the quality of the subtracted images. The grey-scale histogram of the subtracted images contains two

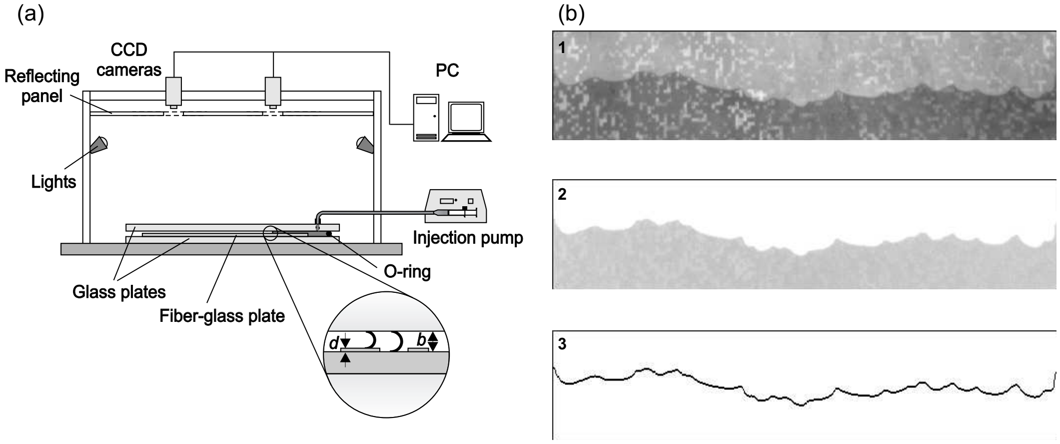

Figure 2.10: (a) Sketch of the experimental setup. (b) A portion of an image to illustrate the process of extracting the interface profile. 1: The original image. 2: The subtracted image. 3: The contour resolved.

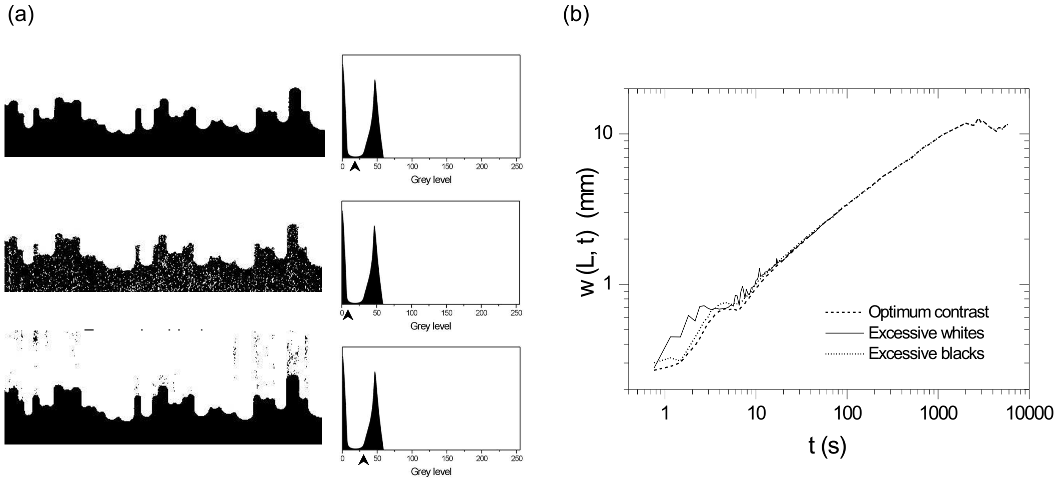

Figure 2.11: (a) Sensitivity of the subtracted images to the threshold value, with optimum threshold (top), excess of whites (center), and excess of blacks (bottom). (b) Interfacial *rms* width as a function of time for the previous three cases.

well separated gaussian distributions for blacks and whites, which allows to apply the threshold reliably. However, to test the sensitivity of the analyzed data to the image analysis process, we have reanalyzed images forcing an excess of blacks or an excess of whites. An example is presented in Fig. 2.11(a) for T 1.50. At the right of the black and white contour there are the histograms of the subtracted images with an arrow indicating the position in the histogram of the threshold value applied. An example of how the analysis of the data can be affected by the image analysis process is shown in Fig. 2.11(b) for $w(L,t)$, which shows that short times are specially sensitive to errors in image analysis due to the smaller interface roughening at the first stages of the interface evolution.

In general, for any quantity measured in data analysis, we have observed that the influence of a different disorder configuration is much more important than the possible errors that could come from image analysis. This makes our image analysis method reliable for the characterization of the interface profiles and the description of the roughening processes.

Examples of the time evolution of resolved interfaces from $t = 0$ s to saturation are shown in Fig. 2.12 for SQ 1.50 and in Fig. 2.13 for T 1.50. Real–life motion pictures are available in the accompanying CD, `SQUARES-1.AVI` for SQ 1.50 and `TRACKS.AVI` for T 1.50.

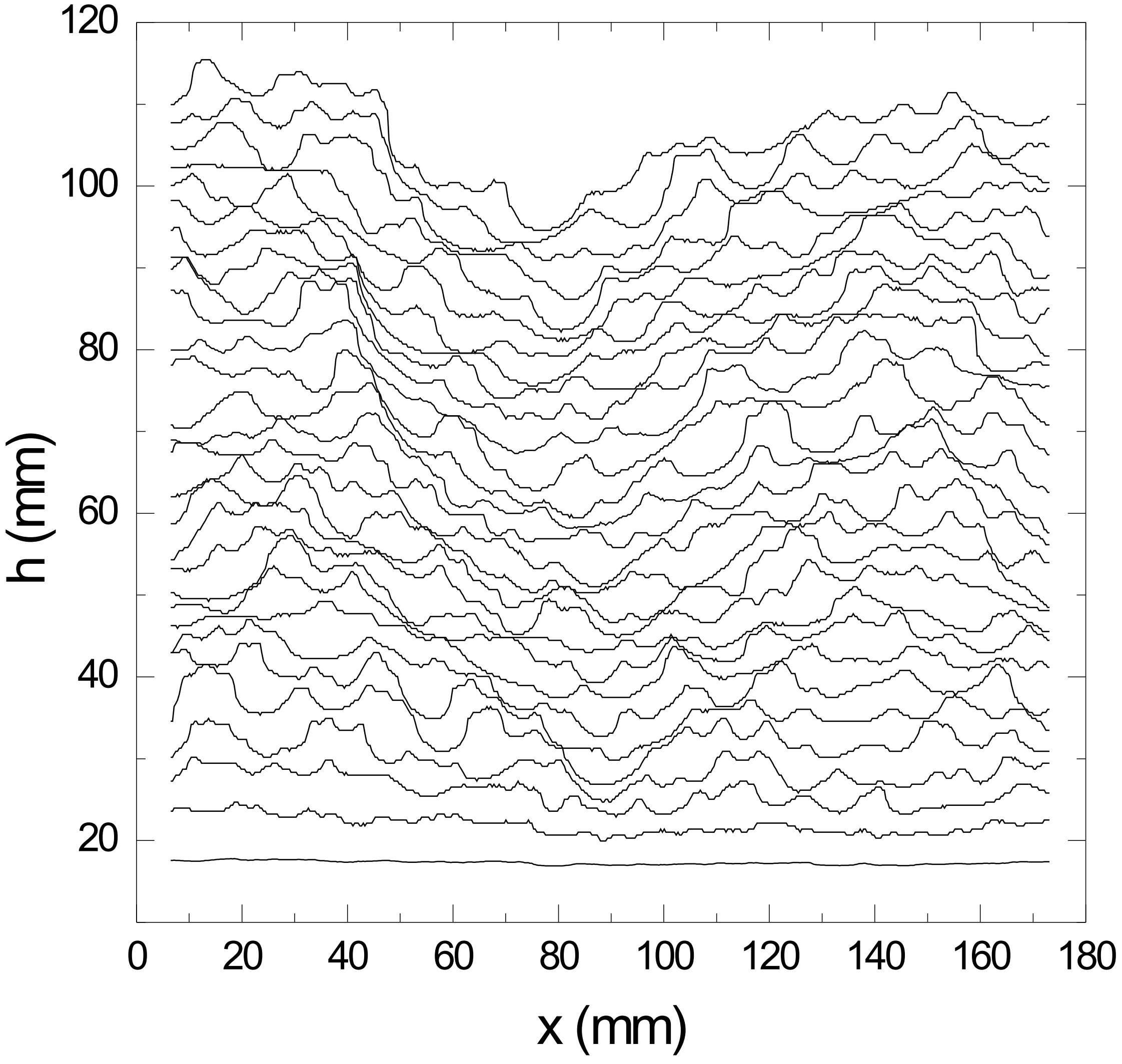

Figure 2.12: Example of a typical experiment with disorder SQ 1.50, gap spacing $b = 0.36$ mm, and velocity $v = 0.08$ mm/s. The temporal evolution of the oil–air interface is from $t = 0$ s to $t = 1160$ s in increments of 40 s. Notice that in some locations the interface gets locally pinned, while in others the particular configuration of the disorder gives interfaces faceted.

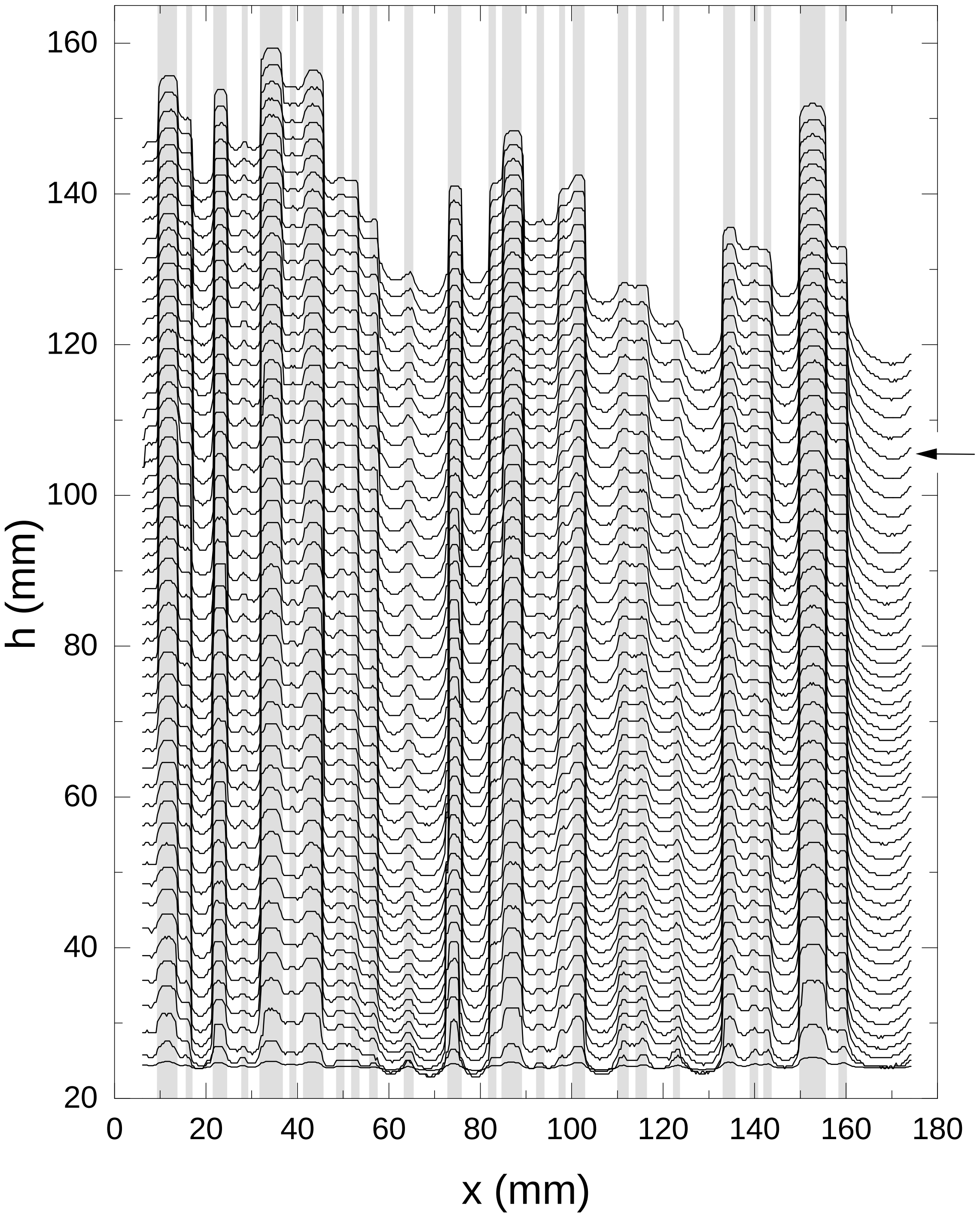

Figure 2.13: Example of a typical experiment with disorder T 1.50, gap spacing $b = 0.36$ mm, and velocity $v = 0.08$ mm/s. The temporal evolution of the oil–air interface is from $t = 0$ s to $t = 1440$ s in increments of 30 s. For this particular disorder configuration saturation is at about $t = 900$ s (indicated with an arrow in the plot).

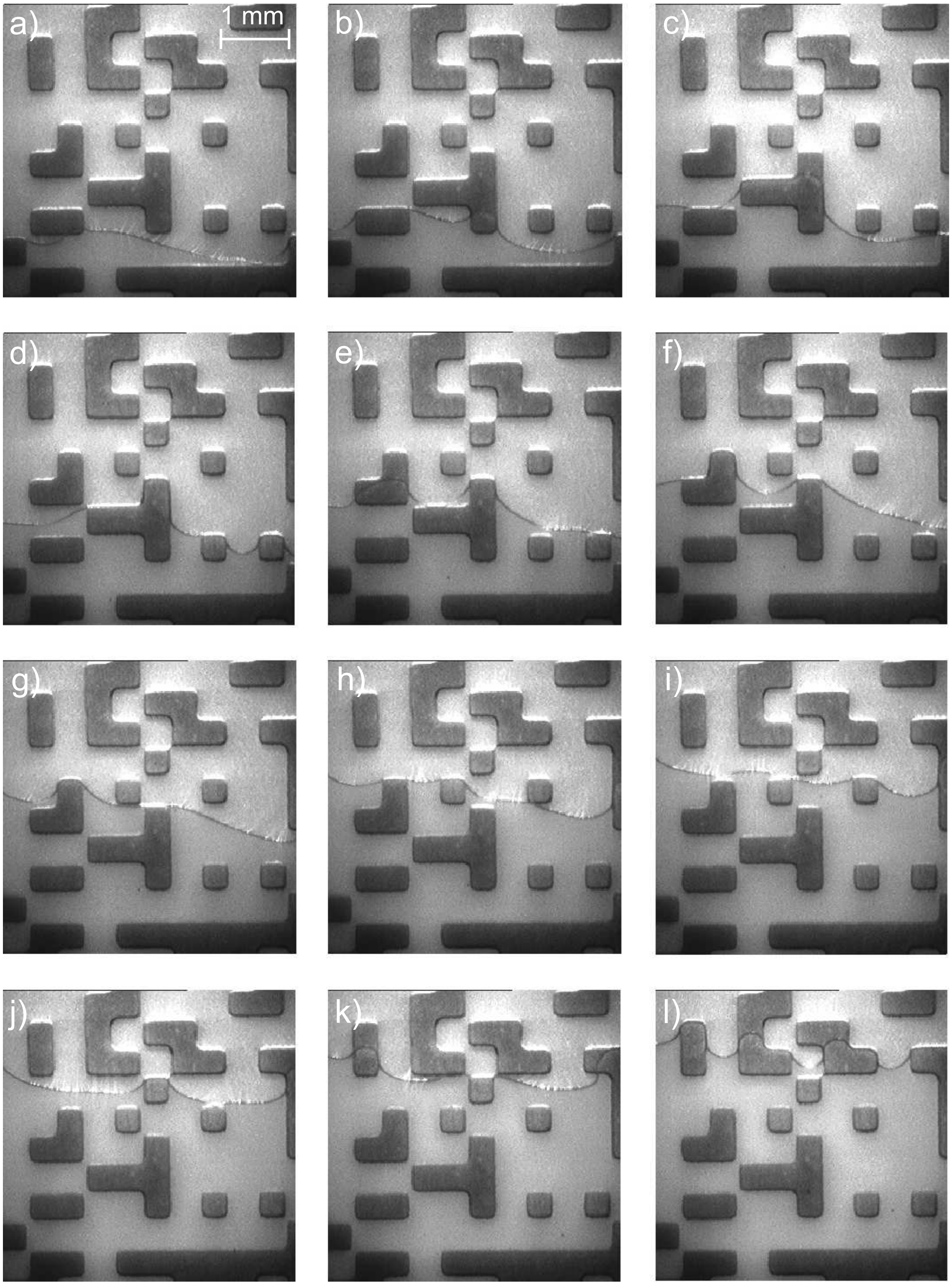

Figure 2.14: Twelve consecutive close-up views of the oil–air interface advancing over the disorder. The oil is driven from bottom to top. The experimental parameters are $b = 0.36$ mm, $v = 0.08$ mm/s, and disorder SQ 0.40.

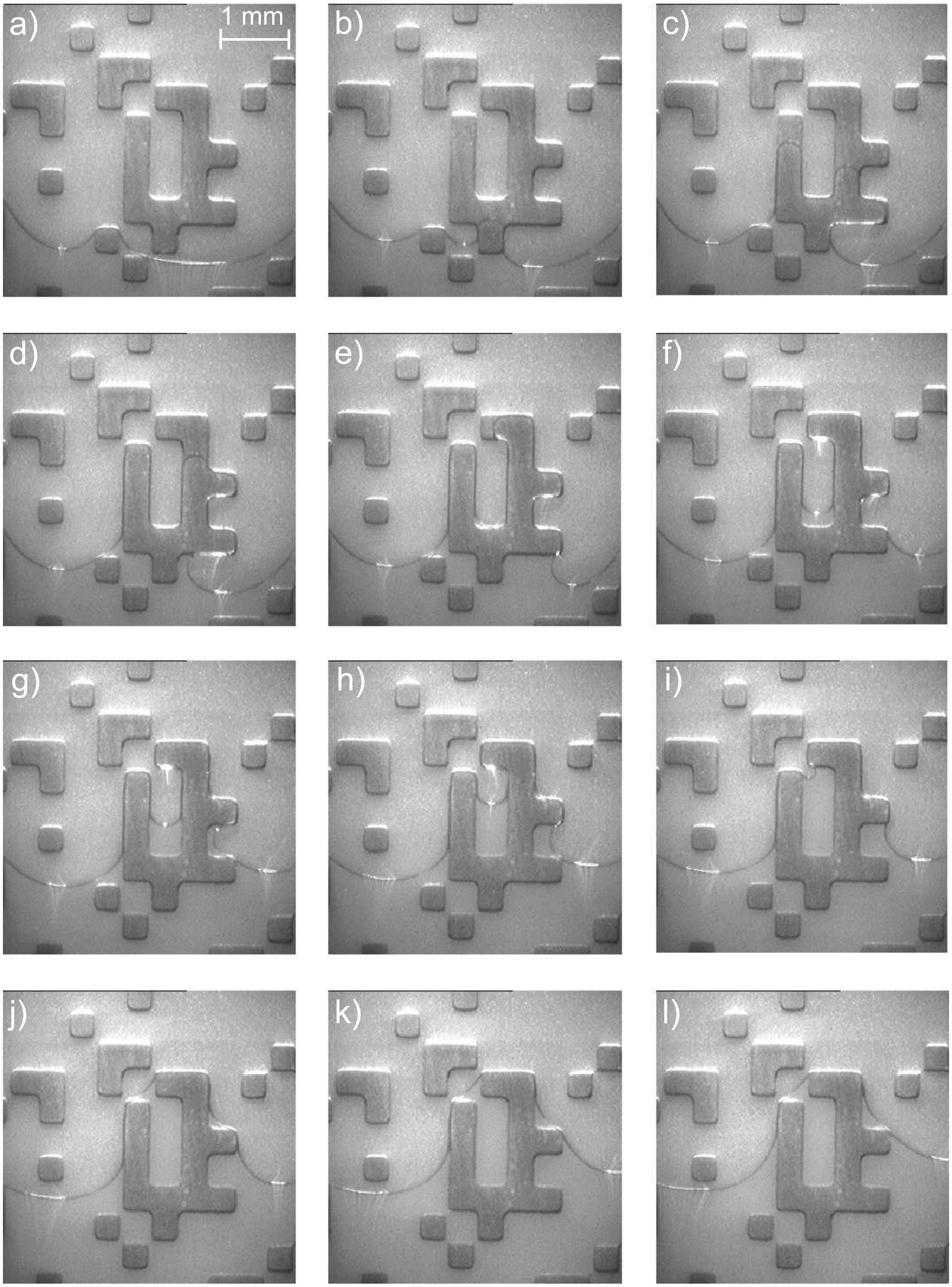

Figure 2.15: Twelve consecutive close-up views of the oil–air interface advancing over the disorder. The oil is driven from bottom to top. The experimental parameters are $b = 0.16$ mm, $v = 0.08$ mm/s, and disorder SQ 0.40.

2.3.2 Overhangs treatment

In general, the profile $h(x,t)$ obtained from image analysis is a single–valued profile. We had to deal with the problem of overhangs only for very small gap spacings (≤ 0.23 mm) and disorders SQ and SQ-n. In this case the interface follows the shape of the disorder obstacles (see for example Fig. 2.15) and in some particular locations it gets air trapped behind. However, the amount of trapped air has been always small, with a maximum of about 5 % of the total area occupied by the fluid. When overhangs have been detected in a given experiment, they have been eliminated taking the highest value of h, as shown in Fig. 2.16.

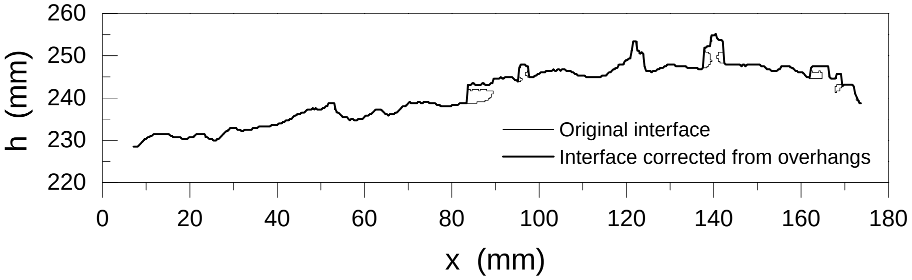

Figure 2.16: Example of overhangs treatment. The multivaluations in the interface profile are overcome by taking the highest value of h. The experimental parameters of this example are $b = 0.16$ mm, $v = 0.08$ mm/s, and disorder SQ 1.50.

On the other hand, in the analysis of the interfaces with T disorder it is frequent to observe that the position of a track edge fluctuates between two neighboring pixels (see for example the top image in Fig. 2.11(a)). To solve this problem, on the track edges we have always taken the lowest value of the left column as first point, and the highest value of the right column as second point, in the case of increasing h; and the highest left and lowest right in the case of decreasing h.

2.3.3 Data treatment

The profile $h(x,t)$, obtained from the analysis of the images, contains 515 points corresponding to a lateral size of 190 mm, with a lateral size step $\Delta x = 0.37$ mm. Because the oil tends to advance at the side walls of the cell, we have a distortion of the front at the sides of the cell. This distortion is maximum for the largest gap spacing ($b = 0.75$ mm) and has been estimated in 8 mm. To minimize the effect of the distortion we have cut 8 mm from both ends of all interfaces, reducing them to a final lateral size of 174 mm (470 pixels). Finally, and specifically necessary for the computation of the power spectrum, we have forced periodic boundary conditions by subtracting the straight line that connects the two ends of the interface. This is a common procedure [SHN98] that eliminates the artificial overall slope -2 in the power spectrum due to the discontinuity at the two ends [SVR95].

The power spectrum is computed using a FFT algorithm [PFTV93] which needs a number of points power of 2. For this reason we have extended the number of data points to 512 using linear interpolation, so that the final lateral resolution (sampling interval in the FFT) is $\Delta x = 0.34$ mm. Apart from the power spectrum, the fact of having a number of data points power of 2 is very convenient for the analysis of $w(l,t)$ using progressively smaller window sizes. The interpolation procedure has some influence to the computation of the power spectrum because all scales are affected. However, using other methods such as zero–padding [PFTV93], we have checked that the different power spectra have the same slope. In addition, and from an experimental point of view, we have observed that slopes measured in the power spectra corresponding to different disorder realizations have a much larger dispersion than slopes corresponding to power spectra calculated using the same interface, with and without data interpolation.

Another question is how other analysis, such as $w(l,t)$, the growth of the mean slopes $\langle\overline{(\nabla h)^2}\rangle^{1/2}$, or the statistical distribution of height differences, are affected by the interpolation procedure. We have reanalyzed the experiments using different Δx and observed that the above quantities are almost insensitive to Δx, even for values of Δx much larger than the usual value. An example is presented in Fig. 2.17, which shows the analysis of $w(L,t)$ for disorder T 1.50 using different values of Δx.

2.3.4 Experimental procedure and intrinsic width

The oil is injected at constant flow-rate using a syringe pump that can give flow–rates Q in the range 1–299 ml/h. The oil enters the cell through two wide holes, drilled on the top plate near one end of the cell. The other end of the cell is left open. To start the experiment with as flat an interface as possible, the oil is first slowly placed on the last transverse copper track, which is 2 mm ahead the disorder pattern. Next, the syringe pump is set to its maximum injection rate until the whole interface has reached the disorder (about 3 s later). The pump is then set to the nominal injection rate of the experiment, and $t = 0$ is defined as the time at which the average height of the interface (measured on the images) reaches the preset nominal velocity.

Although we can get a reasonably flat interface at $t = 0$ s (see for example the first interface in Figs. 2.12 and 2.13), there is always an initial roughness $w(0)$. This initial roughness or *intrinsic width* [BS95] is strongly dependent on the disorder realization and, in addition, does not permit to observe the growth of the small scales at short times. For these reasons we have always plot the *subtracted width* $W(l,t)$, defined as $W(l,t) = \langle w^2(l,t) - w^2(l,0)\rangle^{1/2}$, where the brackets indicate average over disorder realizations. This correction is an standard procedure and is frequently applied both in experiments (specially in sputtering, see for example Ref. [JZC96]) and numerical simulations [TvS00]. An example of the variation of the interfacial roughness as a function of time with and without this correction is shown in Fig. 2.18.

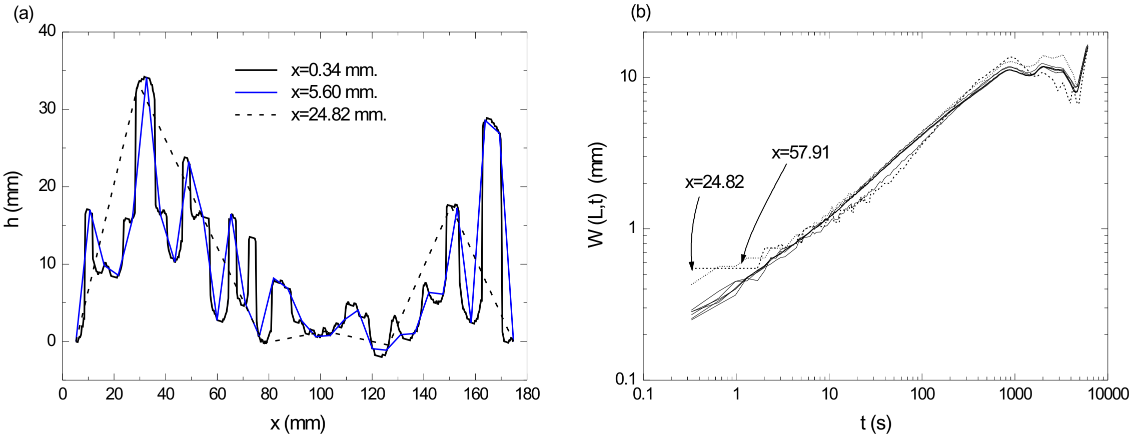

Figure 2.17: (a) Examples of interfaces interpolated with different Δx. (b) $W(L,t)$ as a function of time for increasing Δx from $\Delta x = 0.34$ mm to $\Delta x = 57.91$ mm in powers of two. The curve for raw data is also included. The experimental parameters are $b = 0.36$ mm, $v = 0.08$ mm/s, and disorder T 1.50.

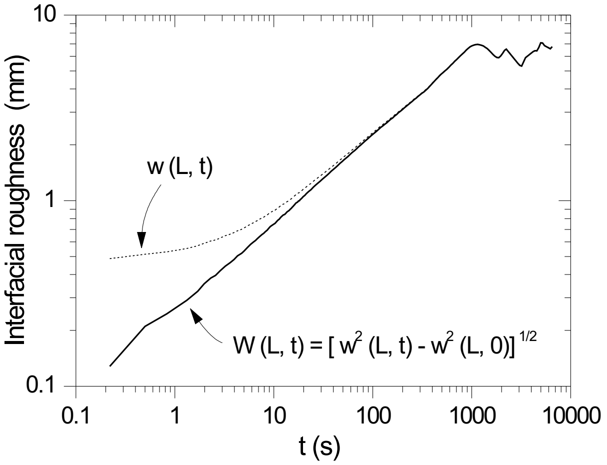

Figure 2.18: Correction of the intrinsic width in a single experiment. The experimental parameters are $b = 0.36$ mm, $v = 0.08$ mm/s, and disorder T 0.40.

2.4 Hele–Shaw flows and the characterization of the cell

Our experimental setup consists on a Hele-Shaw cell [HS98] that contains a quenched disorder in the bottom plate. The simplest model of a Hele–Shaw cell was initially formulated [ST58] considering two parallel plates separated a narrow gap b which is much smaller than any other characteristic length scale of the system, i.e. the length and the width of the cell.

The flow inside the cell is described using the Navier–Stokes equation and one considers the fluid uncompressible. In conditions of low Reynolds numbers ($Re \ll 1$) the flow can be considered quasistationary and, averaging out the velocity along the direction perpendicular to the plates, we get that the velocity of the interface $\vec{v}$ in the plane of the cell is given by

$$\vec{v} = -\frac{b^2}{12\mu}\left(\vec{\nabla}p - \vec{F}_{ext}\right), \tag{2.1}$$

where $\vec{v}$ is the interface velocity, μ the dynamic viscosity, $\vec{\nabla}p$ the pressure gradient, and $\vec{F}_{ext}$ an external force. The constant of proportionality $b^2/12$ comes from averaging out the velocity profile of the flow in the direction perpendicular to the plates.

Eq. (2.1) is known as Darcy's law and is the same equation that governs the flow of a fluid inside a porous medium. In this case, however, the constant of proportionality must be replaced by a new constant that takes into account the geometry of the porous medium, the permeability k. In absence of external forces, Eq. (2.1) reads

$$\vec{v} = -\frac{k}{\mu}\vec{\nabla}p. \tag{2.2}$$

The determination of the permeability of a real porous media is extremely difficult due to the complexity of the media [Dul91] and it is frequent to use theoretical and numerical models.

2.4.1 Permeability of the disorder cell

We have determined the permeability of our Hele-Shaw cell with quenched disorder experimentally. There are some very interesting studies that deal with the determination of the permeability in 2D porous media with a geometry similar to our disorder [SMB$^+$93; KKT97]. However, these results cannot be applied to our Hele-Shaw cell because we have a variable gap spacing. They can provide some useful information to our problem in the limit $b \rightarrow d$, where d is the height of the copper obstacles. In the determination of the permeability of our cell we have used some of the results available in these studies to characterize much better our results.

The experimental setup that we have used is similar to the one used at constant injection rate (Fig. 2.10(a)) but the injection system has been replaced by a constant pressure device. It consists of an oil column of adjustable constant height in the range from 200 ± 2 mm to 1000 ± 5 mm. The permeability is determined by measuring the oil–air interface average velocity for different heights of the oil column and using Darcy's law.

Because for small heights of the column oil the capillary pressure at the interface cannot be negligible, we have alternatively measured the permeability by measuring the amount of oil per unit time, Q, that is withdrawn at the end of the cell. With the information of the width of the cell A and the average gap spacing $\widetilde{b}$ we can calculate the velocity of the flow.

Fig. 2.19 shows the results obtained. At large gap spacings, $d/b \rightarrow 0$, the disorder has no effect on the fluid flow, and the permeability tends to the expected value for an ordinary Hele–Shaw cell, $k_0 = b^2/12$, independently of the disorder configuration. At very small gaps, $d/b \rightarrow 1$, the permeability decreases, and tends to a non–zero value k_1 for $d/b = 1$, that clearly depends on the disorder configuration. We have found it convenient to write k_1 in the form

$$k_1 = d^2 \Lambda / 12, \tag{2.3}$$

where Λ is a function that depends on the porosity ϕ and the geometry of the disorder. The simplest functional form that interpolates between these two limits can be written as:

$$k = \frac{b^2}{12} \left(1 - (1 - \Lambda^{1/2}) \frac{d}{b} \right)^2 . \tag{2.4}$$

The coefficient Λ can be obtained in general from a fit of the permeability to the experimental data.

In the particular case of disorder T and $d/b = 1$, an analytic expression of Λ can be derived by recognizing that the cell in this case is formed by a parallel array of rectangular capillaries. Following Avellaneda *et al.* [AT91], in this geometry Λ is directly the porosity ϕ, which in the limit $d/b = 1$ is given simply by $\phi = 1 - f$. Hence, since we have $f = 0.35$, we obtain $\Lambda = 0.65$. This result fits well the experimental data not only in the limit $d/b = 1$ but also in the whole range of d/b (solid line in Fig. 2.19). Notice also that the results presented in Fig. 2.19 show that there are no important differences between T 1.50 mm and T 0.40 mm. This observation

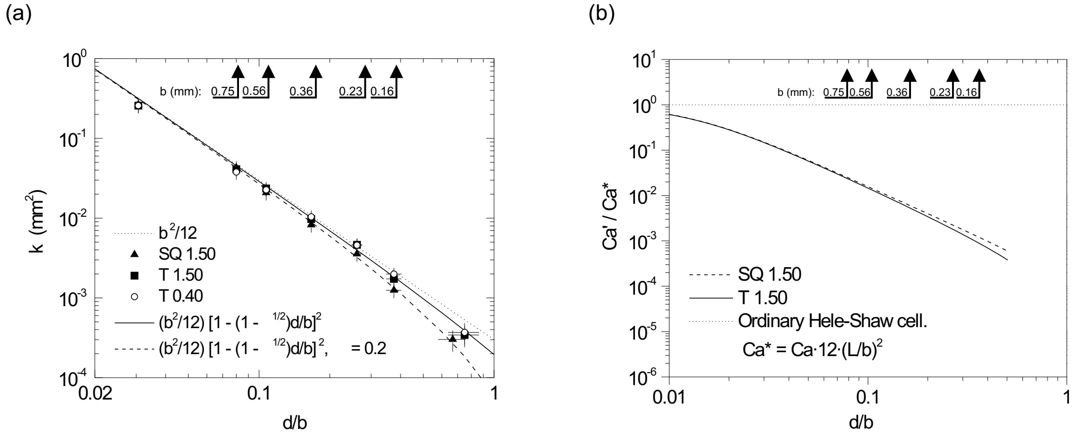

Figure 2.19: (a) Measurements of the permeability, k, as a function of the disorder strength, d/b, for $d = 0.06$ mm. The dotted line is the permeability of an standard Hele–Shaw cell (without disorder), and the dashed and solid lines are fits to the experimental data for SQ and T disorder configurations, respectively. (b) Ratio of the modified capillary number for the cell with disorder, Ca', to the modified capillary number for an ordinary Hele-Shaw cell, Ca*, as a function of the disorder strength, d/b. The dashed and solid lines correspond to disorders SQ 1.50 and T 1.50. The dotted line represents the asymptotic limit Ca'=Ca* The arrows point to the values of d/b for the gap spacings used in the experiments.

generalizes the theoretical result that in the limit $d/b = 1$ the width of the rectangular capillaries does not modify the permeability [AT91]. For SQ and SQ–n disorder, due to the difficulty of finding a general expression for k_1 (see Refs. [KKT96; KKT97]), we have fitted k to our experimental results (dashed line in Fig. 2.19) and have obtained a numerical value $\Lambda = 0.20$.

2.4.2 Modified capillary number

We can introduce a dimensionless number to describe the relative strength of viscous to capillary forces. The simplest number that relates viscous and capillary forces is the *capillary number* Ca= $\mu v/\sigma$. In order to account for the properties of the disorder, which are not contained in the previous definition of Ca, it is customary to introduce a *modified capillary number*. For an ordinary Hele-Shaw cell (without disorder), the modified capillary number, which we call Ca*, comes out from the dimensionless form of the Hele–Shaw equations [Hom87]:

$$\mathrm{Ca}^* = \mathrm{Ca} \cdot 12 \left(\frac{L}{b}\right)^2 . \qquad (2.5)$$

To define a modified capillary number Ca' for our particular cell with disorder, we consider on one side the average viscous pressure drop across the cell, given by

$$\delta p_{vis} = L \cdot |\nabla p_{vis}|, \tag{2.6}$$

with $\nabla p_{vis} = -v\mu/k$ (Darcy's law). L, the cell width, provides the macroscopic length scale. On the other side, a measure of the capillary pressure drop is given by

$$\delta p_{cap} = \sigma \left(\frac{2}{b-d} - \frac{2}{b} + \frac{1}{L} \right). \tag{2.7}$$

The last contribution accounts for the curvature of the interface in the plane of the cell, and is relevant only when $d/b \to 0$, i.e. when the destabilizing role of the disorder vanishes.

Defining Ca' $= \delta p_{vis}/\delta p_{cap}$ and using (2.6) and (2.7), we get

$$\text{Ca'} = \text{Ca} \cdot \frac{12L}{b^2 \left(1 - (1-\Lambda^{1/2})\frac{d}{b}\right)^2 \left(\frac{2}{b-d} - \frac{2}{b} + \frac{1}{L}\right)}. \tag{2.8}$$

The function Ca'/Ca* is shown in Fig. 2.19(a) for disorders SQ and T. When $d/b \to 0$ the destabilizing role of the disorder is negligible, as expected, and Ca'/Ca* tends to 1 (ordinary Hele-Shaw cell). As d/b increases, the increasing strength of the disorder is manifest in the progressive decrease of Ca'/Ca*. It is important to notice that our definition of Ca' is not valid for $d/b = 1$, because flow is essentially different when the free gap disappears. In the range of d/b explored in our experiments the permeability of the cell remains always very close to that of an ordinary Hele–Shaw cell (Fig. 2.19(b)), and the decrease of Ca'/Ca* is essentially due to the capillary forces associated with the menisci in the z direction.

In the range of gap spacings experimentally explored, $0.16 \leqslant b \leqslant 0.75$ mm, the ratio between the free gap $b - d$ and the total gap b varies between 62% and 92%. These large ratios, combined with the high viscosity and small surface tension of the silicone oil compared with other fluids (i.e. water), are responsible for the large values of Ca' in our experiments, in comparison to the values reported for pure porous media. Considering for example the disorder T 1.50 mm, Ca' varies from a value 1.33 (for $b = 0.16$ mm and the minimum interface velocity, 0.04 mm/s) to a value 17.0 (for $b = 0.75$ mm and the maximum interface velocity, 0.4 mm/s).

Chapter 3

Summary of results

3.1 Experimental results at constant injection rate

3.1.1 Weak quenched disorder

The experimental results with *weak* quenched disorder are characterized by a scaling of the interfacial fluctuations that is best described in the framework of Family–Vicsek dynamic scaling. They correspond to experimental parameters characterized by large interface velocities, large gap spacings, or short persistence length in the direction of growth.

We have measured the growth exponent β from the scaling of $W(L, t)$ with time, and for different gap spacings and interface velocities. We have found $\beta \simeq 0.50$, which is almost independent of the gap spacing, driving velocity, and disorder configuration. This is illustrated in Figs. 3.1(a) and 3.1(b), which show $W(L, t)$ plots for disorders SQ 1.50 and T 1.50, and for different driving velocities. The roughness exponent α has been measured by means of the scaling of the power spectrum $S(k, t)$ with k at saturation, and its value checked using alternative analysis. In contrast with the robustness of β, the measured roughness exponents are more sensitive to the experimental parameters and two regimes separated by a crossover wavenumber k_c have been characterized, α_1 at short length scales, and α_2 at long length scales. We have observed that in general α_1 increases with the velocity, while α_2 decreases. Examples of the power spectra for different velocities are presented in Figs. 3.2(a) and 3.2(b) for SQ 1.50 and T 1.50 respectively. It is remarkable to notice that, as the velocity is reduced, there is a tendency to a unique power law that extents all scales, and with slope around -2.4 ($\alpha \simeq 0.7$) for SQ 1.50. It is also noticeable the fact that, although the roughness exponents α_1 that can be extracted from the slopes of the power spectra are different for SQ 1.50 and T 1.50, at very large average interface velocities they tend to a limiting value around $\alpha_1 \simeq 1.3$. The values of the roughness exponents measured at different velocities and for different disorder configurations are summarized in Table 3.1.

The crossover wavenumber k_c separates two regimes, one at small k in which the long length scale fluctuations are damped by the viscous pressure field, and the other at large k in which the short length scale fluctuations are damped by the interfacial tension in the plane of the cell. k_c scales with the velocity as $k_c \sim v^{-\zeta}$, with $\zeta = 0.47$, $\zeta = 0.28$, and $\zeta \simeq 0$ for disorders SQ, SQ-n and T respectively. The fact that ζ tends to zero as the persistence of the disorder increases is due to the damping role of the

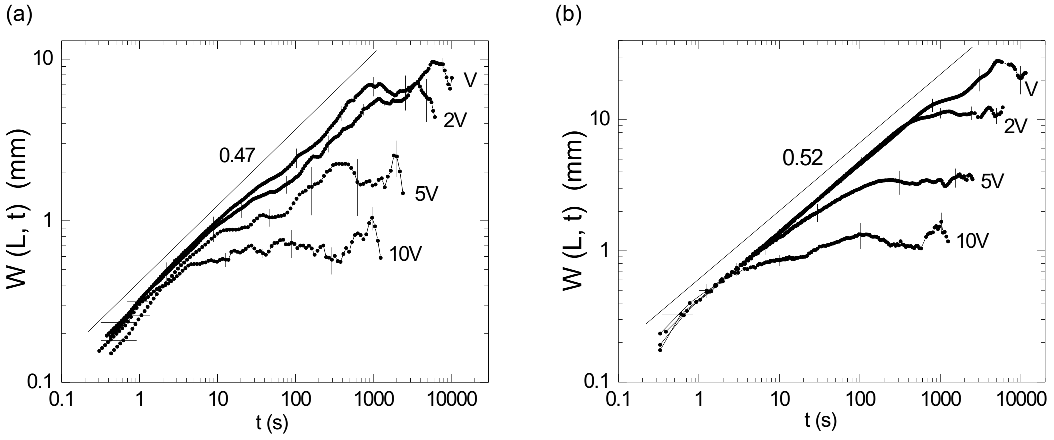

Figure 3.1: Dependence of the growth exponent on velocity. (a) $W(L,t)$ for disorder SQ 1.50. (b) $W(L,t)$ for disorder T 1.50. The gap spacing is $b = 0.36$ mm and $V = 0.04$ mm/s.

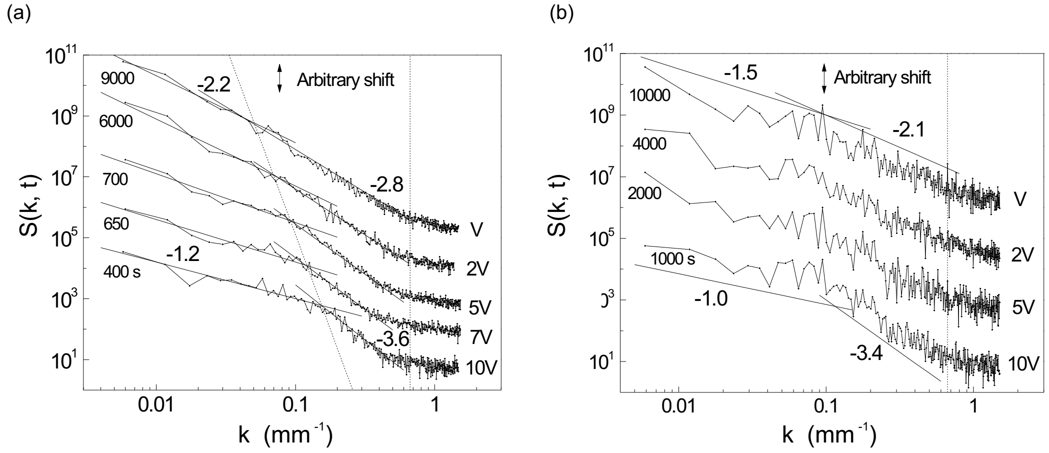

Figure 3.2: Dependence of the roughness exponents on velocity. (a) $S(k,t)$ for disorder SQ 1.50 (b) $S(k,t)$ for disorder T 1.50. The gap spacing is $b = 0.36$ mm and $V = 0.04$ mm/s.

Disorder	Low Ca' ($\lesssim 3$)		Moderate Ca' ($3 <$ Ca' < 10)		Large Ca' ($\gtrsim 10$)	
	α_1	α_2	α_1	α_2	α_1	α_2
SQ 1.50	$0.6-0.9$	–	$\simeq 1$	$\simeq 0.6$	$\simeq 1.3$	$\simeq 0$
SQ-n 1.50	$0.6-0.9$	–	$\simeq 0.9$	$\simeq 0.5$	$\simeq 1.3$	$\simeq 0$
T 0.40	Anomalous scaling		$\simeq 0.7$	$\simeq 0.5$	$\simeq 1.3$	$\simeq 0$
T 1.50	Anomalous scaling		$\simeq 0.5$	$\simeq 0.2$	$\simeq 1.3$	$\simeq 0$

Table 3.1: Summary of the values of the roughness exponents in the limit of weak quenched disorder.

in–plane interfacial tension, which is effectively suppressed for a totally persistent disorder in the direction of growth.

In the limit of very large driving velocities the roughness exponents α_1 and α_2 tend asymptotically to $\alpha_1 \simeq 1.3$ and $\alpha_2 \simeq 0$ respectively, in agreement with recent theoretical results of nonlocal models [DRE+99; PC02].

3.1.2 Strong quenched disorder

We have carried out experiments varying the gap spacing, the driving velocity, and the configuration of the disorder, and measured the scaling exponents. These results are characterized by the presence of intrinsic anomalous scaling.

With these experiments we have obtained the first experimental evidences of in-

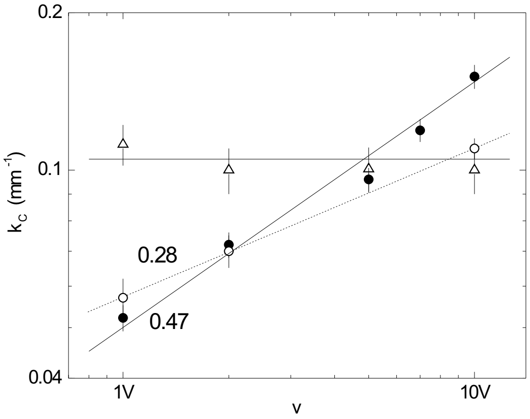

Figure 3.3: Dependence of the crossover wavenumber k_c on velocity v for three disorder configurations: SQ 1.50 (solid circles), SQ-n 1.50 (open circles) and T 1.50 (triangles). $b = 0.36$ mm and $V = 0.04$ mm/s.

trinsic anomalous scaling in Hele–Shaw flows. Three conditions are needed to observe the anomaly: i) a disorder sufficiently persistent in the direction of growth, ii) strong (but not dominant) capillary forces, and iii) viscous forces properly balanced with the capillary forces. In these conditions, we have determined the five scaling exponents that characterize the anomaly for different gaps spacings (strength of capillary forces) and velocities (strength of viscous forces). The typical interfaces are characterized by large height differences at the edges of the tracks (Fig. 3.4(a)), and their growth is responsible for the different behavior of global and local scales. The global and local growth exponents β and β^* have been obtained from the study of the interfacial fluctuations as a function of time, $W(l = L, t)$ and $W(l = L/256, t)$ respectively (Fig. 3.4(b)). The local growth exponent β^* appears progressively displacing β as we reduce the window size, in agreement with the anomalous scaling assumption. The local roughness exponent α_{loc} has been measured by means of the scaling of the power spectrum $S(k, t)$ at saturation (Fig. 3.5(a)). The collapse of the power spectrum (Fig. 3.5(b)) has provided the global roughness exponent α, the dynamic exponent z, and has allowed a refinement of the whole set of scaling exponents.

We have obtained for $b = 0.36$ mm and $v = 0.08$ mm/s the following set of scaling exponents

$$\begin{aligned} &\beta = 0.50 \pm 0.04, \ \beta^* = 0.25 \pm 0.03, \\ &\alpha = 1.0 \pm 0.1, \ \alpha_{loc} = 0.5 \pm 0.1, \ z = 2.0 \pm 0.2. \end{aligned} \tag{3.1}$$

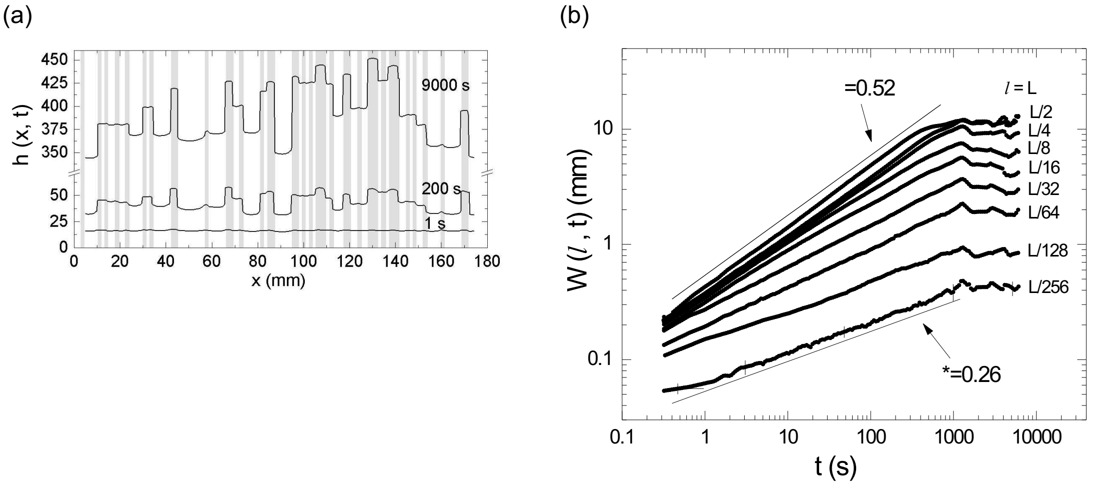

Figure 3.4: (a) Typical interfaces in experiments that present anomalous scaling. (b) $W(l, t)$ plots for different window sizes, decreasing from $l = L$ (global scales) to $l = L/256$ (local scales). The experimental parameters are $b = 0.36$ mm, $v = 0.08$ mm/s, and disorder T 1.50.

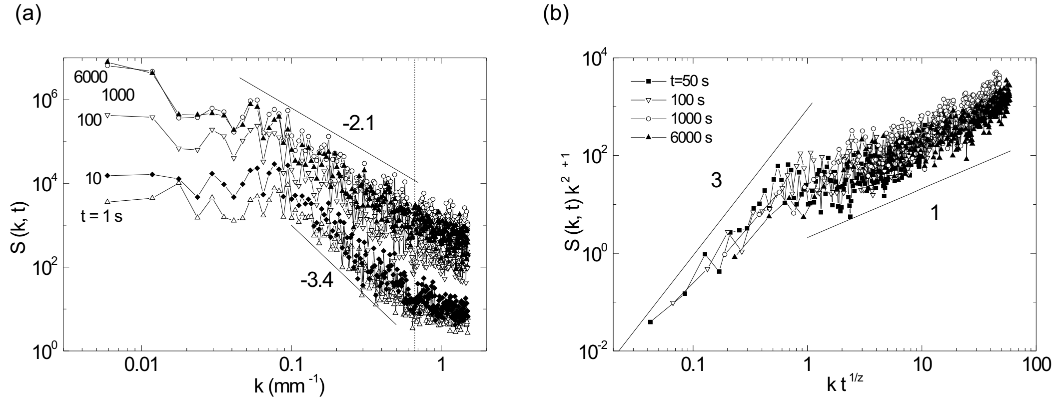

Figure 3.5: (a) Temporal evolution of the power spectrum for the same experimental parameters as Fig. 3.4. The vertical line gives the the value of k associated to the spatial scale of the disorder. (b) Collapse of the power spectra for $t > 10$ s.

These values have been confirmed using alternative analysis, such as the variation of the local slopes, the presence of multiscaling, and the statistical distribution of height differences.

To understand the physical origin of the anomalous scaling we have performed experiments solely driven by capillary forces, i.e. with $Q = 0$, and found that the velocity on a single track is given by the simple relaxation law $v = v_M\ t^{-1/2}$, with v_M an initial overshoot. For $Q \neq 0$ a detailed investigation of the interface motion on the tracks has allowed a description of the anomalous scaling in terms of i) the different velocity of the points of the interface that are advancing over copper tracks (v_+) and fiberglass channels (v_-), which can be expressed in the form $v_\pm = v \pm (v_M - v)\ t^{-1/2}$, and ii) the coupling in the interface motion between neighboring tracks.

To study the range of validity of the anomaly we have explored in depth the effect of the gap spacing, driving velocity, and disorder configuration. Three different regimes have been found, and are reflected in the phase diagram shown in Fig. 3.6:

1. For dominant capillary forces, $b \lesssim 0.15$ mm, an scaling regime cannot be characterized due to the lack of a growing correlation length in the x direction (light grey area in Fig. 3.6). The same result is obtained for larger b when a regular modulation of the gap spacing is introduced.

2. For strong (but not dominant) capillary forces and for driving velocities below a threshold value we observe anomalous scaling. Although the scaling exponents depend on the experimental parameters, we have obtained values around $\beta = 0.50$, $\beta^\star = 0.25$, $\alpha = 1.0$, $\alpha_{loc} = 0.5$, and $z = 2.0$ (dark grey area in Fig. 3.6). For

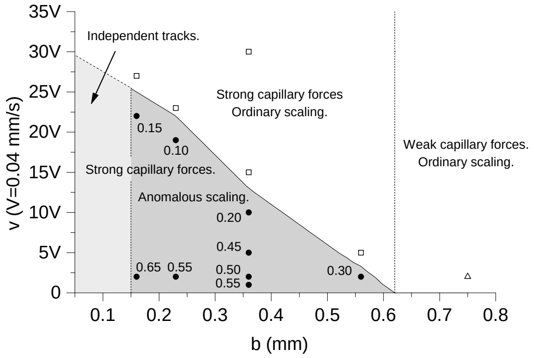

Figure 3.6: Phase diagram for the anomalous scaling. The symbols indicate the parameters explored experimentally. The numbers next to the symbols in the anomalous scaling region give the value of $2\theta/z$. The solid line represents the curve $v = v_M(b)$.

driving velocities above the threshold value, anomalous scaling is unobservable and the Family–Vicsek scaling assumption describes better the scaling of the interfacial fluctuations.

3. For weak capillary forces and for any velocity the scaling is Family-Vicsek.

3.2 Experimental results at constant pressure

We have replaced the injection pump by a constant pressure device consisting of a silicone oil column of selectable height H (Fig. 3.7). We have performed experiments exploring different heights, with fixed gap spacing $b = 0.36$ mm and disorder configuration SQ 1.50. We have observed that the average position of the interface, $\langle h\rangle(t) = \langle h(x,t)\rangle_x$, obeys Washburn's law $\langle h\rangle(t) \sim t^{1/2}$ (Fig. 3.8(a)). For a critical value of H, $H_c \simeq -25$ mm, the interface is close to the pinning point and the average interface velocity of the interface is almost zero. For values of $H > H_c$ the interface always advances. Close to H_c the interface displays local pining and some regions of the interface advance in avalanches (Fig. 3.8(b)).

We have measured the growth and roughness exponents β and α. For $H = -17$ mm, close to H_c, we have obtained $\beta = 0.64 \pm 0.03$ (Fig. 3.9(a)). This large value of the growth exponent is attributed to i) the decay of the average interface velocity with time following Washburn's law, and ii) the fact that the interface is driven at constant pressure, which allows the fluid to take all necessary mass to grow, in contrast to the experiments at constant injection rate, where the amount of mass is

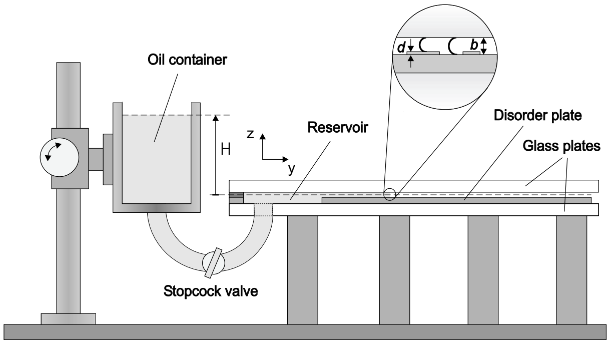

Figure 3.7: Detail of the experimental setup at constant pressure.

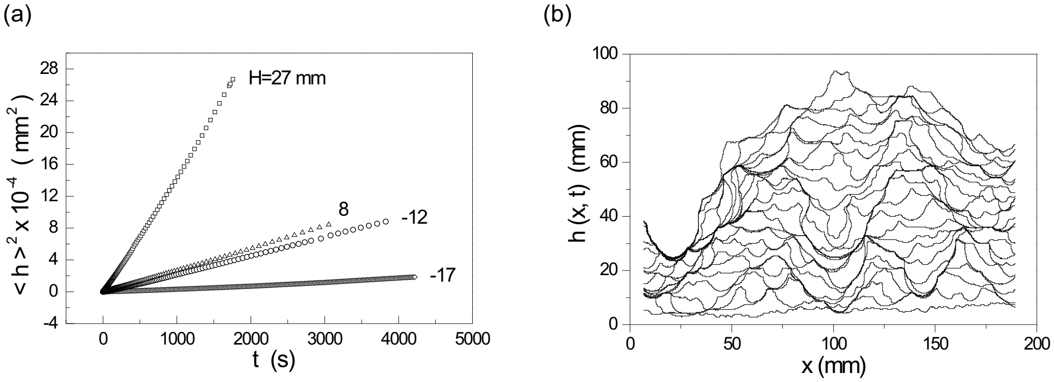

Figure 3.8: (a) Plots of $\langle h\rangle^2(t)$ for different heights of the oil column, which follow a linear behavior if the Washburn's law is obeyed. (b) Temporal evolution of interfaces for $H = -17$ mm. The interfaces shown are plotted every 120 s.

limited by the injection pump. The measured roughness exponent at short times is $\alpha = 0.7 \pm 0.1$ (Fig. 3.9(b)) and extends to all scales, in contrast to the experiments at constant injection rate where there is a clear crossover. At short times we measure $\alpha = 1.1 \pm 0.1$, which is due to the highest velocity of the interface at the initial stages. The variation of the roughness exponent as a function of different applied pressures (different H) show that, as H approaches to H_c, the roughness exponent tends to a limiting value around $\alpha = 0.6 - 0.7$. This result, in addition to $\beta \simeq 0.64$, suggests that in the critical point the dynamics could be local and described by the QKPZ universality class, with $\alpha = \beta \simeq 0.63$.

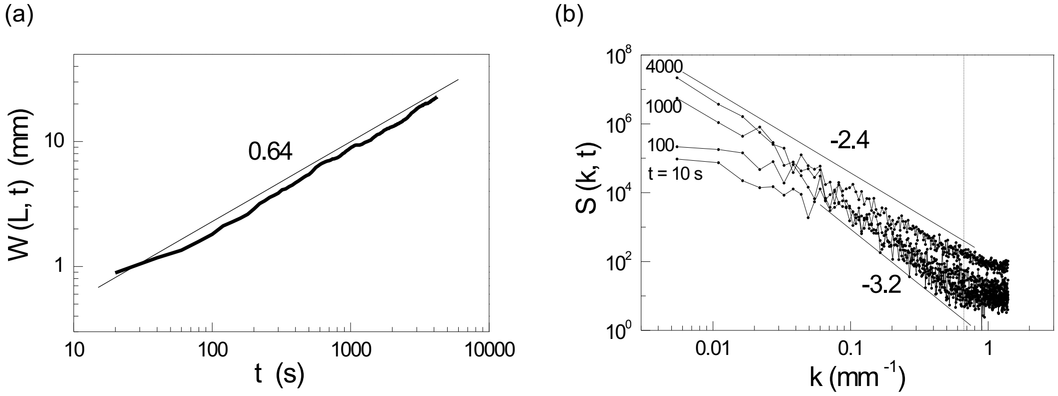

Figure 3.9: Experimental results at constant pressure. (a) Interfacial width as a function of time. (b) Temporal evolution of the power spectrum. The vertical line in (b) indicates the value of k associated to the spatial scale of the disorder.

Chapter 4

Publications

The pages that follow contain the five papers where most of the main results of this thesis have been published. The papers, shown in order of publication, are the following:

- A. Hernández–Machado, J. Soriano, A.M. Lacasta, M.A. Rodríguez, L. Ramírez–Piscina, and J. Ortín, *Interface roughening in Hele–Shaw flows with quenched disorder: Experimental and theoretical results*, Europhys. Lett. **55**, 194 (2001).
- J. Soriano, J. Ortín, and A. Hernández–Machado, *Experiments of interfacial roughening in Hele-Shaw flows with weak quenched disorder*, Phys. Rev. E **66**, 031603 (2002).
- J. Soriano, J.J. Ramasco, M.A. Rodríguez, A. Hernández–Machado, and J. Ortín, *Anomalous roughening of Hele–Shaw flows with quenched disorder*, Phys. Rev. Lett. **89**, 026102 (2002).
- J. Soriano, J. Ortín, and A. Hernández–Machado, *Anomalous roughening in experiments of interfaces in Hele-Shaw flows with strong quenched disorder*, Phys. Rev. E, submitted, cond-mat/0208432 (2002).
- J. Soriano, J. Ortín, and A. Hernández–Machado, *Forced imbibition of a viscous fluid by a disordered Hele–Shaw cell*, preprint.

4.1 *Interface roughening in Hele–Shaw flows with quenched disorder: Experimental and theoretical results*, **Europhys. Lett. 55, 194 (2001)**

EUROPHYSICS LETTERS 15 July 2001

Europhys. Lett., **55** (2), pp. 194–200 (2001)

Interface roughening in Hele-Shaw flows with quenched disorder: Experimental and theoretical results

A. Hernández-Machado[1,2](*), J. Soriano[1], A. M. Lacasta[3], M. A. Rodríguez[4], L. Ramírez-Piscina[3] and J. Ortín[1]

[1] *Departament ECM, Facultat de Física, Universitat de Barcelona*
Diagonal 647, E-08028 Barcelona, Spain
[2] *Groupe de Physique des Solides, Université Pierre-et-Marie-Curie*
Tour 23, 2 place Jussieu, 75251 Paris Cedex 05, France
[3] *Departament de Física Aplicada, Universitat Politècnica de Catalunya*
Avda. Dr. Marañon 44, E-08034 Barcelona, Spain
[4] *Instituto de Física de Cantabria, CSIC*
Avenida Los Castros, E-39005 Santander, Spain

(received 22 November 2000; accepted in final form 14 May 2001)

PACS. `47.55.Mh` – Flows through porous media.
PACS. `68.35.Ct` – Interface structure and roughness.
PACS. `05.40.-a` – Fluctuation phenomena, random processes, noise, and Brownian motion.

Abstract. – We study the forced fluid invasion of an air-filled model porous medium at constant flow rate, in $1+1$ dimensions, both experimentally and theoretically. We focus on the nonlocal character of the interface dynamics, due to liquid conservation, and its effect on the scaling properties of the interface upon roughening. Specifically, we study the limit of large flow rates and weak capillary forces. Our theory predicts a roughening behaviour characterized at short times by a growth exponent $\beta_1 = 5/6$, a roughness exponent $\alpha_1 = 5/2$, and a dynamic exponent $z_1 = 3$, and by $\beta_2 = 1/2$, $\alpha_2 = 1/2$, and $z_2 = 1$ at long times, before saturation. This theoretical prediction is in good agreement with the experiments at long times.The ensemble of experiments, theory, and simulations provides evidence for a new universality class of interface roughening in $1+1$ dimensions.

Studies on the morphology of interfaces moving in disordered media under nonequilibrium conditions constitute an active field of research [1]. One relevant example is the forced invasion of an air-filled porous medium by a viscous wetting fluid such as oil or water, which gives rise to a nonequilibrium rough interface [2–6]. The roughening process of an initially flat interface is described in terms of the interfacial root-mean-square width w. In many systems w follows a Family-Vicsek dynamical scaling [7]: $w \sim t^{\beta}$ for $t < t_{\times}$, $w \sim L^{\alpha}$ for $t > t_{\times}$ and $t_{\times} \sim L^{z}$, with $\alpha = z\beta$. Here $t_{\times}$ is a saturation time, β the growth exponent, α the roughness exponent, and z the dynamic exponent. The roughness exponent can also be obtained from the power spectrum

---

(*) E-mail: `aurora@ecm.ub.es`

© EDP Sciences

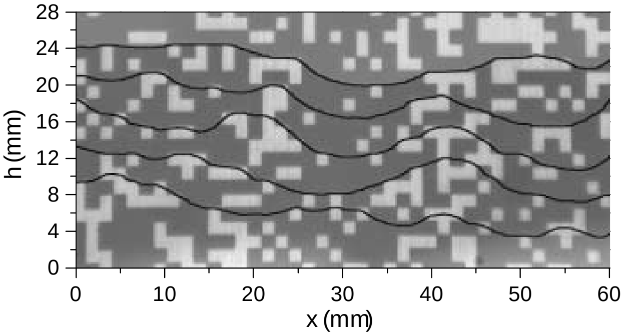

Fig. 1 – Several consecutive close-up views of a piece of the oil-air interface, taken at 150 s time intervals. The flow rate is $Q = 10$ ml/h.

$S(q,t)$, which is less sensitive to finite-size effects. We have [8] $S(q,t) = q^{-(2\alpha+1)} s_{\mathrm{FV}}(qt^{1/z})$, where s_{FV} obeys $s_{\mathrm{FV}}(u) \sim$ const when $u \gg 1$, and $s_{\mathrm{FV}}(u) \sim u^{2\alpha+1}$ when $u \ll 1$.

Experiments of forced fluid invasion (FFI) in air-filled packings of glass beads, in $1+1$ dimensions, have given roughness exponents in the range $\alpha = 0.6$–0.9 [2–5]. The dispersion reflects the fact that the effective values of α, determined by measuring widths over several scales at saturation, depend on the capillary number C_a [4]. On the other hand, there are few experimental determinations of the exponent β, because the large relative strength of capillary to viscous forces made the growth regime extremely short in most experiments.

In this letter we report new experimental results of dynamic interfacial roughening in FFI, in $1+1$ dimensions, at *constant injection rate*. In our case the model porous medium is a Hele-Shaw cell with controlled spatial fluctuations of the gap thickness. While the viscous pressure field and the surface tension in the plane of the cell keep the interface smooth on large length scales, fluctuations in the gap thickness produce local fluctuations in capillary pressure which roughen the interface. Thus the governing physics is the same as in a real two-dimensional porous medium, and we have the possibility of controlling the statistical properties and the relative strength of the disorder.

In our experiments a silicone oil [9] displaces air in a horizontal Hele-Shaw cell, 190×550 mm^2, made of two glass plates 19 mm thick. Fluctuations in the gap thickness are provided by a fiber glass substrate which contains a random distribution of square copper islands filling 35% of the substrate. Each island is 0.06 ± 0.01 mm thick and has 1.500 ± 0.005 mm lateral size (fig. 1). The gap spacing from the substrate to the top plate is $b = 0.36 \pm 0.05$ mm. Since the maximum width of the meniscus is only one half the gap width, the interface can be considered one-dimensional at the length scale of the copper islands. The oil is injected at one side of the cell using a constant flow rate syringe pump. A flat front is first prepared by keeping the oil at rest in a transverse copper track separated 2 mm from the beginning of the noise. Initially the oil is pushed at high flow rate (300 ml/h) for about 4 s to keep the interface smooth while it enters the noise. Next, at a time defined as $t = 0$, the flow rate is set to its nominal value Q, and the oil-air interface is monitored as a function of time using two CCD cameras, with a final spatial resolution of 0.37 mm/pixel. This imposes a cut-off at small length scales, about twice the maximum width of the meniscus. We choose a range of flow rates ($10 \leq Q \leq 100$ ml/h) such that the contact line overcomes the copper islands rather easily, without pinning or forming overhangs. For $Q = 10$ ml/h (fig. 1) the average interface velocity is $v = 0.038 \pm 0.005$ mm/s, which we take as a reference.

Our results for $w(t)$ are presented in fig. 2(a). As expected, both the saturation time and the interfacial width w at saturation depend on the average velocity at which the interface

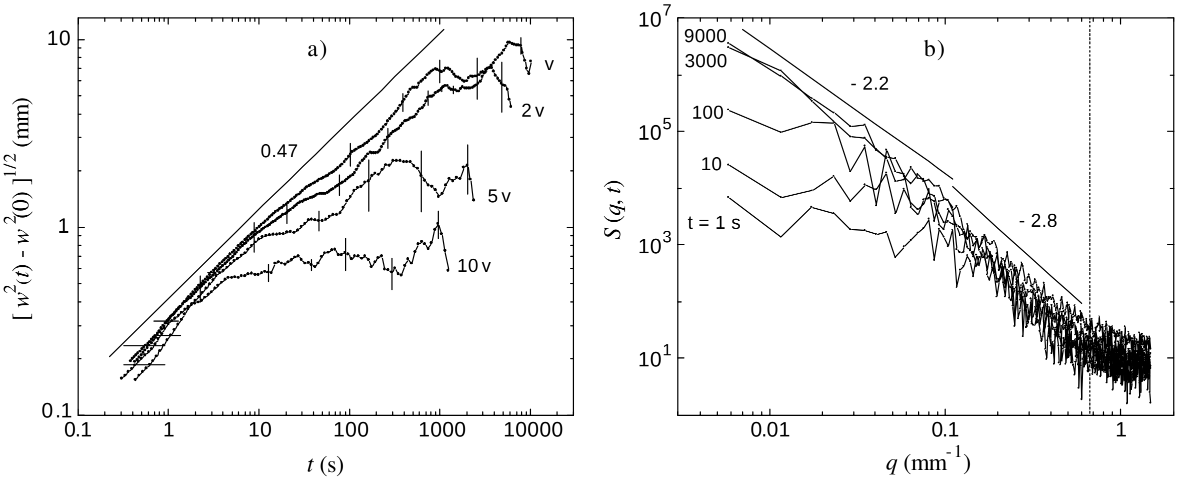

Fig. 2 – a) Double-logarithmic plot of $w(t)$ for four different interface velocities. Each curve is an average over 6 experiments (3 runs on 2 different realizations of the noise). In each experiment $w^2(0)$ has been subtracted from $w^2(t)$, in order to minimize the effect of the initial condition. The error bars give a measure of the overall dispersion between different experiments. b) Power spectrum of the interface profiles at successive time intervals, for the experiments at velocity v. The vertical line indicates the spatial scale of the disorder.

is driven. We observe also large fluctuations in the interfacial width, consistent with the observations reported in [4]. The fluctuations in w are highly reproducible in experimental runs with the same realization of the disorder. Disregarding fluctuations, the growth of the interfacial width is consistent with a power law $w \sim t^{\beta}$, with $\beta = 0.47 \pm 0.04$, extending about three orders of magnitude in t (for measurements at velocity v) until the width saturates.

The power spectrum for the set of measurements at velocity v is shown in fig. 2(b). At short times the spectrum displays a *plateau* for small q and a power law decay at large q as expected. As the interface advances in the disorder the value of the *plateau* increases, and we observe the emergence of another scale-independent (power law) behaviour for an increasingly growing range of spatial scales, in agreement with the scaling of $S(q,t)$ expected for $u = qt^{1/z} \ll 1$. This behaviour is also observed at velocity $2v$. The measured exponents are -2.2 ± 0.2 ($\alpha = 0.6 \pm 0.1$) at small q (long length scales) and -2.8 ± 0.2 ($\alpha = 0.9 \pm 0.1$) at large q (short length scales). The spectra of the experimental interfaces have been calculated imposing periodic boundary conditions. To this purpose, we have subtracted from the interface the straight line joining its two ends. This correction eliminates an artificial slope that is specially important at saturation, where the difference in height between the two ends is maximum [10].

One interesting aspect of roughening in fluid flows is the *nonlocal* nature of the interfacial dynamics, due to liquid conservation. The importance of nonlocality in this problem has been already pointed out by a number of authors [4,6,11]. Very recently, this issue has been addressed explicitly in the theoretical formulation of FFI at constant pressure [12] and of spontaneous imbibition [12,13]. In this letter we address the same issue for FFI at constant flow rate. This driving condition has not been explored theoretically yet, in spite of being often used in experiments.

Our model is based on a time-dependent Ginzburg Landau model with conserved order parameter (model B in ref. [14]):

$$\frac{\partial \phi}{\partial t} = \nabla M \nabla(-\phi + \phi^3 - \epsilon^2 \nabla^2 \phi). \tag{1}$$

ϕ is the order parameter with equilibrium values $\phi_{\mathrm{eq}} = \pm 1$, and ϵ is the interfacial width. M is the mobility, which we consider fluctuating in space:

$$M(\phi, \boldsymbol{r}) = \begin{cases} K(1+\xi(\boldsymbol{r})) & \text{for oil} \quad (\phi > 0)\,, \\ 0 & \text{for air} \quad (\phi < 0)\,, \end{cases} \tag{2}$$

with K a macroscopic mobility and $\xi(\boldsymbol{r})$ a weak static disorder with a spatial correlation:

$$\langle \xi(\boldsymbol{r})\xi(\boldsymbol{r}')\rangle = 2DC\left(\frac{|\boldsymbol{r}-\boldsymbol{r}'|}{\lambda}\right), \tag{3}$$

where λ is the disorder correlation lenght and C is normalized. Dubé *et al.* [13] have proposed a similar formulation for spontaneous imbibition. In their problem the interface is driven only by capillary forces, and moves with average velocity $\bar{v} \sim t^{-1/2}$. Here, instead, nonlocal viscous forces are dominant over the local fluctuations of capillary pressure: our interface is driven by a constant flux γ_0, which gives rise to a steady-state rough interface moving with constant noise-dependent $\bar{v}$. The disorder is also introduced differently in the two approaches. In our two-dimensional model the fluctuations in gap thickness are represented (phenomenologically) by a fluctuating mobility.

The macroscopic limit of the model is obtained by an asymptotic expansion in orders of ϵ, following a procedure described in ref. [15]:

$$\begin{aligned} \nabla(1+\xi(\boldsymbol{r}))\nabla P &= 0\ , \\ P &= -\Gamma\kappa\ , \\ v_{\mathrm{n}} &= -K(1+\xi(x, y_{\mathrm{int}}))(\nabla P)_n\ , \end{aligned} \tag{4}$$

where the pressure field in the bulk of the liquid is given by $P = (\phi(\boldsymbol{r},t) - \phi_{\mathrm{eq}})/(2\phi_{\mathrm{eq}})$, the surface tension is given by $\Gamma = (2\phi_{\mathrm{eq}})^{-2}\int \mathrm{d}y(\partial_y\phi_{\mathrm{st}})^2$, ϕ_{st} is the steady planar solution of eq. (1), κ is the curvature of the interface, and v_{n} its normal velocity. $\xi(x, y_{\mathrm{int}})$ is taken at the interface. The deterministic part of eq. (4) reproduces the macroscopic equations for oil-air displacements in a Hele-Shaw cell [16].

The interfacial equation in Fourier space can be derived from eq. (4) using Green function analysis. We define $\bar{P} = P + \bar{\gamma}_0/K(y - \bar{\gamma}_0 t)$, where $\bar{\gamma}_0 = \gamma_0/(4\phi_{\mathrm{eq}})$. In this case, the Green function $G(\boldsymbol{r},\boldsymbol{r}')$ obeys $\nabla^2 G = \delta(\boldsymbol{r}-\boldsymbol{r}')$. The interfacial equation for the local deviations of the interface from its mean position, $h(x,t) = y_{\mathrm{int}} - \bar{v}t$, reads (to first order in ξ):

$$\begin{aligned} \int \mathrm{d}s' G(s,s')\frac{v_{\mathrm{n}}(s') - \bar{\gamma}_0\hat{n}\hat{y}}{K} &= \frac{1}{2}\left[-\Gamma\kappa(s) + \frac{\bar{\gamma}_0}{K}\left(h(s) + (\bar{v}-\bar{\gamma}_0)t\right)\right] + \\ + \int \mathrm{d}s'\hat{n}\nabla G(s,s')\left[-\Gamma\kappa(s') + \frac{\bar{\gamma}_0}{K}\left(h(s') + (\bar{v}-\bar{\gamma}_0)t\right)\right] &+ \int \mathrm{d}s' G(s,s')\frac{v_{\mathrm{n}}}{K}\xi(s', y_{\mathrm{int}}), \end{aligned} \tag{5}$$

where s is the contour variable on the interface and $\hat{n}$ and $\hat{y}$ are the unitary vectors perpendicular to the interface and along the y-direction, respectively. We have neglected volume terms which do not contribute to the scaling. A distinguishing feature of eq. (5) is the presence of integral terms, which account for the *nonlocal* character of the interfacial dynamics. The deterministic part is equivalent to the equation for unstable displacements (air displacing oil, $\bar{\gamma}_0 < 0$) derived in refs. [17,18].

In this problem, due to the presence of a correlated disorder, two different time scales of dynamic origin are present. One of them is related to the ballistic dynamics of the interface due to the driving and corresponds to the time in which the interface advances the noise

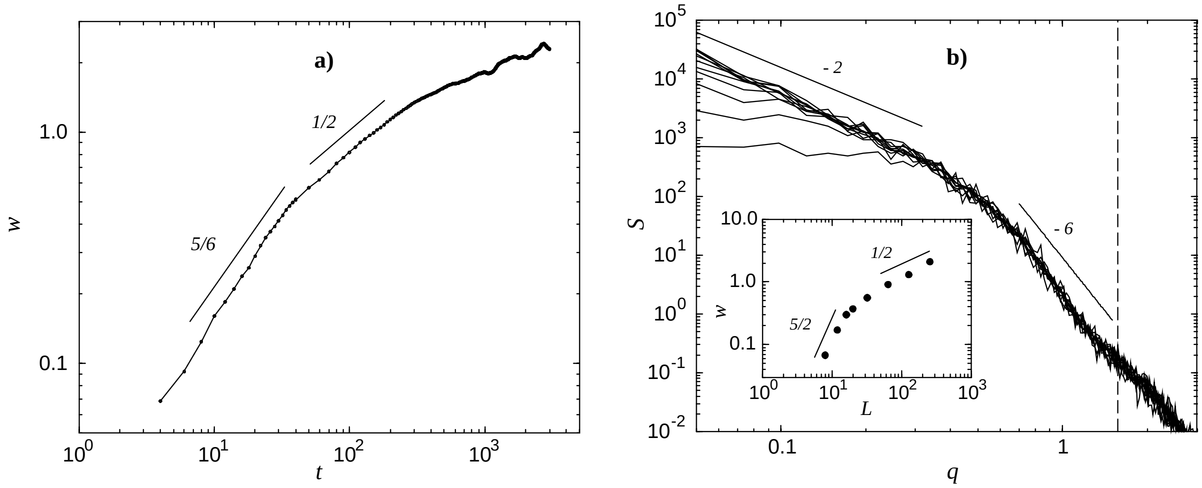

Fig. 3 – a) Temporal evolution of the interfacial width, from the numerical integration of eqs. (1), (2), for a system of size $L = 256$. b) Power spectrum at different time intervals, for the same case as (a). The vertical line is the spatial scale of the disorder. The interfacial width at saturation *vs.* the system size L is shown in the inset.

characteristic length in the y-direction, $t_0 = \lambda/\bar{\gamma}_0$. The other temporal scale corresponds to the dynamics that couples different points of the interface. For scales not much greater than λ this dynamics is diffusive. The associated temporal scale is the time required by the diffusion along the interface to reach distances of the scale of the disorder, and is given by $t_{\mathrm{D}} = \lambda^2/K$. Here, we consider $t_0 \gg t_{\mathrm{D}}$. This condition is fulfilled if $\lambda \ll K/\bar{\gamma}_0$. In this limit, the noise appears as persistent in the y-direction at scales comparable to λ. Therefore, we will take it as equivalent to a columnar (only x-dependent) noise. In this case, the stationary velocity $\bar{v} = \bar{\gamma}_0 + (\bar{\gamma}_0/L)\int \xi(x)\mathrm{d}x$, where L is the system size in the x-direction.

In Fourier space, for small deviations from a flat interface ($|q|h \ll 1$) we have

$$\frac{\partial \tilde{h}_q}{\partial t} = -K\Gamma q^2|q|\tilde{h}_q - \bar{\gamma}_0|q|\tilde{h}_q + \bar{\gamma}_0\xi_q(1-\delta_{q,0}). \tag{6}$$

We observe that short-wavelength fluctuations are damped by surface tension (first term of the r.h.s.), while long-wavelength fluctuations are damped by the advancement of the front, driven by the external flux (second term of the r.h.s.). Equation (6) leads to two different temporal regimes. The early growth regime is dominated by the first term of (6), and the dynamic exponent is $z_1 = 3$. By linear scaling analysis we obtain $z - \alpha - 1/2 = 0$, which gives $\alpha_1 = 5/2$ and $\beta_1 = 5/6$. Since $\alpha_1 > 1$, the interface is superrough in the early time stages. At longer times the second term of (6) dominates the dynamics, and we get $z_2 = 1$, $\alpha_2 = 1/2$, and $\beta_2 = 1/2$. The characteristic crossover time between the two growth regimes is given by $t_{\mathrm{c}} \sim \zeta_{\mathrm{c}}^3 \sim (K\Gamma/\bar{\gamma}_0)^{3/2}$.

We have checked these predictions by numerical integration of eqs. (1), (2) in a rectangular lattice with periodic boundary conditions in the x-direction. A constant flux γ_0 has been maintained by fixing the value of ϕ at a certain distance behind the interface (typically 20 space units). To mimic the experiments, we have assumed that the oil mobility can take two different values, so that ξ is a dichotomous noise of values $\pm D$. The noise is defined in boxes of side $l_{\mathrm{d}} = 4$ space units, randomly distributed with probability 0.35 for the positive value. The values of l_{d} and γ_0 satisfy the requirement of noise persistence in the y-direction. Our results for $\gamma_0 = 0.05$, $K = 1$, $\epsilon = 1$ and $D = 0.5$, averaged over 25 realizations of the noise, are presented in figs. 3(a) and (b).

Figure 3(a) is a log-log plot of $w(t)$, including the analytical prediction for the growth exponents. The numerical results are consistent with a crossover between $\beta_1 = 5/6$ at short times and $\beta_2 = 1/2$ at longer times. Figure 3(b) shows a log-log plot of $S(q,t)$. At short times the spectrum displays a *plateau* for small q, followed by a power law corresponding to $\alpha_1 \simeq 5/2$ for large q. At longer times, $S(q,t)$ shows a data collapse at small q into a power law corresponding to $\alpha_2 \simeq 1/2$. The same results are obtained from the analysis of w *vs.* system size L, shown in the inset of fig. 3(b). We observe the predicted crossover between the two growth regimes. Using the scaling relation $\alpha = z\beta$, the dynamic exponents are $z_1 \simeq 3$ at short times and $z_2 \simeq 1$ at long times, in agreement with the analytical results.

Although we have experimental indications of very fast growth in the earliest time stages, we have not been able to identify experimentally the short-time scaling regime predicted by the model. This regime is difficult to access experimentally because it is very short, it is obscured by the transient originated by setting Q to its nominal value, and, in addition, the short-time behaviour of $w(t)$ is strongly dependent on the definition of $t = 0$. Nevertheless, the experimental power spectrum shows that the short length scales saturate with a larger roughness exponent than the long length scales, which points to a different mechanism at the two scales, in the same direction as the model. The experimental and calculated values of the roughness exponent at short length scales do not coincide because the details of the physical mechanisms operative at the shortest length scales (capillary phenomena) are not properly captured by the model.

Concerning the long time and long length scaling regime, several authors have argued that FFI should fall in the KPZ universality class ($\beta = 1/3$ and $\alpha = 1/2$ in $1+1$ dimensions) in the limit of large C_a considered here [4, 19]. Our experimental and theoretical results contradict this prediction for the exponent β, which is consistently found to be $\beta \simeq 1/2$. Concerning the roughening exponent α, however, previous experimental measurements [4] and our own experiments give $\alpha > 0.6$ or larger. Although the value of α decreases with increasing C_a, the theoretical limit $\alpha = 0.5$ is presumably not accessible because the saturation width w falls to magnitudes comparable to the gap thickness or to the typical pore size as C_a becomes very large.

In conclusion, we have studied the dynamics of interfacial roughening in the forced fluid invasion of a model porous medium at constant flow rate, in $1+1$ dimensions. We have focused on displacements in which the viscous pressure field dominates over the fluctuations in capillary pressure (large C_a, weak disorder), and found a new universality class with two distinct time regimes.

* * *

We acknowledge the financial support of the Dirección General de Enseñanza Superior (Spain) under projects BFM2000-0628-C03-01 and BFM2000-0624-C03-02.

REFERENCES

[1] Meakin P., *Fractals, Scaling and Growth far from Equilibrium* (Cambridge University Press, Cambridge) 1998; Tauber U. C. and Nelson D. R., *Phys. Rep.*, **289** (1997) 157; Kardar M., *Phys. Rep.*, **301** (1998) 85.

[2] Rubio M. A., Edwards C. A., Dougherty A. and Gollub J. P., *Phys. Rev. Lett.*, **63** (1989) 1685.

[3] Horvath V. K., Family F. and Vicsek T., *J. Phys. A*, **24** (1991) L25.

[4] He S., Kahanda G. L. M. K. S. and Wong P.-z., *Phys. Rev. Lett.*, **69** (1992) 3731.

[5] Wong P.-z., *MRS Bull.*, **19** (1994) 32.

[6] Delker T., Pengra D. B. and Wong P.-z., *Phys. Rev. Lett.*, **76** (1996) 2902.

[7] Family F. and Vicsek T., *J. Phys. A*, **18** (1985) L75.

[8] López J. M. and Rodríguez M. A., *Phys. Rev. E*, **54** (1996) R2189; López J. M, Rodríguez M. A. and Cuerno R., *Physica A*, **246** (1997) 329.

[9] The silicone oil has kinematic viscosity $\nu = 50$ mm^2/s, density $\rho = 0.99$ g/cm^3, and surface tension with air $\sigma = 20.7$ mN/m at room temperature.

[10] Although the different height at the end points should ideally be attributed to long-wavelength fluctuations (small q), we believe that in our experimental setup it is dominated by the wetting of the gap spacers by the invading oil, which changes the physics at the two ends. For this reason, we have ignored 8 mm of the interface at each of the two ends, and imposed the linear correction explained in the text. Measurements of w as a function of the size l of a local window demonstrate that the correction does not modify the measured exponents.

[11] Krug J. and Meakin P., *Phys. Rev. Lett.*, **66** (1991) 703.

[12] Ganesan V. and Brenner H., *Phys. Rev. Lett.*, **81** (1998) 578.

[13] Dubé M., Rost M., Elber K. R., Alava M., Majaniemi S. and Ala-Nissila T., *Phys. Rev. Lett.*, **83** (1999) 1628; *Eur. Phys. J. B*, **15** (2000) 701; Dubé M., Rost M. and Alava M., *Eur. Phys. J. B*, **15** (2000) 691.

[14] Hohenberg P. C. and Halperin B. I, *Rev. Mod. Phys.*, **49** (1977) 435.

[15] Yeung C., Mozos J. L., Hernández-Machado A. and Jasnow D., *J. Stat. Phys.*, **70** (1993) 1149; Mozos J. L., PhD thesis (Universitat de Barcelona) 1993.

[16] Saffman P. G. and Taylor G. I., *Proc. R. Soc. London, Ser. A*, **245** (1958) 312.

[17] Jasnow D. and Viñals J., *Phys. Rev. A*, **41** (1990) 6910.

[18] Langer J. S. and Turski L. A, *Acta Metall.*, **25** (1977) 1113.

[19] Kessler D. A., Levine H. and Tu Y., *Phys. Rev. A*, **43** (1991) 4551.

4.2 *Experiments of interfacial roughening in Hele-Shaw flows with weak quenched disorder*, **Phys. Rev. E 66, 031603 (2002)**

PHYSICAL REVIEW E **66**, 031603 (2002)

Experiments of interfacial roughening in Hele-Shaw flows with weak quenched disorder

Jordi Soriano,* Jordi Ortín, and A. Hernández-Machado
Departament d'Estructura i Constituents de la Matèria, Universitat de Barcelona, Avenida Diagonal 647, E-08028 Barcelona, Spain

(Received 4 January 2002; published 16 September 2002)

We have studied the kinetic roughening of an oil-air interface in a forced imbibition experiment in a horizontal Hele-Shaw cell with quenched disorder. Different disorder configurations, characterized by their persistence length in the direction of growth, have been explored by varying the average interface velocity v and the gap spacing b. Through the analysis of the rms width as a function of time, we have measured a growth exponent $\beta \simeq 0.5$ that is almost independent of the experimental parameters. The analysis of the roughness exponent α through the power spectrum has shown different behaviors at short (α_1) and long (α_2) length scales, separated by a crossover wave number q_c. The values of the measured roughness exponents depend on experimental parameters, but at large velocities we obtain $\alpha_1 \simeq 1.3$ independently of the disorder configuration. The dependence of the crossover wave number with the experimental parameters has also been investigated, measuring $q_c \sim v^{0.47}$ for the shortest persistence length, in agreement with theoretical predictions.

DOI: 10.1103/PhysRevE.66.031603 PACS number(s): 47.55.Mh, 68.35.Ct, 05.40.−a

I. INTRODUCTION

The kinetic roughening of growing surfaces is a problem of fundamental interest in nonequilibrium statistical physics. The interest arises from theoretical, experimental, and numerical evidence of scale invariance and universality of the statistical fluctuations of rough interfaces in a large variety of systems [1–3]. One candidate system is the roughening of a driven interface separating two fluids in a porous medium. This problem has important practical applications, and has time and length scales easily accessible in the laboratory. It allows different possible realizations, depending on the relative viscosities and wetting properties of the fluids involved [4].

One of these possible realizations that has received considerable attention in recent years is *imbibition*, i.e., the situation in which a viscous wetting fluid (typically oil or water) displaces a second less-viscous, nonwetting fluid (typically air), which initially fills the porous medium. The motion of imbibition interfaces can be *spontaneous*, i.e., driven solely by capillary forces, or *forced* externally at either constant applied pressure or constant injection rate.

Although there have been many experimental investigations of the scaling properties of imbibition interfaces in the last years, some results, particularly the quantitative values of scaling exponents, remain controversial. The current situation for the case of spontaneous imbibition is reviewed in Ref. [5]. The situation for the case of forced imbibition is summarized in Sec. II. The limitations of the experiments, in our opinion, arise first from the lack of precise knowledge of the properties of the disorder introduced by the model porous medium, and second from the related difficulty in tuning the relative strength of stabilizing to destabilizing forces in the flow. In the present work we have attempted to avoid these two limitations by using a particular model porous medium, consisting of a Hele-Shaw cell with precisely designed and controlled random variations in gap spacing.

In our setup, an initially planar interface becomes statistically rough on a mesoscopic scale, as a result of the interplay between (i) the stabilizing effects of the viscous pressure field in the fluid and the surface tension in the plane of the cell, on long and short length scales, respectively, and (ii) the destabilizing effect of local fluctuations in capillary pressure, arising from the random fluctuations in gap spacing, on short length scales. Although they have a different physical origin, the role of local fluctuations in capillary pressure, in our setup, is very similar to the role of wettability defects in the *imperfect Hele-Shaw cell* introduced by de Gennes [6], and studied by Paterson and co-workers [7].

In this paper we present a systematic experimental study of forced imbibition of our model porous medium, by a wetting silicone oil driven at constant flow rate. Since the competing forces in our system are the same as in a real porous medium the physics governing roughening is very similar in the two cases. The relative importance of viscous forces can be finely tuned by changing the injection rate of the invading fluid, and the strength of capillary fluctuations can be tuned by adjusting the distance between the two glass plates. The sequence of photographs in Fig. 1 provides examples of the resulting interfaces.

The outline of the paper is as follows. Section II reviews the scaling properties of rough interfaces and their experimental characterization in two-dimensional forced imbibition. Sec. III describes the experimental setup; Sec. IV introduces several parameters, such as permeability and modified capillary number, useful to characterize the experiments; and Sec. V explains the methodology used in data analysis. The experimental results are described in Sec. VI, and are analyzed and discussed in Sec. VII. The final conclusions are given in Sec. VIII.

II. SCALING OF ROUGH INTERFACES

To be specific, let us consider a two-dimensional system with cartesian coordinates (x,y) of lateral size L in the x direction and of infinite extension in the y direction. The interface is driven in the direction of positive y, and its po-

---

*Electronic address: soriano@ecm.ub.es

©2002 The American Physical Society

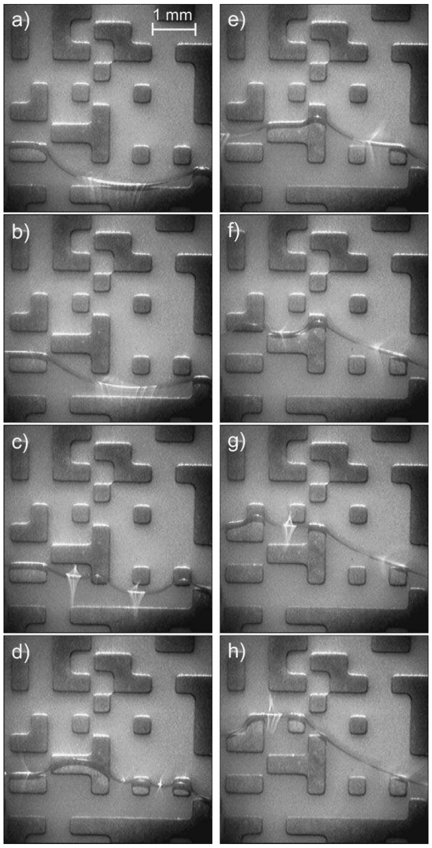

FIG. 1. Eight consecutive close-up views of the oil-air interface advancing over the disorder. In each picture the oil is driven from bottom to top. The experimental parameters are gap spacing $b = 0.36$ mm, average interface velocity $v = 0.08$ mm/s, and disorder square of 0.40 mm. The time interval between images is 0.8 s.

sition at time t is parametrized by the function $y = h(x,t)$. We assume that the interface is initially planar, $h(x,0) = 0$. Let $w(l,t)$ (the rms interfacial width) denote the typical amplitude of transverse excursions on a scale l, parallel to the interface, at time t. For the complete interface

$$w(L,t) = \{\langle [h(x,t) - \tilde{h}(t)]^2 \rangle_x\}^{1/2}, \tag{1}$$

where $\tilde{h}(t) = \langle h(x,t) \rangle_x$. The notation $\langle \cdots \rangle_x$ represents a spatial average in the interval $[0,L]$, where L is the system size. The standard picture of kinetic roughening is summarized in the dynamical scaling assumption of Family and Vicsek [8]:

$$w(L,t) = L^{\alpha} g(t/L^z), \tag{2}$$

where α is the *roughening* (or static) exponent and z is the *dynamic* exponent. The scaling function g is

$$g(u) \sim \begin{cases} u^{\alpha/z} & \text{for} \quad t \ll L^z, \\ \text{const} & \text{for} \quad t \gg L^z. \end{cases} \tag{3}$$

This picture assumes that the lateral correlation length of the interface fluctuations increases in time as $t^{1/z}$ in the x direction. For all length scales l within this correlation length the interface is rough, $w(l) \sim l^{\alpha}$. As the lateral correlation length increases, the interfacial width increases correspondingly with time as $w \sim t^{\alpha/z}$, which defines a *growth* exponent $\beta = \alpha/z$. Finally, when the lateral correlation length exceeds the system size L at a crossover time $t_{\times} \sim L^z$, the interface fluctuations saturate.

One way of measuring α is through the analysis of the interfacial width as a function of different system sizes L, i.e., $w(L) \sim L^{\alpha}$, at saturation. From an experimental point of view, however, it is not practical to perform experiments at different L. Usually, it is preferred to measure α by analyzing w for different window sizes l with $l \leqslant L$. The scaling of $w(l)$ gives a *local* roughness exponent α_{loc}, which is usually identified with the *global* exponent α. This kind of analysis must be performed with some caution, however, because it can only provide $\alpha_{loc} \leqslant 1$ and hence fails for super-rough interfaces $(\alpha > 1)$. Moreover, a number of problems of kinetic roughening present intrinsic anomalous scaling, characterized by different values of local and global exponents [9,10].

These difficulties can be overcome by analyzing the power spectrum of the interfacial fluctuations, defined as

$$S(q,t) = \langle H(q,t) H(-q,t) \rangle, \tag{4}$$

where

$$H(q,t) = \sum_x [h(x,t) - \tilde{h}(t)] e^{iqx}. \tag{5}$$

The notation $\langle \cdots \rangle$ indicates average over disorder configurations. The mean width w is related to $S(q,t)$ through

$$w^2(L,t) = \left(\frac{\Delta}{L}\right)^2 \sum_q S(q,t), \tag{6}$$

where Δ is the sampling interval in the x direction. For a two-dimensional(2D) system, the equivalent of the Family-Vicsek scaling assumption for the power spectrum reads [9]

$$S(q,t) = q^{-(2\alpha+1)} s(q t^{1/z}), \tag{7}$$

where the scaling function is given by

$$s(u) \sim \begin{cases} u^{2\alpha+1} & \text{for} \quad u \ll 1, \\ \text{const} & \text{for} \quad u \gg 1. \end{cases} \tag{8}$$

The power spectrum can give values $\alpha > 1$ and hence is applicable to super-rough interfaces. On the other hand, the presence of intrinsic anomalous scaling can be detected by a systematic shift of the power spectra computed at successive time intervals [9].

The scaling concept has allowed a classification of kinetic roughening problems in universality classes characterized by different families of scaling exponents. The first class is described by the thermal Kardar-Parisi-Zhang (KPZ) equation [11], which provides a local description of interfacial roughening in the presence of an additive white noise. The KPZ scaling exponents are $\beta = 1/3$ and $\alpha = 1/2$ in two dimensions.

If the nonlinear term of the KPZ equation is suppressed, the resulting equation is known as the thermal Edwards-Wilkinson (EW) equation [12], which gives $\beta = 1/4$ and $\alpha = 1/2$ in two dimensions. When, instead of being purely thermal, the noise in the KPZ equation is supposed to depend on the interface height *h*, the equation displays a depinning transition. At the pinning threshold the interface behavior of the complete equation with the nonlinear term ("quenched KPZ") can be mapped to the directed percolation depinning (DPD) model, whose scaling exponents in two dimensions are $\beta = \alpha \simeq 0.633$. Suppressing the nonlinearity yields the "quenched EW" equation, for which $\beta \simeq 0.88$ and $\alpha \simeq 1$ in two dimensions [13].

In the case of imbibition, there are two important issues that make the above classification of limited applicability. The first one is the quenched nature of the disorder. It has been argued that for very large driving the disorder may still be considered as fluctuating in time (thermal) noise, but in general the disorder must be treated as a static quenched noise. The second issue is the nonlocal character of the dynamics due to fluid transport in the cell [14,15]. This issue has received important attention recently, with the introduction of imbibition models that take fluid transport explicitly into account, giving rise to nonlocal interfacial equations [16–19].

The models presented in Ref. [16–19] are consistent with the well-known macroscopic equations of the problem (Darcy's law and interfacial boundary conditions). They differ in the way the noise is included in the equations and in the noise properties. The starting point of Ganesan and Brenner [16] is a random field Ising model. The permeability is taken to be spatially uniform and the noise exhibits long-range spatial correlations. In the case of forced imbibition and based on a Flory-type scaling, the model predicts that the roughness exponent α depends on the capillary number Ca, with asymptotic values $\alpha = 3/4$ for the smallest drivings and $\alpha = 1/2$ for the largest drivings. The approaches of Dubé *et al.* [18,19] and Hernández-Machado *et al.* [17] are both based on a conserved Ginzburg-Landau model, where the noise is introduced in a fluctuating chemical potential or in the mobility, respectively, without long-range correlations. Dubé *et al.* [18,19], however, consider only the case of spontaneous imbibition, which could give results very different from the case of forced imbibition, especially for the growth exponent β. By numerical integration they obtain $\alpha = 1.25$ and $\beta = 0.3$. Hernández-Machado *et al.* [17] study the case of forced imbibition, and predict a different scaling of the short and long length scales, with exponents $\beta_1 = 5/6$, $\alpha_1 = 5/2$ in the former regime and $\beta_2 = 1/2$, $\alpha_2 = 1/2$ in the latter.

A common feature of these models, pointed out in Refs. [17–19], is the presence of a new lateral length scale ξ_c related to the interplay of interfacial tension and liquid conservation. For $q \gg 1/\xi_c$, the dominant stabilizing contribution is the interfacial tension in the plane of the cell, while for $q \ll 1/\xi_c$ it is the fluid flow. The interplay leads to a dependence of q_c $(=1/\xi_c)$ on v of the form $q_c \sim v^{1/2}$.

As mentioned in the Introduction, the experimental characterization of the scaling properties of interfaces in two-dimensional forced imbibition remains conflicting. Most experiments have been conducted in model porous media consisting of air-filled Hele-Shaw cells packed with glass beads. In a first experiment of this sort on water-air interfaces, carried out by Rubio *et al.* [20], a roughening exponent $\alpha = 0.73 \pm 0.03$ was measured, independent of Ca and bead size, for Ca values in the range 10^{-3}–10^{-2}. A controversial reanalysis of their data by Horváth *et al.* gave $\alpha = 0.91 \pm 0.08$ [21,22], which these authors compared to $\alpha = 0.88 \pm 0.08$ obtained in their own replication of the experiment. In a subsequent work [23], using glycerol instead of water, Horváth *et al.* reported a clear power law growth regime with a growth exponent $\beta \simeq 0.65$, and different values $\alpha \simeq 0.81$ and $\alpha \simeq 0.49$ at short and long wave numbers, respectively, at saturation. The last set of experiments of this kind is due to He *et al.* [15], who explored a very large range of Ca (from 10^{-5} to 10^{-2}) and found large fluctuations of the roughness exponent in the saturation regime, between 0.65 and 0.91. In these experiments *w* was shown to fluctuate wildly during growth, and it was impossible to give a value of the growth exponent β.

Other experiments have been directed to characterize the statistical properties of the avalanches displayed by imbibition fronts at sufficiently small Ca. The results are also conflicting. The first study [24] was done on the same air-glycerol interfaces of Ref. [23], and gave a power law distribution of avalanche sizes. The second one [25], on air-water interfaces, reported an exponential distribution.

In our experiments, the possibility of tuning the different competing forces has allowed an accurate measurement of the growth exponent β by enlarging the growth regime before saturation. Fine tuning of the forces has also allowed us to measure the crossover length ξ_c, and its dependence on velocity v.

III. EXPERIMENTAL SETUP

In our experiments a silicone oil (Rhodorsil 47 V) displaces air in a horizontal Hele-Shaw cell, 190×550 mm^2, made of two glass plates 20 mm thick. The oil has kinematic viscosity $\nu = 50$ mm^2/s, density $\rho = 998$ kg/m^3, and surface tension oil-air $\sigma = 20.7$ mN/m at room temperature. Fluctuations in the gap thickness are provided by a fiberglass substrate, fixed on the bottom glass plate, containing a large number of copper islands that randomly occupy the sites of a square grid. The height of the islands is $d = 0.06 \pm 0.01$ mm. The gap spacing *b*, defined as the separation between the substrate and the top plate, is set by placing several calibrated spacers on the perimeter of the substrate, over the disorder, as shown in Fig. 2. We have used gap thicknesses in the range $b = 0.16 - 0.75$ (± 0.05) mm.

The disorder pattern is designed by the computer and manufactured using printed circuit technology. In order to clearly identify the oil-air interface when it moves over the copper islands, the plates have been chemically treated to accelerate copper oxidation. Otherwise the copper islands are too bright to recognize the interface contour. The silicone oil wets perfectly both fiberglass and copper, and no differences in the wetting properties due to the oxidation protocol have been observed.

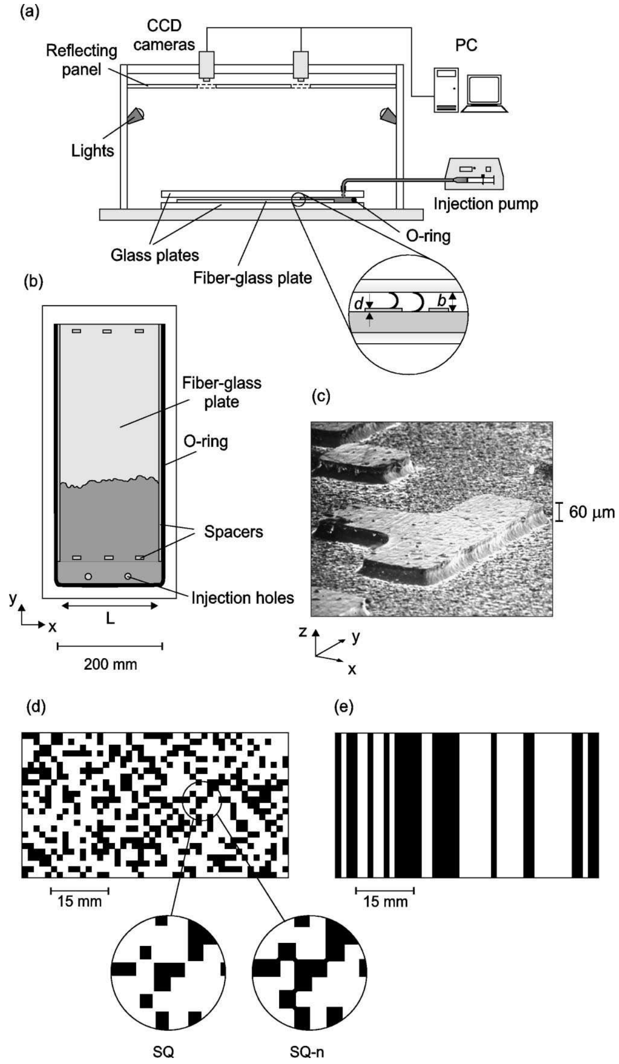

FIG. 2. Sketch of the experimental setup. (a) Side view. (b) Top view. (c) (SEM) image of the copper islands on the fiberglass plate. (d) and (e) Partial views of the disorder pattern for (d) squares (SQ, SQ-n) and (e) tracks (T). The copper islands are the black regions. The enlargements in (d) show the detailed structure of the disorder pattern for SQ and SQ-n.

For each experiment, the glass plates are cleaned with soap and water and rinsed with distilled water and acetone. The fiberglass plate is cleaned using blotting paper only, which leaves a thin layer of oil to avoid further oxidation of the copper surface, ensures a complete wetting in both fiberglass and copper, and improves the interface contrast in the captured images. Next, the fiberglass plate is fixed over the bottom glass plate using a thin layer of removable glue. The cell is completed by placing the spacers, the upper glass plate, and the O ring around the fiberglass plate (Fig. 2). Finally, the two glass plates are firmly clamped together to ensure the homogeneity of the gap spacing and the tightness of cell sides closed by the O ring.

The oil is injected at constant flow rate using a syringe pump Perfusor ED-2. The syringe pump can be programmed to give flow rates Q in the range 1–299 ml/h with less than 2% fluctuation around the nominal value. The oil enters the cell through two wide holes, drilled on the top plate near one end of the cell. The other end of the cell is left open. To start the experiment with as flat an interface as possible, the oil is first slowly injected into a transverse copper track, on the fiberglass plate, which is 2 mm ahead of the disorder pattern. Next, the syringe pump is set to its maximum injection rate until the whole interface has reached the disorder (about 3 s later). The pump is then set to the nominal injection rate of the experiment, and $t=0$ is defined as the time at which the average height of the interface (measured on the images) reaches the preset nominal velocity.

The oil-air interface evolution is monitored using two JAI CV-M10BX progressive scan charge-coupled device (CCD) cameras (each camera acquiring half of the side of the cell). The 1/2″ CCD sensor contains $782(H)\times 582(V)$ pixels. In our experiment, we have used an exposure time of 1/25 s in order to minimize the illumination. Each camera is equipped with a motorized zoom lens Computar M10Z1118MP with a focal length in the range 11–110 mm (1:10 zoom ratio). The cameras are connected to an imaging technology PCVision frame grabber installed in a personal computer. A Visual Basic application controls both cameras and stores the images for further analysis.

The images are taken with a spatial resolution of 0.37 mm per pixel, a size of 768×574 pixels, and 256 gray scale levels per pixel. The acquisition is logarithmic in time, with temporal increments that vary from 0.33 s to 180 s. Between 100 and 300 images are taken per experiment. Because the background is the same for all the images captured with the same camera, the interface is enhanced by subtracting the first image to all other images, and thresholding the result to get a black and white contour of the interface. The contour is resolved with 1-pixel accuracy using edge detection methods, and data are stored for further analysis. This method is automatically performed, with an error in the interface recognition comparable to the width of the oil-air meniscus, about one-half of the gap width. Figure 3 presents two examples of the digitized interfaces, compared with the original images.

IV. CHARACTERIZATION OF THE EXPERIMENTS

A. Disorder properties

Three kinds of disorder patterns have been used. Two of them are obtained by random selection of the sites of a square lattice [Fig. 2(d)]. In the first one (SQ) we allow nearest-neighbor connections only, leaving next-nearest neighbors separated by 0.08 mm. In the second one (SQ-n) both nearest-neighbor and next-nearest-neighbor connections are allowed. The third kind of disorder pattern (T) is formed by parallel tracks, continuous in the y direction and randomly distributed along x [Fig. 2(e)]. The filling fraction f (fraction of lattice sites occupied by copper) is 35 % in the three cases. However, the persistence length $\tilde{l}$ of the disorder in the direction of growth is very different in the three different disorder patterns. This length is measured in the following way:

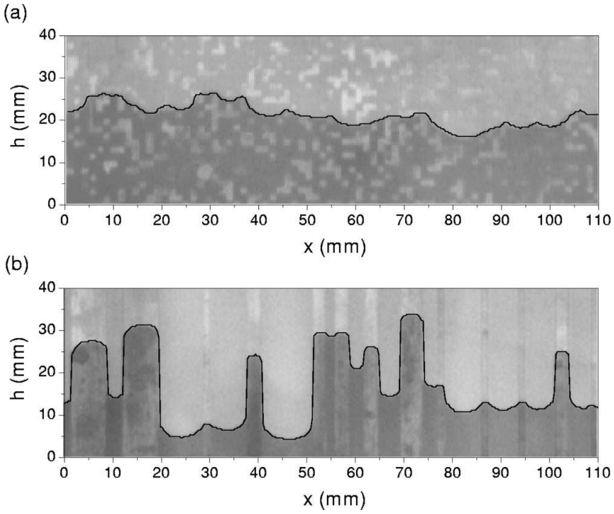

FIG. 3. Interface profiles for two types of disorder configurations, SQ 1.50 mm (a) and T 1.50 mm (b), compared with the original digital images. The copper islands are the brighter spots of the image background. The experimental parameters are $b = 0.36$ mm and $v = 0.08$ mm/s in the two cases.

(i) we consider every site x of the lattice along the lateral direction, and measure the average length $l(x)$ of the island formed by the connected copper sites at $x-\Delta x$, x, and $x+\Delta x$, where Δx is the lattice spacing; (ii) we average $l(x)$ over the lateral direction in the interval $(0,L)$. As can be seen in the inset of Fig. 4, $\tilde{l}$ increases by a factor of 2.4 when changing from SQ to SQ-n, and up to the total length of the cell for T. Another characteristic of the disorder is the cluster size that gives the number of disorder unit cells of the copper aggregations. The statistical distribution of copper clusters is shown in the main plot of Fig. 4.

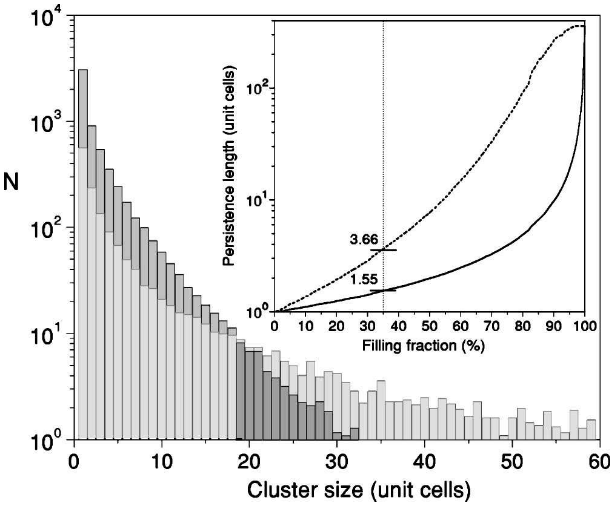

FIG. 4. Statistical distribution of the copper clusters for a filling fraction $f = 0.35$. Clusters with only nearest-neighbor contacts (SQ) are represented in dark gray. Clusters with nearest-neighbor and next-nearest-neighbor contacts (SQ-n) are represented in light gray. The inset shows the persistence length of the disorder $\tilde{l}$ as a function of the filling fraction f. The solid and dashed lines correspond to the SQ and SQ-n cases, respectively. The vertical line indicates the filling fraction used in our experiments.

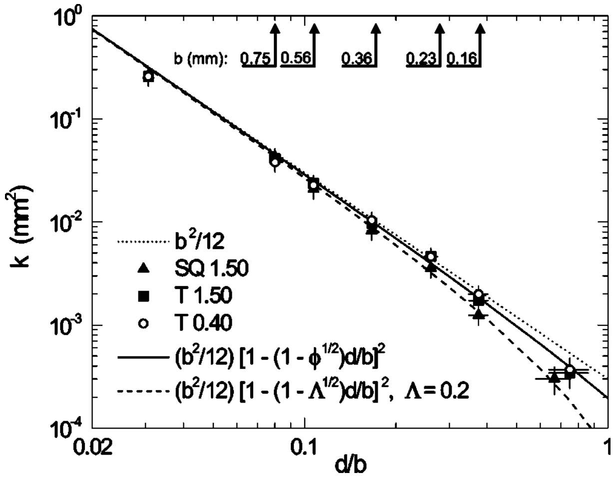

FIG. 5. Measurements of the permeability k as a function of the disorder strength d/b for $d = 0.06$ mm. The dotted line is the permeability of a standard Hele-Shaw cell (without disorder), and the dashed and solid lines are fits to the experimental data for SQ and T disorder configurations, respectively. The arrows point to the values of d/b for the gap spacings used in the experiments.

We have used two values of the lattice spacing in the lateral direction, $\Delta x = 1.50 \pm 0.04$ mm and 0.40 ± 0.04 mm. From here on we refer to the disorder used in a given experiment by SQ, SQ-n, or T, followed by the lateral size in millimeters of the disorder unit cell, 1.50 or 0.40.

B. Permeability

To characterize the fluid flow through our Hele-Shaw cell with disorder, we have determined the permeability of the cell for the different disorder patterns as a function of the gap spacing. The experimental setup used for this purpose is similar to the one shown in Fig. 2, but the injection system has been replaced by a constant pressure device. It consists of an oil column of adjustable constant height in the range from 200 ± 2 mm to 1000 ± 5 mm. The permeability is determined by measuring the oil-air interface average velocity for different applied pressures (heights of the oil column) and using Darcy's law,

$$\vec{v} = -\frac{k}{\mu}\vec{\nabla}p, \tag{9}$$

where $\vec{v}$ is the interface velocity, k the permeability, μ the dynamic viscosity, and $\vec{\nabla}p$ the pressure gradient.

Figure 5 shows the results obtained. At large gap spacings, $d/b \rightarrow 0$, the disorder has no effect on the fluid flow and the permeability tends to the expected value for an ordinary Hele-Shaw cell, $k_0 = b^2/12$, independently of the disorder configuration. At very small gaps, $d/b \rightarrow 1$, the permeability decreases and tends to a nonzero value k_1 for $d/b = 1$, which clearly depends on the disorder configuration. We have found it convenient to write k_1 in the form

$$k_1 = d^2\Lambda/12, \tag{10}$$

where Λ is a function that depends on the porosity ϕ and the geometry of the disorder. The simplest functional form that interpolates between these two limits can be written as:

$$k = \frac{b^2}{12}\left[1-(1-\Lambda^{1/2})\frac{d}{b}\right]^2. \tag{11}$$

The coefficient Λ can be obtained in general from a fit of the permeability to the experimental data.

In the particular case of disorder T and $d/b=1$, an analytic expression of Λ can be derived by recognizing that the cell in this case is formed by a parallel array of rectangular capillaries. Following Avellaneda and Torquato [26], in this geometry Λ is directly the porosity ϕ, which in the limit $d/b=1$ is given simply by $\phi = 1-f$. Hence, since we have $f=0.35$, we obtain $\Lambda = 0.65$. This result fits well the experimental data not only in the limit $d/b=1$ but also in the whole range of d/b (solid line in Fig. 5). Notice also that the results presented in Fig. 5 show that there are no important differences between T 1.50 mm and 0.40 mm. This observation generalizes the theoretical result that in the limit $d/b=1$ the width of the rectangular capillaries does not modify the permeability [26]. For SQ and SQ-*n* disorder, due to the difficulty of finding a general expression for k_1 (see Refs. [27,28]), we have fitted k to our experimental results (dashed line in Fig. 5) and have obtained a numerical value $\Lambda = 0.20$.

C. Capillary pressure

Assuming local thermodynamic equilibrium, the capillary pressure jump at the interface is given by

$$p^+ - p^- = \sigma(\kappa_\parallel + \kappa_\perp), \tag{12}$$

where $\kappa_\parallel$ and $\kappa_\perp$ are the main curvatures of the interface in the plane of the cell and perpendicular to it, respectively.

$\kappa_\parallel$ varies from 0 for $d/b \ll 1$, to $2/r$ for $d/b \simeq 1$, where $r \simeq 1.75$ mm is the average diameter of the copper obstacles. In the range of gap spacings explored we have measured curvatures in the range $3.3\times 10^{-3} \leqslant \kappa_\parallel \leqslant 1.15\ \text{mm}^{-1}$. Notice that $\kappa_\parallel \ll \kappa_\perp$ in all the range of gap spacings used in the experiments.

In ordinary Hele-Shaw flows (without disorder) $\kappa_\perp$ is roughly the same in all points of the interface and therefore adds only a constant contribution to the pressure jump. In our case, however, when the interface is over the copper islands (gap thickness $b-d$), we have

$$\kappa_\perp = \frac{2}{b}\left(\frac{1}{1-d/b}\right), \tag{13}$$

and when it is over the fiberglass substrate (gap thickness b),

$$\kappa_\perp = \frac{2}{b}, \tag{14}$$

assuming complete wetting.

This difference in curvature, given by

$$\Psi = \frac{2}{b}\left(\frac{d/b}{1-d/b}\right), \tag{15}$$

makes the interface experience a capillary instability when it passes from one gap spacing to the other. In the range of gap spacings studied, $0.16 \leqslant b \leqslant 0.75$ mm, we get $7.5 \geqslant \Psi \geqslant 0.23\ \text{mm}^{-1}$. We have verified that for gap spacings $b \gtrsim 2$ mm, which correspond to $\Psi \lesssim 0.031\ \text{mm}^{-1}$, the fluctuations in capillary pressure are no longer sufficient to roughen the interface appreciably.

D. Modified capillary number

Once the permeability of the cell has been characterized, we can introduce a dimensionless number to describe the relative strength of viscous to capillary forces. The simplest number that relates viscous and capillary forces is the *capillary number* $\text{Ca} = \mu v/\sigma$. In order to account for the properties of the disorder, which are not contained in the previous definition of Ca, it is customary to introduce a *modified capillary number*. For an ordinary Hele-Shaw cell (without disorder), the modified capillary number, which we call Ca*, comes out from the dimensionless form of the Hele-Shaw equations [29]:

$$\text{Ca}^* = \text{Ca}\times 12\left(\frac{L}{b}\right)^2. \tag{16}$$

To define a modified capillary number Ca′ for our particular cell with disorder, we consider on one side the average viscous pressure drop across the cell, given by

$$\delta p_{vis} = L|\nabla p_{vis}|, \tag{17}$$

with $\vec{\nabla} p_{vis} = -\vec{v}\mu/k$ (Darcy's law). The cell width L provides the macroscopic length scale. On the other side, a measure of the capillary pressure drop is given by

$$\delta p_{cap} = \sigma\left(\frac{2}{b-d} - \frac{2}{b} + \frac{1}{L}\right). \tag{18}$$

The last contribution accounts for the curvature of the interface in the plane of the cell, and is relevant only when $d/b \to 0$, i.e., when the destabilizing role of the disorder vanishes.

Defining $\text{Ca}' = \delta p_{vis}/\delta p_{cap}$ and using Eq. (11), (17), and (18), we get

$$\text{Ca}' = \text{Ca}\frac{12L}{b^2\left[1-(1-\Lambda^{1/2})\dfrac{d}{b}\right]^2\left(\dfrac{2}{b-d} - \dfrac{2}{b} + \dfrac{1}{L}\right)}. \tag{19}$$

The ratio Ca′/Ca* as a function of d/b is shown in Fig. 6 for disorders SQ and T. When $d/b \to 0$ the destabilizing role

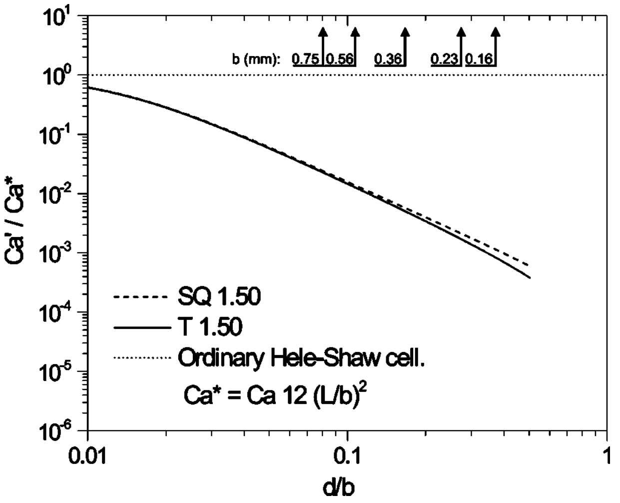

FIG. 6. Ratio of the modified capillary number for the cell with disorder, Ca′, to the modified capillary number for an ordinary Hele-Shaw cell, Ca*, as a function of the disorder strength d/b. The dashed and solid lines correspond to disorders SQ 1.50 and T 1.50. The dotted line represents the asymptotic limit $\mathrm{Ca}' = \mathrm{Ca}^*$. The arrows point to the values of d/b for the gap spacings used in the experiments.

of the disorder is negligible, as expected, and $\mathrm{Ca}'/\mathrm{Ca}^*$ tends to 1 (ordinary Hele-Shaw cell). As d/b increases, the increasing strength of the disorder is manifest in the progressive decrease of $\mathrm{Ca}'/\mathrm{Ca}^*$. It is important to notice that our definition of Ca’ is not valid for $d/b = 1$, because the flow would be essentially different when the free gap disappears. In the range of d/b explored in our experiments the permeability of the cell remains always close to that of an ordinary Hele-Shaw cell (Fig. 5), and the decrease of $\mathrm{Ca}'/\mathrm{Ca}^*$ is essentially due to the capillary forces associated with the menisci in the z direction.

In the range of gap spacings experimentally explored, $0.16 \leqslant b \leqslant 0.75$ mm, the ratio between the free gap $b-d$ and the total gap b varies between 62% and 92%. These large ratios, combined with the high viscosity and small surface tension of the silicone oil compared with other fluids (i.e., water), are responsible for the large values of Ca′ in our experiments, in comparison to the values reported for pure porous media. Considering , for example, the disorder T 1.50 mm, Ca′ varies from a value 1.33 (for $b = 0.16$ mm and the minimum interface velocity 0.04 mm/s) to a value 17.0 (for $b = 0.75$ mm and the maximum interface velocity 0.4 mm/s).

V. DATA ANALYSIS

The wetting of the lateral gap spacers by the invading oil changes the physics at the two ends of the interface. To minimize this disturbance, which is particularly important at large gap spacings, we have disregarded 8 mm at each side of the cell, thereby reducing the measured interface from 190 to 174 mm in the x direction. The final number of pixels of the interface after this correction is reduced from 515 to 470. For data analysis convenience these pixels are converted into $N = 512$ equispaced points, through a linear interpolation. The final spacing between two consecutive points is $\Delta = L/N = 0.34$ mm. Although the linear interpolation introduces an artificial resolution 7% larger than the resolution of the original image, the increase does not affect the final analysis.

The interfaces measured at the smallest gap spacings and velocities may present overhangs. These multivaluations, which are rather exceptional, have been eliminated by taking for each value of x the corresponding largest value of $h(x)$.

In addition, we have forced periodic boundary conditions for $h(x,t)$ by subtracting the straight line connecting the two ends of the interface. This procedure is well documented in the literature of kinetic roughening [30]. The linear correction imposed to the interfaces has significant effects on the power spectrum. The Fourier spectrum of an interface, which is discontinuous at the two end points, is dominated by an overall behavior of the form q^{-2}. Forcing periodic boundary conditions eliminates the overall slope -2 [31]. Moreover, the analysis of $w(l)$ is insensitive to the linear correction of the interface (except for values of l comparable to the system size) and gives results consistent with those obtained from $S(q,t)$ only for interfaces with periodic boundary conditions.

Since the maximum width of the meniscus is only one-half of the gap width (in conditions of complete wetting), the interface can be considered one-dimensional at the length scale of the copper islands. The resolution of the interface fluctuations in the y direction is ± 1 pixel at a given point. Nevertheless, the measurement of the global interfacial

TABLE I. Summary of the parameters explored for each kind of disorder.

Disorder	Gap spacing (mm)	Interface velocity ($V = 0.04$ mm/s)
SQ 1.50	0.16,0.23,0.36,0.56,0.75	$2V$
SQ 1.50	0.36	V,$2V$,$5V$,$7V$,$10V$
SQ-*n* 1.50	0.36	V,$2V$,$10V$
T 1.50	0.16,0.36,0.56,0.75	$2V$
T 1.50	0.36	V,$2V$,$5V$,$10\,V$
SQ 0.4	0.36	$2V$
T 0.4	0.36	$2V$

width w is much more precise because the width is an average over the $N=512$ points of the interface.

Given that, according to our choice of the time origin, the whole interface is already inside the disorder at $t=0$, $w(0) \neq 0$. For this reason, we have decided to characterize the interface fluctuations by the *subtracted width* W, defined by $W^2(t)=w^2(t)-w^2(0)$ [1,32]. Notice that, since the data analysis is based on power law dependences, short times are very sensitive to the definition of $t=0$ and to the value $w(0)$. After analyzing the data for different definitions of $t=0$ and checking the influence of subtracting $w(0)$, we have found that the analysis based on the subtracted width is the most objective and less sensitive to the details of the experimental procedure. The error bars shown in the $W(t)$ plots indicate the dispersion of the different individual experiments with respect to the average curve plus the uncertainty in the determination of $t=0$.

Finally, the crossover time $t_\times$ has been measured on the $W(t)$ log-log plots as the time when the power law with slope β crosses the horizontal straight line that corresponds to the average value of the interfacial width at saturation, W_s.

VI. EXPERIMENTAL RESULTS

The parameters explored in our experiments are summarized in Table I. The minimum velocity selected in the experiments, $v=0.04$ mm/s (which will be taken as reference unit for interfacial velocities), has been chosen to ensure that the interface is always single valued for gap spacings $b \gtrsim 0.36$ mm. We have used three different disorder realizations for SQ and SQ-n and four for T. For each disorder realization and each set of experimental parameters (v,b), we have carried out three runs for SQ and SQ-n and two runs for T.

A. Variable velocity

1. SQ of 1.50 mm

We have started the study exploring five different velocities, from V to $10\,V$, using an intermediate gap spacing $b=0.36$ mm. We have not selected velocities lower than V to avoid overhangs and trapped air. An example of the interfaces obtained at different velocities is presented in Fig. 7. All the experiments shown correspond to the same disorder configuration, and the average position of the selected interfaces is also the same for the different velocities. The most noticeable aspect of the sequence of interfaces is that the short length scales are not affected significantly by the velocity, contrary to the long length scales, which become progressively smoother as the velocity increases.

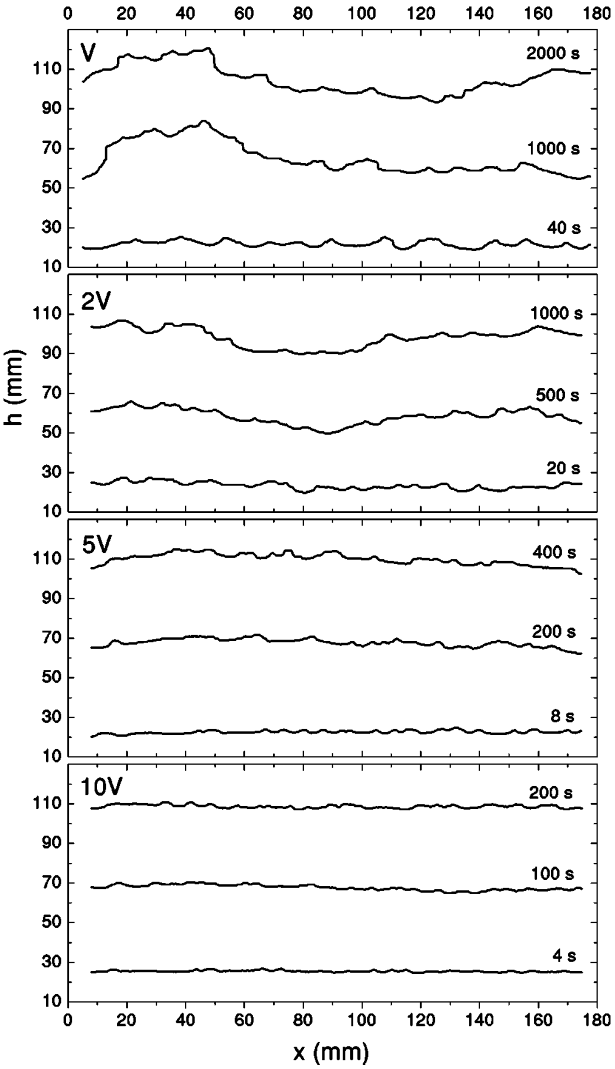

FIG. 7. Sequence of interfaces at different velocities, for $b=0.36$ mm and disorder SQ 1.50 mm, corresponding to $\mathrm{Ca}'=1.85$, 3.69, 9.24, and 18.5. The disorder realization is the same in the four sequences. The reference velocity is $V=0.04$ mm/s.

Figure 8 shows the $W(t)$ plot for four different velocities. We have omitted the curve for $7V$ because it is too close to the $10\,V$ curve. All curves display a power law growth regime with approximately the same growth exponent $\beta=0.47\pm0.04$, independent of the velocity. Saturation times and saturation widths depend clearly on the velocity, both decreasing at increasing velocities. This general behavior is not so clear for the two smallest velocities, for which the corresponding $t_\times$ and W_s are practically the same. This can be a consequence of the fact that the interface at very low velocity gets locally pinned at the end of the copper obstacles, hindering an arbitrary deformation of the interface. The strong fluctuations of W that can be observed both during growth and at saturation are also remarkable. These fluctuations have two origins: the intrinsic metastabilities in systems with quenched-in disorder [15], and to a lesser degree the inhomogeneities in the gap thickness caused by small deformations in the fiberglass substrate or small differences in the height of the copper obstacles. To smooth out the fluctuations it would have been necessary to increase the number of disorder configurations and runs to a number that would be prohibitive. Nevertheless, the largest fluctuations usually appear deep in saturation and do not change the results presented here.

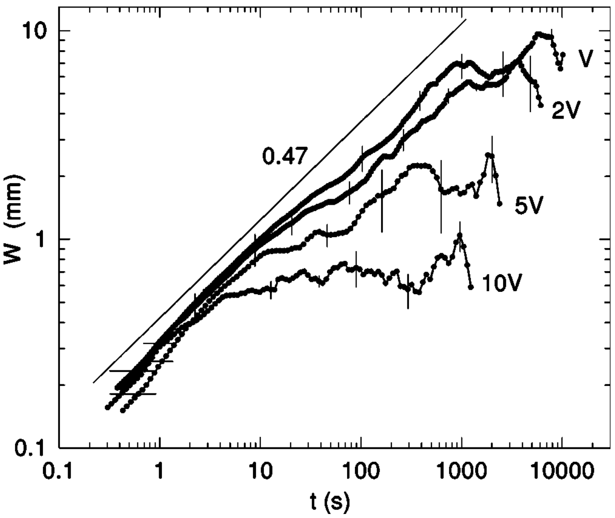

FIG. 8. Interfacial width $W(t)$ for disorder SQ 1.50 mm, gap spacing $b=0.36$ mm, and four different velocities. The straight line drawn to guide the eye is the power law $W \sim t^{0.47}$.

Figure 9 shows the analysis of the interface fluctuations through the power spectrum. An example of the temporal evolution of the spectrum, which corresponds to the experiments at velocity $2V$, is presented in Fig. 9(a). Since larger length scales become progressively saturated with time, the spectrum at short times displays a power law decay for large q only. As time increases the power law extends to smaller q until a second power law behavior emerges, which reaches the smallest q, corresponding to the system size L, at saturation. The first power law regime (large q) will be characterized by a roughness exponent α_1, and the second one (small q) by a roughness exponent α_2. In the range of parameters explored we have always observed $\alpha_1 > \alpha_2$. It is interesting to notice that the first regime shows a slightly time-dependent behavior. α_1 is progressively smaller as time increases and reaches a constant value at saturation. This temporal dependence disappears at either high interface velocities or large gap spacings.

The power spectrum at saturation for five different velocities is shown in Fig. 9(b). The different behavior at short and long length scales is visible in all cases, but the crossover from one regime to another (characterized by the wave number q_c at the crossing point of the two power laws) increases systematically with increasing velocities.

The exponent α_1 (large q) increases with the interface velocity, from a value $\alpha_1 = 0.9 \pm 0.1$ (slope$= -2.8 \pm 0.2$) at velocity V to a value $\alpha_1 = 1.3 \pm 0.1$ (slope$= -3.6 \pm 0.2$) at velocity $10V$. We have observed that the variation is not linear, but tends to the limiting value $\alpha_1 = 1.3$ at large velocities.

The exponent α_2 (small q) decreases with the interface velocity, varying from $\alpha_2 = 0.6 \pm 0.1$ (slope$= -2.2 \pm 0.2$) at velocity V to $\alpha_2 = 0.1 \pm 0.1$ (slope$= -1.2 \pm 0.2$) at velocity $10V$. This exponent seems to be insensitive to the velocity at low velocities.

Figure 9(c) shows the alternative analysis carried out to determine the roughness exponents using $W(l)$. Notice that

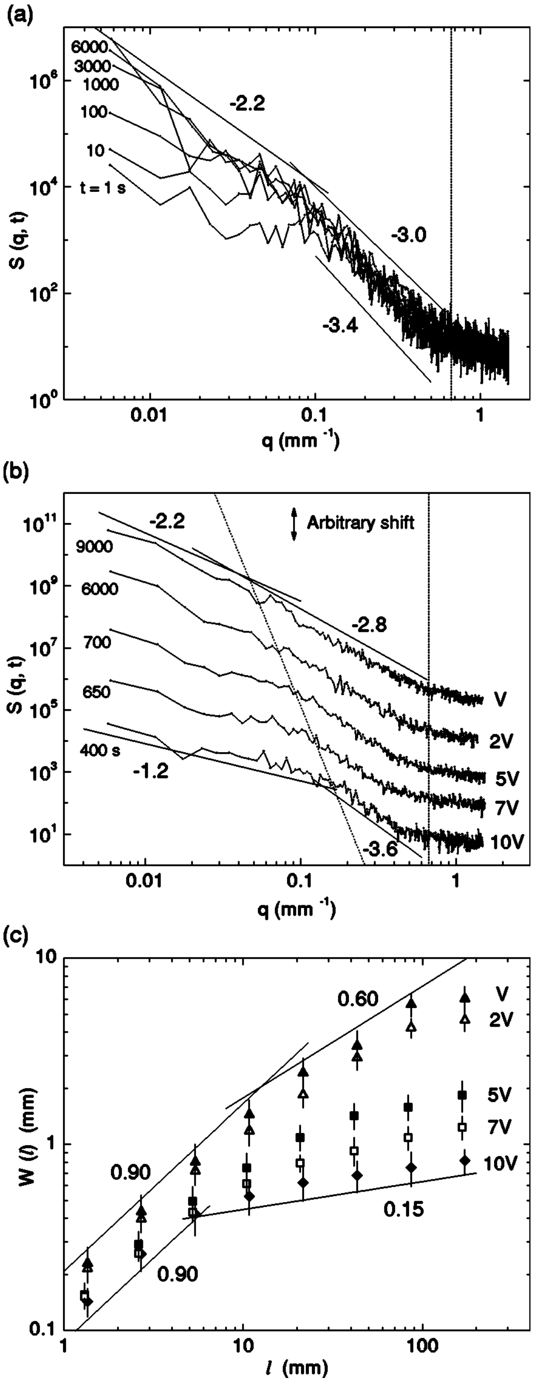

FIG. 9. Determination of the roughness exponents for experiments at five different velocities, with $b=0.36$ mm and disorder SQ 1.50 mm. (a) Example of the temporal evolution of the power spectrum for velocity $2V$ ($\mathrm{Ca}' = 3.69$). (b) Power spectra at saturation for the five velocities studied. The curves have been shifted in the vertical direction for clarity. (c) Analysis of the local width $W(l)$. The vertical lines in (a) and (b) give the value of q associated with the spatial scale of the disorder. The tilted line crossing the power spectra in (b) fits the values of the crossover wave number q_c at the different velocities. The other straight lines are power law fits from which the roughness exponents can be deduced.

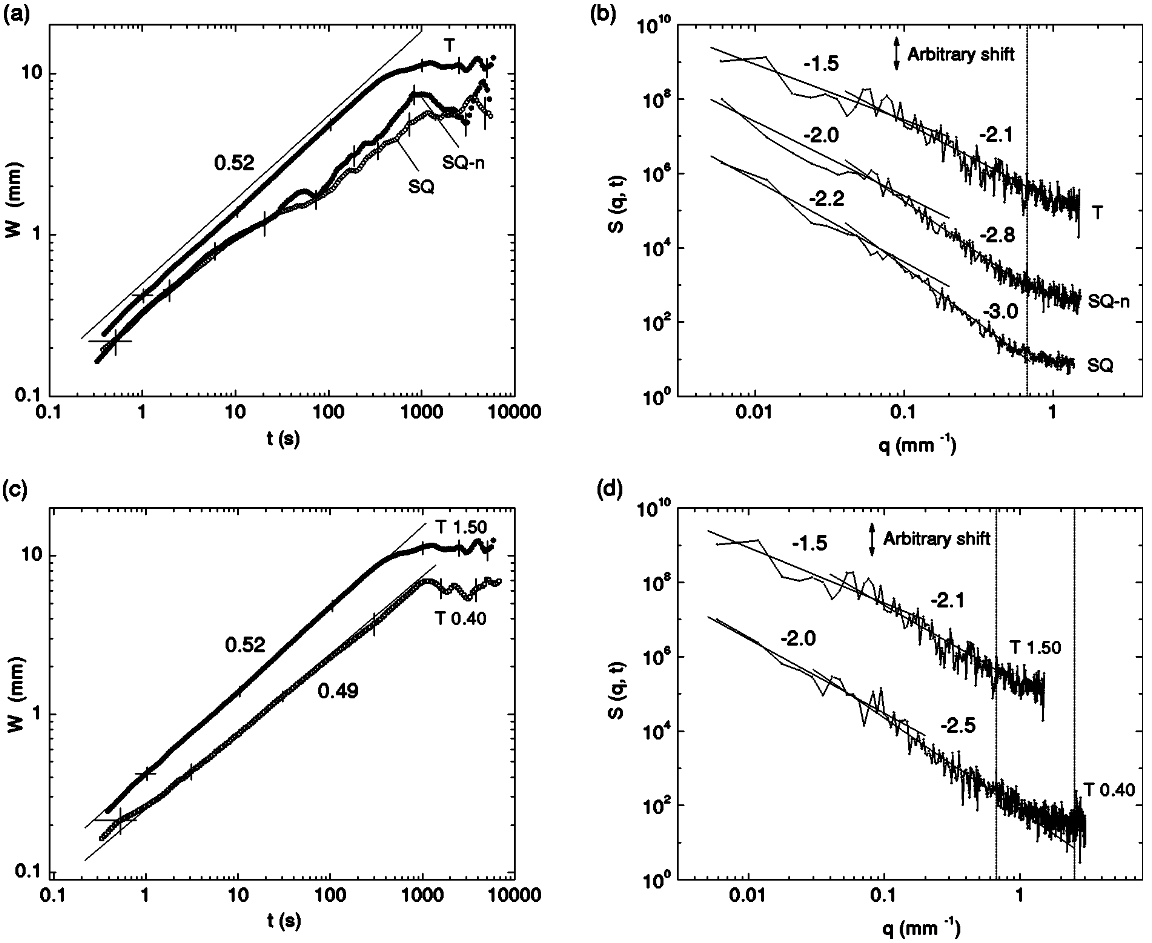

FIG. 10. Interfacial width $W(t)$ (a) and power spectra $S(q,t)$ (b) for three kinds of disorder with unit cell of size 1.50 mm. (c) and (d) show the same magnitudes for disorder T of two different sizes, 0.40 and 1.50 mm. The spectra have been shifted in the vertical direction for clarity. The vertical lines give the value of q associated with the spatial scale of the disorder. In all the experiments $b=0.36$ mm and $v=2V$ ($\mathrm{Ca}'=3.25$ for T, and 3.69 for SQ and SQ-n).

because this is a local analysis it is limited to a maximum value $\alpha=1$. At short length scales we obtain $\alpha_1=0.90\pm0.1$ for all the velocities. The value $\alpha_1=1$ that we should have obtained for $v\geqslant 2V$ is unreachable because the fluctuations in $W(l)$ contribute always in the direction of decreasing α_1. At long length scales the values obtained for α_2 are consistent with the values measured from the power spectrum.

2. Effect of increasing the persistence of the disorder

We have carried out a series of experiments oriented to explore how different kinds of disorder patterns affect the interfacial dynamics, and the possible universality of our results. The gap spacing and velocity used in all cases are $b=0.36$ mm and $2V$.

When the correlation length of the disorder in the y direction is increased (changing the disorder pattern from SQ to SQ-n and then to T), we observe important differences in the behavior of both $W(t)$ and $S(q,t)$. The correlation length $\tilde{l}$ of the disorder in the y direction is quantified through the average extent of the disorder cells in the y direction, introduced in Sec. IV A. For a basic disorder cell of size 1.50 mm, $\tilde{l}\simeq 2$ mm for SQ, $\tilde{l}\simeq 5$ mm for SQ-n, and $\tilde{l}=\infty$ for T. The immediate consequence of a progressively larger correlation length is the persistence of the capillary forces for longer times. The effect on $W(t)$ is that the large fluctuations observed during growth disappear as $\tilde{l}$ increases. In the extreme limit of disorder T, $W(t)$ is a neat power law with an exponent $\beta=0.52\pm0.03$, as can be seen in Fig. 10(a). Other relevant aspects are that the saturation times can be clearly identified and the fluctuations in saturation have a minor amplitude. Whereas the important fluctuations of $W(t)$ both during growth and saturation, together with substantial differences between different runs and disorder configurations, are characteristic of the experiments with SQ, for T the experiments show that different runs with the same disorder configuration lead to practically identical results, and differ only slightly when the disorder configuration is changed.

The increasing correlation length in the direction of growth has important consequences in the power spectrum.

On one side, the observation of a smaller roughness exponent α_1 as time increases for disorder SQ [Fig. 9(a)] is more evident as we go to SQ-*n* and T. The exponent α_1 obtained for different disorders, however, tends to a single value at large gap spacings and high velocities (weak capillary forces). On the other side, the spectra at saturation shown in Fig. 10(b) clearly indicate that a progressively larger $\tilde{l}$ reduces the measured roughness exponents, from $\alpha_1 = 1.0 \pm 0.1$ to $\alpha_1 = 0.5 \pm 0.1$ and from $\alpha_2 = 0.6 \pm 0.1$ to $\alpha_2 = 0.2 \pm 0.1$, as the disorder changes from SQ to T. This trend is confirmed by experiments using SQ 0.40 ($\tilde{l} \simeq 0.6$), where the evolution of α_1 with time is not observed due to the short $\tilde{l}$ and, at saturation, gives exponents $\alpha_1 \simeq 1.1$ and $\alpha_2 \simeq 0.5$.

Another interesting modification that can be introduced in the disorder is the size of the basic disorder cell. In addition to our usual experiments with lateral size 1.50 mm, we have made experiments with disorder T of lateral size 0.40 mm. The $W(t)$ curves for both cases are shown in Fig. 10(c). Both curves give approximately the same growth exponent, around $\beta = 0.50$. The small differences in slope around this value can be attributed to the reduced number of disorder configurations studied. The most noticeable difference is the saturation width, which is smaller for the small disorder size. The power spectrum at saturation for the two cases is shown in Fig. 10(d). Notice that in the case of T 0.40 mm, the measured exponents α_1 and α_2 increase considerably and approach the values measured for SQ or SQ-*n* of 1.50 mm.

3. T of 1.50 mm

Here we present a systematic study of the disorder T 1.50, in the same line as for SQ 1.50 (Sec. VI A 1). The disorder T 1.50 ensures that the interface is always single valued at any gap spacing and velocity, which allows exploring a wide range of experimental parameters.

Figure 11 shows an example of the interfaces obtained in the experiments with T 1.50 mm at different velocities and fixed gap spacing. As we observed for SQ 1.50, the interfaces become progressively flatter as the velocity is increased. However, there are interesting differences. The first one is the possibility of exploring the regime of very low velocities, thanks to the fact that the continuity of the copper tracks makes local pinning impossible. However, there are two reasons for not selecting velocities lower than *V*. First, we have observed that for $v \lesssim V/4$ the oil fingers become so elongated that the interface pinches off at some distance behind the finger tip. And, second, because the oil tends to advance preferentially over the copper tracks, at very short times the oil over the fiberglass recedes (due to mass conservation) and parts of the interface again reach the transverse copper tracks at the beginning of the cell. This limits the velocity to a minimum value *V* for this gap spacing.

As discussed before, having tracks impedes the local pinning of the interface. As a result, the metastabilities observed for disorder SQ are not present here. Most of the fluctuations of $W(t)$ disappear, as shown in Fig. 12 for the four velocities studied. All the curves have approximately the same growth exponent $\beta = 0.52 \pm 0.03$. The transition from the growth regime to the saturation regime is rather smooth and makes it difficult to measure the values of $t_\times$ and W_s. Although two identical runs (with the same disorder configuration) give almost identical $W(t)$ curves, different disorder configurations give curves with slightly different β, $t_\times$, and W_s. In the former case the values vary between $\beta = 0.48$ and $\beta = 0.55$. The fluctuations observed at saturation are attributed to small inhomogeneities in the gap thickness, which affect particularly the experiments at the lowest velocities. Although the amplitude of the fluctuations decreases when we increase the number of disorder configurations, the almost perfect reproducibility of experiments with identical disorder configuration makes it difficult to have good statistics using a reduced number of disorder configurations.

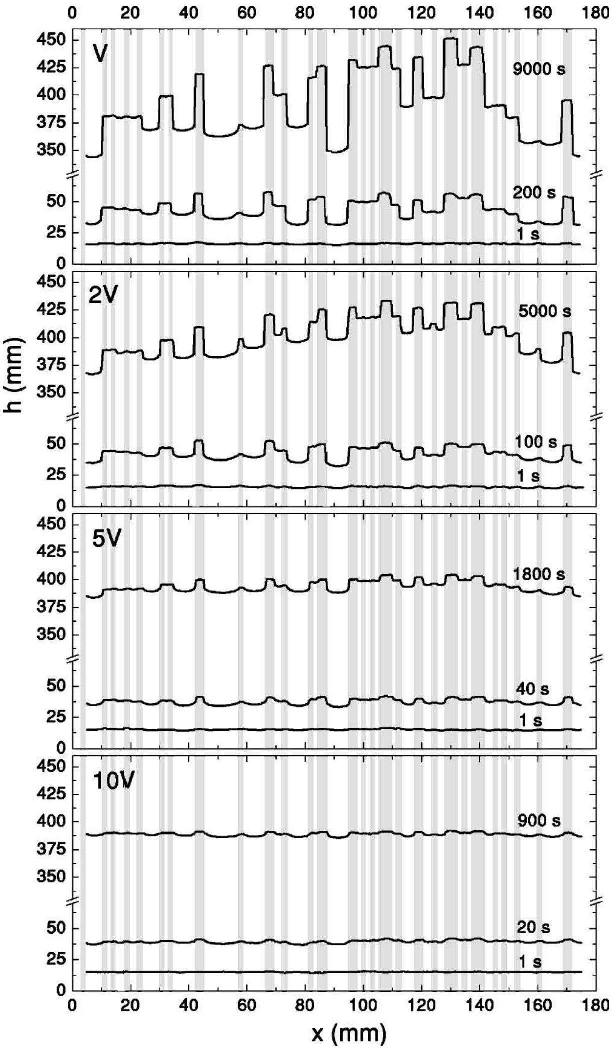

FIG. 11. Sequence of interfaces for disorder T 1.50 mm and gap spacing $b = 0.36$ mm, at different velocities, corresponding to $\mathrm{Ca}' = 1.62$, 3.25, 8.13, and 16.3. The disorder pattern is shown in gray.

The analysis of the power spectrum for the four velocities is shown in Fig. 13. The deterministic character of the interfacial growth makes the interfacial fluctuations not self-averaging. This leads to considerable fluctuations in the power spectrum, which cannot be completely reduced with-

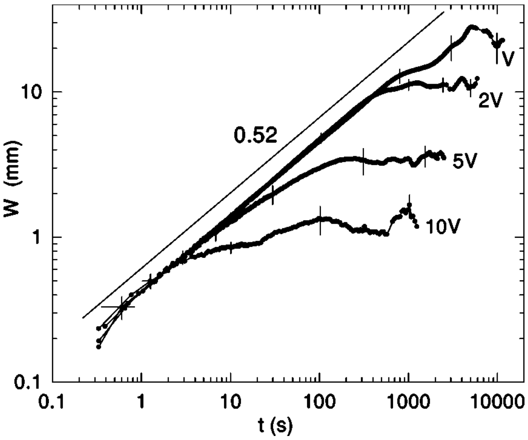

FIG. 12. Interfacial width $W(t)$ for disorder T 1.50, gap spacing $b=0.36$ mm, and four different velocities. The straight line drawn to guide the eye is the power law $W \sim t^{0.52}$.

out using a large number of disorder configurations. Qualitatively, the power spectrum presents the same behavior observed for SQ, with two different regimes separated by a crossover point q_c. The roughness exponent α_1 increases with the velocity, varying from $\alpha_1=0.5\pm0.1$ (slope -2.1 ± 0.1) for velocity V to $\alpha_1=1.2\pm0.1$ (slope -3.4 ± 0.1) for velocity $10\,V$. We have observed that at high velocities α_1 reaches the same limiting value as it was measured for SQ 1.50.

B. Variable gap spacing

1. SQ of 1.50 mm

Variations in the gap thickness modify the strength of the capillary forces in the vertical direction, which are destabilizing, in relation to the viscous forces and to the capillary forces in the plane of the cell, which are stabilizing. The sequence of interfaces at different b and equal velocity $(2V)$ of Fig. 14 indicate that roughening at large scales is inhibited for the smallest gap spacing $b=0.16$ mm, and the interface remains globally flat. Notice that the oil-air interface adapts perfectly to the disorder configuration. The gap spacings must be increased to values larger than $b=0.23$ mm to observe all scales contributing to the roughening process.

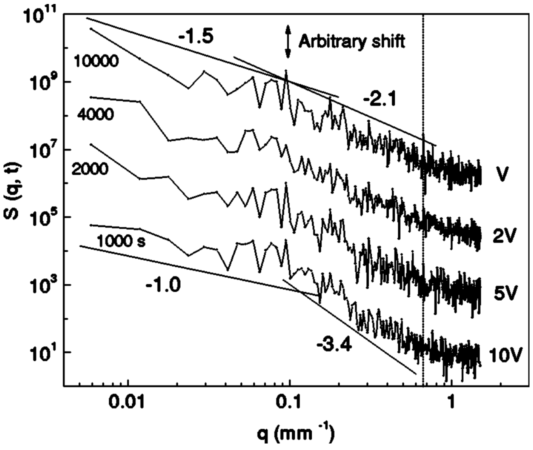

FIG. 13. Determination of the roughness exponents from the power spectra for experiments at four different velocities, with $b=0.36$ mm and disorder T 1.50. The curves have been shifted in the vertical direction for clarity. The vertical line gives the value of q associated with the spatial scale of the disorder. The other straight lines are power law fits from which the roughness exponents can be deduced.

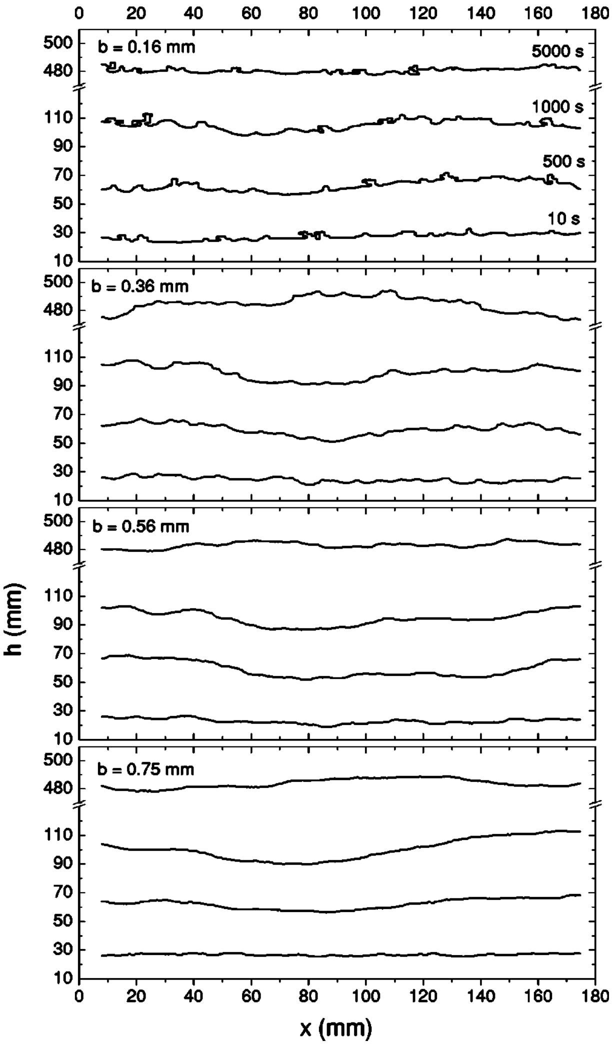

FIG. 14. Sequence of interfaces at velocity $2V$ and disorder SQ 1.50, at different gap spacings corresponding to, from smaller to larger gap spacing, Ca′ = 3.65, 3.70, 3.66, and 3.62. The disorder realization is the same in the four sequences. The reference velocity is $V=0.04$ mm/s.

The results of $W(t)$ for different gap spacings are presented in Fig. 15(a). The results show that the saturation times and widths are practically independent of gap spacing. This is a demonstration that increasing the gap thickness is not equivalent to increasing the velocity, although both changes result in larger Ca′. The growth exponent β at the smallest gap spacings centers around $\beta=0.40$ but is subjected to a large error bar due to a significant presence of

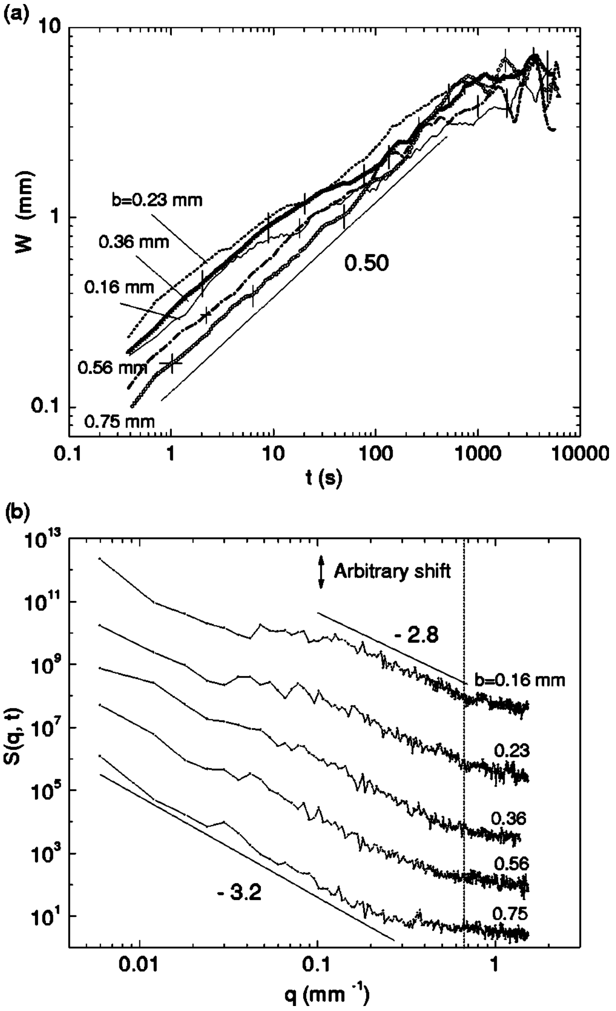

FIG. 15. Experimental results at velocity $2V$ and disorder SQ 1.50 at five different gap spacings. (a) Interfacial width $W(t)$. A power law with slope 0.5 has been drawn to guide the eye. (b) Power spectra at saturation ($t=6000$ s). The curves have been shifted in the vertical direction for clarity. The vertical line gives the value of q associated with the spatial scale of the disorder.

multivaluations in the interface. As b increases there is a clear tendency towards a well-defined power law, over three orders of magnitude in time, resulting in an exponent $\beta=0.50\pm0.02$.

Although all the experiments start with the same initial condition, the transition from an almost flat interface, with $W\simeq 0$, to a set of almost parallel $W(t)$ curves, suggests that the growth at very short times is strongly dependent on gap thickness.

The different role of velocity and gap spacing is also apparent from the power spectrum of the interfaces at saturation, shown in Fig. 15(b). For the smallest gap spacing $b=0.16$ mm, the spectrum is nearly flat at small q, reflecting that the largest scales do not grow (Fig. 14). The only contribution to this part of the spectrum comes from the memory of the global shape of the initial front, which, at the smallest gap spacings, cannot be prepared perfectly flat. The power law dependence at larger q extends from $q_c\simeq 0.15$ to $q=0.67$ (which corresponds to the lateral size of the disorder cell). As b increases, the nearly q-independent behavior at small q changes to a power law behavior (exponent α_1), and the crossover value q_c shifts to smaller q. For gap spacings as large as $b=0.75$ mm this shift leads to a single power law dependence, which could be strongly affected by finite-size effects. The measured exponents in the short length scale regime increase with b, from $\alpha_1=0.9\pm0.1$ (slope -2.8 ± 0.2) to $\alpha_1=1.1\pm0.1$ (slope -3.2 ± 0.2).

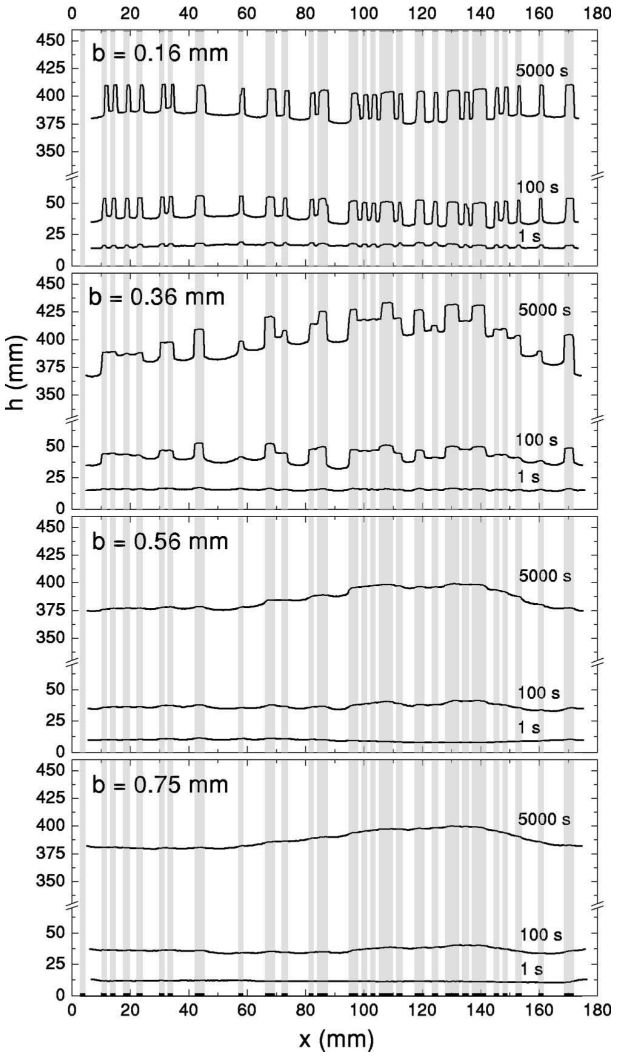

FIG. 16. Sequence of interfaces at velocity $2V$ and disorder T 1.50, at different gap spacings corresponding to, from smaller to larger gap spacing, $\mathrm{Ca}'=2.67$, 3.25, 3.38, and 3.41.

2. T of 1.50 mm

The gap spacing has been varied in the range $0.16\leqslant b\leqslant 0.75$, keeping the velocity fixed at $2V$. Figure 16 shows a sequence of the temporal evolution of the interfaces for four different gap spacings. The most remarkable aspect is the significant difference in the shape of the interfaces between $b=0.16$ mm and the other gap spacings. For $b=0.16$ mm,

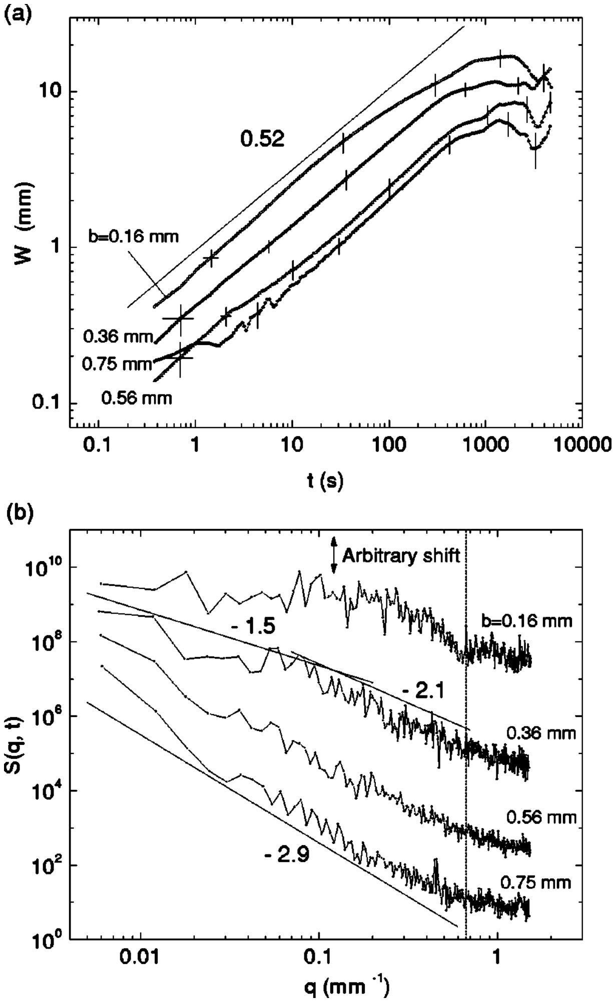

FIG. 17. Experimental results at velocity $2V$ and disorder T of 1.50 mm, at four different gap spacings. (a) Interfacial width $W(t)$. A power law with slope 0.52 has been drawn to guide the eye. (b) Power spectra at saturation ($t=6000$ s). The curves have been shifted in the vertical direction for clarity. The vertical line gives the value of q associated with the spatial scale of the disorder.

the capillary forces are strong enough to inhibit correlations between neighboring tracks. Similar to the experiments with SQ 1.50 and the smallest gap, we do not expect saturation of scales larger than the average lateral size of the tracks. For $b \geqslant 0.36$ mm the behavior is different: the interfacial height is correlated from the size of the basic disorder cell up to the system width. The interface at long length scales adopts a final shape at saturation identical for the three gaps, dominated by the spatial distribution of the disorder pattern. At short length scales the amplitude of the fingers depends on the relative strength of the capillary forces, tuned by the gap spacing.

Figure 17(a) shows the $W(t)$ curves for the four gap spacings. The slopes are practically the same in all four cases, the saturation times are also very similar, and the saturation widths are progressively larger as the gap spacing is reduced. The fact that the interfacial fluctuations with $b=0.16$ mm reach saturation is a consequence of driving the system with a finite velocity that impedes an infinite deformation of the interface.

In Fig. 17(b), we represent the spectra for the four velocities at saturation. The fact that for $b=0.16$ mm the interfacial height is uncorrelated for distances larger than the average lateral size of the tracks (2.3 mm, corresponding to $q=0.43$) is clearly observed, since for $q \lesssim 0.4$ we observe a *plateau* in the power spectrum. The only hint of a power law regime is at large q, from $q \gtrsim 0.4$ to the limit given by the disorder size, an interval too short to measure any roughness exponent. The other gap spacings show qualitatively the same behavior observed for SQ. The large q saturate with an exponent α_1 that is progressively larger as we increase the gap spacing, varying from $\alpha_1=0.5\pm0.1$ (slope -2.1 ± 0.2) for $b=0.36$ mm to $\alpha_1=0.9\pm0.1$ (slope -2.9 ± 0.2) for $b=0.75$ mm. The regime characterized by α_2 is only identifiable for $b=0.36$ mm. For the other gap spacings, our results indicate that we have a unique power law over all length scales. Here again, however, the results for the largest gap spacings could be severely influenced by finite-size effects.

VII. ANALYSIS AND DISCUSSION

The variation of the roughness exponents with velocity and gap spacing, for SQ and T disorder configurations, is summarized in Fig. 18. We observe that α_1 and α_2 have opposite behaviors as the interface velocity increases.

The exponent α_1, characteristic of roughening at short length scales, increases with v. It becomes larger than 1 (super-rough interface) already at moderate velocities. To understand this behavior, we refer to Fig. 9(a), where it is shown that α_1 is large at very short times and decreases progressively as time goes on at velocity $2V$. The initial super roughness is due to the initially local dynamics of the interface fluctuations as the interface gets in contact with the disorder for the first time. At sufficiently large velocities, however, the subsequent decrease of α_1 is not observed, and the initial super roughness gets frozen in. The reason is that the saturation time $t_\times$ is comparable to the average time spent by the interface to go across the distance $\tilde{l}$ (the average length of the disorder in the y direction) estimated as $\tau=\tilde{l}/v$. For example, for SQ 1.50, $b=0.36$ mm and $v=10\ V$, we have $t_\times=5$ s and $\tau=\tilde{l}/v\simeq6$ s. This also explains the fact that α_1 takes similar values for SQ and T at high velocities, since whenever $t_\times\simeq\tau$ the continuity of the disorder in the y direction is irrelevant. In particular, we have evidence that α_1 becomes identical for SQ and T at very large velocities. The interface is saturated at all times, making the interfacial dynamics in SQ equivalent to an average of the dynamics over a number of T configurations. For gap spacings around $b=0.36$ mm, we have observed that this condition is satisfied for $v\gtrsim13V$. An identical value $\alpha_1\simeq1.3$ has been obtained for both SQ and T by performing experiments at $30V$ ($t_\times\ll\tau$). This value of α_1 is distinctively larger than previous experimental results, and coincides within error bars with the value 1.25 found numerically

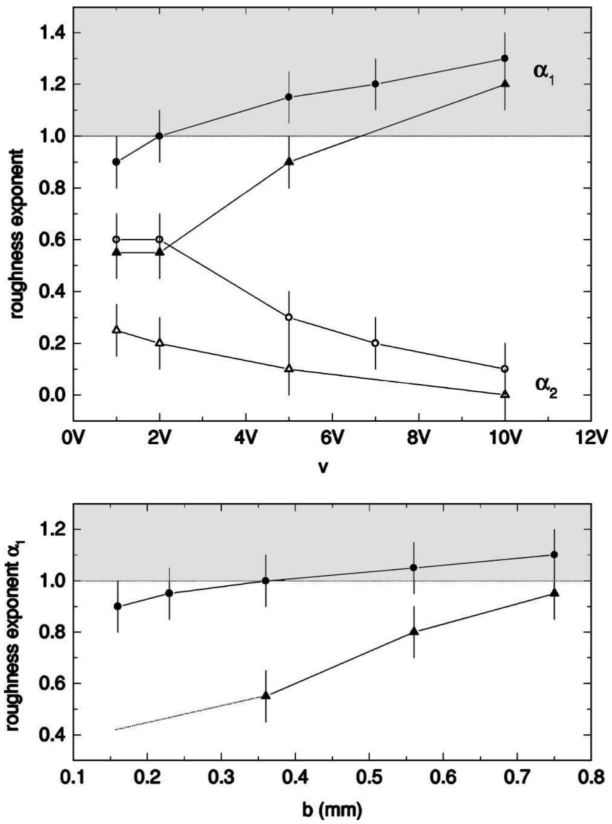

FIG. 18. Variation of the roughness exponents with interface velocity (top) and gap spacing (bottom), for SQ 1.50 (circles) and T 1.50 (triangles). Solid and open symbols correspond to α_1 and α_2, respectively. The region of super-rough interfaces ($\alpha > 1$) is shown in gray. The lines are drawn to guide the eye.

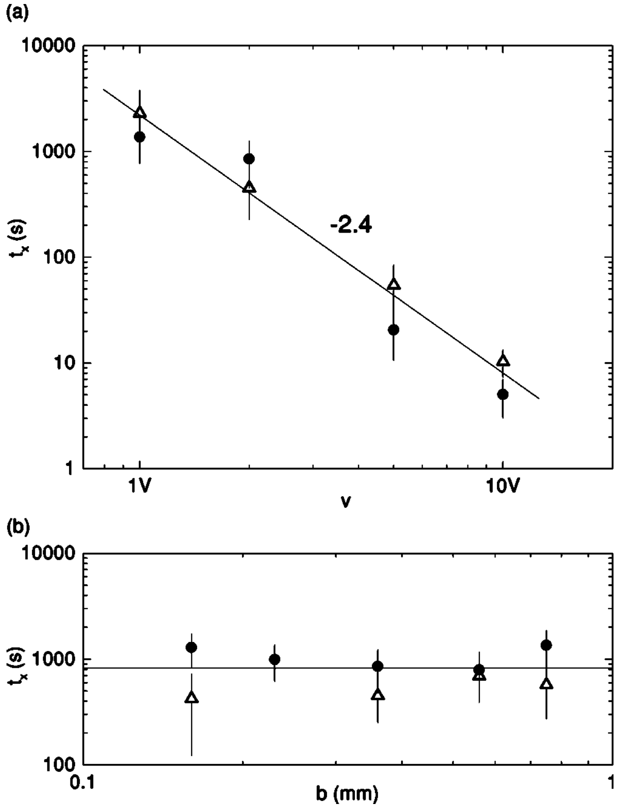

FIG. 19. Saturation time $t_\times$ as a function of velocity v (top) and gap spacing b (bottom) for SQ 1.50 (circles) and T 1.50 (triangles). The straight lines have been drawn to guide the eye.

in Ref. [19] taking account of the nonlinearities. A super rough interface ($\alpha > 1$) is also obtained by scaling analysis in Ref. [17], but with a larger exponent.

The exponent α_2 (long length scales) measured in our experiments decreases with v. Its actual behavior, however, could be obscured by finite-size effects. The reason is that nonlocal effects on the interfacial dynamics (due to the fluid flow from the reservoir) become progressively more significant as v increases. For experimental reasons we have not studied finite-size effects in any systematic way. However, we have checked that experiments performed at velocity V and system size $L/2$ give the same exponent α_2 as those at velocity $2V$ and system size L. The simultaneous dependence of α_2 on velocity and system size can be estimated from $W(t)$ for both SQ and T. We have observed [Figs. 19(a) and 20(a)] that the saturation time $t_\times$ and the saturation width W_s are power laws of the velocity v of the form $t_\times \sim v^{-\delta}$ and $W_s \sim v^{-\gamma}$, with $\delta \simeq 2.5$ and $\gamma \simeq 1.1$ for SQ, and $\delta \simeq 2.3$ and $\gamma \simeq 1.2$ for T. Combining these relations with the Family-Viseck scaling assumption (2), and taking into account that the saturation times and widths correspond to the long time regime (long length scales), we get

$$\alpha_2 \sim -\beta\delta \frac{\log_{10} v}{\log_{10} L} \tag{20}$$

with $\gamma = \beta\delta$. Given that the system size L has been kept fixed in the experiments, the relation (20) predicts that the roughness exponent α_2 obtained from the experiments will depend on v. The validity of this result is confirmed in Fig. 21, where the values of α_2 are plotted vs $\log_{10} v$.

From the observation that the difference between α_1 and α_2 decreases as v is reduced (Fig. 18) and taking into account that capillary forces become also more important, we argue that in the limit of very low velocities the power spectrum would display a unique power law extending over all scales with a roughness exponent in the interval $0.6 - 0.9$, compatible with the observations in [15,20–23]. This limit is unreachable for SQ because at velocities $v \lesssim V/2$ the interface gets locally pinned and develops overhangs. In the case of T there is no pinning or multivaluation, but the interface stretches to such a point that easily pinches off at long times, before saturation. These and other questions, present only in the regime of flows dominated by capillary forces, are studied in Ref. [33].

Concerning the influence of the gap spacing, b two main effects must be taken into account. First, the mobility is proportional to b^2 and hence increases with b, enhancing the stabilizing effect of the viscous pressure field (on long length scales) and the interfacial tension in the plane of the cell (on short length scales). Second, increasing b weakens the destabilizing effect of the capillary forces induced by the disorder, which act on short length scales. The overall result is that the

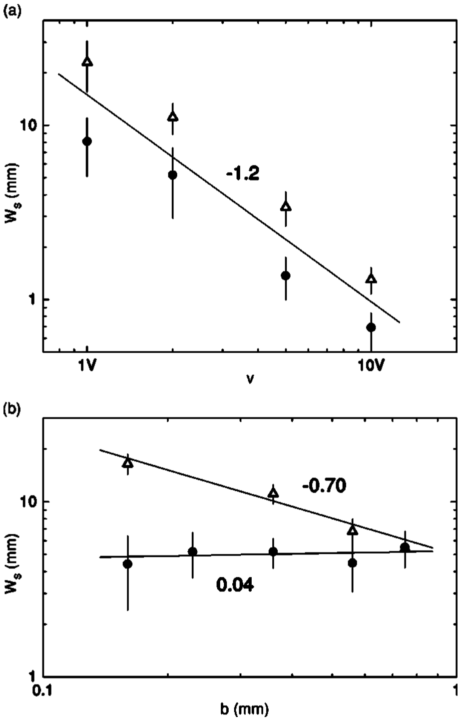

FIG. 20. Saturation width W_s as a function of velocity v (top) and gap spacing b (bottom) for SQ 1.50 (circles) and T 1.50 (triangles). The straight lines have been drawn to guide the eye.

curves $W(t)$ are shifted towards smaller widths as b increases, as shown in Figs. 15(a) and 17(a). The shift is such that Wb collapses the curves for different gap spacings into a single one, in both SQ and T cases. The fact that large values of b make the presence of the disorder irrelevant can be observed through the values of the roughness exponents α, which show a tendency to converge into a single value $\alpha \simeq 1$ at large gap spacings and for any disorder configuration.

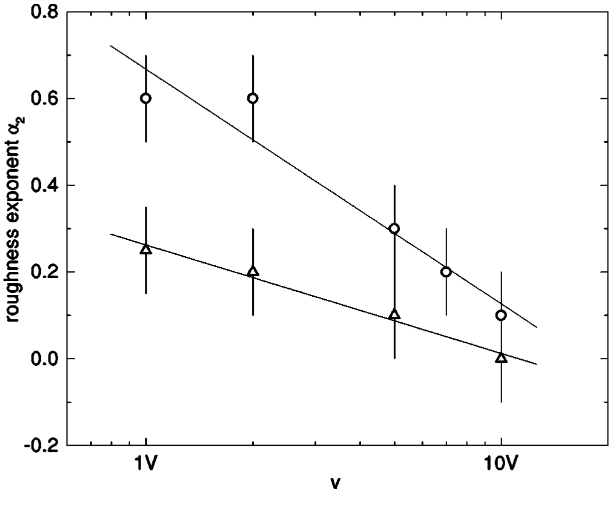

FIG. 21. Roughness exponent α_2 as a function of $\log_{10}v$ for SQ 1.50 (circles) and T 1.50 (triangles). The straight lines have been drawn to guide the eye.

TABLE II. Summary of the values of the roughness exponents.

Disorder (mm)	Low Ca′ (≲ 3)		Moderate Ca′ (3<Ca′< 10)		Large Ca′ (≳ 10)	
	α_1	α_2	α_1	α_2	α_1	α_2
SQ 1.50	0.6−0.9		≃1	≃0.6	≃1.3	≃0
SQ-*n* 1.50	0.6−0.9		≃0.9	≃0.5	≃1.3	≃0
T 0.40	New regime		≃0.7	≃0.5	≃1.3	≃0
T 1.50	New regime		≃0.5	≃0.2	≃1.3	≃0

Another observation is that the saturation regime is always reached at almost the same saturation time $t_\times$, independently of the gap spacing, as Fig. 19(b) reveals. The interfacial width at saturation, however, has a different origin depending on gap spacing. For small b the width is due to fluctuations at the shortest length scales, while for large b it is due to fluctuations at longer length scales. This can be observed on the interfaces and is clearly reflected in the power spectrum [Figs. 15(b) and 17(b)]. The passage from short to long length scales is continuous with b. It can be shown that replacing the variable q by the dimensionless variable qb produces the collapse of the power law region of the power spectra in Fig. 15(b).

Table II shows the main results obtained for the roughness exponents α_1 (short length scales) and α_2 (long length scales) at different disorder configurations and drivings. For small Ca′, capillary forces are dominant at all scales and the dynamics is very sensitive to the disorder configuration. For SQ and SQ-*n*, the interfaces get locally pinned and the measured exponents are close to those obtained in DPD, or in experiments where capillary forces are dominant [15,20–23]. In the limit of persistent disorder, the nature of the disorder impedes pinning, but the effect of the destabilizing capillary forces combined with the correlations between neighboring tracks leads to a new regime that can be described using the anomalous scaling ansatz [33]. This new regime also extends to the region of moderate Ca′ for T disorder. For moderate Ca′, viscous forces are dominant at long length scales, and two clear regimes separated by a crossover wave number q_c can be characterized. For SQ and SQ-*n* we get roughness exponents $\alpha_1 \gtrsim 1$ and $\alpha_2 \simeq 0.5-0.6$. For T, we get a qualitatively similar behavior, but we obtain lower values of the exponents due to finite-size effects at long length scales and the dominant capillary forces at short length scales. For large Ca′, the viscous forces cause the initial super roughness at short times and short length scales to get frozen in, obtaining the same roughness exponent $\alpha_1 \simeq 1.3$ for all the disorder configurations.

Our experimental results can now be compared with the predictions of the nonlocal models [16–19] discussed in Sec. II. It appears that none of the models can account for the different results obtained in the whole range of capillary numbers explored. Although the Flory-type argument used by Ganesan and Brenner [16] is difficult to justify in this nonequilibrium situation, they obtain roughness exponents

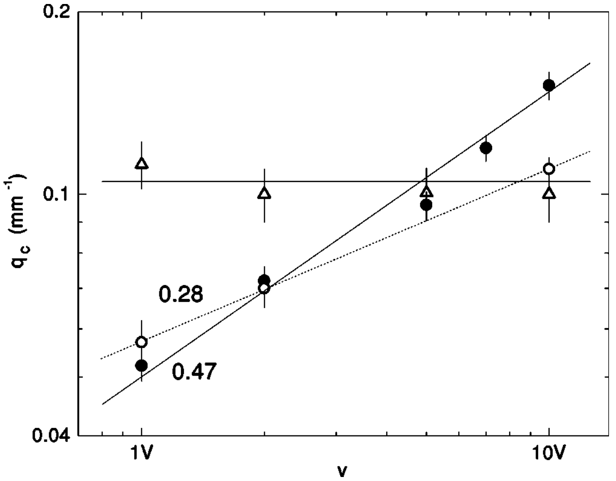

FIG. 22. Dependence of the crossover wave number q_c on velocity v for three disorder configurations: SQ 1.50 (solid circles), SQ-*n* 1.50 (open circles), and T 1.50 (triangles).

($\alpha_1 = 3/4$ and $\alpha_2 = 1/2$) consistent with our values for small and moderate Ca′. The exponents obtained by Hernández-Machado *et al.* [17] for the long length scales at moderate Ca′, $\alpha_2 = 1/2$ and $z = 1$ ($\beta_2 = 1/2$), are in agreement with our experimental values in the long time regime, where the viscous forces are dominant. The value of α for short length scales, corresponding to the short time regime of the model, gives a super rough behavior ($\alpha_1 > 1$) dominated by surface tension in the plane, but larger than the exponent measured in the experiment. For large capillary numbers the numerical result of Dubé *et al.* [18,19], $\alpha_1 = 1.3$, is in agreement with our experimental results, but not the result $\beta_1 = 0.3$ because, as pointed out above, these authors assume a spontaneous imbibition. At this point it would be interesting to know whether a model containing a quenched disorder both in the mobility and in the chemical potential would be able to explain the experimental results for the whole regime of Ca′ studied here, and especially the regime of large Ca′ in forced imbibition. This remains an open question.

Our last analysis is the variation of q_c with v. The crossover wave number q_c separates the regime in which the long length scale fluctuations (small q) are damped by the viscous pressure field, from the regime in which the short length scale fluctuations (large q) are damped by the interfacial tension in the plane of the cell. Since the relative importance of the viscous pressure field increases with Ca′, it is expected that q_c will increase with v. Specifically, a linear analysis of the interfacial problem shows that the viscous damping is proportional to $v|q|$ and the interfacial tension damping is proportional to $q^2|q|$, which results in $q_c \propto v^{0.5}$ [17,19].

In Fig. 22, we show the behavior of q_c with v for different kinds of disorder. The error bars are relatively large because the exact location of q_c in the experimental power spectra is difficult to ascertain. For SQ 1.50 we find that $q_c \propto v^{0.47}$, in good agreement with the theoretical prediction. It is interesting to note that as we go to disorders of larger $\tilde{l}$ (increasing persistence), q_c tends to be less sensitive to v. For T 1.50, we observe that q_c becomes independent of v within error bars. The reason can be understood in the framework of the following scenario: at a local level (see Fig. 1) the motion of the interface in the SQ disorder can be viewed as a series of events formed by a period of nearly steady motion, a subsequent period of fast advance over a copper island (accompanied by an abrupt change of sign of the in-plane curvature), and a third period of fast advance over fiberglass due to relaxation of the local in-plane curvature. Thus, damping of the short length scales due to the interfacial tension in the plane of the cell is basically effective only in this last period when the interface depins from the copper islands. As the persistence of the disorder in the y direction is larger, the relaxation periods are less frequent. This can be observed through the histogram of Fig. 4. When we increase the persistence of the disorder changing from SQ to SQ-*n*, the number of the smallest copper aggregations reduces almost by one order of magnitude. In the limiting case of T 1.50 the disorder is continuous in the y direction, and the damping role of the in-plane interfacial tension is effectively suppressed.

VIII. CONCLUSIONS

We have presented experiments of forced fluid imbibition in a Hele-Shaw cell with quenched disorder. We have used three main kinds of disorder patterns SQ, SQ-*n*, and T, characterized by an increasing persistence length $\tilde{l}$ in the direction of growth. We have measured a robust roughness exponent $\beta \simeq 0.5$ that is almost independent of the disorder configuration, interface velocity, and gap spacing, although the behavior of the interfacial width presents important fluctuations both during growth and at saturation, which progressively disappear as the disorder is more persistent in the y direction. The roughness exponent α, however, shows a clear dependence on the experimental parameters, as summarized in Table II, and discussed in the preceding section. Finally, we have focused on the dependence of the crossover wave number as a function of the interface velocity v and $\tilde{l}$. For the shortest $\tilde{l}$, $q_c \sim v^{0.47}$, and becomes independent of v as the disorder is persistent in the y direction.

The absence of pinning in experiments with disorders of increasing $\tilde{l}$ allows a detailed investigation of the regime of large capillary forces. This regime presents some interesting features that are studied in detail in Ref. [33].

ACKNOWLEDGMENTS

We are grateful to M.A. Rodríguez, L. Ramírez-Piscina, J. Casademunt, K.J. Måløy, and J. Schmittbuhl for fruitful discussions. The research has received financial support from the Dirección General de Investigación (MCT, Spain), Project No. BFM2000-0628-C03-01. J. O. acknowledges the Generalitat de Catalunya for additional financial support. J.S. is also supported financially by the DGI (MCT, Spain).

[1] A.-L. Barabási and H. E. Stanley, *Fractal Concepts in Surface Growth* (Cambridge University Press, Cambridge, 1995).
[2] J. Krug, Adv. Phys. **46**, 139 (1997).
[3] P. Meakin, *Fractals, Scaling and Growth far from Equilibrium* (Cambridge University Press, Cambridge, 1998).
[4] P.-Z. Wong, MRS Bull. **19**, 5 (1994), and references therein.
[5] M. Dubé, M. Rost, and M. Alava, Eur. Phys. J. B **15**, 691 (2000).
[6] P.G. de Gennes, J. Phys. A **47**, 1541 (1986).
[7] A. Paterson, M. Fermigier, P. Jenffer, and L. Limat, Phys. Rev. E **51**, 1291 (1995); A. Paterson and M. Fermigier, Phys. Fluids **9**, 2210 (1997).
[8] F. Family and T. Vicsek, J. Phys. A **18**, L75 (1985).
[9] J.M. López and M.A. Rodríguez, Phys. Rev. E **54**, R2189 (1996); J.M. López, M.A. Rodríguez, and R. Cuerno, Physica A **246**, 329 (1997).
[10] J.J. Ramasco, J.M. López, and M.A. Rodríguez, Phys. Rev. Lett. **84**, 2199 (2000).
[11] M. Kardar, G. Parisi, and Y.C. Zhang, Phys. Rev. Lett. **56**, 889 (1986).
[12] S.F. Edwards and D.R. Wilkinson, Proc. R. Soc. London, Ser. A **381**, 17 (1982).
[13] H. Leschhorn, Phys. Rev. E **54**, 1313 (1996); H. Leschhorn, T. Nattermannn, S. Stepanow, and L.-H. Tang, Ann. Phys. (N.Y.) **6**, 1 (1997).
[14] J. Krug and P. Meakin, Phys. Rev. Lett. **66**, 703 (1991).
[15] S. He, G.L.M.K.S. Kahanda, and P.Z. Wong, Phys. Rev. Lett. **69**, 3731 (1992).
[16] V. Ganesan and H. Brenner, Phys. Rev. Lett. **81**, 578 (1998).
[17] A. Hernández-Machado, J. Soriano, A.M. Lacasta, M.A. Rodríguez, L. Ramírez-Piscina, and J. Ortín, Europhys. Lett. **55**, 194 (2001).
[18] M. Dubé, M. Rost, K.R. Elder, M. Alava, S. Majaniemi, and T. Ala-Nissila, Phys. Rev. Lett. **83**, 1628 (1999).
[19] M. Dubé, M. Rost, K.R. Elder, M. Alava, S. Majaniemi, and T. Ala-Nissila, Eur. Phys. J. B **15**, 701 (2000).
[20] M.A. Rubio, C.A. Edwards, A. Dougherty, and J.P. Gollub, Phys. Rev. Lett. **63**, 1685 (1989).
[21] V.K. Horváth, F. Family, and T. Vicsek, Phys. Rev. Lett. **65**, 1388 (1990).
[22] M.A. Rubio, A. Dougherty, and J.P. Gollub, Phys. Rev. Lett. **65**, 1389 (1990).
[23] V.K. Horváth, F. Family, and T. Vicsek, J. Phys. A **24**, L25 (1991).
[24] V.K. Horváth, F. Family, and T. Vicsek, Phys. Rev. Lett. **67**, 3207 (1991).
[25] A. Dougherty and N. Carle, Phys. Rev. E **58**, 2889 (1998).
[26] M. Avellaneda and S. Torquato, Phys. Fluids A **3**, 2529 (1991).
[27] A. Koponen, M. Kataja, and J. Timonen Phys. Rev. E **54**, 406 (1996).
[28] A. Koponen, M. Kataja, and J. Timonen Phys. Rev. E **56**, 3319 (1997).
[29] G.M. Homsy, Annu. Rev. Fluid Mech. **19**, 271 (1987).
[30] I. Simonsen, A. Hansen, and O.M. Nes, Phys. Rev. E **58**, 2779 (1998).
[31] J. Schmittbuhl, J.-P. Vilotte, and S. Roux, Phys. Rev. E **51**, 131 (1995).
[32] G. Tripathy and W. van Saarloos, Phys. Rev. Lett. **85**, 3556 (2000).
[33] J. Soriano, J.J. Ramasco, M.A. Rodríguez, A. Hernández-Machado, and J. Ortín, Phys. Rev. Lett. **89**, 026102 (2002); J. Soriano, J. Ortín, and A. Hernández-Machado, (unpublished).

4.3 *Anomalous roughening of Hele–Shaw flows with quenched disorder*, Phys. Rev. Lett. 89, 026102 (2002)

VOLUME 89, NUMBER 2 PHYSICAL REVIEW LETTERS 8 JULY 2002

Anomalous Roughening of Hele-Shaw Flows with Quenched Disorder

J. Soriano,[1] J. J. Ramasco,[2,3] M. A. Rodríguez,[2] A. Hernández-Machado,[1,4] and J. Ortín[1]
[1]*Departament ECM, Facultat de Física, Universitat de Barcelona, Diagonal 647, E-08028 Barcelona, Spain*
[2]*Instituto de Física de Cantabria, CSIC, Avenida Los Castros, E-39005 Santander, Spain*
[3]*Departamento de Física Moderna, Universidad de Cantabria, E-39005 Santander, Spain*
[4]*Groupe de Physique des Solides, Université Pierre-et-Marie-Curie, Tour 23, 2 place Jussieu, 75251 Paris Cedex 05, France*

(Received 7 December 2001; published 24 June 2002)

The kinetic roughening of a stable oil-air interface moving in a Hele-Shaw cell that contains a quenched columnar disorder (tracks) has been studied. A capillary effect is responsible for the dynamic evolution of the resulting rough interface, which exhibits anomalous scaling. The three independent exponents needed to characterize the anomalous scaling are determined experimentally. The anomalous scaling is explained in terms of the initial acceleration and subsequent deceleration of the interface tips in the tracks coupled by mass conservation. A phenomenological model that reproduces the measured global and local exponents is introduced.

DOI: 10.1103/PhysRevLett.89.026102 PACS numbers: 68.35.Ct, 05.40.–a, 47.55.Mh

The kinetic roughening of surfaces and interfaces in nonequilibrium conditions has received a great deal of attention in last few years. This is a subject of technological importance in surface growth, and it is of fundamental relevance as an example of scaling far from equilibrium [1].

Roughening originates from the competition between stabilizing and destabilizing mechanisms at different length scales. As a result of the competition, the correlation length of the interfacial fluctuations along an initially flat front increases monotonously with time, until it reaches the system size and the roughness saturates. The statistical properties of the roughening front are usually given in terms of the (rms) width w of the interfacial fluctuations. In the absence of characteristic scales, many systems follow the dynamic scaling hypothesis of Family-Vicsek (FV) [2], in which short and long length scales have the same scaling behavior: $w(l) \sim t^{\beta}$ for $t < t_{\times}$, $w(l) \sim l^{\alpha}$ for $t > t_{\times}$, and $t_{\times} \sim l^{z}$. Here l is the lateral size of the window used to measure w, $t_{\times}$ is the saturation time, β is the growth exponent, α is the roughness exponent, and z is the dynamic exponent. The scaling relation $\alpha = z\beta$ reduces to two the number of independent exponents that characterize the universality class of the problem under study.

In recent years, however, experiments on molecular beam epitaxy [3], sputtering [4], fracture mechanics [5], and electrodeposition [6] have revealed a rich variety of situations in which the scaling of the global and the local interface fluctuations are substantially different. Long length scales are then characterized by the same FV scaling exponents, while short length scales follow the so-called *anomalous scaling ansatz* [7]: $w(l,t) \sim t^{\beta}$ for $t < t_l$, $w(l,t) \sim l^{\alpha_{loc}} t^{\beta^*}$ for $t_l < t < t_{\times}$, and $w(l,t) \sim l^{\alpha_{loc}} L^{\alpha - \alpha_{loc}}$ for $t_{\times} < t$. The local time $t_l \sim l^{z}$, and the saturation time $t_{\times} \sim L^{z}$, where L is the system size in the direction along the front. Here β^* and α_{loc} are new *local* growth and roughness exponents, respectively, which characterize the scaling at short length scales ($l \ll L$). There is a new scaling relation $\alpha - \alpha_{loc} = z\beta^*$. Since now there are five exponents and two scaling relations, the anomalous scaling is characterized by three independent exponents. Usually the roughness exponents are determined through the power spectrum, which is less sensitive than w to finite size effects. The spectrum scales as $S(k,t) = k^{-(2\alpha+1)} s_A(kt^{1/z})$, where s_A obeys $s_A(u) \sim u^{2\alpha+1}$ when $u \ll 1$ and $s_A(u) \sim u^{2\theta}$ when $u \gg 1$. Here $\theta = \alpha - \alpha_{loc}$. The anomalous scaling leads to the usual FV scaling when $\theta = 0$ (short and long length scales are characterized by the same roughness exponents) and $\beta^* = 0$ (the temporal correlations of the short length scales disappear). Recently it has been shown that the anomalous scaling can be related to the presence of high slopes in the front that have nontrivial dynamics [8].

In this Letter we report the first observations of anomalous roughening in experiments of Hele-Shaw flows with quenched disorder. We consider an initially flat front between oil and air, driven at a small constant average velocity v in a horizontal Hele-Shaw cell with a columnar quenched disorder. The disorder consists of continuous copper tracks on a fiberglass substrate in the advancing direction of growth and randomly distributed in the perpendicular direction (Fig. 1). In this situation, the correlation of the disorder in the advancing direction is infinite. The local motion relative to the average position of the front is driven by capillary forces, caused by the different curvatures of the advancing front in the third dimension, depending on whether the oil is on a copper track or on the fiberglass substrate. An analysis of the rms width of the rough interface at short and long length scales plus a collapse of the power spectra of the interfacial fluctuations enables an independent determination of the three exponents characteristic of anomalous scaling.

We associate the anomalous roughening with the initial acceleration and subsequent deceleration of the liquid on the copper tracks, caused by capillarity, and the coupling

© 2002 The American Physical Society

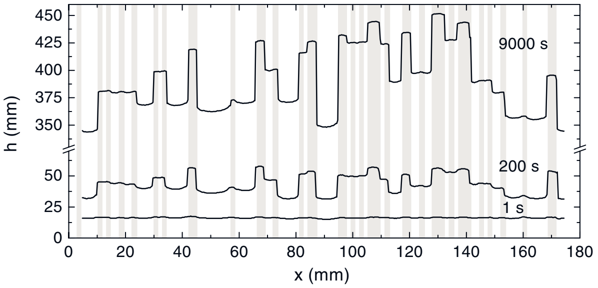

FIG. 1. Sequence of typical oil-air interfaces. The silicone oil moves upwards in the picture, and the disorder pattern is represented in grey. The experimental parameters are $b = 0.36$ mm and $v = 0.04$ mm/s.

of the motion over tracks and over fiberglass due to mass conservation. The anomaly decreases as v increases, and disappears when v is large enough to override the local acceleration and deceleration [9]. To explain the experimental results, we propose a phenomenological model which gives global and local exponents in good agreement with the experimental exponents.

The experiments have been performed in a horizontal Hele-Shaw cell, 190×550 ($L \times H$) mm^2, made of two glass plates 20 mm thick. A fiberglass substrate with copper tracks, manufactured using printed circuit technology, is attached to the bottom plate. The unit copper track is $d = 0.06 \pm 0.01$ mm high and 1.50 ± 0.04 mm wide. The tracks are placed randomly in a grid of 1.5 mm lattice spacing, along the x direction, up to a 35% occupation. There are no lateral correlations of the disorder at distances larger than the width of the unit track. The distance between the top plate and the substrate defines the gap spacing b, which has been varied in the range $0.16 \leq b \leq 0.75$ mm. We have used four different disorder configurations and carried out two identical runs per disorder configuration. A silicone oil (kinematic viscosity $\nu = 50$ mm^2/s, density $\rho = 998$ kg/m^3, and surface tension oil-air $\sigma = 20.7$ mN/m at room temperature) is injected into one side of the cell at a constant volumetric injection rate. The oil wets similarly and almost completely the surfaces which it is in contact with (glass, substrate, and copper). The evolution of the interface is monitored using two charge-coupled device cameras mounted along the growth direction and fixed. The final resolution is 0.37×0.37 mm^2/pixel, providing four pixels per unit track in the x direction. We have carried out a series of reference experiments to calibrate sidewall effects and possible inhomogeneities in gap spacing. Our results make us confident that these disturbances do not have a relevant effect on the dynamic scaling presented in this work. Extensive details of the experimental setup will be given in a forthcoming publication [10].

In Fig. 2 we present the results for the interfacial width as a function of time at different length scales l, from L to $L/256$. We plot $W(l,t) = [w^2(l,t) - w^2(l,0)]^{1/2}$ to minimize the influence of the initial condition [4,11].

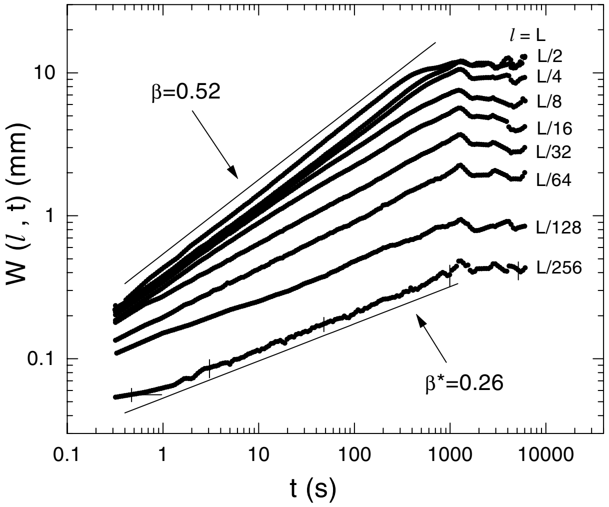

FIG. 2. Experimental determination of β and β^*. The window size l decreases from L to $L/256$. The experimental parameters are $b = 0.36$ mm and $v = 0.08$ mm/s.

We obtain clear power law dependencies, providing $\beta = 0.52 \pm 0.02$ at the longest length scales and $\beta^* = 0.26 \pm 0.03$ at the two shortest length scales. It is worth mentioning that a different method, based on the growth of the local slopes [8], gives the same value of β^*. The fact that this local exponent is significantly different from 0 is a sign of anomalous scaling of the measured fronts.

The temporal evolution of the power spectrum is presented in Fig. 3(a). At very short times we observe a regime with $S(k) \sim k^{-3.4}$. It is a superrough transient regime created when the fluid on the tracks reaches its maximum velocity after coming into contact with the disorder. The main regime appears further on, with $S(k) \sim k^{-2.1}$, and a vertical shift that progressively decreases with time and disappears at saturation ($t \gtrsim 450$ s). The vertical shift of the power spectra is a sign of intrinsic anomalous scaling, in which the spectral exponent [12] can be identified with the local roughness exponent, so that $\alpha_{loc} = 0.55 \pm 0.10$.

Using the above procedure, the three independent exponents β, β^*, α_{loc} have been obtained directly from the experiments. The other two exponents α, z can be obtained from the scaling relations. In order to verify the whole scaling, however, we prefer to determine the critical exponents by performing the best collapse of the spectra compatible with the experimental results. The collapse, presented in Fig. 3(b), leads to the following set of scaling exponents:

$$\beta = 0.50 \pm 0.04, \quad \beta^* = 0.25 \pm 0.03, \qquad (1)$$
$$\alpha = 1.0 \pm 0.1, \quad \alpha_{loc} = 0.5 \pm 0.1, \quad z = 2.0 \pm 0.2.$$

We have also looked into the possibility of multiscaling [13] through the scaling of the generalized correlations

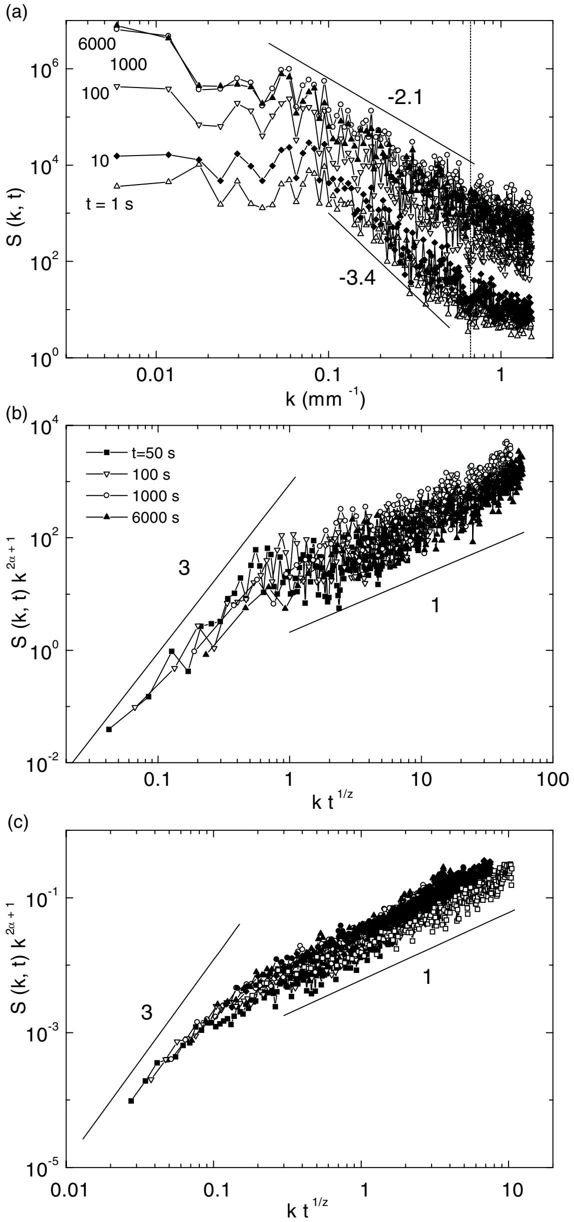

FIG. 3. (a) Temporal evolution of the power spectrum for the same experiments as Fig. 2. The vertical line gives the value of k associated with the lateral size of the unit copper track. (b) Collapse of the experimental power spectra for $t > 10$ s. (c) Collapse of the power spectra obtained from numerical simulations of the interfacial equation (2).

of order q, of the form $\{[h(x+l,t) - h(x,t)]^q\}^{1/q} \sim l^{\alpha_q}$. Different exponents for α_q, $\alpha_2 \simeq 0.6$, $\alpha_4 \simeq 0.3$, and $\alpha_6 \simeq 0.2$, were obtained, which confirm the existence of multiscaling in the experiment.

To understand the origin of anomalous scaling, we should look at the interfacial dynamics in greater detail. An initially flat oil-air interface, moving at a nominal average velocity v, experiences local accelerations at those points that touch a copper track for the first time. The local velocity of these points jumps to a maximum in a characteristic time of 1 s and then relaxes as $t^{-1/2}$ to v. The maximum velocity reached in a copper track increases with track width and decreases with gap spacing. As shown in Fig. 4, the average interface velocity over copper tracks or over fiberglass channels follows $v_\pm = v \pm (v_M - v)t^{-1/2}$, respectively, where v_M is the maximum of the average velocity over tracks. This functionality varies slightly with gap spacing due to the increasing correlation between neighboring tracks. It does not apply for $b \gtrsim 0.6$ mm. This behavior of different velocities v_+ and v_- is directly correlated with the shift of the power spectra, indicative of anomalous scaling: the shift is maximum at very short times and disappears close to saturation, similar to the difference between the average velocities shown in Fig. 4. When we inhibit the relaxation of the velocity over copper tracks by either injecting at $v > v_M$ or using large b, the anomalous scaling disappears. This scenario has been studied experimentally by exploring different velocities and gap spacings. Figure 5 shows a phase diagram representing the regions where the anomalous scaling is present (grey region, $\theta \neq 0$) or not (white regions, $\theta = 0$). The solid line represents the function $v_M(b)$, and the vertical line the limit between strong and weak capillary forces.

The critical exponents of the anomalous scaling depend on gap spacing and velocity. We have seen that the anomalous exponent θ tends to $\theta = 0$ as we increase either the velocity or the gap spacing. This exponent is particularly sensitive to variations of the gap spacing. For $b \gtrsim 0.6$ mm, $\theta = 0$ at any velocity. The experimental parameters $b = 0.36$ mm and $v = 0.08$ mm/s, deep in the grey region of Fig. 5, give the appropriate conditions to fully characterize the anomalous scaling experimentally. Smaller gap spacings mean that the correlation length in the x direction cannot grow to scales larger than the average track width, and larger gap spacings give too weak an

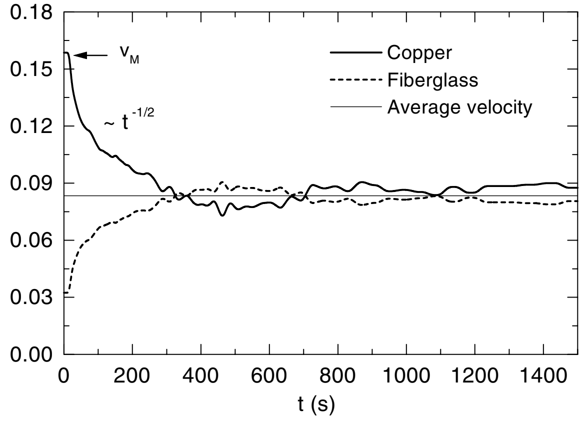

FIG. 4. Average interface velocity over copper tracks and over fiberglass, for $b = 0.36$ mm and $v = 0.08$ mm/s.

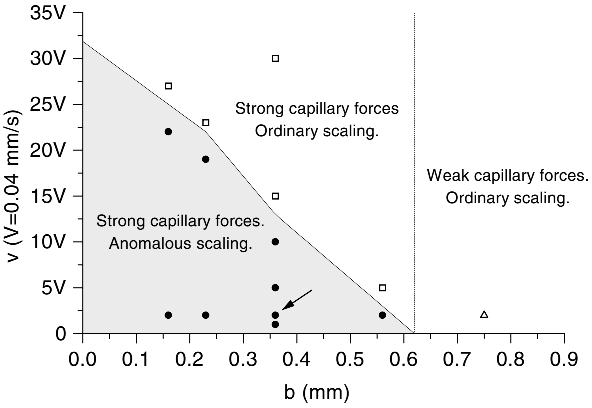

FIG. 5. Phase diagram $v(b)$ indicating the regions where the anomalous scaling is observable. The symbols represent the different regions explored experimentally, and the arrow indicates the parameters used in this Letter.

anomalous scaling because the $t^{-1/2}$ law is obeyed only on the widest tracks.

Finally, in order to reproduce the experimental behavior in a phenomenological way, we have developed an interfacial equation of the form

$$\partial_t h = \partial_x D(x) \partial_x h + v + (v_M - v) t^{-1/2} \eta(x), \qquad (2)$$

where $h = h(x, t)$, and $\eta(x)$ is a dichotomous noise with values $+1$ and -1 (columnar disorder). The diffusive coupling accounts for the dynamics with $z = 2$ found in experiments, and the other two terms account for the behavior of $v_\pm$ observed experimentally. Although the term $t^{-1/2}$ introduces some nonlocality in the model, this is essentially different from nonlocal models [14] introduced recently to account for mass conservation. The simplest version (constant D) reproduces the experimental behavior at long length scales ($\alpha = 1, \beta = 0.5, z = 2$), but not at short length scales, since numerical simulations of the model give $\beta^* = 0$ and $\alpha_{loc} = \alpha = 1$. The reason is that the simulated interfaces do not display the large fluctuations at the copper track edges observed in the experimental fronts (Fig. 1). This can be imposed analytically in Eq. (2) through an inhomogeneous diffusion coefficient $D(x)$. Numerically, we have introduced this effect by spatially averaging the interface inside each track once each n time steps. We thus recover interfaces that are morphologically analogous to experimental interfaces. Now the exponents derived from the scaling of the power spectra, shown in Fig. 3(c), and the multiscaling exponents, reproduce the values determined experimentally. In summary, Eq. (2) enables the relevant effects in the experiment to be both identified and calibrated.

In conclusion, we have presented the first experimental evidence of anomalous scaling in the dynamic roughening of a fluid interface in a Hele-Shaw cell with quenched disorder, and we have studied the experimental conditions for the appearance of the observed anomaly. The exponents β, β^*, and α_{loc} have been measured independently and their value has been refined by imposing the scaling relations through a collapse of the power spectra. Finally we have introduced an interfacial equation (2) that models the capillary phenomena observed in the experiments, at a phenomenological level. The model reproduces both the morphology of the interfaces and the values of the anomalous scaling exponents.

We are grateful to J. M. López for fruitful discussions. The research has received financial support from the Dirección General de Investigación (MCT, Spain) under Projects No. BFM2000-0628-C03-01 and No. BFM2000-0628-C03-02. J. S. and J. J. R. have received financial support from the Spanish Ministry of Science and the Spanish Ministry of Education, respectively.

[1] P. Meakin, *Fractals, Scaling and Growth Far from Equilibrium* (Cambridge University Press, Cambridge, 1998); M. Kardar, Phys. Rep. **301**, 85 (1998); J. Krug, Adv. Phys. **46**, 139 (1997).
[2] F. Family and T. Vicsek, J. Phys. A **18**, L75 (1985).
[3] H.-N. Yang *et al.,* Phys. Rev. Lett. **73**, 2348 (1994).
[4] J. H. Jeffries *et al.,* Phys. Rev. Lett. **76**, 4931 (1996).
[5] S. Morel *et al.,* Phys. Rev. E **58**, 6999 (1998); Phys. Rev. Lett. **85**, 1678 (2000); J. M. López and J. Schmittbuhl, Phys. Rev. E **57**, 6405 (1998).
[6] S. Huo and W. Schwarzacher, Phys. Rev. Lett. **86**, 256 (2001).
[7] J. M. López and M. A. Rodríguez, Phys. Rev. E **54**, R2189 (1996); J. M. López *et al.,* Physica (Amsterdam) **246A**, 329 (1997).
[8] J. M. López, Phys. Rev. Lett. **83**, 4594 (1999).
[9] The anomaly also decreases as the persistence of the disorder in the advancing direction is reduced, e.g., when tracks are replaced by square islands [10].
[10] J. Soriano, J. Ortín, and A. Hernández-Machado, Phys. Rev. E (to be published).
[11] G. Tripathy and W. van Saarloos, Phys. Rev. Lett. **85**, 3556 (2000).
[12] J. J. Ramasco *et al.,* Phys. Rev. Lett. **84**, 2199 (2000).
[13] J. Krug, Phys. Rev. Lett. **72**, 2907 (1994).
[14] V. Ganesan and H. Brenner, Phys. Rev. Lett. **81**, 578 (1998); M. Dubé *et al.,* Phys. Rev. Lett. **83**, 1628 (1999); A. Hernández-Machado *et al.,* Europhys. Lett. **55**, 194 (2001).

4.4 *Anomalous roughening in experiments of interfaces in Hele-Shaw flows with strong quenched disorder*, **Phys. Rev. E, submitted, cond-mat/0208432 (2002).**

Anomalous Roughening in Experiments of Interfaces in Hele-Shaw Flows with Strong Quenched Disorder

Jordi Soriano,* Jordi Ortín, and A. Hernández-Machado
Departament d'Estructura i Constituents de la Matèria
Universitat de Barcelona, Av. Diagonal, 647, E-08028 Barcelona, Spain
(Dated: December 5, 2002)

We report experimental evidence of anomalous kinetic roughening in the stable displacement of an oil–air interface in a Hele–Shaw cell with strong quenched disorder. The disorder consists of a random modulation of the gap spacing which is transverse to the growth direction (tracks). Experiments were performed by varying the average interface velocity and the gap spacing, and measuring the scaling exponents. The following values of the scaling exponents were obtained; $\beta \simeq 0.50$, $\beta^* \simeq 0.25$, $\alpha \simeq 1.0$, $\alpha_{loc} \simeq 0.5$, and $z \simeq 2$. When there is no fluid injection, the interface is driven solely by capillary forces, and a higher value of β of approximately $\beta = 0.65$ is measured. The presence of multiscaling and the particular morphology of the interfaces, characterized by large height differences that follow a Lévy distribution, confirms the existence of anomalous scaling. From a detailed study of the motion of the oil–air interface we show that the anomaly is a consequence of different local velocities on the tracks plus the coupling in the motion between neighboring tracks. The anomaly disappears at high interface velocities, weak capillary forces, or when the disorder is not sufficiently persistent in the growth direction. We have also observed the absence of scaling when the disorder is very strong or when a regular modulation of the gap spacing is introduced.

PACS numbers: 47.55.Mh, 68.35.Ct, 05.40.-a

I. INTRODUCTION

The study of the morphology and dynamics of rough surfaces and interfaces in disordered media has been a subject of much interest in recent years [1], and is an active field of research with relevance in technological applications and materials characterization. These surfaces or interfaces are usually self–affine, i.e. statistically invariant under an anisotropic scale transformation. In many cases, the interfacial fluctuations follow the dynamic scaling of Family–Vicsek (FV) [2], which allows a description of the scaling properties of the interfacial fluctuations in terms of a growth exponent β, a roughness exponent α, and a dynamic exponent z. However, many growth models [3–8], experiments of fracture in brittle materials, such as rock [9] or wood [10–12], as well as experiments on sputtering [13], molecular beam epitaxy [14], and electrodeposition [15] have shown that the FV scaling is limited, and a new ansatz, known as *anomalous scaling* [7, 16, 17], must be introduced. The particularity of the anomalous scaling is that local and global interfacial fluctuations scale in a different way, thus in general the global growth and roughness exponents, β and α respectively, differ from local exponents β^* and α_{loc}.

An interesting observation from the experiments on fracture in wood, where tangential and radial fractures were studied [12], is that the morphology of the interfaces for the former were characterized by large slopes, in contrast to the smoother appearance of the latter. As pointed out by López *et al.* [9], the origin of anomalous scaling in these experiments seems to be related to these large slopes in the morphology of the interfaces.

In a previous work [18] we presented an experimental study of forced fluid invasion in a Hele-Shaw cell with quenched disorder. We focused on the limit of weak capillary forces and studied different types of disorder configurations at different interface velocities and gap spacings. We obtained $\beta \simeq 0.50$, which was almost independent of the experimental parameters. However, the measured roughness exponents were dependent on the experimental parameters, and two regimes were characterized, α_1 at short length scales and α_2 at long length scales. We also observed that in conditions of totally persistent disorder in the direction of growth, and for sufficiently strong capillary forces, a new regime emerged. This new regime must be described within the framework of anomalous scaling and was discussed in a recent Letter [19]. The scaling exponents were obtained for a specific set of experimental parameters, and the range of validity of the anomaly was explored. We also introduced a phenomenological model that reproduces the interface dynamics observed experimentally and the scaling exponents.

The objective of the present paper is to analyze the experimental evidence of anomalous scaling in a systematic way, introducing additional techniques for the detection of anomalous scaling, such as multiscaling and the statistical distribution of height differences. The experimental range of anomalous scaling is studied in depth, and we investigate the effects of average interface velocity, gap spacing, and disorder configuration. We also consider the situation in which the interface is solely driven by capillary forces, which allows the behavior of the interface to be better understood at the disorder scale and its relationship with the scaling exponents at particular

---

*Electronic address: `soriano@ecm.ub.es`

limits of the experiments.

The outline of the paper is as follows. In Sec. II we review the anomalous scaling ansatzs. In Sec. III we introduce the experimental set-up, and in Sec. IV we describe the methodology used in data analysis. The main experimental results are presented and analyzed in Sec. V. The discussion and final conclusions are given in Section VI.

II. SCALING ANSATZS

The statistical properties of a one–dimensional interface defined by a function $h(x,t)$ (interface height at position x and time t) are usually described in terms of the fluctuations of h. If we consider an interface of lateral size L, the *rms* width calculated over a window $l < L$ is defined as $w(l,t) = \langle [h(x,t) - \tilde{h}(t)]^2 \rangle_x^{1/2}$, where $\tilde{h}(t) = \langle h(x,t) \rangle_x$, and $\langle\ \rangle_x$ is a spatial average in the x direction. While the *global* width $w(L,t)$ follows the Family-Vicsek (FV) dynamic scaling [2], in the anomalous scaling assumption the *local* width $w(l,t)$ follows a different scaling given by

$$w(l,t) \sim \begin{cases} t^{\beta} & \text{if} \quad t \ll l^z, \\ l^{\alpha_{loc}} t^{\beta^*} & \text{if} \quad l^z \ll t \ll L^z, \\ l^{\alpha_{loc}} L^{\alpha-\alpha_{loc}} & \text{if} \quad L^z \ll t. \end{cases} \qquad (1)$$

Here β and α are the global growth and roughness exponents respectively. z is the dynamic exponent, with $\alpha = z\beta$. $\beta^* = (\alpha - \alpha_{loc})/z$ is the local, anomalous growth exponent, and α_{loc} the local roughness exponent. The local time is given by $t_l \sim l^z$ and the saturation time by $t_\times \sim L^z$. Therefore, in the case of anomalous scaling, five scaling exponents (three of them independent) are needed to characterize the scaling behavior of the surface. It is common to define $\theta = \alpha - \alpha_{loc}$ as the *anomalous exponent*, which measures the degree of anomaly [16, 17]. When $\theta = 0$ and $\beta^* = 0$ local and global scales behave in the same way, and we recover the usual FV scaling, i.e. $w(l,t) \sim t^\beta$ for $t \ll l^z$, and $w(l,t) \sim l^\alpha$ for $t \gg l^z$.

It is common to define a scaling function for the behavior of $w(l,t)$ in the form $w(l,t)/l^\alpha = g(l/t^{1/z})$. From Eq. (1), $g(u)$ is expected to scale as

$$g(u) \sim \begin{cases} u^{-(\alpha-\alpha_{loc})} & \text{if} \quad u \ll 1, \\ u^{-\alpha} & \text{if} \quad u \gg 1. \end{cases} \qquad (2)$$

One of the implications of anomalous scaling is that the local width saturates when the system size also saturates, i.e. at times $t_\times$, and *not* at the local time t_l as occurs in FV scaling. It is also interesting to note that anomalous scaling can be identified in an experiment by plotting the local width $w(l,t)$ as a function of time for different window sizes. According to Eq. (1) the different curves would show a vertical shift proportional to $l^{\alpha_{loc}}$.

The roughness exponents are usually determined by studying the power spectrum of the interfacial fluctuations, $S(k,t) = \langle H(k,t)H(-k,t) \rangle$, where $H(k,t) = \sum_x [h(x,t) - \tilde{h}(t)] \exp(ikx)$. While in the FV assumption, the power spectrum scales as

$$S(k,t) = k^{-(2\alpha+1)} s(kt^{1/z}), \qquad (3)$$

where s is the scaling function

$$s(u) \sim \begin{cases} u^{2\alpha+1} & \text{if} \quad u \ll 1, \\ \text{const} & \text{if} \quad u \gg 1, \end{cases} \qquad (4)$$

in the anomalous scaling $s(u)$ is given by

$$s(u) \sim \begin{cases} u^{2\alpha+1} & \text{if} \quad u \ll 1, \\ u^{2\theta} & \text{if} \quad u \gg 1. \end{cases} \qquad (5)$$

For times $t \gg t_\times$ the power spectrum scales as $S(k,t) \sim k^{-(2\alpha_{loc}+1)} t^{2\theta/z}$ and not simply as $k^{-(2\alpha+1)}$ of the ordinary scaling.

In general, one differentiates between two types of anomalous scaling: *super-roughness* and *intrinsic anomalous scaling*. Super-roughness is characterized by $\alpha_{loc} = 1$ and $\alpha > 1$, although the structure factor follows the ordinary scaling given by Eqs. (3) and (4). Thus, for super-roughness, the power spectrum provides information about the global roughness exponent α. The intrinsic anomalous scaling strictly follows the scaling given by Eq. (5). This implies that the decay of the power spectrum with k only gives a measure of α_{loc}, not of α. Moreover, the particular temporal dependence of the scaling of the power spectrum allows identification of the existence of intrinsic anomalous scaling by the presence of a vertical shift of the spectral curves at different times. One has to be cautious with this particularity because the observation of a vertical shift, however, does not necessarily imply the existence of intrinsic anomalous scaling. The different forms of anomalous scaling are included in a generic dynamic scaling ansatz recently introduced by Ramasco *et al.* [20].

III. EXPERIMENTAL SET-UP AND PROCEDURE

The experimental set-up used here has been described previously in Refs. [18, 19]. The set-up consists of a horizontal Hele–Shaw cell which contains a pattern of copper tracks placed on a fiberglass substrate. The tracks are d=0.06 ± 0.01 mm high and are randomly distributed along the lateral direction x without overlap, and fill 35 % of the substrate. The lateral size of the unit track is 1.50 ± 0.04 mm, but wider tracks are obtained during design when two or more unit tracks are placed adjacently together. The separation between the fiberglass substrate and the top glass defines the gap spacing b, which was varied in the range $0.16 \le b \le 0.75$ mm. A silicone oil (Rhodorsil 47 V) is injected on one side of the cell at constant volumetric injection rate Q and displaces the air initially present. A typical example of the morphology of an interface and its temporal evolution is shown in Fig. 1 [21].

Although the disorder made by tracks (which will be called T 1.50, the numerical value indicating the width of the unit track in mm) has been the main disorder pattern used in the experiments, other disorder configurations have been employed. These configurations are characterized by a random distribution of squares with a lateral size of 1.50 or 0.40 mm, and will be called SQ 1.50 and SQ 0.40 respectively. A full description and characterization of these disorders, plus all additional details about the experimental set-up and procedure can be found in Refs. [18, 19].

IV. DATA ANALYSIS

A. Characterization of scaling

As explained in Sec. II, we have studied the roughening process of the interfaces by means of the interfacial *rms* width $w(l,t)$ and the power spectrum $S(k,t)$. The scaling of $w(l,t)$ with time provides the global (for $l = L$) and local (for $l \ll L$) growth exponents β and β^*. The exponent β^* has also been measured using an alternative scheme, proposed by López [22], in which the scaling of the mean local slopes with time is analyzed.

The local roughness exponents α_{loc} were obtained from the scaling of the power spectrum $S(k,t)$ with k. The results obtained were checked using other methods, such as the dependency of the height-height correlation function $C(l,t)$ or $W(l,t)$ on the *window* size l, in both cases scaling as $l^{\alpha_{loc}}$. Similar results to those from $S(k,t)$ were obtained within error bars.

Finally, within the framework of intrinsic anomalous scaling, the only direct way to measure the global roughness exponents α, and in addition $z = \alpha/\beta$, is to study the scaling of $C(L,t)$ or $w(L,t)$ with the *system* size L. Both quantities scale as L^{α}. Because it is not practical to perform experiments by varying the system size, we have not measured global roughness exponents directly. Instead, they have been obtained from the collapse of $S(k,t)$ or $w(l,t)$. Note that information about the value of α is contained in both the vertical displacement of the spectral curves with time (Eqs. (3) and (5)) and the vertical shift of the $w(l,t)$ curves for different window sizes (Eq. (1)). The error bars that we give in the final numerical value of a particular scaling exponent take into account the various methods of analysis and the error in the different collapses.

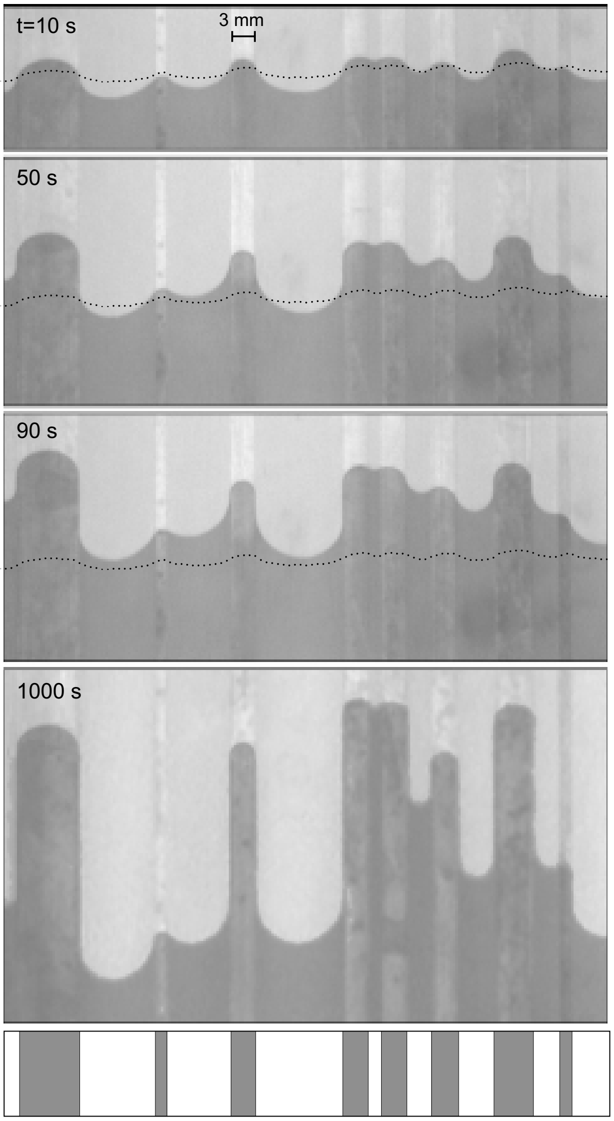

FIG. 1: Close-up views of the oil–air interface with disorder T 1.50. The first three pictures are early stages, while the last photo corresponds to saturation. The position of the copper tracks is shown in the lower box. The dotted line shows the position and shape of the interface profile at $t = 0$ s. The experimental parameters are $v = 0.08$ mm/s, $b = 0.36$ mm.

B. Side wall effects

The profile $h(x,t)$, obtained from the analysis of the images, contains 515 points corresponding to a lateral size of 190 mm. Because the oil tends to advance along the side walls of the cell, we have a distortion of the front that penetrates a distance p from each side wall. This penetration length depends on the average interface velocity and is especially sensitive to variations in gap spacing. An example is presented in Fig. 2(a), which shows the effect of the distortion on an interface with experimental parameters $v = 0.08$ mm/s, $b = 0.75$ mm and disorder SQ 1.50.

To evaluate the effect of the distortion, we have measured the penetration length p at different gap spacings b for two disorder configurations, SQ 1.50 and T 1.50.

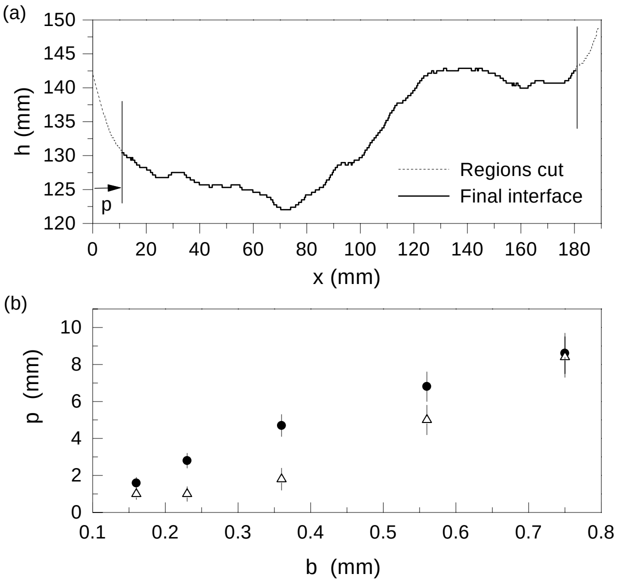

FIG. 2: (a) Example of an interface with strong side wall distortions. The dashed lines represent the regions cut at the end of the interface, and the solid line the interface finally studied. The experimental parameters are $v = 0.08$ mm/s, $b = 0.75$ mm and disorder SQ 1.50. (b) Penetration length p as a function of the gap spacing b for SQ 1.50 (dots) and T 1.50 (triangles).

The penetration length is measured at short times, when the interface is globally flat except at the side walls. Fitting a straight line to the central region of the interface enables us to determine p as the distance between the side wall and the point where the interface deviates from the straight line. The results for the two disorder configurations analyzed are presented in Fig. 2(b), and show that p increases quickly with gap spacing. For $b = 0.75$ mm, the largest value studied, p is about 8 mm. Notice also that the presence of columnar disorder significantly reduces the effect of the distortion for the smallest gap spacings. To minimize the effect of the distortion, we have cut 8 mm from both ends of all interfaces, as shown in Fig. 2(a), reducing them to a final lateral size of 174 mm containing 470 pixels, which gives a spatial resolution of $\Delta x = 0.37$ mm.

C. Data treatment

For data analysis convenience (particularly in the computation of the power spectrum), we have extended the number of points to $N = 512$ using linear interpolation, which gives a final spatial resolution of $\Delta x = 0.34$ mm. We verified that the interpolation does not vary our results.

Because the initial stages of roughening are so fast, the interface profile at $t = 0$ s is not a flat interface, but a profile with an initial roughness $w(0)$, as can be observed in Fig. 1 (dotted line). This roughness, on one hand, does not enable observation of the growth of the small scales at short times; on the other hand, $w(0)$ changes from one disorder configuration to another, which makes the early stages strongly dependent on the particular disorder realization. To eliminate these effects, we will always plot the *subtracted width* $W(l,t)$, defined as $W(l,t) = \langle w^2(l,t) - w^2(l,0)\rangle^{1/2}$, where the brackets indicate average over disorder realizations. This correction is a standard procedure in the field of growing interfaces, and is reported in both experiments and numerical simulations [1, 13, 23].

The final treatment we use is to enforce periodic boundary conditions by subtracting the straight line that connects the two ends of the interface. This procedure, well documented in the literature on kinetic roughening [24], eliminates an artificial overall slope -2 in the power spectrum due to the discontinuity at the two ends [25].

V. EXPERIMENTAL RESULTS AND ANALYSIS

A. Evidence of anomalous scaling

The first evidence of anomalous scaling in these experiments was presented in our previous work [19] and corresponded to the experimental parameters $v = 0.08$ mm/s and $b = 0.36$ mm. The global and local growth exponents, measured from $W(l,t)$, were $\beta = 0.52 \pm 0.02$ (corresponding to $l = L$) and $\beta^* = 0.26 \pm 0.03$ (for $l = L/256$). The fact that β^* is clearly different from zero is robust evidence of anomalous scaling. We also studied the evolution of the power spectrum, which gave two clear power law dependences, at short times with slope -3.4 ± 0.1, and at saturation with slope -2.1 ± 0.1. The former was a transient regime, whose origin is the strong dominance of the capillary forces at very short times. The latter provided the local roughness exponent, $\alpha_{loc} = 0.55 \pm 0.10$.

Here we consider an alternative analysis that completes those presented in Ref. [19] and provide alternative ways to confirm the existence of anomalous scaling.

To check the reliability of the exponent β^* we have studied the scaling of the mean local slopes with time, $\rho(t) = [\overline{\langle(\nabla h)^2\rangle_x}]^{1/2}$, where the brackets denote a spatial average along x and the overbar denotes average over disorder configurations. Usually $\rho(t)$ scales with time as $\rho(t) \sim t^{\kappa}$, with $\kappa < 0$ for the ordinary scaling and $\kappa > 0$ for anomalous scaling. In this last case, κ is identified with the local growth exponent β^*. The result, presented in Fig. 3, is $\beta^* = 0.30 \pm 0.05$, in good agreement with the result of β^* using $W(l = L/256, t)$.

The values of α and z were obtained in Ref. [19] by plotting $S(k,t)k^{2\alpha+1}$ as a function of $kt^{1/z}$. This collapse refined the numerical values of the experimental results

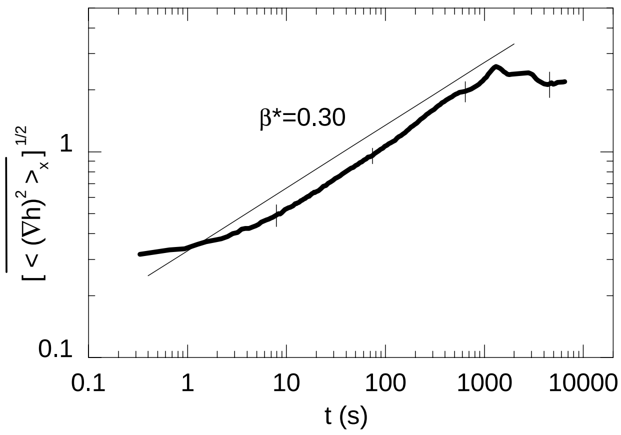

FIG. 3: Analysis of the mean local slopes as a function of time. The experimental parameters are $v = 0.08$ mm/s, $b = 0.36$ mm and disorder T 1.50.

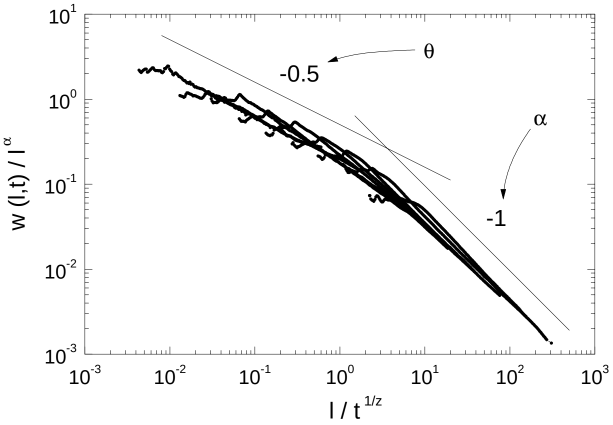

FIG. 4: Collapse of the $W(l, t)$ plots using the scaling function of Eq. (2). The experimental parameters are $v = 0.08$ mm/s, $b = 0.36$ mm and disorder T 1.50.

and gave

$$\beta = 0.50 \pm 0.04,\ \beta^* = 0.25 \pm 0.03,$$
$$\alpha = 1.0 \pm 0.1,\ \alpha_{loc} = 0.5 \pm 0.1,\ z = 2.0 \pm 0.2. \quad (6)$$

Here, the exponents θ and α have also been determined by means of the scaling function defined in Eq. (2). This collapse, shown in Fig. 4, gives $\theta = \alpha - \alpha_{loc} = 0.5$ and $\alpha = 1$.

The presence of anomalous scaling can also be identified by checking for multiscaling [4]. For this purpose, we have studied the scaling of the generalized correlations of order q, of the form $C_q(l) =$

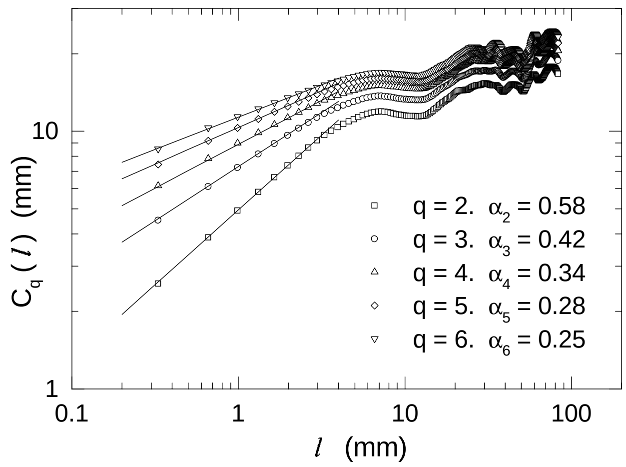

FIG. 5: Multiscaling analysis through the computation of the q–order height-height correlation function for interfaces at saturation. The experimental parameters are $v = 0.08$ mm/s, $b = 0.36$ mm and disorder T 1.50.

$\{(h(x + l, t) - h(x, t))^q\}^{1/q} \sim l^{\alpha_q}$, where α_q are local roughness exponents. The results obtained are shown in Fig. 5, which gives the values of α_q at different orders q. We obtain a progressive decrease of the measured exponent, varying from $\alpha_2 \simeq 0.58$ to $\alpha_6 \simeq 0.25$, which confirms the existence of multiscaling in the experiment and, therefore, of anomalous scaling.

B. Experimental range of anomalous scaling

Once the existence of anomalous scaling is well characterized for a specific set of experimental parameters, we are now interested in analyzing the range of validity of the anomaly. We have performed a series of experiments by varying v and fixing the gap spacing to $b = 0.36$ mm together with a series of experiments varying b and fixing the average interface velocity to $v = 0.08$ mm/s. As we can identify the existence of anomalous scaling by looking at the behavior of the smallest scales, i.e. the existence of a $\beta^* \neq 0$, we present the results by plotting the local growth exponent β^* for the different experiments.

1. *Interface velocity*

The results of β^* at different v are presented in Fig. 6. For a wide range of interface velocities, from V to $10\,V$, where $V = 0.04$ mm/s is the minimum velocity investigated and will be used as a reference velocity, the measured exponent β^* is not very sensitive to changes in the velocity and it varies from 0.35 ± 0.04 for velocity V to

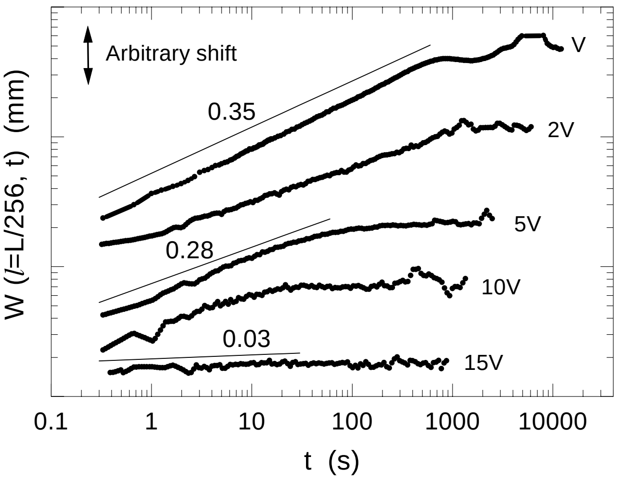

FIG. 6: W(l,t) curves for a window size $l = L/256$ and different interface velocities. The gap spacing is $b = 0.36$ mm and the disorder T 1.50 in all cases. $V = 0.04$ mm/s. The curves are vertically shifted for clarity.

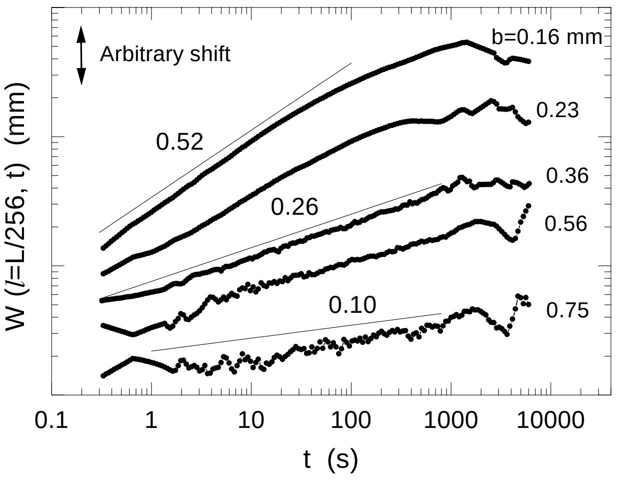

FIG. 7: W(l,t) curves for a window size $l = L/256$ and different gap spacings. The interface velocity is $v = 2V = 0.08$ mm/s and the disorder T 1.50 in all cases. The curves are vertically shifted for clarity.

0.28 ± 0.04 for velocity $10\,V$. For velocities $v \gtrsim 15V$, however, the measured value of β^* quickly decays to a value close to zero, indicating that above a threshold velocity (about $13V$ for $b = 0.36$ mm) the anomaly disappears.

In terms of the power spectrum, when the velocity is varied from V to $15V$ we always observe a vertical shift of the spectral curves, and the power spectrum at different times can be collapsed to obtain the set of scaling exponents. Above the threshold velocity the power spectrum follows ordinary scaling, i.e. without vertical displacement.

2. Gap spacing

The results of β^* at different b are presented in Fig. 7. It is clear from the different plots that the exponent β^* is rather sensitive to variations of the gap spacing. Three different behaviors can be observed: i) For *small* values of b ($b = 0.16$ mm), where capillary forces are dominant, we obtain $\beta^* = 0.52 \pm 0.04$, which is identical to the corresponding value of β. This similitude is discussed in Sec. V E. ii) For *intermediate* values of b (in the range $0.23 \leq b \leq 0.56$ mm) we obtain values of β^* that vary from 0.35 ± 0.05 for $b = 0.23$ mm to 0.25 ± 0.04 for $b = 0.56$ mm. This range of gap spacings is characterized by strong (but not dominant) capillary forces, and is the region where the anomalous scaling can be fully characterized. iii) For *large* values of b ($b \gtrsim 0.60$ mm) we obtain $\beta^* = 0.10 \pm 0.04$ for $b = 0.75$ mm, and β^* nearly zero for larger gap spacings. In this regime capillary forces are not sufficiently strong, and the anomalous scaling disappears. The analysis of β^* through the scaling of the mean local slopes has given identical results within error bars, although the sensitivity of this analysis to short–time transients makes it less reliable.

As regards the power spectrum, in the range $0.23 \leq b \leq 0.56$, the vertical shift of the spectral curves is present, and a regime characterized by anomalous scaling can be described. For $b = 0.16$ mm, although the spectral curves are vertically shifted, a scaling regime cannot be identified. The power spectra can be collapsed, but reliable α, α_{loc}, and z exponents cannot be obtained. For $b \gtrsim 0.60$ mm, a vertical shift in the power spectra is not observed, and the scaling of the interfacial fluctuations is best described within the framework of FV ordinary scaling.

3. Disorder properties

Other modifications carried out to study the range of validity of the anomalous scaling are the track width and the persistence of the disorder along the growth direction. Fig. 8 shows the variation of the local interfacial fluctuations for four different disorder configurations. The gap spacing and velocity have been fixed to $b = 0.36$ mm and $v = 2V$ respectively. For T 0.40 we obtain a similar result to that obtained with T 1.50, and $\beta^* = 0.29 \pm 0.05$ was measured. However, there is evidence that the anomaly decreases as the width of the basic track is reduced, and it disappears when the width of the basic track is $\lesssim 0.20$ mm due to the fact that the in–plane curvature of the copper track becomes similar to the curvature of the

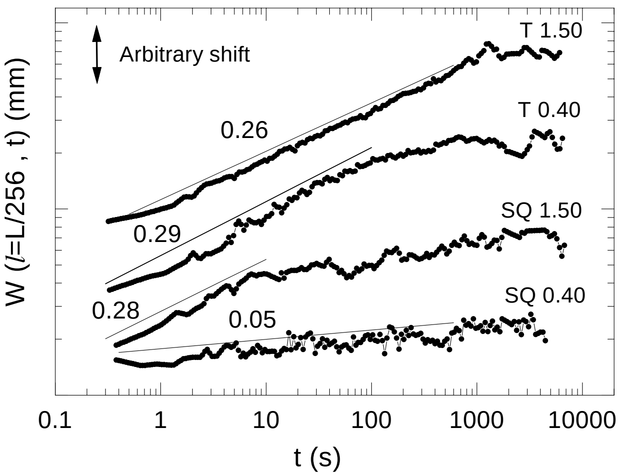

FIG. 8: W(l,t) curves for a window size $l = L/256$ and different disorder configurations with progressively shorter persistence in the growth direction. $b = 0.36$ mm and $v = 2V = 0.08$ mm/s in all cases. The curves are vertically shifted for clarity.

meniscus in the z direction.

Now different disorder configurations with progressively smaller persistence in the growth direction are examined. For SQ 1.50, although the saturation time for the full system is at $t_\times \simeq 1000$ s, we observe that the local interfacial fluctuations saturate at a much shorter time, which is more characteristic of ordinary scaling. However, we still observe traces of anomalous scaling at earlier times, for which $\beta^* = 0.28 \pm 0.04$. This is really not very surprising if we take into account the fact that, for this disorder, the first array of squares is equivalent to T 1.50, but is only 1.50 mm long. Thus, at very short times, the growth follows the same behavior as tracks. With a driving velocity 0.08 mm/s, the interface takes about $10 - 20$ s to cross the first array of squares, which is the same time interval for which the anomalous scaling is observed. For SQ 0.40, with $t_\times \simeq 300$ s, we measure $\beta^* = 0.05 \pm 0.04$, indicative of the absence of anomalous scaling.

4. Characterization by the statistical distribution of height differences

We have also considered an alternative analysis to confirm the results of anomalous scaling. In a recent work, Asikainen *et al.* [26] showed that the presence of anomalous scaling can be associated with the presence of multiscaling, on one hand, and to high jumps in the morphology of the interfaces on the other. According to these authors, the distribution function of the height differences, $P(\Delta h)$, with $\Delta h \equiv |h(x_{i+1}) - h(x_i)|$, scales following a Lévy distribution, $P(\Delta h) \sim \Delta h^{-\gamma}$, where $0 < \gamma < 2$; while for ordinary scaling $P(\Delta h)$ follows a Gaussian distribution. We have checked this prediction with our experimental results. Fig. 9(a) compares the shape of three different interfaces with different degrees of anomalous scaling. In all cases $v = 2V$ and $b = 0.36$ mm. All the interfaces are in the saturation regime. For T 1.50 (the most representative case of anomalous scaling) the interface presents high jumps at the edges of the copper tracks. For T 0.40 some regions present high jumps, but in general the interface looks smoother. This case shows anomalous scaling, but the degree of the anomaly is much weaker than the previous case. For SQ 1.50 the interface is very smooth and the interfacial fluctuations are best described with the FV scaling, with only traces of anomalous scaling at very short times. The interfaces in these three cases are similar to those reported in fracture of wood by Engøy *et al.* in Fig. 1 of Ref. [12]. In particular, the interfaces for T 1.50 or T 0.40 look like interfaces obtained from tangential fracture in wood; both are characterized by high jumps and anomalous scaling. Along the same lines, the interfaces for SQ 1.50 are similar to those obtained from radial fracture. These similarities indicate that the role of the wood fibres is probably equivalent to the role of the copper tracks in our system as the origin of the anomalous scaling.

The distribution functions $P(\Delta h)$ for the different interface morphologies are shown in Fig. 9(b) and (c). For T 1.50 we have two different regimes. Up to $\Delta h \simeq 2$ mm (dashed line in the plot) we have the contribution of the height differences corresponding to the structure within tracks. For $\Delta h > 2$ mm (solid line), the contribution to the distribution function arises from the edges of the tracks. This latter contribution is responsible for the anomalous scaling, and scales with Δh with an exponent 0.6 ± 0.1. A similar result is observed for T 0.40. In this case, if we do not consider the contribution of the structure inside tracks (up to 1 mm), we obtain a power law dependency with exponent 2.0 ± 0.2. The fact that the anomaly is weaker for T 0.40 compared with T 1.50 is illustrated in this case by the larger value of the slope. If we compare the distribution functions of T 1.50 and SQ 1.50 we observe that, in the latter case, there is only a contribution from small height differences. In this case $P(\Delta h)$ would scale with an exponent 3.6, far from the values expected for anomalous scaling.

C. Experiments at Q=0

The previous results indicate that a more detailed study on the role of capillary forces at the disorder scale has to be carried out in order to understand the origin of the anomalous scaling. For this reason we have performed experiments at $Q = 0$, where interfacial growth is driven solely by capillary forces.

The experiments at $Q = 0$ were performed by initially

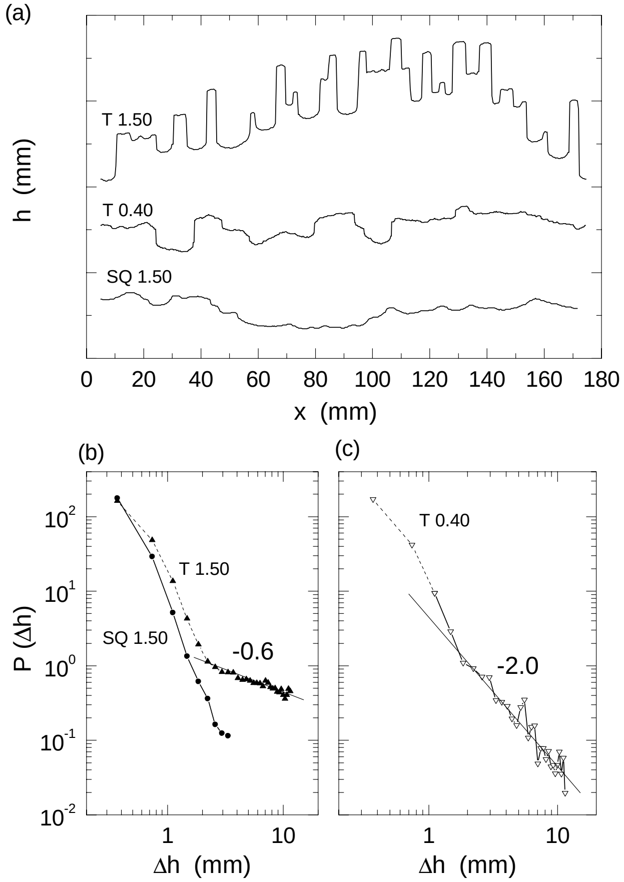

FIG. 9: (a) Samples of interfaces for different disorder configurations and identical experimental parameters $v = 2V = 0.08$ mm/s and $b = 0.36$ mm. (b) Distribution function $P(\Delta h)$, with $\Delta h \equiv |h(x_{i+1}) - h(x_i)|$, for local height differences, comparing T 1.50 and SQ 1.50. (c) The same for T 0.40. See text for details of the power law fits.

driving the interface at high velocity up to the center of the cell. The injection is then stopped and the experiment started. We studied five gap spacings, in the range $0.16 \le b \le 0.75$ mm, and characterized the interface velocity on copper tracks and fiberglass channels. For small gap spacings, up to $b \simeq 0.36$ mm, the morphology of the interface adopts a finger–like configuration, which ultimately causes the interface to pinch–off at long time intervals. For this reason we have reduced the duration of the experiments to 1500 s for all gap spacings.

Fig. 10 shows a comparison of the interfaces at $t = 500$ s with different gap spacings. The horizontal line represents the average position of the interface at $t = 0$. For $b = 0.16$ mm the points of the interface on the different tracks move almost independently, with weak coupling between neighboring tracks: the oil on copper tracks always advances, while the oil on fiberglass channels, except for some particular locations, always recedes, driven by the different capillary forces associated with the different curvature of the menisci on copper tracks and the fiberglass substrate. As we increase the gap spacing, the coupling in the motion of the interface tips on copper tracks with neighboring tracks is progressively more intense. For $b = 0.36$ mm the advance on a specific copper track is coupled with its neighbors. The oil advances or recedes in a given track or channel depending on the particular disorder realization. Only the widest copper tracks or fiberglass channels have an independent motion. For $b = 0.56$ mm the coupling reaches larger regions of the cell, and for $b = 0.75$ the capillary forces are no longer sufficient to allow a large deformation of the interface.

It is also noticeable that the average position of the interface does not remain at rest. Indeed, it advances in the same direction as the oil on the copper tracks. This is a consequence of the three-dimensional nature of the experiment. The total mass of fluid in the cell is conserved, but not the area measured on the images. However, the measured velocity of the advance of the interface is very low. For $b = 0.36$ mm, for example, the velocity is about $V/10$.

The first analysis that we have performed with the experiments at $Q = 0$ is to study the growth of interfacial fluctuations with time. Fig. 11(a) shows the $W(L,t)$ curves for four different gap spacings. We observe power laws with a growth exponent β that decreases from 0.65±0.04 for $b = 0.16$ mm to 0.50±0.04 for $b = 0.75$ mm. Clearly, when the capillary forces are sufficiently strong to allow for both the advance of the oil on the copper tracks and the recession of the oil on the fiberglass channels, we obtain a larger value of the growth exponent than in all other cases. A similar behavior is observed for β^*, which varies from 0.65±0.04 for $b = 0.16$ mm to 0.15 ± 0.05 for $b = 0.75$ mm.

As regards the behavior of the power spectrum, shown in Fig. 11(b), the fact that the experiments do not reach a saturation regime makes the analysis of the power spectrum incomplete. Qualitatively, we have observed a vertical shift of the spectral curves as time increases for gap spacings up to $b = 0.56$ mm. For $b = 0.75$ mm the vertical shift is not present, confirming the absence of anomalous scaling for values of $b \ge 0.60$ mm for any interface velocity. At long times we have measured local roughness exponents that vary from $\alpha_{loc} = 0.6 \pm 0.1$ for $b = 0.36$ mm to $\alpha_{loc} = 0.9 \pm 0.1$ for $b = 0.75$ mm. For $b = 0.16$ mm no clear scaling can be identified.

The second analysis that we have performed has been a detailed study of the motion of the interface on copper tracks or fiberglass channels separately. In Fig. 12 we represent $\langle h \rangle_T$, the mean height for those points of the interface that are advancing on copper tracks, as a function of time. For gap spacings in the range $0.16 \le b \le 0.36$ mm, $\langle h \rangle_T$ is a power law of time with an exponent 0.50 ± 0.03. For larger gap spacings, the exponent is progressively smaller and the power law regime is only identifiable at

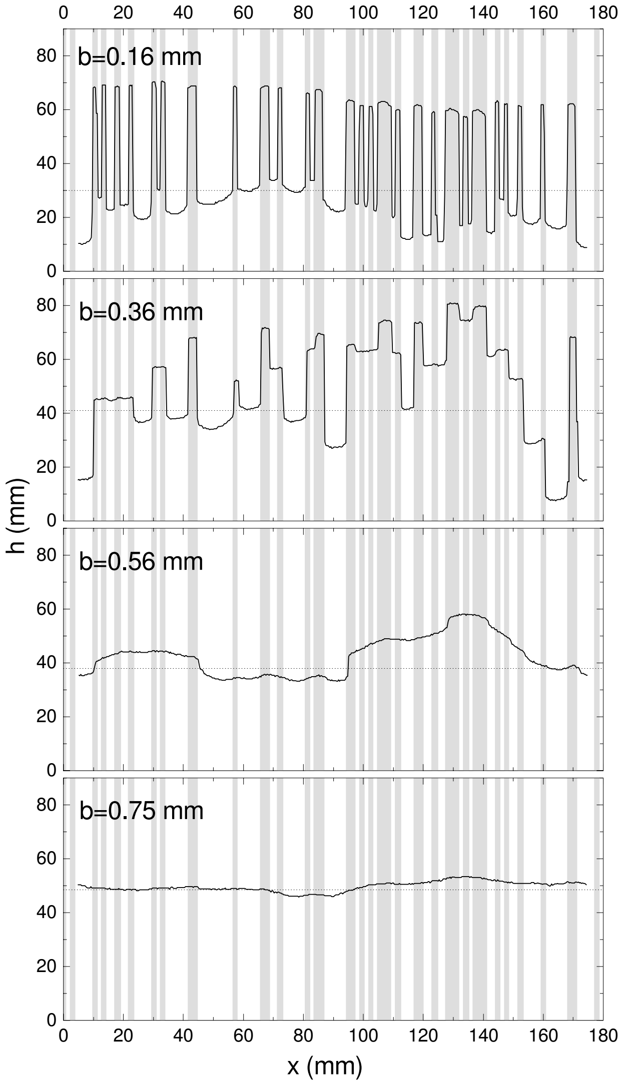

FIG. 10: Example of interfaces at $Q = 0$ with different gap spacings and disorder T 1.50. All the interfaces correspond to $t = 500$ s. The horizontal dotted line indicates the position of the interface at $t = 0$ s.

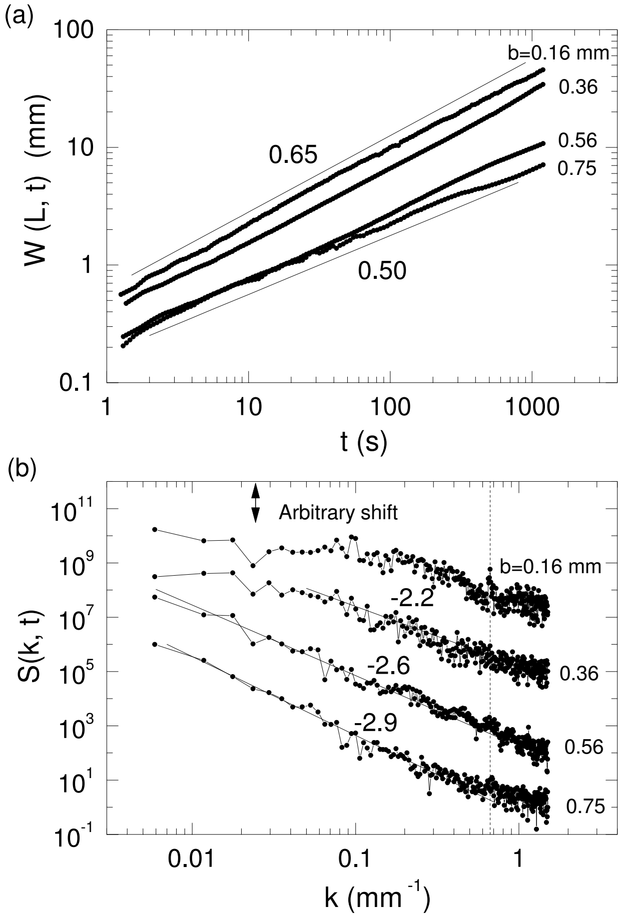

FIG. 11: Experimental results for $Q = 0$ at four different gap spacings and disorder T 1.50. (a) Interfacial width $W(L, t)$. The straight line with slope 0.65 corresponds to a fit of the experiments with $b = 0.16$ mm and 0.36 mm. The straight line with slope 0.50 is a fit to the experiment with $b = 0.75$ mm. Each curve is an average over two disorder realizations, with two runs per disorder realization. (b) Power spectra $S(k, t)$ at $t = 1000$ s. The curves have been shifted in the vertical direction for clarity. The vertical line gives the value of k associated with the spatial scale of the disorder.

short times. A similar analysis can be carried out for the fiberglass channels. In this case we obtain the same behavior in the range $0.16 \leq b \leq 0.36$ mm, with an exponent 0.50 ± 0.03. For $b \geq 0.56$ mm no clear scaling can be identified.

Finally, we have also studied the motion on individual tracks in order to find out the role of track width D. The results are shown in Fig. 13. A track is *uncoupled* when the motion of the interface tip on the track grows as $h \sim t^{0.5}$ independently of its neighbors' configuration. Conversely, the interface motion over a *coupled* track depends on the particular location of this track in the disorder realization, and the behavior $h \sim t^{0.5}$ is not observable or cannot be characterized at all times. The behavior of coupled tracks is illustrated in Figs. 14(a) and 14(b), which show two examples for $D = 1.5$ mm and $D = 3.0$ mm respectively. In both cases $b = 0.36$ mm. These figures show that two tracks of the same width present different growth depending on their neighbors' configuration. While the uncoupled track grows as $h \sim t^{0.5}$, the coupled track follows the same behavior only at short times and afterwards reaches a station-

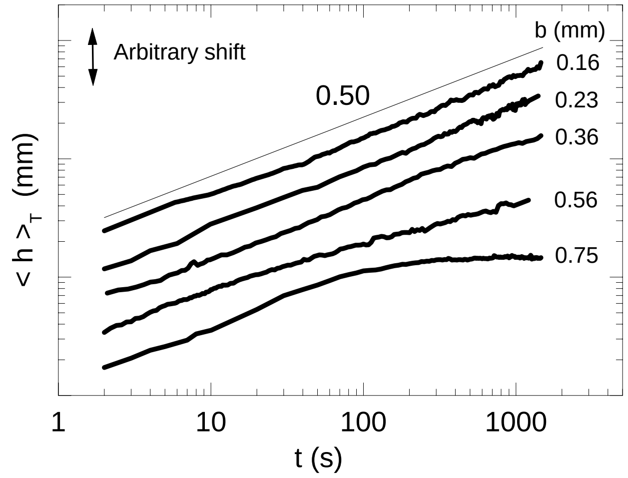

FIG. 12: Log-log plot of the average height as a function of time for the interface points advancing on copper tracks, for different gap spacings and disorder T 1.50. $Q = 0$ in all cases. The curves are vertically shifted for clarity.

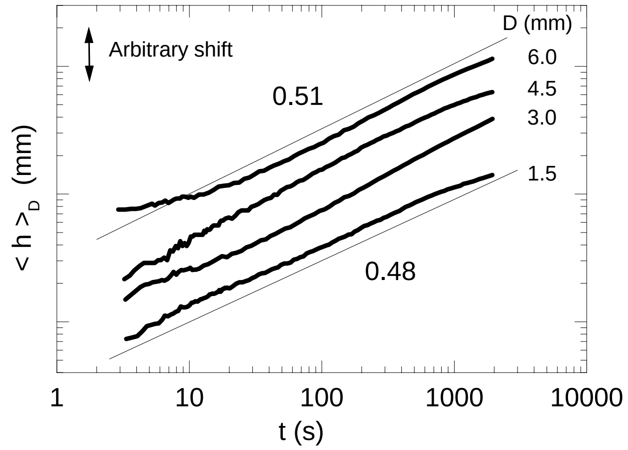

FIG. 13: Log-log plot of the average height as a function of time for the interface points advancing on uncoupled copper tracks of a specific width D. The experimental parameters are $Q = 0$, $b = 0.36$ mm, and disorder T 1.50. The curves are vertically shifted for clarity.

ary height. A comparison of Figs. 14(a) and 14(b) also shows that the wider the track, the weaker the coupling. The widest tracks in a given disorder realization and for $b \leq 0.36$ mm remain uncoupled during all the experiment. In addition, for small gap spacings, $b \leq 0.16$ mm, all tracks are uncoupled.

From these studies we conclude that it is possible to

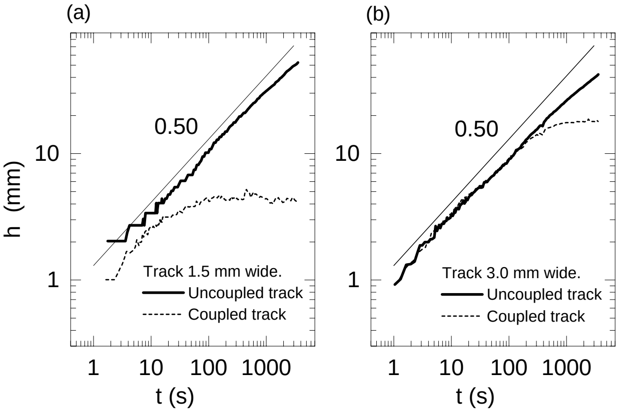

FIG. 14: Log-log plot of the average height as a function of time for the interface points advancing on a copper track of a specific width D. (a) $D = 1.5$ mm. (b) $D = 3.0$ mm. In the two cases $Q = 0$ and $b = 0.36$ mm.

describe the interface motion on a single copper track, v_{+}^{i}, or fiberglass channel, v_{-}^{i}, by the simple law

$$v_{\pm}^{i}(t) = \pm\, A_{\pm}^{i}(b, D_{\pm}^{i})\; t^{-1/2} \qquad \text{for} \qquad t \geqslant 1 \text{ s}, \qquad (7)$$

where $A_{\pm}^{i}(b, D_{\pm}^{i})$ is a positive prefactor that depends on the gap spacing b and the individual copper track or fiberglass channel width D^{i}. In general A^{i} increases with D^{i} and decreases with b. Averaging out the prefactor $A_{\pm}^{i}$ over different track or channel widths we obtain a characteristic maximum velocity $v_{M\pm}$ for a given gap spacing. Eq. (7) now becomes

$$v_{\pm}(t) = \pm\, v_{M\pm}(b)\; t^{-1/2} \qquad \text{for} \qquad t \geqslant 1 \text{ s}. \qquad (8)$$

Our experimental observations show that Eq. (8) is valid for gap spacings in the range $0.16 \leq b \leq 0.36$ mm. For $b \geq 0.56$ mm Eq. (8) only holds for copper tracks and at short times. The temporal range in which this behavior is observed goes to zero as the capillary forces become weaker.

In general $v_{M_{+}} > v_{M_{-}}$ due to the different gap spacing in copper tracks and in fiberglass channels. This difference, however, is progressively smaller as b increases. For gap spacings around $b = 0.36$ mm, it is reasonable to consider $v_{M_{+}} \simeq v_{M_{-}} \equiv v_{M}$. The time $t = 1$ s, determined from systematic experimental observations, is a typical time in which the velocity jumps from the average interface velocity out of the disorder to v_{M} inside the disorder.

D. From $Q = 0$ to low injection rates

Eq. (8) gives the velocity on copper tracks or fiberglass channels when $Q = 0$ (no injection). In the presence of injection, when the interface is driven at an average interface velocity $v \neq 0$, the behavior observed experimentally is modified in the form

$$v_{\pm}(t) = v \pm (v_M - v)\, t^{-1/2}, \tag{9}$$

where $v_M = v_M(b)$ and v_+ and v_- are the velocities averaged over copper tracks and fiberglass channels respectively. Thus, when the interface makes contact with the disorder, the velocity on copper tracks jumps to a maximum v_M in a characteristic time of 1 s and then relaxes as $t^{-1/2}$ to the nominal velocity. In fiberglass channels, the velocity is zero or even negative at short times, and as time goes on, the velocity increases until it reaches the nominal velocity at long times. Fig. 1 illustrates this behavior. At short times, $t \simeq 10$ s, all the oil on copper tracks advances, while the oil in the widest fiberglass channel recedes. At $t \simeq 50$ s the oil in fiberglass channels has stopped receding. At later times, the velocity at different points of the interface tends asymptotically to the nominal velocity, reached at saturation.

At low injection rates, the external velocity v can be tuned appropriately to have an initial regime in which the oil advances on copper tracks and recedes on fiberglass channels, followed by a regime in which the oil advances at all points of the interface. This leads to two scaling regimes for $W(L,t)$, at short times with a growth exponent $\beta \simeq 0.65$, which corresponds to a regime dominated by strong capillary forces, and at longer times with a growth exponent $\beta \simeq 0.50$, which corresponds to a regime where capillary and viscous forces are better balanced. We have illustrated this behavior by performing experiments at low v. In particular, we have studied velocities $V/2$ and $V/10$ using a gap spacing $b = 0.36$ mm and disorder T 1.50. The results are presented in Fig. 15. The difficulty of these experiments is that the interface pinches–off on the longest fingers before it reaches saturation, so we can only find out the growth regime. For $V/2$ we observe the two power law regimes described above. For $V/10$, only the first regime can be observed before the interface breaks. These results are qualitatively in agreement with the analysis of Hernández-Machado *et al.* [27], who predicted two scaling regimes, $\beta_1 = 5/6$ at short times (surface tension in the plane dominant) and $\beta_2 = 1/2$ at long times (viscous pressure dominant). However, the presence of anomalous scaling and the complicated role of capillary forces in our experiments makes a direct comparison with Ref. [27] difficult.

Another result than can be obtained from Eq. (9) is a prediction for the saturation time $t_\times$ as a function of the average interface velocity v. We can estimate $t_\times$ for a given v and gap spacing b by considering that saturation takes place when all tracks reach the nominal velocity v. This is not strictly exact due to the coupling between neighboring tracks, but it gives a good estimate of the dependency $t_\times(v)$, as shown in Fig. 16. For a given experiment with velocity $v < v_M$ the saturation takes place when the function $v_M\, t^{-1/2}$ crosses the nominal velocity. Thus, as shown in the inset of the figure, $t_\times$ is expected to scale as $t_\times \sim v^{-2}$. This result is confirmed by our experiments with disorder T 1.50 and $b = 0.36$ mm (open triangles in the inset).

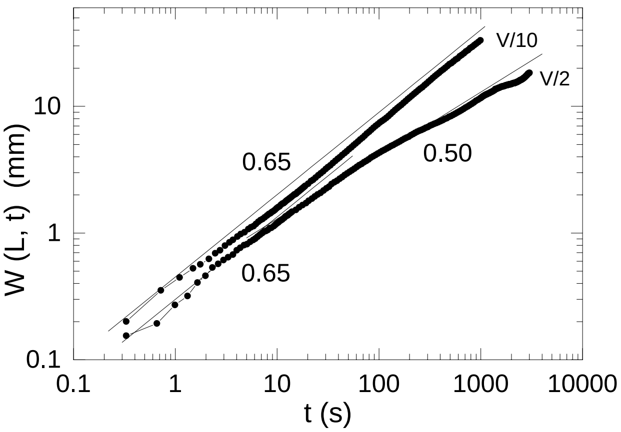

FIG. 15: log-log plot of $W(L,t)$ for experiments at low velocity with disorder T 1.50. The end of the experiments is the moment at which the interfaces pinch–off. The gap spacing is $b = 0.36$ mm in both cases, and $V = 0.04$ mm/s. Each curve is an average over two disorder configurations, with one run per disorder configuration.

E. Experiments with a regular modulation of the gap spacing

In order to analyze the importance of the coupling between neighboring tracks, we have performed experiments with a regular modulation of the gap spacing, consisting of copper tracks 6 mm wide separated by fiberglass channels 6 mm wide. Interface velocity and gap spacing are set to $v = 0.08$ mm/s and $b = 0.36$ mm respectively. The regular modulation and the temporal evolution of the resulting interfaces are presented in Fig. 17(a). Due to the symmetry of the regular pattern there is no growing correlation length along the direction of the interface. For this reason, a dynamic scaling of the interfacial fluctuations cannot even be defined. The growth of the interfacial width is due to the independent, equivalent growth of interface fingers on copper tracks, whose motion follow the $t^{-1/2}$ behavior (Eq. 9). The system saturates when the fingers reach the nominal velocity. This is shown in Fig. 17(b), which shows the evolution of $W(l,t)$ for the global ($l = L$) and local ($l = L/256$) scales. The figure reveals that both scales grow in the same way. The absence of dynamic scaling is also confirmed by the power spectrum, shown in Fig. 17(c). We obtain a nearly flat spectrum, with a large peak at the value of k that corresponds to the spatial periodicity of the underlying regular pattern. We also observe a vertical shift of the spectra

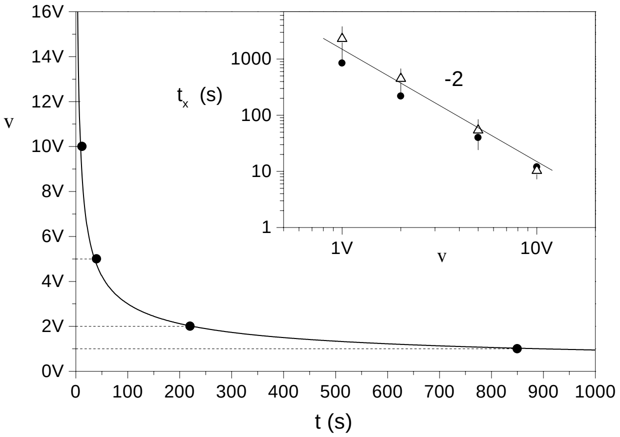

FIG. 16: Prediction of the dependency of $t_\times$ with v. Main plot: for a given average velocity v, the system saturates when the average velocity on copper tracks decays to v. Inset: a log-log plot of the $t_\times$ obtained by the previous method (filled dots) as a function of v gives a straight line with slope -2. The triangles are the experimental results for T 1.50 and $b = 0.36$ mm.

at different times, caused by the progressive elongation of the oil fingers on copper tracks during growth.

These experiments with regular modulation of the gap spacing illustrate the need for a growing correlation length along the interface to reach a dynamic scaling regime. In a similar way to these experiments, the lateral growth of the correlation length can also be inhibited even if the modulation of the gap spacing is random, provided that the experimental parameters are such that the interface motion on the tracks is not coupled and that Eq. (9) holds for each track. Thus, for very small gap spacings ($b \leq 0.16$ mm) and $v \geq V$ we observe a growth of the interfacial width with exponent $\simeq 0.5$ for both global and local scales. Similarly, in the experiments at $Q = 0$ with $b = 0.16$ mm the same exponent $\simeq 0.65$ is measured for both global and local scales. The power spectrum of this last case also demonstrates the lack of dynamic scaling, as can be seen in the top plot of Fig. 11(b). When the modulation of the gap spacing is regular, the transition to saturation is sharp due to the fact that all tracks have the same width, and thus all the oil fingers reach the nominal velocity at the same time. For a random pattern the transition to saturation is smooth, and does not take place strictly until the widest copper tracks (those that have the highest value of A^i_+) reach the nominal velocity. The plot for $b = 0.16$ mm of Fig. 7 illustrates this behavior.

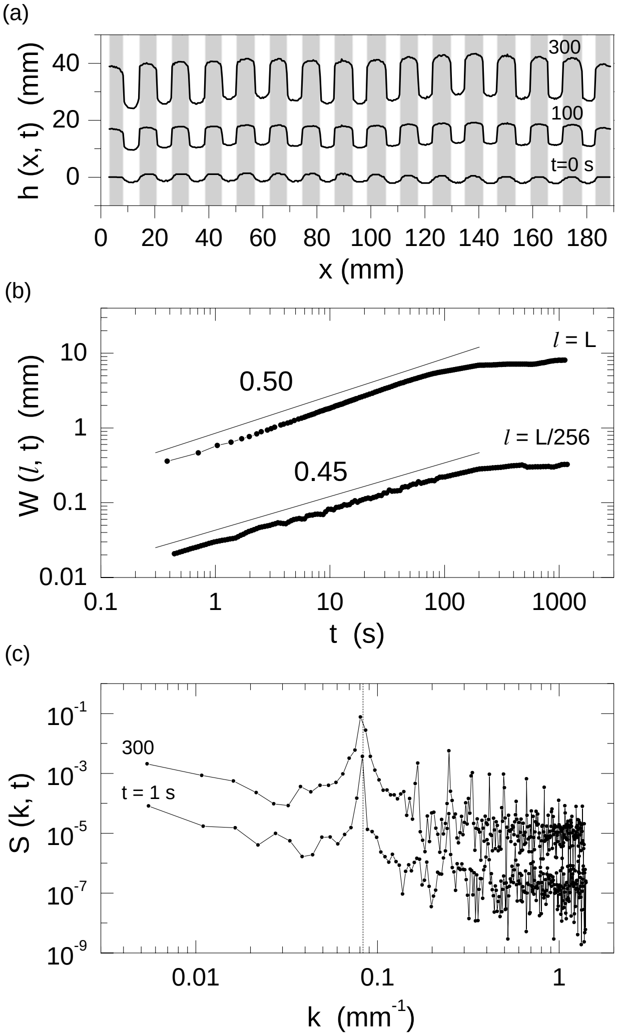

FIG. 17: Experiments with a regular modulation of the gap spacing, using tracks 6 mm wide. The experimental parameters are $v = 2V = 0.08$ mm/s and $b = 0.36$ mm. (a) Temporal evolution of the interfaces. (b) $W(l, t)$ plots for global ($l = L$) and local ($l = L/256$) scales. (c) Power spectrum at $t = 300$ s. The vertical line indicates the values of k corresponding to the spatial periodicity of the regular pattern.

VI. DISCUSSION AND CONCLUSIONS

Our experimental results show that two ingredients are necessary to observe anomalous scaling in a disordered Hele–Shaw cell: i) strong destabilizing capillary forces, sufficiently persistent in the direction of growth, and ii) coupling in the interface motion between neighboring tracks. These two ingredients give rise to large slopes at the track edges together with a growing correlation length along the interface. This scenario is repre-

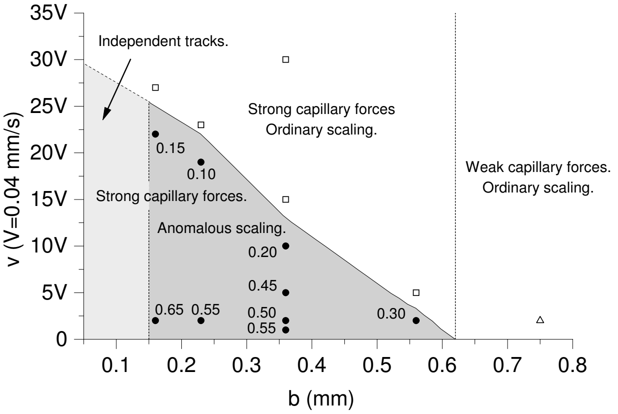

FIG. 18: Phase diagram for the anomalous scaling. The symbols indicate the parameters explored experimentally. The numbers next to the symbols in the anomalous scaling region give the value of $2\theta/z$. The solid line represents the curve $v = v_M(b)$.

sented in the phase diagram of Fig. 18, which shows the different regions of scaling explored experimentally. Each point of the diagram is an average of 6 experiments (3 disorder configurations and 2 runs per disorder configuration). The dark grey area represents the region where anomalous scaling has been identified. We have indicated the value of $2\theta/z$, which is the value needed to vertically collapse the spectral curves and, therefore, indicates the degree of anomaly. For $0.16 < b < 0.60$ mm, and for driving velocities below $v_M(b)$, the capillary forces are strong enough to allow an initial acceleration and subsequent deceleration of the oil fingers on copper tracks, but are sufficiently weak to allow coupling between neighboring tracks. For $v > v_M$, the viscous forces become dominant, and the anomalous scaling is unobservable. For $b \geq 0.60$ mm, the capillary forces are not sufficiently strong and we have ordinary scaling for any velocity. Finally, for $b \leq 0.16$ mm (light grey area in Fig. 18), the capillary forces are dominant, and the oil fingers on copper tracks and fiberglass channels have independent motion. In this situation a dynamic scaling scenario is not adequate because there is no growing correlation length along the interface. $W(l,t)$ grows as a power law of time, but this is a consequence of the independent behavior for each track given by Eq. (9). Although it is not possible to determine the scaling exponents, it is still possible to perform a vertical collapse of the spectral curves because only the *difference* between α and α_{loc} (i.e. θ) is needed. This provides the values of $2\theta/z$ for $b = 0.16$ mm.

In conclusion, experiments are reported of anomalous kinetic roughening in Hele–Shaw flows with quenched disorder. The displacement of an oil–air interface for different strengths of the capillary forces, flow velocity, and disorder configurations has been studied. It has been observed that scaling of the interfacial fluctuations follows the intrinsic anomalous scaling ansatz in conditions of sufficiently strong capillary forces, low velocities, and a persistent disorder in the growth direction. A random distribution of tracks has been used as representative of a persistent disorder. A different scaling for the global and local interfacial fluctuations has been measured, with exponents $\beta \simeq 0.50$, $\beta^* \simeq 0.25$, $\alpha \simeq 1.0$, $\alpha_{loc} \simeq 0.5$, and $z \simeq 2$. The presence of anomalous scaling has been confirmed by the existence of multiscaling. When capillary forces become dominant or when a regular track pattern is used, however, there is no growing correlation length along the interface, and therefore no dynamic scaling. A detailed study of the interface dynamics at the scale of the disorder shows that the anomaly is a consequence of the different interface velocities on copper tracks and fiberglass channels plus the coupled motion between neighboring tracks. The resulting dynamics gives interface profiles characterized by large height differences Δh at the edges of the copper tracks. These Δh follow an anomalous Lévy distribution characteristic of systems which display anomalous scaling.

VII. ACKNOWLEDGEMENTS

We are grateful to M. A. Rodríguez, J. Ramasco, and R. Cuerno for fruitful discussions. The research has received financial support from the Dirección General de Investigación (MCT, Spain), project BFM2000-0628-C03-01. J. O. acknowledges the Generalitat de Catalunya for additional financial support.

---

[1] A.-L. Barabási and H.E. Stanley, *Fractal Concepts in Surface Growth*, Cambridge University Press, Cambridge (1995).
[2] F. Family and T. Vicsek, J. Phys. A **18**, L75 (1985).
[3] M. Schroeder, M. Siegert, D. E. Wolf, J. D. Shore, and M. Plischke, Europhys. Lett. **24**, 563 (1993)
[4] J. Krug, Phys. Rev. Lett. **72**, 2907 (1994).
[5] S. Das Sarma, C. J. Lanczycki, R. Kotlyar, and S. V. Ghaisas, Phys. Rev. E **53**, 359 (1996)
[6] C. Dasgupta, S. Das Sarma, and J.M. Kim, Phys. Rev. E **54**, R4552 (1996)
[7] J.M. López and M.A. Rodríguez, Phys. Rev. E **54**, R2189 (1996)
[8] M. Castro, R. Cuerno, A. Sánchez, and F. Domínguez-Adame, Phys. Rev. E **57**, R2491 (1998)
[9] J.M. López and J. Schmittbuhl, Phys. Rev. E **57**, 6405 (1998).
[10] S. Morel, J. Schmittbuhl, J.M. López, and G. Valentin,

Phys. Rev. E **58**, 6999 (1998).

[11] S. Morel, J. Schmittbuhl, E. Bouchaud, and G. Valentin, Phys. Rev. Lett. **85**, 1678 (2000).

[12] T. Engøy, K. J. Måløy, A. Hansen, and S. Roux, Phys. Rev. Lett. **73**, 834 (1994).

[13] J.H. Jeffries, J.-K. Zuo, and M.M. Craig, Phys. Rev. Lett. **76**, 4931 (1996).

[14] H.-N. Yang, G.-C. Wang, and T.-M. Lu, Phys. Rev. Lett. **73**, 2348 (1994).

[15] S. Huo and W. Schwarzacher, Phys. Rev. Lett. **86**, 256 (2001).

[16] J.M. López, M.A. Rodríguez, and R. Cuerno, Phys. Rev. E **56**, 3993 (1997)

[17] J.M. López, M.A. Rodríguez, and R. Cuerno, Physica A **246**, 329 (1997).

[18] J. Soriano, J. Ortín, and A. Hernández-Machado, Phys. Rev. E. **66**, 031603 (2002).

[19] J. Soriano, J.J. Ramasco, M.A. Rodríguez, A. Hernández-Machado, and J. Ortín, Phys. Rev. Lett. **89**, 026102 (2002).

[20] J.J. Ramasco, J.M. López, and M.A. Rodríguez, Phys. Rev. Lett. **84**, 2199 (2000).

[21] Real–life motion pictures of the experiments are available at http://debian01.ecm.ub.es.

[22] J. M. López. Phys. Rev. Lett. 83, 4594 (1999).

[23] G. Tripathy and W. van Saarloos, Phys. Rev. Lett. **85**, 3556 (2000).

[24] I. Simonsen, A. Hansen, and O. M. Nes, Phys. Rev. E **58**, 2779 (1998).

[25] J. Schmittbuhl, J.-P. Vilotte, and S. Roux, Phys. Rev. E **51**, 131 (1995).

[26] J. Asikainen, S. Majaniemi, M. Dubé, and T. Ala-Nissila, Phys. Rev. E. **65**, 052104 (2002).

[27] A. Hernández–Machado, J. Soriano, A.M. Lacasta, M.A. Rodríguez, L. Ramírez–Piscina, and J. Ortín, Europhys. Lett. **55**, 194 (2001).

4.5 *Forced imbibition of a viscous fluid by a disordered Hele–Shaw cell*, **preprint**

Forced imbibition of a viscous fluid by a disordered Hele–Shaw cell

Jordi Soriano,* Jordi Ortín, and A. Hernández-Machado
Departament d'Estructura i Constituents de la Matèria
Universitat de Barcelona, Av. Diagonal, 647, E-08028 Barcelona, Spain

(Dated: January 15, 2003)

We report experiments of the forced imbibition of a viscous fluid by a disordered Hele–Shaw cell with random variations of the gap spacing. We find that the average position of the interface follows Washburn's law, $\langle h\rangle \sim t^{1/2}$. The measured values of the growth and roughness exponents at long times are $\beta = 0.64 \pm 0.03$ and $\alpha = 0.7 \pm 0.1$ respectively, substantially different from $\beta = 0.5$ and $\alpha = 0.5$ obtained in forced fluid invasion experiments at similar capillary numbers. The measured values are compatible with the QKPZ universality class, suggesting that a local interfacial dynamics can account for the experimental observations in the range of length scales explored.

PACS numbers: 47.55.Mh, 68.35.Ct, 05.40.-a

I. INTRODUCTION

The dynamics of immiscible fluid–fluid displacements in porous media has been a subject of much interest in last years [1]. It is a fundamental issue in many industrial and environmental problems, such as petroleum recovery, irrigation, or retention of waste waters. The process is called *forced imbibition* when an invading viscous fluid that wets preferentially the medium displaces a resident fluid by the application of an external pressure. In contrast, *forced fluid invasion* takes place when the invading fluid gets into the medium at constant injection rate. If the invading fluid is more viscous than the resident one the advancing interfacial front is compact and the height of the interface is a single–valued function of position $\vec{x}$ and time t, $h = h(\vec{x}, t)$ [2]. In many cases the interfacial fluctuations follow the dynamic scaling of Family–Vicsek (FV) [3], which allows a description of the scaling properties of the interfacial fluctuations in terms of a growth exponent β, a roughness exponent α, and a dynamic exponent z.

Many experiments of imbibition have been performed in the last years. In a first tentative, paper was used as a disordered medium, and the dynamics of ink–air or coffee–air fronts were studied [4–8]. Other experiments were performed in Hele–Shaw geometry (two parallel glass plates separated by a narrow distance b) and a random distribution of glass beads was used as a disordered medium [9–11]. Using the same geometry other methods of generating a disordered medium have been explored, including random variations in gap spacing produced by a predesigned surface relief of the bottom plate [12–14] or by roughened plates [15]. In the latter case spontaneous imbibition fronts in capillary rise were studied.

In previous works [12–14] we presented experimental studies of *forced fluid invasion* in a Hele-Shaw cell with a tailored quenched disorder, produced by dicotomic variations in the thickness of the bottom plate distributed randomly in the cell. First we focused on the limit of weak quenched disorder [12] and studied different types of disorder configurations at different average interface velocities v and gap spacings b. The results obtained showed that the interfacial fluctuations scaled with time through a growth exponent $\beta \simeq 0.50$, which was almost independent of experimental parameters. The values of the roughness exponents distinguished two regimes, α_1 at short length scales and α_2 at long length scales. In the limit of high interface velocities we obtained $\alpha_1 \simeq 1.3$ and $\alpha_2 \simeq 0$, independently of the disorder configuration, while for moderate and low velocities different values were obtained depending on the disorder configuration, and different scaling regimes were reported. Next we investigated the limit of strong quenched disorder [12] and observed that for sufficiently strong capillary forces the scaling of the interfacial fluctuations fitted in the framework of anomalous scaling. We measured the following set of scaling exponents: $\beta = 0.50$, $\beta^* = 0.25$, $\alpha = 1.0$, $\alpha_{loc} = 0.5$, and $z = 2.0$.

The objective of the present paper is to report results of *forced imbibition* experiments carried out in the same Hele–Shaw cell as the experiments of forced fluid invasion just described. The outline of the paper is as follows. In Sec. II we review the Family–Vicsek ansatz for the scaling of the interfacial fluctuations. In Sec. III we describe briefly the modifications introduced in our experimental setup in order to perform forced imbibition experiments. The experimental results are presented and analyzed in Sec. IV, and the final conclusions are drawn in Sec. V.

II. FAMILY–VICSEK DYNAMIC SCALING

The statistical properties of a one–dimensional interface defined by a function $h(x, t)$ (interface height at position x and time t) are usually described in terms of the fluctuations of h. The *global* width in a system of lateral size L is defined as $w(L, t) = \langle [h(x, t) - \langle h\rangle(t)]^2\rangle_x^{1/2}$, where $\langle h\rangle(t) = \langle h(x, t)\rangle_x$, and $\langle\ \rangle_x$ is an spatial average in the x direction. In the dynamic scaling assumption of

---

*Electronic address: `soriano@ecm.ub.es`

Family–Vicsek (FV) [3], $w(L,t)$ scales as

$$w(L,t) = L^{\alpha} f(L/t^{1/z}), \tag{1}$$

where z is the dynamical exponent and $f(u)$ the scaling function

$$f(u) \sim \begin{cases} \text{const} & \text{if} \quad u \ll 1, \\ u^{-\alpha} & \text{if} \quad u \gg 1. \end{cases} \tag{2}$$

Here α is the roughness exponent and characterizes the scaling of the *rms* width at saturation, $w(L, t \gg L^z) \sim L^{\alpha}$. L^z characterizes the saturation time, $t_{\times} \sim L^z$. It is customary to introduce a growth exponent β, which characterizes the growth of the interfacial fluctuations before saturation, $w(L, t \ll L^z) \sim t^{\beta}$. The exponents α, β, and z verify the scaling relation $\alpha = z\beta$.

An important feature of the FV assumption is that the scaling behavior of the surface can also be obtained by looking at the *local* width over a window of size $l \ll L$. The scaling is then

$$w(l,t) \sim \begin{cases} t^{\beta} & \text{if} \quad t \ll l^z, \\ l^{\alpha} & \text{if} \quad t \gg l^z. \end{cases} \tag{3}$$

The roughness exponent α is usually obtained by studying the power spectrum of the interfacial fluctuations, $S(k,t) = \langle H(k,t) H(-k,t) \rangle$, where $H(k,t) = \sum_x [h(x,t) - \langle h \rangle (t)] \exp(ikx)$. In the FV assumption, the power spectrum scales as

$$S(k,t) = k^{-(2\alpha+1)} s(kt^{1/z}), \tag{4}$$

where s is the scaling function

$$s(u) \sim \begin{cases} u^{2\alpha+1} & \text{if} \quad u \ll 1, \\ \text{const} & \text{if} \quad u \gg 1. \end{cases} \tag{5}$$

Hence, the power spectrum scales as $S(k,t) \sim k^{-(2\alpha+1)}$ at saturation ($kt^{1/z} \gg 1$).

III. EXPERIMENTAL SETUP AND PROCEDURE

The experimental setup is similar to the one used in the forced fluid invasion experiments, described in Refs. [12, 13]. In summary, it consists of a Hele–Shaw cell of size 190×500 mm^2 (L × H) made of two glass plates separated a narrow gap of thickness $b = 0.36$ mm. Fluctuations in the gap spacing are provided by copper obstacles ($d = 0.06$ mm high, 1.50 mm lateral size) that are randomly distributed over a fiberglass substrate, without overlap, filling 35% of the substrate (disorder SQ 1.50 [12]).

In the present set of experiments we have replaced the constant flow–rate injection pump by a constant pressure device that consists on an oil column of selectable height H, in the range from -50 to 100 mm, in steps of 0.01 mm. A silicone oil (Rhodorsil 47 V) with kinematic viscosity $\nu = 50$ mm^2/s, density $\rho = 998$ kg/m^3, and surface tension oil–air $\sigma = 20.7$ mN/m at room temperature, penetrates into the cell, displacing the air initially present, through two wide holes drilled in the bottom glass. The holes connect to a reservoir with the disorder plate placed just ahead (Fig. 1).

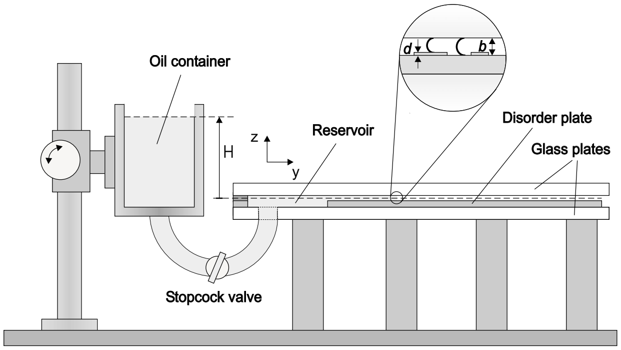

FIG. 1: Sketch of the experimental setup.

The experimental procedure used to prepare the initial interface is the following: The reservoir in the cell is carefully filled at low external pressure, and the connection between the cell and the oil column is then closed using a stopcock valve. Next, using a syringe, the oil–air interface is pushed gently up to a transverse copper track placed at the beginning of the disorder plate and 2 mm behind the disorder pattern. Then the connection to the oil column is opened again and the experiment started. The evolution of the oil–air interface is monitored using two CCD cameras. A computer records the images acquired and stores them for processing.

IV. EXPERIMENTAL RESULTS AND DISCUSSION

We have explored different heights of the column oil, in the range $-25 \leq H \leq 100$ mm. As a first result, we observe that the average interface velocity obeys Washburn's law, $\langle h \rangle \sim t^{1/2}$ for $H \gtrsim -25$ mm, as shown in Fig. 2. For a critical value of $H = H_c \simeq -25$ mm, the interface is close to the pinning threshold, and the average interface velocity is zero. For values of H below the critical value the interfaces recedes.

Two examples of the temporal evolution of the interface for $H > H_c$ are shown in Fig. 3. For $H = 8$ mm (Fig. 3(a)), which corresponds to an initial average interface velocity $v_0 = 0.11$ mm/s, all points of the interface always advance until the end of the cell. For $H = -17$ mm (Fig. 3(b)), with $v_0 = 0.02$ mm/s, the interface gets locally pinned and the interface moves through avalanches at some particular locations.

When measuring the growth of the interfacial *rms* width as a function of time for different values of H, we

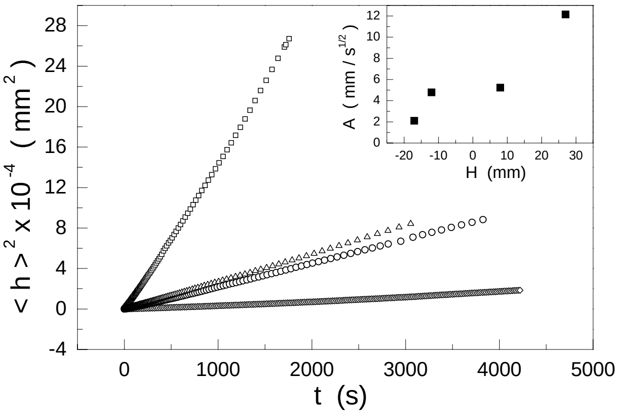

FIG. 2: Main plot: Squared average interface position as a function of time, for different oil column heights $H = -17$ mm (diamonds), -12 mm (circles), 8 mm (triangles), and 27 mm (squares), showing that the imbibition process follows Washburn's law, $\langle h \rangle = At^{1/2}$. Inset: Dependence of Washburn's law prefactor A (squared) on column height H.

have noticed that the operation of connecting the oil column to the cell to start the experiment causes a distortion of the initial front. Thus, it is difficult to characterize the scaling of the interfacial fluctuations at very short times. To minimize the effect of possible disturbances of the initial front, we have always considered the subtracted width $W(l,t)$, defined as $W(l,t) = [w^2(l,t) - w^2(l,0)]^{1/2}$, and discarded the earliest growth stages (up to $10-20$ s).

We have focused on measuring the values of β and α for an oil column height $H = -17$ mm. In these conditions the imposed (negative) pressure gradient nearly compensates the traction due to capillarity, so that the interface is driven very close to the pinning threshold. The average interface velocity (initially $v_0 = 0.02$ mm/s) decreases a 6% in the experiment.

The plot of $W(L,t)$ as a function of time for these experiments is shown in Fig. 4(a). Disregarding the earliest time stages, we obtain a power law regime with slope $\beta = 0.64 \pm 0.03$. This exponent is distinctly higher than the exponent 0.5 measured in our forced fluid invasion experiments at similar capillary number (interface velocity). This fastest growth rate must be attributed to the combination of two effects: i) the decay of the velocity with time (Washburn's law), and ii) the fact that, since the invading liquid is driven at constant pressure, there is no limitation of mass input.

The temporal evolution of the power spectrum is presented in Fig. 4(b). At the earliest time stages we observe indications of a power law for large k (short length scales) with slope -3.2 ± 0.1, that would correspond to a roughness exponent $\alpha = 1.1 \pm 0.1$. This large value of α at short times has also been observed in our previous experiments at constant injection rate [12], and it is related to the dominance of the capillary forces at short times. At late times, in spite of the fact that the interfacial width does not show hints of reaching saturation, the power spectrum becomes scale invariant over the whole range of measured length scales, with slope -2.4 ± 0.1 ($\alpha = 0.7 \pm 0.1$).

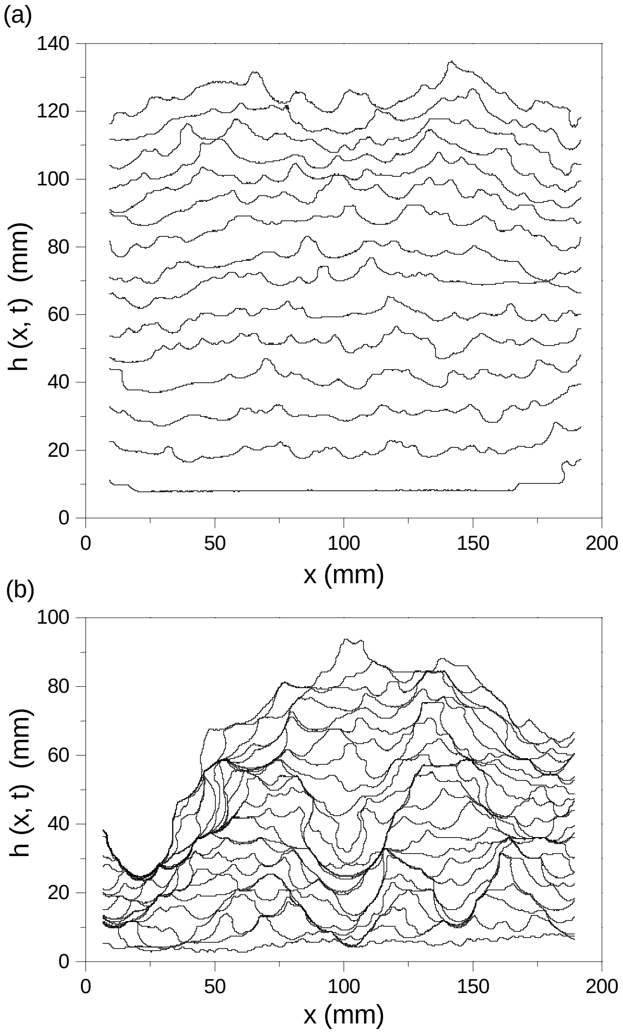

FIG. 3: Temporal evolution of the oil–air interface at two different heights of the column oil. (a) $H = 8$ mm, the initial average velocity of the interface is $v = 0.11$ mm/s, and the interfaces are plot every 100 s. (b) $H = -17$ mm, the initial average velocity of the interface is $v = 0.02$ mm/s, and the interfaces are plot every 120 s. The gap thickness is $b = 0.36$ mm in both cases.

The fact that we reach a unique power law at long times, for interface velocities close to $v = 0.02$ mm/s and smaller, is consistent with our previous results at constant injection rate, where we observed two regimes in the power spectrum, α_1 at large k and α_2 at small k. The two regimes were separated by a crossover wavenumber k_c that progressively moved to small k as the velocity was reduced. We suggested that at smaller velocities we could observe a unique power law spanning all length scales, but that limit was not explored because of the presence of local pinning. Our present results confirm that prediction.

The effect of the imposed external pressure on the scaling of the power spectrum is presented in Fig. 4(c). Four power spectra, corresponding to four different heights H of the oil column, are plot at the largest times available (when the interfaces reach the end of the cell). The results for the highest driving pressures confirm that a large roughness exponent (close to 1.0) is associated with the scaling of the shortest length scales, achieved at relatively large interface velocities. This result is consistent with the behaviour of the spectrum at short times in Fig 4(b). As the pinning threshold is approached, and the interface velocity tends to zero, however, scale invariance is observed over all length scales, and with a roughness exponent much smaller than 1.0. We measure $\alpha = 0.7$ at the smallest driving pressure, but we cannot rule out that α takes even a slightly smaller value at the true pinning threshold.

In this respect, it is interesting to observe that our scaling exponents β and α are very similar to the exponents that define the so called 'quenched Kardar–Parisi–Zhang' (QKPZ) universality class, namely $\alpha = \beta = 0.63$. This agreement can indicate that, below a critical average interface velocity, the dynamics changes from nonlocal (in the line of the models proposed by Hernández–Machado *et al.* [17], and Pauné *et al.* [16]), to a local dynamics properly described by the QKPZ universality class. This possibility would apply only to the range of length scales explored in the present experiments. Nonlocality could still be relevant at shorter length scales, as the recent experiments of Geromichalos et al. [15] seem to indicate.

V. CONCLUSIONS

We have studied experimentally the forced imbibition of a viscous wetting oil by a disordered Hele–Shaw cell.

The average position of the interface follows Washburn's law in a wide range of forcing pressures.

The fluctuations of the oil–air interface are scale invariant, and fit in the Family-Vicsek dynamic scaling ansatz. Close enough to the pinning threshold, we measure a growth exponent $\beta = 0,64 \pm 0.03$ and a roughness exponent $\alpha = 0.7 \pm 0.1$, distinctly different from the exponents obtained in forced fluid invasion experiments at comparable capillary numbers.

The exponents measured suggest that the interfacial dynamics of this problem could belong to the QKPZ universality class ($\beta = \alpha = 0.63$). This being the case, forced imbibition dynamics would be essentially different from forced fluid invasion dynamics. The fact that the

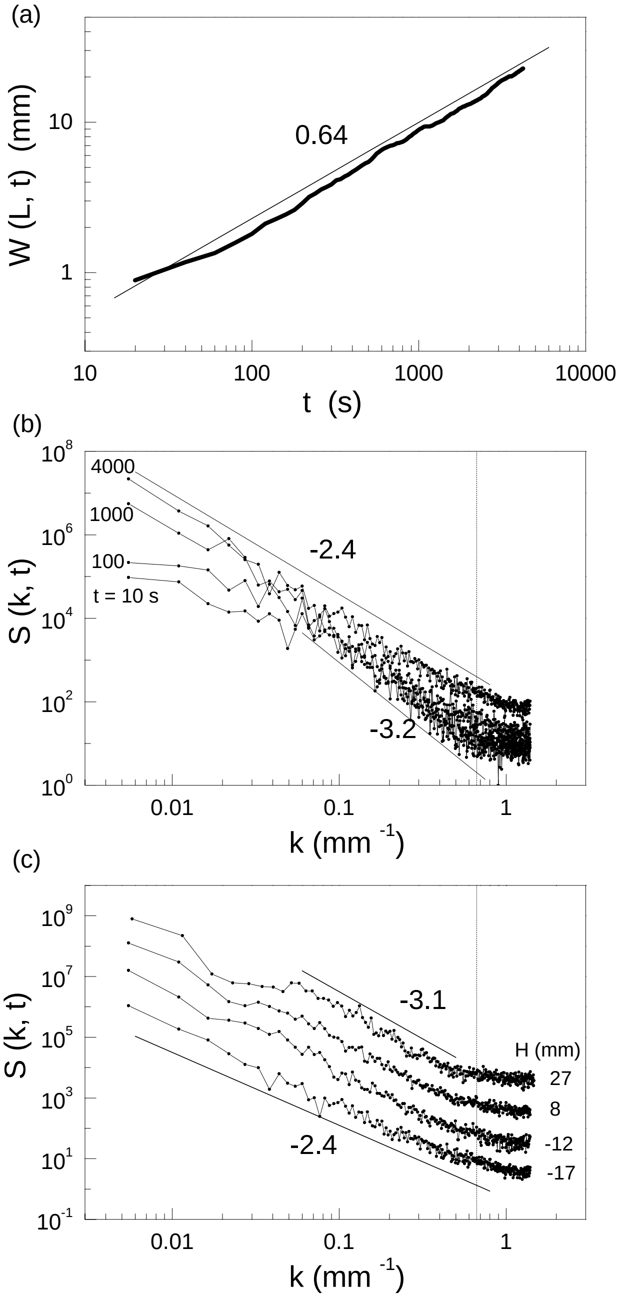

FIG. 4: (a) Log–log plot of the interfacial width as a function of time, for $H = -17$ mm, showing power–law growth with exponent $\beta = 0.64 \pm 0.03$. (b) Log–log plot of the temporal evolution of the power spectrum for $H = -17$ mm. The spectrum at the largest times available displays a power–law with exponent -2.4, corresponding to a roughness exponent $\alpha = 0.7 \pm 0.1$. (c) Power spectra at the largest times available, for different external pressures as given by the heights H of the oil column. All the curves shown correspond to averages of six measurements (two measurements on each disorder configuration for three different disorder configurations). The vertical lines in (b) and (c) show the value of k associated with the lateral size of the disorder unit cell.

interface velocity decays monotonously during the imbibition process (Washburn's law), and that the condition of mass conservation does not impose a limit on the average interface velocity (the boundary condition being a constant external pressure), seem to restrict *nonlocal* effects on the dynamics to very short length scales, below the range studied in our experiments.

VI. ACKNOWLEDGEMENTS

We are grateful to Albert Comerma and Manel Quevedo for technical support. The research has received financial support from the Dirección General de Investigación (MCT, Spain), project BFM2000-0628-C03-01. J.O. acknowledges the Generalitat de Catalunya for additional financial support.

---

[1] M. Sahimi, *Flow and transport in porous media and fractured rock*, John Wiley and Sons, New York (1995).
[2] A.-L. Barabási and H.E. Stanley, *Fractal Concepts in Surface Growth*, Cambridge University Press, Cambridge (1995).
[3] F. Family and T. Vicsek, J. Phys. A **18**, L75 (1985).
[4] S. V. Buldyrev, A.-L. Barabási, F. Caserta, S. Havlin, H. E. Stanley, and T. Vicsek, Phys. Rev. A, **45**, R8313 (1992).
[5] V.K. Horváth and H. E. Stanley, Phys. Rev. E, **52**, 5166 (1995).
[6] T. H. Kwon, A. E. Hopkins, and S. E. O'Donnell, Phys. Rev. E, **54**, 685 (1996).
[7] O. Zik, E. Moses, Z. Olami, and I. Webman, Euro. Phys. Lett., **38**, 509 (1997).
[8] A. S. Balakin, A. Bravo-Ortega, and D. Morales, Phylos. Mag. Lett., **80**, 503 (2000).
[9] M.A. Rubio, C.A. Edwards, A. Dougherty, and J.P. Gollub, Phys. Rev. Lett., **63**, 1685 (1989).
[10] V.K. Horváth, F. Family and T. Vicsek, J. Phys. A, **24**, L25 (1991).
[11] S.-J. He, L. M. Galathra, K. S. Kahanda, and P.-Z. Wong, Phys. Rev. Lett., **69**, 3731 (1992).
[12] J. Soriano, J. Ortín, and A. Hernández-Machado, Phys. Rev. E., **66**, 031603 (2002).
[13] J. Soriano, J.J. Ramasco, M.A. Rodríguez, A. Hernández-Machado, and J. Ortín, Phys. Rev. Lett. **89**, 026102 (2002).
[14] J. Soriano, J. Ortín, and A. Hernández-Machado, Phys. Rev. E., submitted cond-mat/0208432 (2002).
[15] D. Geromichalos, F. Mugele, and S. Herminghaus, Phys. Rev. Lett., **89**, 104503 (2002).
[16] E. Pauné and J. Casademunt, preprint, cond–mat/0207673 (2002).
[17] A. Hernández–Machado, J. Soriano, A.M. Lacasta, M.A. Rodríguez, L. Ramírez–Piscina, and J. Ortín, Europhys. Lett. **55**, 194 (2001).

Chapter 5

Conclusions and future perspectives

5.1 Conclusions

1. We have developed a technique based on printed circuit technology to design a quenched disorder (*copper obstacles*) of constant height d and well controlled statistical properties. Three kinds of disorder configurations with increasing persistence length in the direction of growth have been investigated.

2. We have designed and built an experimental setup to study the dynamics of the stable displacement of an oil–air interface in a Hele-Shaw cell which contains a quenched disorder in the bottom plate. The roughening process is a consequence of the competition between the stabilizing forces of the viscous pressure field in the fluid and the in–plane interfacial tension, and the destabilizing capillary forces due to the different curvature of the meniscus in the z direction due to the presence of the disorder. The strength of the capillary forces is controlled by means of the gap spacing b, whereas the strength of the viscous forces is controlled through the driving velocity v.

3. We have developed different software tools to control the image acquisition hardware, monitor the evolution of the oil–air interface, process the images acquired, and perform all necessary data analysis.

4. We have performed experiments at constant injection rate and at constant pressure. For the former the fluid velocity is controlled by means of a syringe pump, while for the latter the constant pressure is kept constant through an oil column of selectable height.

5. We have characterized the permeability of the cell for different kinds of disorder configurations and for different strength of the capillary forces. For large gap spacings (weak capillary forces) we recover the permeability of an ordinary Hele–Shaw cell independently of the disorder configuration. For small gap spacings (strong capillary forces) the permeability is strongly dependent on the disorder configuration. In this limit, when the disorder consists on copper tracks, we have derived an analytical expression for the permeability that is in agreement with theoretical predictions. We have also derived an expression for the modified capillary number, Ca', which measures the relative strength of viscous to capillary forces inside the disordered cell.

6. We have carried out experiments exploring different disorder configurations, gap spacings, and driving velocities. We have obtained, on one hand, different scaling exponents when the interface is driven at constant injection rate or at constant pressure. On the other, the scaling exponents depend on the strength of the disorder, and two big families of results can be characterized, those with *weak* quenched disorder and those with *strong* quenched disorder.

7. The experimental results with *weak* quenched disorder are characterized by a scaling of the interfacial fluctuations that can be best described in the framework of Family–Vicsek dynamic scaling. They correspond to experimental parameters giving rise to large interface velocities, large gap spacings, or short persistence length in the direction of growth. In these conditions we have measured $\beta \simeq 0.50$ almost independently of the experimental parameters. The roughness exponents are sensitive to the experimental parameters and two regimes, α_1 at short length scales, and α_2 at long scales have been characterized. The results are summarized in Table 5.1. The crossover length scale that separates the two regimes scales with the velocity as $\sim v^{-0.47}$. In the limit of very large driving velocities these exponents tend asymptotically to $\alpha_1 \simeq 1.3$ and $\alpha_2 \simeq 0$.

8. The experimental results with *strong* quenched disorder are characterized by an intrinsic anomalous scaling. They correspond to experimental parameters in which the disorder is totally persistent in the direction of growth (tracks), and capillary and viscous forces are better balanced. In these conditions we have measured $\beta \simeq 0.50$, $\beta^* \simeq 0.25$, $\alpha = 1.0$, $\alpha_{loc} = 0.5$, and $z = 2.0$. A detailed investigation of the interface motion on the tracks has allowed a description of the anomalous scaling in terms of i) the velocity of the interface on copper tracks (v_+) and fiberglass channels (v_-), which can be expressed in the form

Disorder	Low Ca' ($\lesssim 3$)		Moderate Ca' ($3 <$ Ca' < 10)		Large Ca' ($\gtrsim 10$)	
	α_1	α_2	α_1	α_2	α_1	α_2
SQ 1.50	$0.6 - 0.9$	–	$\simeq 1$	$\simeq 0.6$	$\simeq 1.3$	$\simeq 0$
SQ-n 1.50	$0.6 - 0.9$	–	$\simeq 0.9$	$\simeq 0.5$	$\simeq 1.3$	$\simeq 0$
T 0.40	Anomalous scaling		$\simeq 0.7$	$\simeq 0.5$	$\simeq 1.3$	$\simeq 0$
T 1.50	Anomalous scaling		$\simeq 0.5$	$\simeq 0.2$	$\simeq 1.3$	$\simeq 0$

Table 5.1: Summary of the values of the roughness exponents in the limit of weak quenched disorder.

$v_\pm = v \pm (v_M - v)\ t^{-1/2}$; and ii) the coupling in the interface motion between neighboring tracks. A dynamic scaling regime cannot be identified when a regular modulation of the gap spacing is introduced or when the capillary forces become dominant. The anomalous scaling disappears for large driving velocities (viscous forces dominant), large gap spacings (weak capillary forces) or when the persistence of the disorder is reduced.

9. The presence of anomalous scaling has been confirmed, and the scaling exponents refined, by means of complementary analysis, that include the growth of the average local slopes, multiscaling, and the statistical distribution of height differences.

10. We have performed experiments driven solely by capillary forces, and found that the velocity on a single track is given by the simple relaxation law $v = v_M\ t^{-1/2}$, with v_M an initial overshoot.

11. We have carried out experiments at constant pressure, and explored the regime of weak capillary forces. The fact that the average interface velocity decays as $v \sim t^{1/2}$ and the absence of mass conservation give rise to different scaling exponents from those obtained at constant injection rate, namely $\beta \simeq 0.63$ and $\alpha \simeq 0.7$. For low external pressures the interface gets locally pinned and the interface advances by means of avalanches.

5.2 Future Perspectives

1. **Experimental confirmation of the generic scaling** The generic scaling proposed by Ramasco *et al.* in Ref. [RLR00] describes four different types of

dynamic scaling. We have observed experimentally Family–Vicsek and intrinsic anomalous scaling. It would be interesting to investigate other disorder patterns to obtain super–roughness and faceted surfaces.

2. **Confirmation of theoretical predictions by Pauné et al.**. Recent theoretical results on kinetic roughening in a Hele–Shaw cell with modulated gap spacing, obtained by Pauné *et al* [PC02; Pau02] report predictions for the scaling exponents β and α that in some particular cases are in agreement with the experimental results. However, the theoretical predictions are based on the fact that the edges of the obstacles are smooth, i.e. $\nabla b \ll 1$. We can satisfy this condition in our experiments by covering our disorder plates with a plastic film, which will smooth the edges of the copper obstacles. In particular, Pauné *et al.* showed that for a persistent disorder (tracks) there is no observation of anomalous scaling. Test experiments that we have carried out recently (using the usual disorder plates but covering them with a plastic film) are in agreement with this prediction. These experiments will be carried out in the future exploring different gap spacings and driving velocities.

3. **Intensive investigations at constant pressure**. Our experimental setup at constant pressure is very convenient to perform experiments to characterize avalanches and the pinning/depinning transition. However, although we have started experimental investigations on these topics, we have observed that these experiments are complex and require much more time, so they will be carried out in the forthcoming years.

Other possible experiments that could be carried out with our experimental setup are:

1. **Wetting as a source of disorder**. It could be interesting to perform experiments of anomalous scaling where the destabilizing capillary forces, instead of coming from the different curvature of the meniscii over copper tracks and fiberglass substrate, would arise from different wetting conditions. The experimental setup would consist in an ordinary Hele-Shaw cell where the top and bottom plates would be treated to give a random distribution of strips, some of them giving perfect wetting, and the others complete de–wetting.

2. **Pinching**. An interesting behavior that we have observed in the experiments of anomalous scaling is the pinch–off of long fluid filaments (or fingers). For a sufficiently thin copper track, we have observed that the oil tips advancing

over copper tracks pinch–off for sufficiently small gap spacings. Our printed circuit technique to design a columnar disorder plus our experimental setup are well suited to study this problem in deep using different track widths and gap spacings.

3. **Experiments with viscoelastic fluids**. Some problems in biophysics can be modelled as the flow of a viscoelastic fluid in a Hele-Shaw cell with quenched disorder. An example could be the flow of actin through the cytoskeleton of a living cell. Our experimental setup is well suited to carry on this kind of investigation.

Bibliography

[ABMS95] L. A. N. Amaral, A. Barabási, H. A. Makse, and H. E. Stanley. Scaling properties of driven interfaces in disordered media. *Phys. Rev. Lett.* **52**, 4087 (1995).

[ABS94] L. A. N. Amaral, A. Barabási, and H. E. Stanley. Universality classes for interface growth with quenched disorder. *Phys. Rev. Lett.* **73**, 62 (1994).

[AMDAN02] J. Asikainen, S. Majaniemi, M. Dubé, and T. Ala-Nissila. Interface dynamics and kinetic roughening in fractals. *Phys. Rev. E* **65**, 052104 (2002).

[AT91] M. Avellaneda and S. Torquato. Rigorous link between fluid permeability, electrical conductivity, and relaxation times for transport in porous media. *Phys. Fluids A* **3**, 2529 (1991).

[BBC$^+$92] S. V. Buldyrev, A.-L. Barabási, F. Caserta, S. Havlin, H. E. Stanley, and T. Vicsek. Anomalous interface roughening in porous media: Experiment and model. *Phys. Rev. A* **45**, R8313 (1992).

[BBH$^+$92] S. V. Buldyrev, A.-L. Barabási, S. Havlin, J. Kertsz, H. E. Stanley, and H. S. Xenias. Anomalous interface roughening in 3d porous media: experiment and model. *Physica A* **191**, 220 (1992).

[BBJ$^+$92] A.-L. Barabási, R. Bourbonnais, M. Jensen, J. Kertész, T. Vicsek, and Y.-C. Zhang. Multifractality of growing surfaces. *Phys. Rev. A* **45**, R6951 (1992).

[BBOM00] A. S. Balakin, A. Bravo-Ortega, and D. Morales. Some new features of interface roughening dynamics in paper–wetting experiments. *Phylos. Mag. Lett.* **80**, 503 (2000).

[BFJ$^+$91] A. Birovljev, L. Furuberg, T. Jøssang, K. J. Måløy, and A. Aharony. Gravity invasion percolation in two dimensions: experiments and simulation. *Phys. Rev. Lett.* **67**, 584 (1991).

[BJCST95] E. Ben-Jacob, I. Cohen, O. Shochet, and A. Tenenbaum. Cooperative formation of chiral patterns during growth of bacterial colonies. *Phys. Rev. Lett.* **75**, 2899 (1995).

[BJST$^+$94] E. Ben-Jacob, O. Shochet, A. Tenenbaum, J. Cohen, A. Czirók, and T. Vicsek. Communication, regulation and control during complex patterning of bacterial colonies. *Fractals* **2**, 15 (1994).

[BL77] J. Bonnet and B. Lenormand. Réalisation de micromodèles pour l'étude des écoulements polyphasiques en milieu poreux. *Revue de l'Institut Français du Pétrole* **32**, 477 (1977).

[BLP90] E. Bouchaud, G. Lapasset, and J. Planés. Fractal dimension of fractured surfaces: a universal value. *Europhys. Lett.* **13**, 73 (1990).

[bPES81] P. by Petroleum Extension Service. *Fundamentals of Petroleum, 2nd Edition* (The University of Texas at Austin, Austin, Texas, 1981).

[BS95] A.-L. Barabási and H. Stanley. *Fractal Concepts in Surface Growth* (Cambridge University Press, Cambridge, England, 1995).

[BV91] A.-L. Barabási and T. Vicsek. Multifractality of self–affine fractals. *Phys. Rev. A* **44**, 2730 (1991).

[CCF$^+$90] A. Cancelliere, C. Chang, E. Foti, D. H. Rothman, and S. Succi. The permeability of a random medium: Comparison of simulation with theory. *Phys. Fluids A* **2**, 2085 (1990).

[CRS94] M. Chaouche, N. Rakotomalala, and D. Salin. Invasion percolation in a hydrostatic or permeability gradient: experiments and simulations. *Phys. Rev. E* **49**, 4133 (1994).

[dG78] P. G. de Gennes and E. Guyon. Lois génerales pour l'injection d'un fluide dans un milieu poreux aléatorie. *Journal de Mecánique* **17**, No. 3, 403 (1978).

[DRE$^+$99] M. Dubé, M. Rost, K. Elder, M. Alava, S. Majaniemi, and T. Ala-Nissila. Liquid conservation and nonlocal interface dynamics in imbibition. *Phys. Rev. Lett.* **83**, 1628 (1999).

[DRE$^+$00] M. Dubé, M. Rost, K. Elder, M. Alava, S. Majaniemi, and T. Ala-Nissila. Conserved dynamics and interface roughening in spontaneous imbibition: A phase field model. *Eur. Phys. J. B* **15**, 701 (2000).

[DSK96] C. Dasgupta, S. D. Sarma, and J. Kim. Controlled instability and multiscaling in models of epitaxial growth. *Phys. Rev. E* **54**, R4552 (1996).

[Dul91] F. A. L. Dullien. *Porous media, fluid transport and pore structure* (Academic Press, Inc, New York, 1991).

[Dus79] E. B. Dussan. On the spreading of liquid on solid surfaces: static and dynamic contact lines. *Annu. Rev. Fluid Mech.* **11**, 371 (1979).

[EMHR94] T. Engøy, K. J. Måløy, A. Hansen, and S. Roux. Roughness of two-dimensional cracks in wood. *Phys. Rev. Lett.* **73**, 834 (1994).

[EW82] S. Edwards and D. Wilkinson. The surface statistics of a granular aggregate. *Proc. R. Soc. London A* **381**, 17 (1982).

[Fed88] J. Feder. *Fractals* (Plenum Press, New York, 1988).

[FV85] F. Family and T. Vicsek. Scaling of the active zone in the eden process on percolation networks and the ballistic deposition model. *J. Phys. A* **18**, L75 (1985).

[FV91] F. Family and T. Vicsek. *Dynamics of fractal surfaces* (World Scientific, Singapore, 1991).

[GB98] V. Ganesan and H. Brenner. Dynamics of two-phase fluid interfaces in random porous media. *Phys. Rev. Lett.* **81**, 578 (1998).

[GMH02] D. Geromichalos, F. Mugele, and S. Herminghaus. Nonlocal dynamics of spontaneous imbibition fronts. *Phys. Rev. Lett.* **89**, 104503 (2002).

[HFV90] V. Horváth, F. Family, and T. Vicsek. Comment on "self-affine fractal interfaces from immiscible displacement in porous media". *Phys. Rev. Lett.* **65**, 1388 (1990).

[HFV91] V. Horváth, F. Family, and T. Vicsek. Dynamic scaling of the interface in two–phase fluids flow. *J. Phys. A* **24**, L25 (1991).

[HKW92] S.-J. He, G. L. M. K. S. Kahanda, and P. Wong. Roughness of wetting fluid invasion fronts in porous media. *Phys. Rev. Lett.* **69**, 3731 (1992).

[HMSL$^+$01] A. Hernández-Machado, J. Soriano, A. Lacasta, M. Rodríguez, L. Ramírez-Piscina, and J. Ortín. Interface roughening in Hele–Shaw flows with quenched disorder: Experimental and theoretical results. *Europhys. Lett.* **55**, 194 (2001).

[Hof75] R. L. Hoffman. A study of advancing interface. I. interface shape in liquid-gas systems. *J. Colloid Interface Sci.* **50**, 228 (1975).

[Hom87] G. Homsy. Viscous fingering in porous media. *Ann. Rev. Fluid Mech.* **19**, 271 (1987).

[HS98] H. S. Hele-Shaw. The flow of water. *Nature* **58**, 33 (1898).

[HS95] V. Horváth and H. E. Stanley. Temporal scaling of interfaces propagating in porous media. *Phys. Rev. E* **52**, 5166 (1995).

[HS01] S. Huo and W. Schwarzacher. Anomalous scaling of the surface width during Cu electrodeposition. *Phy. Rev. Lett.* **86**, 256 (2001).

[JSAAF$^+$97] J. J. S. Andrade, M. P. Almeida, J. M. Filho, S. Havlin, B. Suki, and H. E. Stanley. Fluid flow through porous media:the role of stagnant zones. *Phys. Rev. Lett.* **79**, 3901 (1997).

[JSASS$^+$95] J. J. S. Andrade, D. A. Street, T. Shinohara, Y. Shibusa, and Y. Arai. Percolation disorder in viscous and nonoviscous flow through porous media. *Phys. Rev. E* **51**, 5725 (1995).

[JZC96] J. Jeffries, J.-K. Zuo, and M. Craig. Instability of kinetic roughening in sputter-deposition growth of pt on glass. *Phy. Rev. Lett.* **76**, 4931 (1996).

[KHO96] T. H. Kwon, A. E. Hopkins, and S. E. O'Donnell. Dynamic scaling behavior of a growing self-affine fractal interface in a paper-towel-wetting experiment. *Phys. Rev. E* **54**, 685 (1996).

[KHW93] J. Kertesz, V. K. Horvath, and F. Weber. Self-affine rupture lines in paper sheets. *Fractals* **1**, 67 (1993).

[KKT96] A. Koponen, M. Kataja, and J. Timonen. Tortuous flow in porous media. *Phys. Rev. E* **54**, 406 (1996).

[KKT97] A. Koponen, M. Kataja, and J. Timonen. Permeability and effective porosity of porous media. *Phys. Rev. E* **56**, 3319 (1997).

[KL85] J. Koplik and H. Levine. Interface moving through a random background. *Phys. Rev. B* **32**, 280 (1985).

[KLT91] D. A. Kessler, H. Levine, and Y. Tu. Interface fluctuations in random media. *Phys. Rev. A* **43**, 4551 (1991).

[KM91] J. Krug and P. Meakin. Kinetic roughening of laplacian fronts. *Phys. Rev. Lett.* **66**, 703 (1991).

[KPZ86] M. Kardar, G. Parisi, and Y. Zhang. Dynamic scaling of growing interfaces. *Phys. Rev. Lett* **56**, 889 (1986).

[Kru94] J. Krug. Turbulent interfaces. *Phys. Rev. Lett.* **72**, 2907 (1994).

[KV94] J. Kertesz and T. Vicsek. *Fractals in science* (Springer Verlag, Heilderberg, 1994).

[KYK97] S.-C. Kim, Z.-H. Yoon, and T.-H. Kwon. Scaling behavior of a self–affine fractal interface in a cement fracture experiment. *Physica A* **246**, 320 (1997).

[KZFW92] G. L. M. K. S. Kahanda, X.-Q. Zou, R. Farrell, and P.-Z. Wong. Columnar growth and kinetic roughening in electrochemical deposition. *Phy. Rev. Lett.* **68**, 3741 (1992).

[LB80] R. Lenormand and S. Bories. *C. R. Acad. Sci. Paris, serie* **B 291**, 279 (1980).

[LJ98] J. M. López and H. J. Jensen. Nonequilibrium roughening transition in a simple model of fungal growth in 1 + 1 dimensions. *Phys. Rev. Lett.* **81**, 1734 (1998).

[Lóp99] J. M. López. Scaling approach to calculate critical exponents in anomalous surface roughening. *Phys. Rev. Lett.* **83**, 4594 (1999).

[LR96] J. López and M. Rodríguez. Lack of self-affinity and anomalous roughening in growth processes. *Phys. Rev. E* **54**, R2189 (1996).

[LRC97] J. López, M. Rodríguez, and R. Cuerno. Power spectrum scaling in anomalous kinetic roughening. *Physica A* **246**, 329 (1997).

[LS98] J. López and J. Schmittbuhl. Anomalous scaling of fracture surfaces. *Phys. Rev. E* **57**, 6405 (1998).

[LT93] H. Leschhorn and L. H. Tang. Comment on "elastic string in a random potential". *Phys. Rev. Lett.* **70**, 2973 (1993).

[LTZ88] R. Lenormand, E. Touboul, and C. Zarcone. Numerical models and experiments on immiscible displacement in porous media. *J. FLuid Mech.* **189**, 165 (1988).

[LZS83] R. Lenormand, C. Zarcone, and A. Sarr. Mechanism of the displacement of one fluid by another in a network of capillary ducts. *J. Fluid Mech.* **135**, 337 (1983).

[MBV00] S. Morel, E. Bouchaud, and G. Valentin. Size effect in fracture: roughening of crack surfaces and asymptotic analysis. *Phys. Rev. B* **65**, 104101 (2000).

[MCSDA98] C. M, R. Cuerno, A. Sánchez, and F. Domínguez-Adame. Anomalous scaling in a nonlocal growth model in the kardar-parisi-zhang universality class. *Phys. Rev. E* **57**, R2491 (1998).

[MF90] M. Matsushita and H. Fujikawa. Diffusion–limited growth in bacterial colony formation. *Physica A* **168**, 498 (1990).

[MFBJ88] K. J. Måløy, J. Feder, F. Boger, and T. Jøssang. Fractal structure of hydrodynamic dispersion in porous media. *Phys. Rev. Lett.* **61**, 2925 (1988).

[MFJ85] K. J. Måløy, J. Feder, and T. Jøssang. Viscous fingering fractals in porous media. *Phys. Rev. Lett.* **55**, 2688 (1985).

[MHH92] K. J. Måløy, A. Hansen, and E. L. Hinrichsen. Experimental measurements of the roughness of brittle cracks. *Phys. Rev. Lett.* **68**, 213 (1992).

[MM96] T. Matsuyama and M. Matsushita. *Fractal Geometry in Biological Systems* (edited by P.M. Iannaccone and M. Khokha, CRC Press, Boca Raton, 1996).

[MMK$^+$97] J. Maunuksela, M. Myllys, O.-P. Kähkönen, J. Timonen, N. Provatas, M. J. Alava, and T. Ala-Nissila. Kinetic roughening in slow combustion of paper. *Phys. Rev. Lett.* **79**, 1515 (1997).

[MSBV00] S. Morel, J. Schmittbuhl, E. Bouchaud, and G. Valentin. Scaling of crack surfaces and implications for fracture mechanics. *Phys. Rev. Lett.* **85**, 1678 (2000).

[MSLV98] S. Morel, J. Schmittbuhl, J. López, and G. Valentin. Anomalous roughening of wood fractured surfaces. *Phys. Rev. E* **58**, 6999 (1998).

[MWR$^+$98] M. Matsushita, J. Wakita, I. Ràfols, T. Matsuyama, H. Sakaguchi, and M. Mimura. Interface growth and pattern formation in bacterial colonies. *Physica A* **249**, 517 (1998).

[Par92] G. Parisi. On surface growth in random media. *Europhys. Lett.* **17**, 673 (1992).

[Pat84] L. Patterson. diffusion–limited aggreation and two–fluid displacements in porous media. *Phys. Rev. Lett.* **52**, 1621 (1984).

[Pau02] E. Pauné. *Interface dynamics in two–dimensional viscous flows*. Ph.D. thesis, Universitat de Barcelona, Barcelona, Spain (2002).

[PC02] E. Pauné and J. Casademunt. Kinetic roughening in two–phase fluid flow through a random Hele–Shaw cell (2002). Cond–mat/0207673.

[PFTV93] W. H. Press, B. P. Flannery, S. A. Teukolsky, and W. T. Vetterling. *Numerical Recipes in C : The Art of Scientific Computing, 2nd Edition* (Cambridge University Press, Cambridge, England, 1993).

[Ram02] J. J. Ramasco. *Invariancia de escala en el crecimiento de superficies e interfases*. Ph.D. thesis, Universidad de Cantabria, Santander, Spain (2002).

[REDG89] M. Rubio, C. Edwards, A. Dougherty, and J. Gollub. Self-affine fractal interfaces from immiscible displacement in porous media. *Phys. Rev. Lett.* **63**, 1685 (1989).

[RH94] S. Roux and A. Hansen. Interface roughening and pinning. *J. Phys. I (France)* **4**, 515 (1994).

[RLR00] J. Ramasco, J. López, and M. Rodríguez. Generic dynamic scaling in kinetic roughening. *Phys. Rev. Lett* **84**, 2199 (2000).

[RZ85] L. R and C. Zarcone. Invasion percolation in an edged network: measurement of a fractal dimension. *Phys. Rev. Lett.* **54**, 2226 (1985).

[Sah95] M. Sahimi. *Flow and transport in porous media and fractured rock* (John Wiley and Sons, New York, 1995).

[SHN98] I. Simonsen, A. Hansen, and O. M. Nes. Determination of the hurst exponent by use of wavelet transforms. *Phys. Rev. E* **58**, 2779 (1998).

[SLKG96] S. D. Sarma, C. J. Lanczycki, R. Kotlyar, and S. V. Ghaisas. Scale invariance and dynamical correlations in growth models of molecular beam epitaxy. *Phys. Rev. E* **53**, 359 (1996).

[SMB$^+$93] L. M. Schwartz, N. Martys, D. P. Bentz, E. J. Garboczi, and S. Torquato. Cross-property relations and permeability estimation in model porous media. *Phys. Rev. E* **48**, 4584 (1993).

[SOHM02a] J. Soriano, J. Ortín, and A. Hernández-Machado. Anomalous roughening in experiments of interfaces in Hele–Shaw flows with strong quenched disorder (2002). Phys. Rev. E, submitted, cond-mat/0208432.

[SOHM02b] J. Soriano, J. Ortín, and A. Hernández-Machado. Experiments of interfacial roughening in Hele–Shaw flows with weak quenched disorder. *Phys. Rev. E* **66**, 031603 (2002).

[SOHM03] J. Soriano, J. Ortín, and A. Hernández-Machado. Forced imbibition of a viscous fluid by a disordered Hele–Shaw cell (2003). Preprint.

[SRR$^+$02] J. Soriano, J. J. Ramasco, M. A. Rodríguez, A. Hernández-Machado, and J. Ortín. Anomalous roughening of Hele–Shaw flows with quenched disorder. *Phys. Rev. Lett.* **89**, 026102 (2002).

[SSW$^+$93] M. Schroeder, M. Siegert, D. E. Wolf, J. D. Shore, and M. Plischke. Scaling of growing surfaces with large local slopes. *Europhys. Lett.* **24**, 563 (1993).

[ST58] P. G. Saffman and G. Taylor. The penetration of a fluid into a porous medium or hele-shaw cell containing a more viscous liquid. *Proc. R. Soc. London A* **245**, 312 (1958).

[SVR95] J. Schmittbuhl, J.-P. Vilotte, and S. Roux. Reliability of self-affine measurements. *Phys. Rev. E* **51**, 131 (1995).

[SWG$^+$86] J. P. Stokes, D. A. Weitz, J. P. Gollub, A. Dougherty, M. O. Robbins, P. M. Chaikin, and H. M. Lindsay. Interfacial stability of immiscible displacement in porous medium. *Phys. Rev. Lett.* **57**, 1718 (1986).

[TL92] L. H. Tang and H. Leschhorn. Pinning by directed percolation. *Phys. Rev. A* **45**, R8309 (1992).

[TvS00] G. Tripathy and W. van Saarloos. Fluctuation and relaxation properties of pulled fronts: A scenario for nonstandard kardar-parisi-zhang scaling. *Phys. Rev. Lett.* **85**, 3556 (2000).

[VCH90] T. Vicsek, M. Cserzo, and V. K. Horváth. Self-affine growth of bacterial colonies. *Physica A* **167**, 315 (1990).

[VSM94] T. Vicsek, M. Shlesinger, and M. Matsushita. *Fractals in natural sciences* (World Scientific, Singapore, 1994).

[Won94] P.-Z. Wong. Flow in porous media: Permeability and displacement patterns. *MRS Bull.* **19**, No. 5, 32 (1994).

[Won98] P.-Z. Wong. The statistical physics of sedimentary rocks. *Phys. Today* **12**, 24 (1998).

[Won99] P.-Z. Wong. *Experimental methods in the physical sciences: Methods of the physics of porous media. Experimental methods in the phyisical sciences, Vol. 35* (Academic Press, Inc, New York, 1999).

[WRI$^+$98] J. Wakita, I. Ràfols, H. Itoh, T. Matsuyama, and M. Matsushita. Experimental investigation on the formation of dense–branching–morphology–like colonies in bacteria. *Journal of the Physical Society of Japan* **67**, 3630 (1998).

[WS81] T. A. Witten and L. M. Sander. Diffusion limited aggregation, a kinetic critical phenomenon. *Phys. Rev. Lett.* **47**, 1400 (1981).

[WW83] D. Wilkison and J. F. Willemsen. Invasion percolation: a new form of percolation theory. *J. Phys. A* **16**, 3365 (1983).

[YWL94] H.-N. Yang, G.-C. Wang, and T.-M. Lu. Instability in low-temperature molecular-beam epitaxy growth of Si/Si(111). *Phy. Rev. Lett.* **73**, 2348 (1994).

[ZMOW97] O. Zik, E. Moses, Z. Olami, and I. Webman. Scaling of propagating capillary fronts. *Euro. Phys. Lett.* **38**, 509 (1997).

[ZZAL92] J. Zhang, Y.-C. Zhang, P. Alstrøm, and M. T. Levinsen. Modelling forest by a paper-burning experiment, a realization of the interface growth mechanism. *Physica A* **189**, 383 (1992).

Author's publications

- Ll. Carrillo, J. Soriano and J. Ortín, *Radial displacement of a fluid annulus in a rotating Hele–Shaw cell*, Phys. Fluids **11**, 778 (1999).
- Ll. Carrillo, J. Soriano and J. Ortín, *Instabilities of a fluid annulus in a rotating Hele–Shaw cell* , Phys. Fluids **12**, 1685 (2000).
- A. Hernández–Machado, J. Soriano, A.M. Lacasta, M.A. Rodríguez, L. Ramírez–Piscina, and J. Ortín, *Interface roughening in Hele–Shaw flows with quenched disorder: Experimental and theoretical results*, Europhys. Lett. **55**, 194 (2001).
- J. Soriano, J. Ortín, and A. Hernández–Machado, *Experiments of interfacial roughening in Hele–Shaw flows with weak quenched disorder*, Phys. Rev. E **66**, 031603 (2002).
- J. Soriano, J.J. Ramasco, M.A. Rodríguez, A. Hernández–Machado, and J. Ortín, *Anomalous roughening of Hele–Shaw flows with quenched disorder*, Phys. Rev. Lett. **89**, 026102 (2002).
- J. Soriano, J. Ortín, and A. Hernández–Machado, *Anomalous roughening in experiments of interfaces in Hele–Shaw flows with strong quenched disorder*, Phys. Rev. E, submitted, cond-mat/0208432 (2002).
- J. Soriano, J. Ortín, and A. Hernández–Machado, *Forced imbibition of a viscous fluid by a disordered Hele–Shaw cell*, preprint (2003).

Part III

Appendices

Appendix A

Software documentation

During the years of this thesis I have developed different applications in C++ intended to provide efficient tools for processing images and data, as well as support applications such as the program for the design of the disorder plates. Because most of this software has become an important tool for the research in our group, their basic documentation is explained in this appendix. The applications that have I designed exclusively for the acquisition of images using the PCVision and PCVision+ frame grabbers are presented in Appendix B.

These are the applications included in this appendix:

- PLATES DESIGN: `PLDESIGN.EXE`.
- TIFF TO BMP CONVERTER: `TIFFCONVERTER.EXE`.
- IMAGE PROCESSING: `SUBPIXEL.EXE`.
- ANALYSIS OF EXPERIMENTAL DATA: `ANALYSIS3.EXE`.

A.1 Design of the disorder plates: `PLDESIGN.EXE`

Jordi Soriano, October 2002.

(This text can be edited and modified using any editor capable of reading RTF formats, such as Word)

BASIC DOCUMENTATION FOR THE PLATES DESIGN PROGRAM.

1. Scope of the program.

This program is the main tool to design the disorder plates that have been used in all the experiments at constant injection rate or constant pressure. The input parameters are all the characteristics that we want to implement in the plate, i.e. size, type of disorder, occupation factor, and some especial features. With this information the program performs all necessary tasks that lead to the generation of two output files, one with the plate information in Autocad LISP language, and a second with the information of the spatial distribution of the disorder. Next, these two files are called from Autocad 13 in order to generate a final `DWG` file that contains the design of the plate in the specific format for the manufacturer.

2. Basic functions in the Main window.

When the application starts we have a main window organized in different sections. In each section we specify different characteristics of the plate. The contents of each section and their functions are explained next.

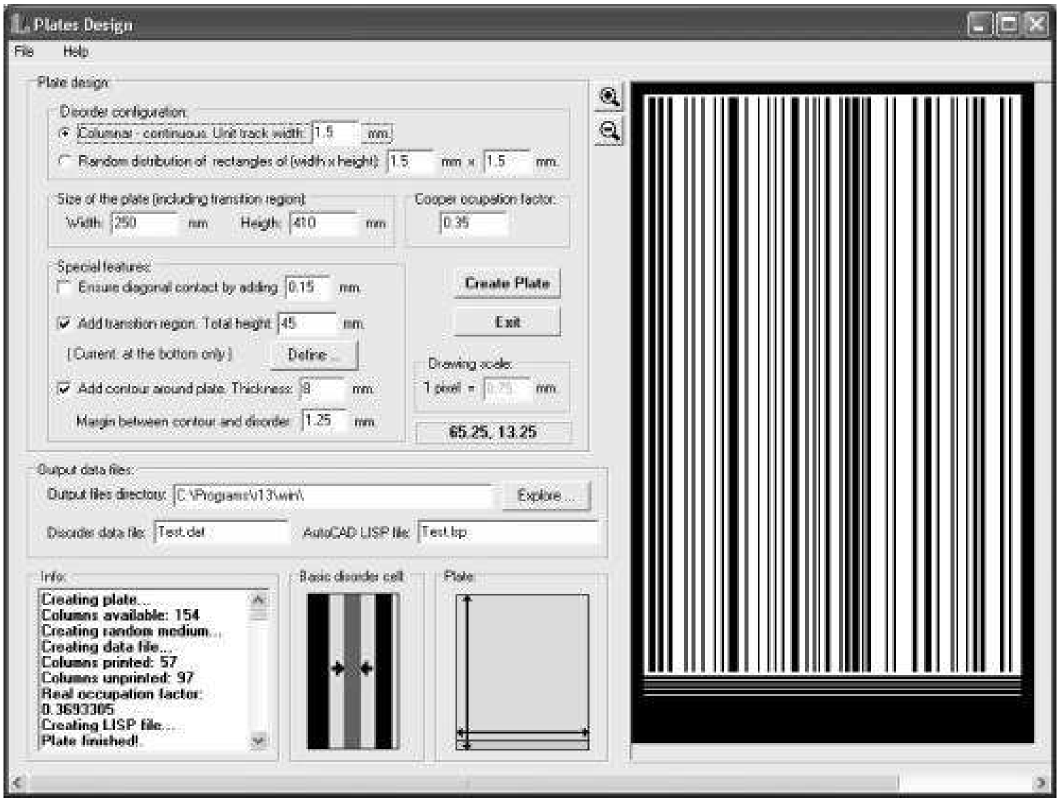

Plate design:

Disorder configuration:
● Columnar - continuous. Unit track width: 1.5 mm.
○ Random distribution of rectangles of (width x height): 1.5 mm x 1.5 mm.

Size of the plate (including transition region):
Width: 250 mm Heigth: 410 mm

Cooper ocupation factor:
0.35

Special features:
☐ Ensure diagonal contact by adding 0.15 mm.
☑ Add transition region. Total height: 45 mm.
(Current: at the bottom only)
☑ Add contour around plate. Thickness: 8 mm.
Margin between contour and disorder: 1.25 mm.

Drawing scale:
1 pixel = 0.75 mm

65.25, 13.25

Output data files:
Output files directory: C:\Programs\r13\win\
Disorder data file: Test.dat
AutoCAD LISP file: Test.lsp

Info:

```
Creating plate...
Columns available: 154
Creating random medium...
Creating data file...
Columns printed: 57
Columns unprinted: 97
Real occupation factor:
0.3693305
Creating LISP file...
Plate finished!
```

2.A. Disorder configuration.

Here we specify the type of disorder that we are interested to implementate. Two options are available:

- **Columnar continuous**: in this case we place a set of tracks, continuous along the *y* direction and randomly distributed along *x*. The tracks occupy the sites of a one-dimensional network. The lattice spacing is what we call the *width of the unit track* and is the value that must be introduced in the corresponding edit box for this disorder configuration. Wider tracks are obtained when two or more unit tracks are placed adjacent. The number of occupied sites depends on the value selected for the **copper occupation factor**, which is number of occupied sites respect to the total sites available. All tracks will have the same height, and the final value will depend on different options of the design, as we will see later.

- **Random distribution of rectangles**: in this case we consider a two dimensional network where the size of the *unit cell* (width x height) is the couple of parameters that the user introduces. The sites will be occupied randomly until the number of occupied sites respect to the total available reaches the preset value of occupation factor. It is important to take into account that, due to the manufacture process, the cells in diagonal are not connected. A correction must be implemented if we are interested in forcing this connection.

The type of disorder configuration selected is represented graphically in an image at the bottom of the main window entitled **basic disorder cell**.

2.B. Size of the plate (including transition regions).

Here we specify the total dimensions of the plate (width x height) in mm. To my knowledge, the **maximum size** available at a reasonable cost in the printed circuit industry is **300 x 560 mm**. The program does not put any limitations to the size of the plate. All special features that the user will incorporate, such as transitions regions or a contour around the plate, will be placed inside these limits. In addition, the *disorder area* will be the region of the cell that is strictly occupied by the disorder. In this region is where the network that will contain the spatial distribution of the disorder is defined.

2.C. Copper occupation factor, *f*.

Is the number of occupied sites respect to the total sites available. The occupied sites will be the copper deposits in the final plate. The total amount of available sites *n* will be calculated using the values of lattice spacing and size of the *disorder area*. The number of sites that will be occupied will be $n \cdot f$, with 0 ? f ? 1. The program will show a warning if we try to put a value of *f* outside these limits. The default value of *f* is 0.35.

2.D. Special features.

- **Ensure diagonal contact**: Activate this checkbox to force diagonal contact of copper islands by enlarging slightly the size of the occupied sites. The typical value that we have use to ensure diagonal contact is 0.15 mm. This additional copper force an overlap between next-nearest neighbors. In the final, manufactured plate, the overlap leaves small bridges of copper that connects copper aggregations in diagonal.

If this checkbox is deactivated no correction will be applied whatever its value.

- **Add transition regions**: the transition regions are transverse copper tracks (i.e. continuous along x) that occupies all the width of the plate. They are usually placed at the beginning of the plate and their purpose is to allow preparing an initial flat front for the interface. The user is free to place up to five transition regions of arbitrary height. However, the program must know which portion of the total length of the plate will be reserved for the transition regions in order to calculate the area available for the disorder. The edit box entitled **total height** must be filled to tell the program the total length that will be reserved for the transition regions. An example at the end will clarify all the ideas explained here.

To specify the properties of the whole reserved area and the vertical position of each transition region we have to click the **Define** button. This will open a new window. We have two groups of options:

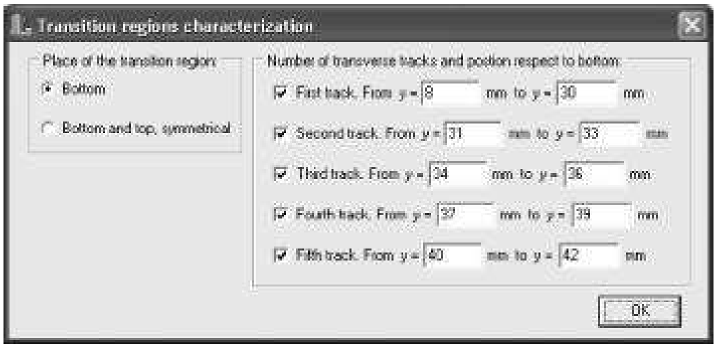

● Bottom
○ Bottom and top, symmetrical

☑ First track. From y = 8 mm to y = 30 mm
☑ Second track. From y = 31 mm to y = 33 mm
☑ Third track. From y = 34 mm to y = 36 mm
☑ Fourth track. From y = 37 mm to y = 39 mm
☑ Fifth track. From y = 40 mm to y = 42 mm

- On the left side of the window we specify if we want only one transition region at the bottom, or two transition regions placed in the extremes of the plate and <u>symmetrical</u> (do not forget this!).

- On the right side of the window we specify the characteristics of each transition region. You may activate as many transition regions as you need. Those that are not activated will be ignored whatever their values. **<u>The position of the transition regions are respected to the bottom plate limits</u>**. This means that if we add a border of copper around the plate (see later) the position of the transition regions does not change due to the presence of the border, so the border can overlap some transition regions. An example in brief will clarify this idea.

Once you have finished specifying the different transition regions, just click OK to return to the main menu.

Important: the end of the last transition region must be located at a position smaller than or equal to the value indicated in the total height. Otherwise this transition region would appear inside the disorder area.

Notice that when you return to the main window, a drawing at the bottom of the window indicate schematically if you have activated or not the transition regions and where they are located. This information is also indicated just below the check box.

- **Add contour around plate**: by checking this option the program will add a contour of copper around the plate. The width of the contour are set up in the corresponding check box. You may also add a margin in order to avoid that the copper deposits would be in contact directly with the border. From an experimental point of view, it is convenient to add this extra margin (typically of 1 mm) to minimize side wall effects.

This option of adding a border has been specifically implemented for the experiments at constant pressure.

Be careful if you activate both the transition regions and the border around plate at the same time, because some transition regions can be overlapped by the border. In addition, the border only reduces the total area available for the disorder laterally. The total height reserved for the transition region is what indeed limits the area available vertically.

2.E. Drawing scale.

The value introduced here only affects the preview of the plate. It simply tells the program how many mm of the designed plate correspond to 1 pixel on the screen. I recommend to use 3 pixels to represent the lateral length of the unit cell. For example, if the unit track width is 1.5 mm we will put 0.5 to the edit box. Once the plate is designed and the preview shown, you may use the magnifying glasses at the left of the image to enlarge or reduce the view of the plate at your convenience. The printed areas (copper in the manufactured plate) will be shown in black, and the unprinted areas (fiberglass substrate) in white.

2.F. Output data files.

Here we specify the directory where the data files will be saved and the name of the two output files. Over all these years the final stage in the design of the plates has been performed using Autocad 13. All explanations that follow, as well as the examples, suppose that the Autocad 13 has been the program used.

- **Output files directory**: For convenience, the two output files must be saved in the directory `WIN` of the folder group where Autocad 13 is installed (for example `C:\PROGRAMS\R13\WIN`). Once the plate is designed and saved, the files stored in ...`\WIN` are no longer necessary in this directory and can be moved to a more convenient place. If you want to save the output files in a specific location and then copy them to the Autocad folder you can specify the new location by typing it directly in the Edit box or by clicking the button **Explore**. This button opens a new window that allows exploring the hard disk. When you have found the desired location (it is also indicated in the blue panel at the bottom) just click **Select directory and close** to return to the main window and update the path information.

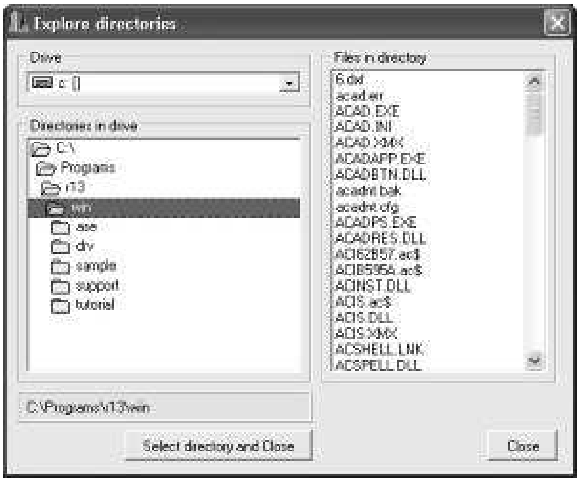

C:\Programs\r13\win

- **Disorder data file**: Here we specify the name of the file that will contain the spatial distribution of the disorder. The format is a single column of data that contain the left-bottom coordinates of the printed unit cells, in mm. Each couple of values represent the (x, y) coordinates. An example of an output file will be given later. The name for this file is usually short (I do not recommend to use long names) and with extension `.DAT`, e.g. `PLATE.DAT`.

- **Autocad LISP file**: The LISP language is a powerful engine used to create macros in Autocad. To generate the final plate the program loads first this file and, using the plate specifications written in the file, will prompt the user for the name of the disorder data file, will read it, and will start the draw of plate. The name for the lisp file can be the same as the disorder file, but with the extension `.LSP`, e.g. `PLATE.LSP`. This lisp file can be edited as a text file and modified if needed. All the parameters of the plate are automatically incorporated in the header of the file for further reference. See **Sec. 4** for a detailed explanation of the steps that must be done to generate a drawing of the final plate.

Note: the program adds automatically a line around the plate limits. It won't appear in the final, real plate but it is necessary to tell the manufacturer where exactly the plate ends.

3. Three examples of different plates.

3.A. Columnar continuous, T 1.50.

i) Specifications:
- Unit track width: 1.50 mm.
- Size of the plate: 350 x 560 mm.
- Occupation factor: 0.35.
- Diagonal contact: (Not applicable).
- Transition regions: 5 regions, only at bottom. Positions:
    - First: from 0 to 10 mm.
    - Second: from 11 to 13 mm.
    - Third: from 14 to 16 mm.
    - Fourth: from 17 to 19 mm.
    - Fifth: from 20.5 to 21 mm.
- The total height specified is 21 mm, so the disorder starts exactly at the end of the last region.
- Contour around plate: None.
- Files name: `Col15b.dat` and `Col15b.lsp`.

(This plate was used for the experiments of anomalous scaling)

ii) Contents of the file `Col15b.dat` (we represent the first 15 pairs of points):

```
0
21
3
21
4.5
21
9
21
10.5
21
12
21
15
21
21
21
25.5
21
33
21
34.5
21
36
```

```
21
37.5
21
45
21
46.5
21
```

iii) Contents of the file `Col15b.lsp`:

```
; This file was generated by 'Plates Design' program.
; 1999, Jordi Soriano.
; Plate design date: 28/06/00. Time: 23:30:31.
; Plate parameters:
;   Plate dimensions: 350 x 560 mm (width x height).
;   Noise type: columnar continuous.
;   Basic column width: 1.5 mm.
;   Basic column height: 539 mm.
;   Maximum columns available: 233.
;   Columns printed: 83.
;   Copper occupation factor: 35.5714 %.
;   Transition area height: 21 mm.
;
; The next function reads a list of pairs (x, y) and draw in
; AutoCAD a filled area that this same function defines as an object.
; This delays the generations of the drawing, but the DXF file produced
; is smaller than the one generated by faster drawings
;
(defun C:LAT ()

  (COMMAND "_LIMITS" "0,0" "350,560")     ; Area limits

  (COMMAND "_ZOOM" "_ALL")

  (setq name (getstring "\n File Name: "))

  (setq fitxer (open name "r"))

  (setq ce (getvar "cmdecho"))     ; Saves this environment var
  (setvar "cmdecho" 0)             ; NO echo --> Faster execution
;

; Now we define an object named q (the shorter the name, the shorter
; the DXF file), which is a filled area with a width equal to the width
; of the disorder column, and a height equal to the length of the plate minus
; the 'transitions areas', if they are present.

  (setq cx "1")
  (COMMAND "_ortho" "_on")
  (COMMAND "_Fill" "_on")
  (COMMAND "_SOLID" "0,0" "0,539" "1.5,0" "1.5,539" "")
  (COMMAND "_BLOCK" "q" "0,0" "0,0" "")
  ;

  (setq cx (read-line fitxer))     ; Read the first point to make the
  (setq cy (read-line fitxer))     ; logic of the while loop work.
  (while cx
    (setq x (atof cx)
          y (atof cy)
    )
    (COMMAND "_INSERT" "q" (list x y) "1" "1" "0"
    )
    (setq cx (read-line fitxer))
    (setq cy (read-line fitxer))
  )
  (close fitxer)

  (COMMAND "_SOLID" "0,0" "0,10" "350,0" "350,10" "")   ; Bottom first transition region.
  (COMMAND "_SOLID" "0,11" "0,13" "350,11" "350,13" "")   ; Bottom second transition region.
  (COMMAND "_SOLID" "0,14" "0,16" "350,14" "350,16" "")   ; Bottom third transition region.
  (COMMAND "_SOLID" "0,17" "0,19" "350,17" "350,19" "")   ; Bottom fourth transition region.
  (COMMAND "_SOLID" "0,20.5" "0,21" "350,20.5" "350,21" "")   ; Bottom fifth transition
region.

  (COMMAND "_LINE" "0,0" "350,0" "350,560" "0,560" "0,0" "")      ; Line around the plate
limits
```

```
  (setvar "cmdecho" ce)
  (COMMAND "_DXFOUT" "" "6")     ; The DXF file is produced automatically
)                                ; with the same name as the drawing
```

iv) Example of the resulting plate (Fig. 1 in the printed version of this documentation).

3.B. Random distribution of squares, SQ-n 1.50.

i) Specifications:
- Dimensions of the unit cell: 1.50 x 1.50 mm.
- Size of the plate: 350 x 557 mm.
- Occupation factor: 0.35.
- Diagonal contact: Yes, adding 0.15 mm.
- Transition regions: 5 + 5 regions, both at top and bottom, symmetrical. Position of the bottom regions:
  - · First: from 0 to 10 mm.
  - · Second: from 11 to 13 mm.
  - · Third: from 14 to 16 mm.
  - · Fourth: from 17 to 19 mm.
  - · Fifth: from 21 to 21.5 mm.
- The total height specified is 21.5 mm, so the disorder starts exactly at the end of the last region.
- Contour around plate: None.
- Files name: `SQ15b.dat` and `SQ15b.lsp`.

ii) Contents of the file `SQ15b.dat` (we represent the first 15 pairs of points):

```
1.5
21.5
6
21.5
9
21.5
13.5
21.5
19.5
21.5
22.5
21.5
25.5
21.5
31.5
21.5
34.5
21.5
36
21.5
39
21.5
43.5
21.5
60
21.5
64.5
21.5
69
21.5
```

iii) Contents of the file `SQ15b.lsp`:

```
; This file was generated by 'Plates Design' program.
; 1999, Jordi Soriano.
; Plate design date: 29/06/00. Time:  1:21:33.
; Plate parameters:
;   Plate dimensions: 350 x 557 mm (width x height).
;   Noise type: random distribution of rectangles.
;   Basic square width: 1.5.
;   Basic square height: 1.5.
;   Maximum squares available: 79919.
;   Squares printed: 27883.
;   Diagonal contact ensured by adding 0.15 mm.
```

```
;   Copper occupation factor: 34.8891 %.
;   Transition area height: 21.5 mm.
;
; The next function reads a list of pairs (x, y) and draw in
; AutoCAD a filled area that this same function defines as an object.
; This delays the generations of the drawing, but the DXF file produced
; is smaller than the one generated by faster drawings
;
(defun C:LAT ()

  (COMMAND "_LIMITS" "0,0" "350,557")     ; Area limits

  (COMMAND "_ZOOM" "_ALL")

  (setq name (getstring "\n File Name: "))

  (setq fitxer (open name "r"))

  (setq ce (getvar "cmdecho"))     ; Saves this environment var
  (setvar "cmdecho" 0)             ; NO echo --> Faster execution
;

; Now we define an object named q (the shorter the name, the shorter
; the DXF file), which is a filled area with a width equal to the width
; of the noise column, and height equal to the lenght of the plate minus
; the 'transitions areas', if they are present.

  (setq cx "1")
  (COMMAND "_ortho" "_on")
  (COMMAND "_Fill" "_on")
  (COMMAND "_SOLID" "0,0" "0,1.62" "1.62,0" "1.62,1.62" "")
  (COMMAND "_BLOCK" "q" "0,0" "0,0" "")
  ;

  (setq cx (read-line fitxer))     ; Read the first point to make the
  (setq cy (read-line fitxer))     ; logic of the while loop work.
  (while cx
    (setq x (atof cx)
          y (atof cy)
    )
    (COMMAND "_INSERT" "q" (list x y) "1" "1" "0"
    )
    (setq cx (read-line fitxer))
    (setq cy (read-line fitxer))
  )
  (close fitxer)

  (COMMAND "_SOLID" "0,0" "0,10" "350,0" "350,10" "")   ; Bottom first transition region.
  (COMMAND "_SOLID" "0,11" "0,13" "350,11" "350,13" "")   ; Bottom second transition region.
  (COMMAND "_SOLID" "0,14" "0,16" "350,14" "350,16" "")   ; Bottom third transition region.
  (COMMAND "_SOLID" "0,17" "0,19" "350,17" "350,19" "")   ; Bottom fourth transition region.
  (COMMAND "_SOLID" "0,21" "0,21.5" "350,21" "350,21.5" "")   ; Bottom fifth transition
region.

  (COMMAND "_SOLID" "0,557" "0,547" "350,557" "350,547" "")   ; Top first transition region.
  (COMMAND "_SOLID" "0,546" "0,544" "350,546" "350,544" "")   ; Top second transition region.
  (COMMAND "_SOLID" "0,543" "0,541" "350,543" "350,541" "")   ; Top third transition region.
  (COMMAND "_SOLID" "0,540" "0,538" "350,540" "350,538" "")   ; Top fourth transition region.
  (COMMAND "_SOLID" "0,536" "0,535.5" "350,536" "350,535.5" "")   ; Top fifth transition
region.

  (COMMAND "_LINE" "0,0" "350,0" "350,557" "0,557" "0,0" "") ; Line arround the plate limits

  (setvar "cmdecho" ce)
  (COMMAND "_DXFOUT" "" "6")     ; The DXF file is produced automatically
)                                ; with the same name as the drawing ; with the same name as
the drawing
```

iv) Example of the resulting plate (Fig. 2 in the printed version of this documentation).

3.C. ‘Constant pressure’ plate with SQ 1.50.

i) Specifications:

- Dimensions of the unit cell: 1.50 x 1.50 mm.
- Size of the plate: 206 x 556 mm.
- Occupation factor: 0.35.
- Diagonal contact: None.
- Transition regions: 1 + 1 region, both at top and bottom, symmetrical. Position of the bottom region: from 58 to 68 mm.
- The total height specified is 69.5 mm, so there is a gap of 1.5 mm between the end of the transition region and the beginning of the disorder.
- Contour around plate: Yes, 8 mm, with a margin of 1.25 mm at each side.
- Files name: `Press110.dat` and `Press110.lsp`.

(Notice that the combination of the contour around plate plus the only transition region allows creating a deposit for the fluid at the extremes of the plate)

ii) Contents of the file `Press110.dat` (we represent the first 15 pairs of points):

```
12.25
69.5
18.25
69.5
21.25
69.5
27.25
69.5
34.75
69.5
45.25
69.5
52.75
69.5
55.75
69.5
60.25
69.5
66.25
69.5
69.25
69.5
75.25
69.5
84.25
69.5
94.75
69.5
97.75
69.5
```

iii) Contents of the file `Press110.lsp`:

```
; This file was generated by 'Plates Design' program.
; 1999-2002, Jordi Soriano.
; Plate design date: 01/07/2002. Time:  0:22:39.
; Plate parameters:
;   Plate dimensions: 206 x 556 mm (width x height).
;   Noise type: random distribution of rectangles.
;   Basic square width: 1.50.
;   Basic square height: 1.50.
;   Maximum squares available: 37100.
;   Squares printed: 12970.
;   Copper occupation factor: 35.07 %.
;   Transition area height: 69.5 mm.
;
; The next function reads a list of pairs (x, y) and draw in
; AutoCAD a filled area that this same function defines as an object.
; This delays the generations of the drawing, but the DXF file produced
; is smaller than the one generated by faster drawings
;
(defun C:LAT ()

  (COMMAND "_LIMITS" "0,0" "208,556")     ; Area limits

  (COMMAND "_ZOOM" "_ALL")
```

```
  (setq name (getstring "\n File Name: "))

  (setq fitxer (open name "r"))

  (setq ce (getvar "cmdecho"))     ; Saves this environment var
  (setvar "cmdecho" 0)             ; NO echo --> Faster execution
;

; Now we define an object named q (the shorter the name, the shorter
; the DXF file), which is a filled area with a width equal to the width
; of the noise column, and a height equal to the length of the plate minus
; the 'transitions areas', if they are present.

  (setq cx "1")
  (COMMAND "_ortho" "_on")
  (COMMAND "_Fill" "_on")
  (COMMAND "_SOLID" "0,0" "0,1.5" "1.5,0" "1.5,1.5" "")
  (COMMAND "_BLOCK" "q" "0,0" "0,0" "")
  ;

  (setq cx (read-line fitxer))     ; Read the first point to make the
  (setq cy (read-line fitxer))     ; logic of the while loop work.
  (while cx
    (setq x (atof cx)
          y (atof cy)
    )
    (COMMAND "_INSERT" "q" (list x y) "1" "1" "0"
    )
    (setq cx (read-line fitxer))
    (setq cy (read-line fitxer))
  )
  (close fitxer)

  (COMMAND "_SOLID" "0,0" "0,8" "206,0" "206,8" "")   ; Bottom border.
  (COMMAND "_SOLID" "0,556" "0,548" "206,556" "206,548" "")   ; Top border.
  (COMMAND "_SOLID" "0,8" "0,548" "8,8" "8,548" "")   ; Left border.
  (COMMAND "_SOLID" "198,8" "198,548" "206,8" "206,550" "")   ; Right border.

  (COMMAND "_SOLID" "8,58" "8,68" "198,58" "198,68" "")   ; Bottom transition region.

  (COMMAND "_SOLID" "8,488" "8,498" "198,488" "198,498" "")   ; Top transition region.

  (COMMAND "_LINE" "0,0" "206,0" "206,556" "0,556" "0,0" "") ; Line around the plate limits

  (setvar "cmdecho" ce)
  (COMMAND "_DXFOUT" "" "6")     ; The DXF file is produced automatically
)                                ; with the same name as the drawing
```

iv) Example of the resulting plate (Fig. 3 in the printed version of this documentation)

4. Creating the final plate using Autocad 13.

The necessary steps to create the final plate are described next. We will suppose that the name of the files are `plate.lsp` and `disorder.dat`.

- Launch Autocad 13 and go to File/New. In “New drawing plate” type the name of the final file, for example `design` (do not put any extension). The click OK.
- In the command window (at the bottom of the application) type

```
(LOAD “PLATE.LSP”)
```

and press enter.

- The file that contains the description has been read. You will notice that the word `LAT` appears just below the last ordered typed. This word is a new instruction designed for reading and drawing the disorder cells. Type `LAT` and press enter.

- The program will show the message `File name:`. Introduce the name of the disorder file, i.e. `disorder.dat` and press enter. The disorder will be drawn plus all the specified features. The last thing the programs asks is the numerical accuracy for the drawing. Just press enter to use the default value of 6.

- The plate is generated and the files `design.dwg` and `design.dxf` generated. The manufacturer only needs the drawing (dwg) file. The other can be used as a security copy. If you want to print out a copy of the design I strongly recommend to import the dwg file from Corel Draw and print it there. In addition the dwg format is vectorial, so from Corel all different sections can be resized if necessary.

5. Menu tools and program options.

All functions in this program are performed through the main window and daughter windows. In the menu there are only the **Exit** and **Help** options.

- **Exit**: Saves the information stored in all fields and closes the application. When the program restarts the fields are updated with the contents previously saved. This information is stored in a file called `PlDesign.cfg`. If the file is deleted by accident or is corrupted, a new one will be generated automatically and default values will be used for the fields.

- **Help** / **Basic Documentation**: Opens this document.

6. Important issues.

- Try to avoid unnecessary overlaps between different areas. Some overlaps are strictly necessary (to ensure diagonal contact, for example) but in general they must be avoided because can cause confusion to the manufacturer. A typical situation of overlap is when we have placed a transition area over another, or when the contour around the plate covers the first transition area.

- The manufacturer of our plates is the company 2CI S.A. Address:

2CI Circuitos impresos
Ciutat de Granada, 130, 1er. 08018 Barcelona
Telf: 934850095
Fax: 933009260
e-mail: 2cisa@2cisa.com
Web: www.2cisa.com

- For perfect operation the program must be located in the following directory: ‘`C:\Jordi\C\PlatesDesign`’. To install it in a different location it must be re-compiled. Contact me for details.

- Be sure that all files in the directory where the program is located are **NOT** Read-only. (This happens when copying the application from a CD-ROM). The program saves the preferences in a file called `PlDesign.cfg`. If this file is read-only the program cannot save the preferences.

- This basic documentation help won’t be displayed if the document is in use by other program, such as Word.

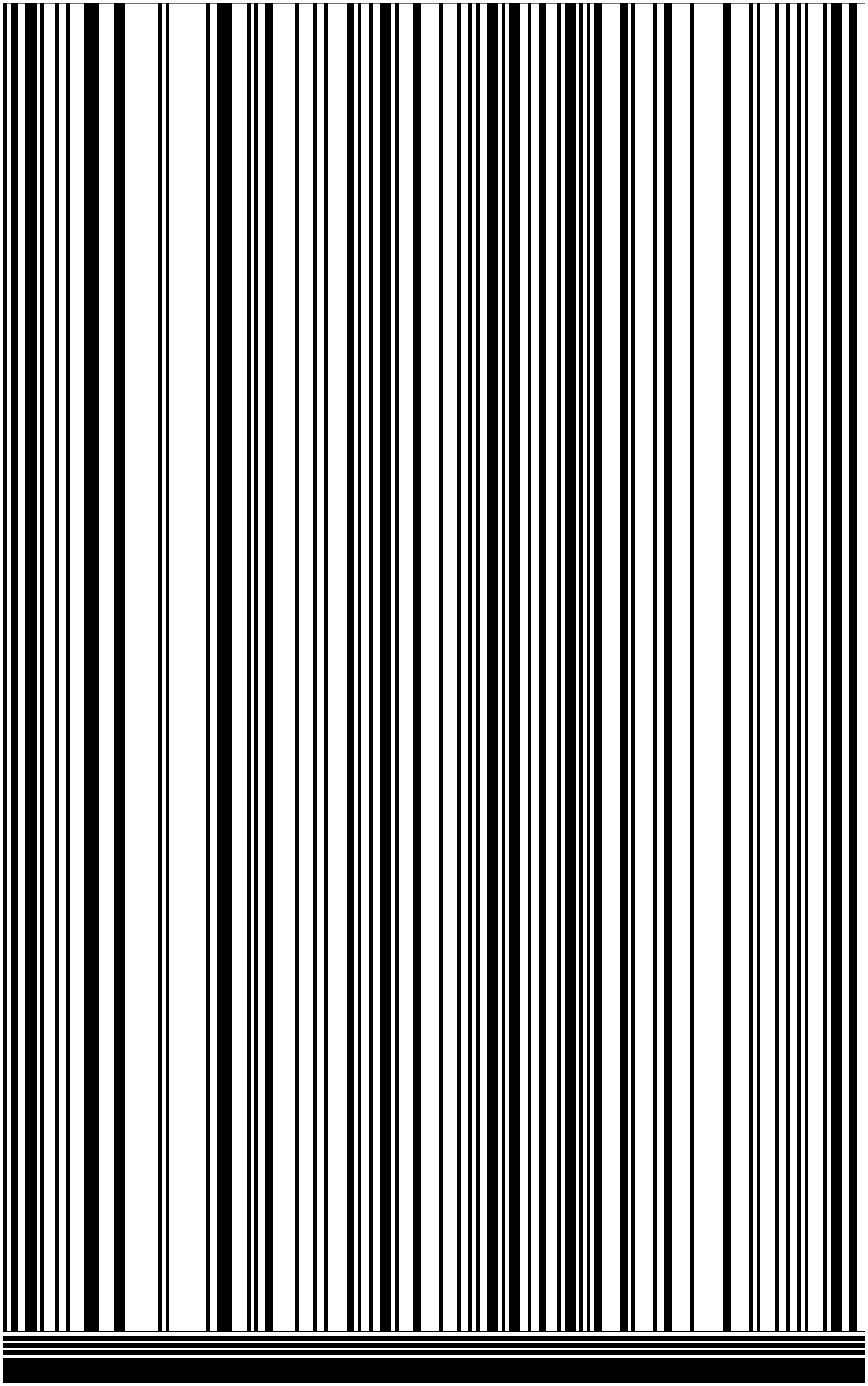

Fig. 1. Plate with disorder T 1.50

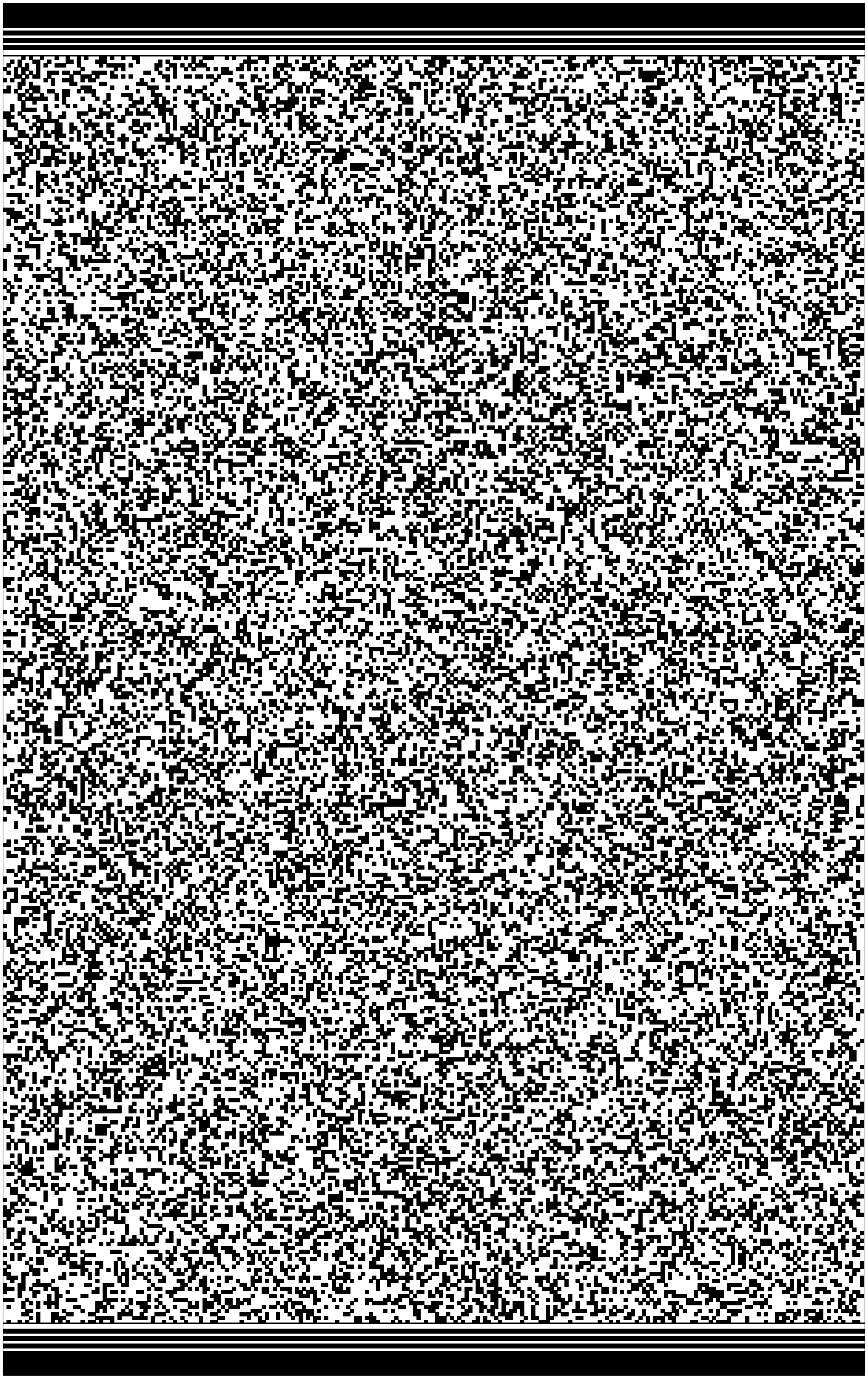

Fig. 2. Plate with disorder SQ-n 1.50

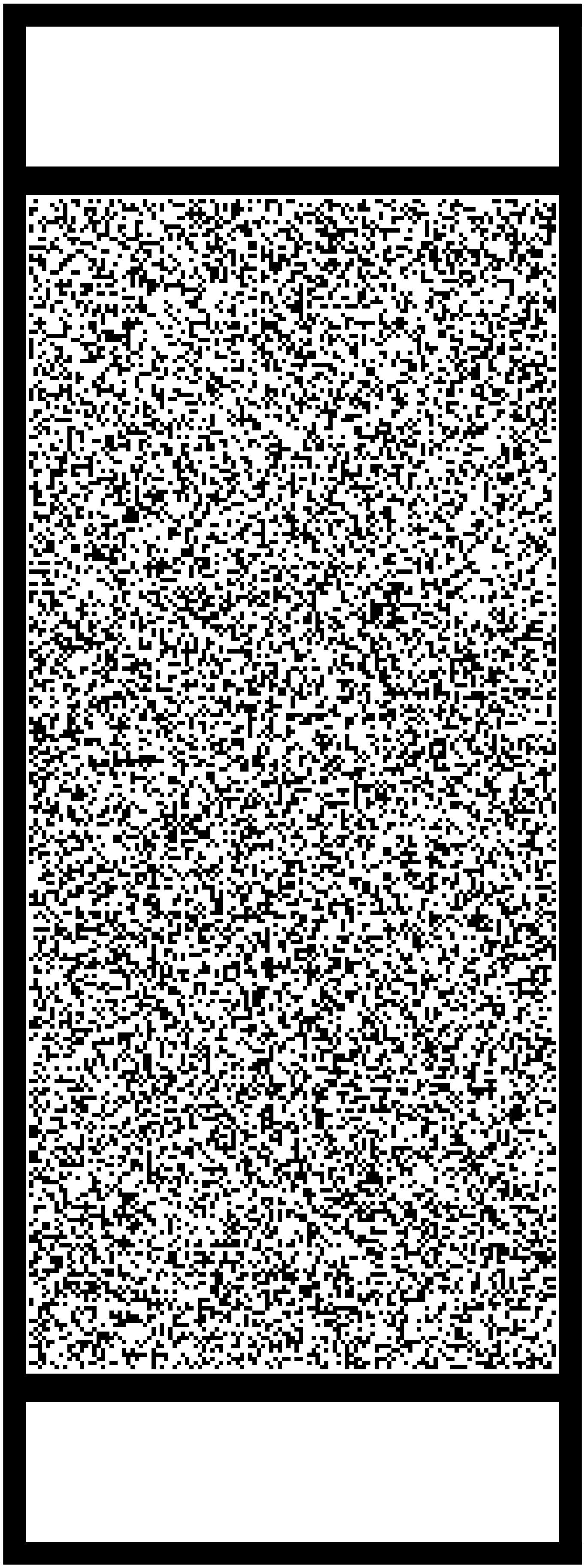

Fig. 3. ‘Constant pressure’ plate with disorder SQ 1.50

A.2 TIFF to BMP converter: `TIFFCONVERTER.EXE`

Jordi Soriano, August 2002.

(This text can be edited and modified using any editor capable of reading RTF formats, such as Word)

BASIC DOCUMENTATION FOR THE TIFF CONVERTER.

1. Scope of the program.

This program is designed to convert the images obtained from the cameras, in TIFF format, to BMP, which is the format supported for the image analysis software. TIFF is the abbreviation of ‘Tagged Image File Format’, and is a powerful –but complex in structure– storage format used in many frame grabbers.

Basically, what the program does is to read a TIFF file, extract the image information, rebuild it in the BMP format, create a BMP header for the image, and save the new image with the same name of the original.

2. Basic functions.

The program only accepts gray-scaled, uncompressed TIFF files, which is the output format of the PCVision and PCVisionPlus frame grabbers. Other input formats may cause program instability. There is no limitation on the size of the images. The program supposes that the images are numbered and in 8:3 format (8 characters for name plus 3 for extension). Images are characterized by a header name plus the number of the image filling 8 characters, such as `IM000000.TIF`, `IM000101.TIF`, or `IM000500.TIF`.

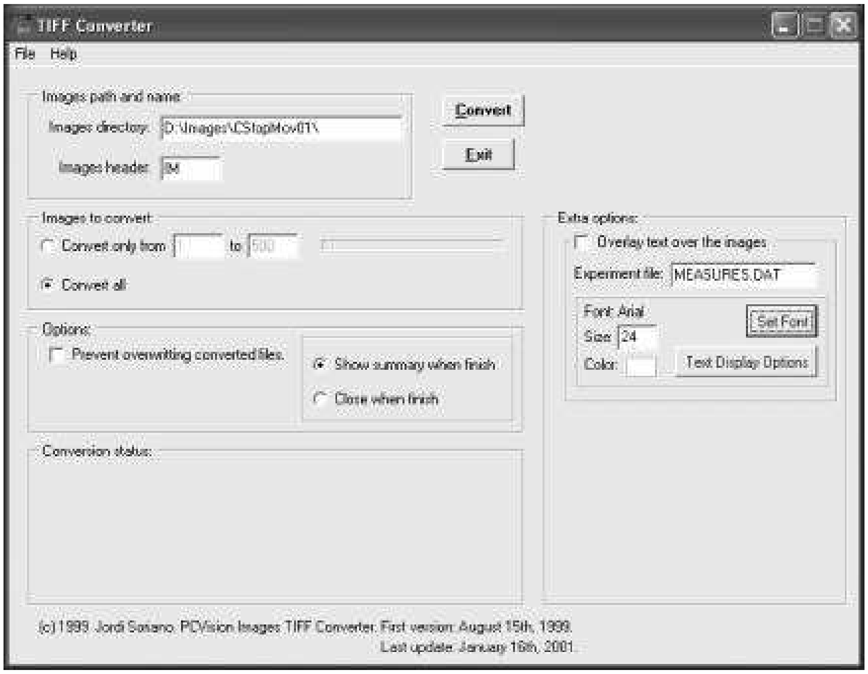

Images path and name
Images directory: D:\Images\CStopMov01\
Images header: IM

Images to convert:
○ Convert only from 1 to 500
● Convert all

Options:
☐ Prevent overwriting converted files.
● Show summary when finish
○ Close when finish

Extra options:
☐ Overlay text over the images
Experiment file: MEASURES.DAT
Font: Arial
Size: 24
Color:

Conversion status:

(c) 1999 Jordi Soriano. PCVision Images TIFF Converter. First version: August 15th, 1999.
Last update: January 16th, 2001.

In the fields **images directory** and **images header** we specify the location of the images in the hard disk and the header name of the images (`IM` in the previous example list). In **Images to convert** we specify which images we want to convert. If we select **Convert All**, all the images with the specified parameters will be converted.

Once all the fields have been completed, we press **Convert** and the conversion will start. If no images could be found, a warning message will appear. Otherwise, the conversion will start and in the **Conversion Status** panel we will receive information about the images converted: images dimensions, color depth (must be gray-scale) and compression (must be no compression).

When the conversion finishes, we can select **close the program automatically** or show a **summary**. Usually there is no problems, so I recommend to select the first option.

The option **Prevent overwriting existing files** allows checking if the converted files already exists. If the option is unchecked, the BMP images will be overwritten.

Important: if there are already BMP files in the directory and we overwrite them , the operation will fail if the images are read only. In this case the program can become unstable when trying to overwrite the images. For this reason, be sure that the files are not read-only unnecessarily. (Usually, some files can be automatically set to read-only when copied from a CD-ROM to the hard disk).

3. Advanced functions.

An interesting function that I have added to the program is the possibility to add a label over the images indicating the acquisition time. This is very useful to create a movie of the experiment with the capture time is displayed in one corner of the images. I do not recommend this option when the objective is to analyze the images, because the added text can difficult the analysis of the images if it crosses the interface.

The action of adding text is very simple. First, you should check **Overlay text over the images**, and then select the Font type, color, and size that you want. Because images are in grayscale, the labels will appear also in gray scale (if you select yellow as the font color, it will appear white; blue will appear light gray, etc). The **experiment file** is the name of the file that contains the information about the image number, camera selected, and capture time. This file is automatically created during an experiment and **must be present in the directory of the images**. A sample experiment file is the following (it has been cut out after image number 20 to reduce length):

```
##################################################
-- AUTOMATIC ACQUISITION EXPERIMENT --
  Images expected: 200
  Duration of the experiment: 6500 s
  Capture type: logarithmic in time
--------------------------------------
Experiment date: 11/04/2000
Experiment time: 20:17:17
Images header name:  IM
Images directory:  c:\IMAGES\Col118\
Info files directory:  c:\IMAGES\Col118\
Experiment code: Col118
Experiment geometry: rectangular
Cell type: sizeable cell
           (upper injection + torical ring)
Plates manufacturer and date: 2CI, November '99
Other plates information:
    Length: 56 cm.
    Code: COL99-20.2 (1.5 mm)
    Orientation: Only one available
    Plate fixing method: Removable stick glue
    Spacers disorder-glass: Yes
    Injection type: Upper glass (two holes)
                    50 ml syringe.
    Upper glass: 2 cm thick
Experiment parameters: b=0.36 mm; Q=20 ml/h; W=190 mm
Images calibration:
  Camera 0:
    width_pixels=768; width_mm=281
```

```
    height_pixels=574; height_mm=213
  Camera 1:
    width_pixels=768; width_mm=281
    height_pixels=574; height_mm=213
Author: Jordi Soriano
Notes:

##################################################

0, 0,  0.00
0, 1,  0.88
0, 2,  1.21
0, 3,  1.54
0, 4,  1.87
0, 5,  2.14
0, 6,  2.47
0, 7,  2.75
0, 8,  3.08
0, 9,  4.01
0, 10,  4.62
0, 11,  4.95
0, 12,  5.22
0, 13,  5.77
0, 14,  6.10
0, 15,  6.76
0, 16,  7.14
0, 17,  7.64
0, 18,  8.02
0, 19,  8.35
0, 20,  8.96
```

In an experiment file the first column is the camera used (0 or 1) and is a field ignored. The second column is the image number, and the third the capture time. All the information between the lines labeled ################## is also ignored. If the experiment file is lost you can create one following this sample.

The next step is to select the position of the text. Click **Text Display Options**. A new window will appear. Use the fields in **Text Position** to set the position of the text over the image. A sample image will help deciding a good location. Finally, use the field **Show time in** to decide if the time will appear in seconds or in HH:MM:SS. The first option is recommended for short experiments (below one hour). The second for long time experiments. In addition, we can decide if the time is the absolute (i.e., as it appears in the time list of the experiment file) or relative to the first image (i.e.., the time of the first image will be subtracted to all others). Select the desired option in **Time range** to set this option.

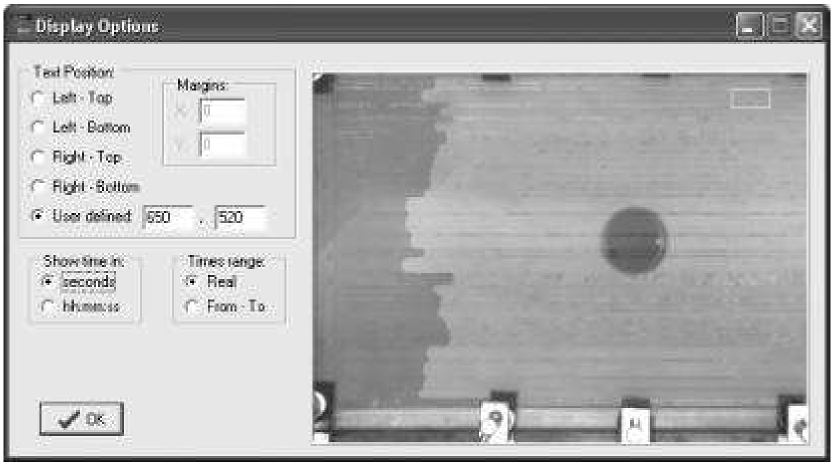

Display Options

Text Position:
○ Left - Top
○ Left - Bottom
○ Right - Top
○ Right - Bottom
● User defined 650 , 520

Margins:
X 0
Y 0

Show time in:
● seconds
○ hh:mm:ss

Times range:
● Real
○ From - To

Possibly you will need a couple of trials before you are satisfied with the position and size of the text. Usually I use a Font Arial, color white, and a size in the range 24 – 36, depending on the images size.

4. Important issues.

- For perfect operation the program must be located in the following directory: ‘`C:\Jordi\C\TIFFConverter`’. To install it in a different location it must be re-compiled. Contact with me for details.

- Be sure that all files in the directory where the program is located are **NOT** Read-only. The program saves the preferences in a file called `Converter.cfg`. If this file is read-only the program cannot save the preferences and will show an error message.

- Be sure that the images are in gray-scale (8 bits color depth). RGB (16, 24, or 32 bits color depth), monochrome or other formats are not supported, as well as compressed TIF.

- Most of the documentation concerning TIFF images can be found on the web. I used the **TIFF Revision 6** documentation from Hewlett-Packard (I have print it out and can be found in our Lab with the documentation of the cameras). To learn more about the TIFF format, edit the source code of this program. It is fully commented.

- This basic documentation help won’t be displayed if the document is in use by other program, such as Word.

A.3 Image analysis: `SUBPIXEL.EXE`

Jordi Soriano, August 2002.

(This text can be edited and modified using any editor capable of reading RTF formats, such as Word)

BASIC DOCUMENTATION FOR THE IMAGE ANALYSIS PROGRAM.

1. Scope of the program.

This program is thought to process the images obtained from experiments. The images have been previously converted from TIF to BMP using TIFFConverter. The program subtracts all images respect to a base image and then reduces the resulting images to a black and white contour by means of applying a threshold level. The contour is then resolved using 1-pixel accuracy and data is stored for further analysis. The program allows to decide the origin of coordinates and the system of reference, so the final data is ready for direct processing.

2. Basic functions on the Main window.

When the application starts we have two tool panels, **Process Operations** and **Input and Output files**, and some windows. These windows will display, during image processing, the source image (i.e. the original image in grey-scale level), the processed image (i.e. the source image after subtracting the base image and applying the desired threshold level), and the histogram of the processed image.

Important: The program supposes that **the name of the images is exactly 8 characters long** (plus the extension), and that the images are numbered. A short header can be used to identify different groups of images. Typically the name of the images is of the style `IM000000.BMP`, `IM000500.BMP`, etc.. The header in this case is ‘`IM`’.

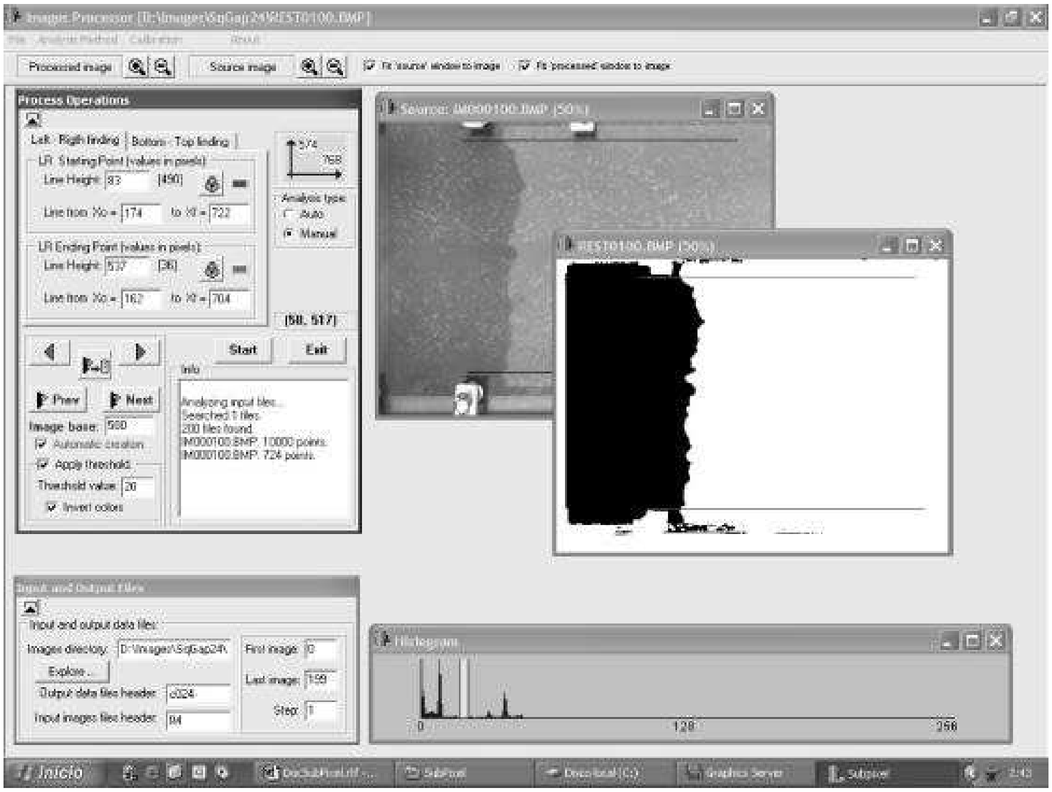

LR Starting Point (values in pixels)
Line Height: 83 [490]
Line from Xo = 174 to Xf = 722

LR Ending Point (values in pixels)
Line Height: 537 [36]
Line from Xo = 162 to Xf = 704

[58, 517]

Image base: 500
☑ Automatic creation
☑ Apply threshold
Threshold value: 20
☑ Invert colors

```
Analyzing input files...
Searched 1 files
200 files found
IM000100.BMP: 10000 points
IM000100.BMP: 724 points
```

Input and output data files:
Images directory: D:\Images\SqGap24\
Output data files header: c024
First image: 0
Last image: 159
Step: 1

2.A. The image windows.

When an image is loaded it appears in the **source window** as it is, whereas in the **process window** the image appears subtracted respect to the base image and with the threshold applied. The images can be enlarged or reduced using the **magnifying glass** tools on the tool bar (white for the process window, orange for the source window). It is also possible to fit the window size to the image at a given magnification by using the **Fit checkboxes** located also in the toolbar.

2.B. The histogram window.

Here is where the histogram of the current subtracted images is displayed. Dark colors (low histogram values, with black=0) are at the beginning of the histogram, while light colors (high histogram values, with white=255) are at the end. The yellow column indicates the position of the threshold level in the histogram. After performing the subtract operation, a well contrasted image should have a histogram characterized by two separated Gaussian distributions for dark and light colors, with the optimum threshold level just in the center of the two Gaussians.

2.C. The *Input and Output Files* panel.

In this panel we tell the program the location and name of the images and which images will be analyzed. We can press the button **Explore** to search the directory where the images are stored in the computer, or type it directly. By clicking the **Explore** button a window opens and a tree diagram of the directories present in the specified drive is displayed. The contents of each directory is also shown. To select a directory, double-click on it. When you have found the desired location, press **Select directory and close** to return to the Main window. The directory information will be updated.

Images directory: D:\Images\SqGap24\
Output data files header: c024-
Input images files header: IM
First image: 1
Last image: 199
Step: 1

In **Input images files header** we specify the header name of the images, and in **Output data files header** we introduce the header name for the output data files, i.e. the data of the analyzed image. The final name of the files will be the header at the beginning, plus the number of the image and finally the extension (`.DAT`). For example:

Input image: `IM000201.BMP` ✍ Output data file: `C01-0201.DAT`

In this example, `C01-` is the header name for the output data files. I recommend not to use more than 4 characters for the header file, in order to be sure that there are 4 characters for the image number. The number of images usually obtained from an experiment is between 100 and 500. See later for details about the output format of the data files.

In **First Image**, **Last Image**, and **Step** we decide the first image to start the analysis, the last one, and the step. i.e. every how many images we jump to the next. Usually Step is set to 1 (all images will be processed consecutively).

Once all the information about the input and output files has been introduced, usually we won't need for a while this tool panel, so it is useful to click the **hide** button (on the top-left corner) to fold the toolbar, so more space is available in the screen. It can be unfolded at any time by clicking the same button.

If all the information is correct in this window, you should press **Start** in the Process Operations panel to start the analysis.

2.D. The *Process Operations* panel.

This is the most important panel, so it gives the main operations to process the images. It is organized in different sections:

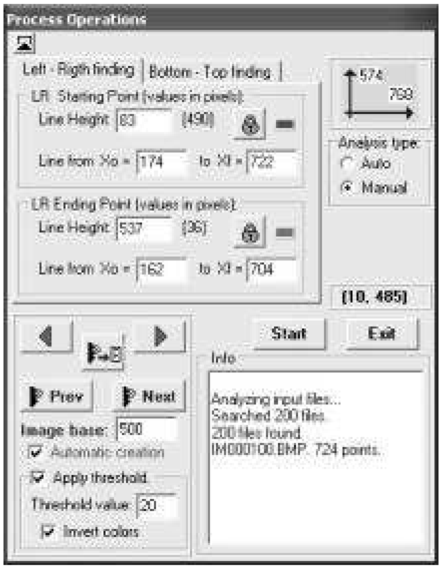

LR Starting Point (values in pixels)
Line Height: 83 (490)
Line from Xo = 174 to Xf = 722

LR Ending Point (values in pixels)
Line Height: 537 (36)
Line from Xo = 162 to Xf = 704

Analysis type: ○ Auto ● Manual

(10, 485)

Image base: 500
☑ Automatic creation
☑ Apply threshold
Threshold value: 20
☑ Invert colors

Analyzing input files...
Searched 200 files
200 files found
IM000100.BMP. 724 points.

- **Analysis type**: Here we decide if the images are processed manually or automatically. In **manual mode** we have to press the button **digitize** (see later) for each image to tell the program that we want to process the current image. In **automatic mode**, the images are digitized automatically using the current value of threshold. A **stop** button is displayed during processing, so we can stop automatic analysis when necessary. If we do not stop it, the automatic process ends when all images are processed.

- **Start button**: By clicking this button we start the analysis of the images. The program will try to find the specified images in the directory, showing an error message if all or some of the selected images could not be found. If the analysis mode is automatic, the program will start immediately, and a **stop** button will appear. If the analysis mode is manual, the program will wait until the user clicks the digitize **button** to process the image.

- **End button**: Exits the program and saves the user preferences. All the information contained in the fields is saved, as well as the windows positions and sizes. When the program starts the next time, it refreshes all menus with the saved information.

- Image base and threshold: The image base is the image that is subtracted to the others. Usually this image base is the background of an experiment, and it is saved before the experiment is started or at the end of it. However, in the cases where the front is stable and advances, it is often to use any image of the experiment as base image if there is no possibility of overlap between the interfaces. In this later case, during the task of analyzing the images it is frequent to change the image base looking for the best contrast.

If the program cannot find the image base, a warning will appear and the analysis will be stopped. Sometimes the original images are good enough to make unnecessary a base image, and applying the threshold directly over the grey-scale images is sufficient. In this case is very convenient to check the **Automatic creation** checkbox, which will create an image base to process the images. This image base is simply an image of the same size but completely white. For security and to prevent overwriting valuable images, the number of the image base will be the specified in the **Analysis Options** menu. The program will never overwrite an existing image. If the **Automatic creation** checkbox is unchecked and the image base does not exist, the program will ask the user to create one.

The checkbox **Apply threshold**, if checked, is used to apply the specified value of threshold, so all colors below the threshold level will be reset to 0, and the others to 255. Check the **Invert Colors** checkbox to change blacks to whites and vice versa. If **Apply threshold** is unchecked, the processed image will be shown with the colors after subtracting, but no contour could be recognized. **The program will recognize the contour only when the threshold is applied.**

The edit box that contains the value of the current threshold value can be changed manually (i.e. typing the value) or using the up and down arrow keys. When pressing **up** or **down** the threshold value will be increased by +1 or by -1 respectively.

- Buttons to analyze the images and recognize the contour: There are five buttons with the following fictions;

Left blue arrow (*Previous image***)**: Moves an image back, subtracting the images and applying the threshold, but without performing the recognition operation.

Right blue arrow (*Next image***)**: Advances one image, subtracting the images and applying the threshold, but without performing the recognition operation.

Recognize button (*Recognize current image*): Tries to recognize the contour and saves data in the corresponding file if successful.

Previous image and recognize (*Jumps to the previous image and recognize the contour*): Jumps to the previous image and tries to recognize the image, saving data if successful.

Next image and recognize (*Jumps to the next image and recognize the contour*): Jumps to the next image and tries to recognize the image, saving data if successful.

- Info window: This window stores important information concerning the operation of finding the files, recognizing the contour, and possible problems. When a contour is recognized the number of points of the contour is indicated in this window. We can identify immediately that something is wrong with the contour when the number of points is much larger than previous contours. The avoid infinite loops if something is wrong, the recognition process is stopped when the number of points is larger than a certain value (usually 10000 or 15000, selected in the **Contour Recognition Options** menu). The contents of this info window is saved in a file for further review. The name of the file and other options is selected in the **Analysis Options** menu.

- Mouse (X,Y) box: This box show the position of the cursor when it is moved over the processed image. **The origin of coordinates is the left-bottom corner**.

- Finding method: This tool is used to tell the program which region of the image will be studied in order to find the interface. If the interface or front that we want to recognize is advancing from bottom to top in the images, we will select **bottom to top finding**. As a contrary, if the image is advancing from left to right, we will select **left to right finding**. In any of the cases, the idea is to draw two lines (starting and ending lines) that will cross the interface. These lines will be used to find the starting and ending points of the contour.

The contour is always recognized in anti-clockwise sense. As a result, if the finding is from left to right, the Starting line must be below the Ending line. When the finding is from bottom to top, the starting line must be on the right, and the ending line on the left.

There are two **lock** buttons. When checked, the fields **Line Height** are blocked and shown in yellow. The function of these buttons are explained in the following example.

Example: Operations to draw the proper lines

We will suppose that the interface is moving from left to right, so we will have to select left to right finding.

i) Select the files that you wish to study.

ii) Select manual analysis method.

iii) Select the image base.

iv) Study the source images in detail to decide which regions we want to analyze, possible problematic objects (reflections, shadows,…) and the direction of advance of the contour that we are interested to recognize.

v) Press start. The first image will be loaded and displayed. Select the desired threshold to get an optimum contrast. Change the colors if necessary to be sure that the interface you want to study has the black region on the left and the white on the right.

vi) Uncheck the lock buttons if they are checked.

vi) The left mouse button is used to set the position and length of the **starting line**. In the process window, left click on a position inside the black region. You will see that the fields **Line Height** and **Line from Xo** will be updated. Then move to right and left click again while holding the shift key. The field **to Xf** will be updated. The starting line is now set. It won't be shown until we press the **Recognize button**.

vii) The right mouse button is used to set the position and length of the **ending line**. In the process window, right click on a position inside the black region. In this case the fields **Line Height** and **Line from Xo** of the ending line are updated. Then move to right and right click again while holding the shift key. The field **to Xf** will be updated. The ending line is now set. It won't be shown until we press the **Recognize button**.

All fields can be changed directly instead of using the mouse, but it is more practical clicking on the images.

In many cases it is important to keep the width of the system fixed (for example in experiments of roughening). For this reason we have to keep fixed the height of the starting and ending lines. The function of the lock buttons is to preserve the values of the height of the starting and ending lines, so when we click over the image these fields are not modified.

viii) Once the lines are set, press the **Recognize button**. The lines will be displayed both over the source image and the process image. (The lines are plot in different colors to clearly identify them. The colors can be changed by clicking to the small color panels). Next, the program will try to find the contour, showing it in blue if success. If the contour corresponds to the desired region, you can continue with the next image clicking **Next image and recognize** or **Previous image and recognize**. If something is wrong, you should change the position of the lines and press **Recognize** again.

An important issue to take into account is that when the starting line cannot find any black point, it searches moving to left until a black point is found or the left side of the image is reached.

If the finding is from bottom to top, the functionality is exactly the same (left click for the starting line, right click for the ending line), but when the first point cannot be found, the program will try to find it moving down.

Important: in both types of finding **the ending line must cross the interface**. At least one point of the interface should be in a black point.

Summary of mouse and keys actions:

- Left mouse: Selects the (X0, Y) position of the starting line.
- Left mouse + shift: Selects the (Xf, Y) position of the starting line.

- Right mouse: Selects the (X0, Y) position of the ending line.
- Right mouse + shift: Selects the (Xf, Y) position of the ending line.

- Up and Down arrows: Increase or decrease the threshold value.

3. Menu tools and program options.

In the menu bar there are the following items:

1. File / Exit.

Exits the program saving all preferences (the same as the Exit button in the Process Operations tool).

2. Analysis method / Analysis Options.

Here we specify some options for the program that affects temporal or extra files.

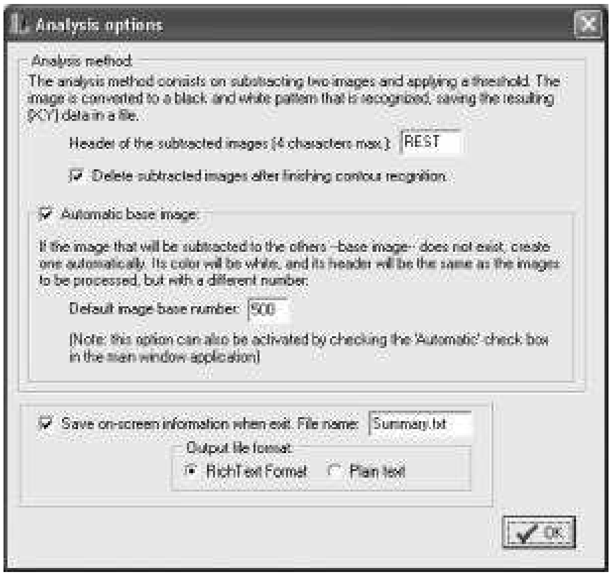

Analysis method

The analysis method consists on substracting two images and applying a threshold. The image is converted to a black and white pattern that is recognized, saving the resulting [X,Y] data in a file.

Header of the subtracted images (4 characters max.): REST

☑ Delete subtracted images after finishing contour recognition.

☑ Automatic base image:

If the image that will be subtracted to the others –base image– does not exist, create one automatically. Its color will be white, and its header will be the same as the images to be processed, but with a different number.

Default image base number: 500

(Note: this option can also be activated by checking the 'Automatic' check box in the main window application)

☑ Save on-screen information when exit. File name: Summary.txt

Output file format:

● RichText Format ○ Plain text

- Header of the subtracted images: Is the base name for the subtracted images, which are created during the analysis process. If the **Delete** check box if checked, these images will be deleted once the analysis is finished. If unchecked, the images will be saved in the hard disk, in the same location as the source files. Note: if the program does not close correctly or hangs up, these images won't be deleted automatically. The user should do that manually.

- Automatic base image: When checked, an automatic base image will be created if not present, with the number specified by the user in the corresponding check box. If unchecked, the program will prompt the user to create one or not. If the image is created, it won't be deleted once we exit the program, so the user will have to delete it manually if there is no interest to keep it.

- Save on-screen information: Saves the text contained in the info panel of the Process Operations tool. The output file will be the specified by the user in the edit box. Two output formats are available: Rich Text Format (RTF), which keep all colors and format (should be read using Word or similar programs), and Plain Text (ASCII-coded text), which can be read using any program. Apart from the text, other important information about the images and its calibration is also stored.

3. Analysis method / Contour Recognition Options.

Here we specify other options that affect directly the process of recognition.

Show Recognized Contour ...
○ during recognition (slower)
● at the end (faster)
○ never

Maximum digitized points
Stop recognition after 5000 points
(This is useful to prevent infinite recognition of the interface when the ending point could not be found)

- Show the recognized contour…: Tells the program when the recognized contour will be shown. **During recognition** will show the blue points of the contour instantly. This option slows down the process substantially, so I recommend using it only for tests. **At the end** shows the contour when the recognition task ends. It is fast and is the option usually used. The option **Never** won't show the contour. It has been added for completeness.

- Maximum digitized points: This option is important to avoid an infinite loop if the program cannot find the ending point. One have to be careful with finger-like interfaces, because the number of points in the interface can be very large. Good values are 10000 or 15000. To tell the user that the recognition process has finished because the maximum number of points has reached, in the info window will appear a warning message.

4. Calibration / Set images calibration.

In this window we set the calibration of the images and the position of the axis in the system of reference. This is essential to save the final contour in physical units (e.g. mm) and with the most adequate system of reference. For example, if the interface advances from left to right in the images, we would prefer to have the final interfaces advancing from bottom to top, so we will have to rotate 90º the system of reference.

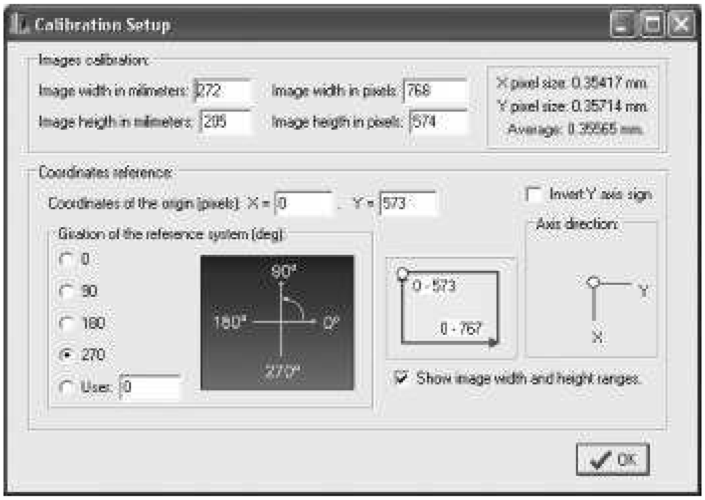

Images calibration:
Image width in milimeters: 272
Image heigth in milimeters: 205
Image width in pixels: 768
Image heigth in pixels: 574
X pixel size: 0.35417 mm.
Y pixel size: 0.35714 mm.
Average: 0.35565 mm.

Coordinates reference:
Coordinates of the origin [pixels]: X = 0 , Y = 573
☐ Invert Y axis sign
Giration of the reference system [deg]:
○ 0
○ 90
○ 180
● 270
○ User: 0
Axis direction:
☑ Show image width and height ranges.

- Images calibration: We introduce here the width and the height of the images in pixels and in mm (or the desired final physical unit). If the user does not want any calibration, just put 1 in all fields. At the right of the window there is a window that tells the user the corresponding pixel size for the calibration.

- Coordinates of reference: Here we specify the origin of our system of reference and its rotation. The origin is represented by means of a white dot, and its position respect to the images is represented in the small diagram. (Below it there is a checkbox that permits also to represent the size of the images in the diagram). The direction of the X and Y axis is indicated in the figure on the right, with the white dot indicating the origin. The position of the two axis is set by specifying the angle of rotation. The Y axis can be changed in sign if necessary to include all possible combinations.

4. Format of the output files.

- The most important output files are the corresponding to the recognized contour. The data obtained are processed to include calibration and to adjust the desired system of reference. Then data are saved to disk, with the format "#.###, #.###". An example of a typical output file is the next. We consider an interface that moves from left to right, with the origin of the system of reference in the top-left corner. The Y axis is pointing to right and the X axis is pointing to the bottom of the image:

```
180.698606, 29.648437
180.339721, 29.648437
180.339721, 29.289062
179.980836, 29.289062
179.621951, 29.289062
```

- Another output file is the one that contains all the information displayed in the info window. An example of this file in plain text is as follows:

```
--------------------------------------------------------
This file was generate by the 'Image Analysis' program.
Date: 23/09/2002, 18:33:19

Calibration setup:
   Image size: 768 x 574 pixels.
   Horizontal resolution: 272 mm =768 pixels.
   Vertical resolution: 205 mm =574 pixels.
```

```
   Average resolution: 0.35565 mm/pixels.

Left to right finding:
   Starting line height: 73
   Ending line height: 535
   Difference: 462
Bottom to top finding:
   Starting line position: 169
   Ending line position: 298
   Difference: 129
-------------------------------------------------------

Analyzing input files...
Searched 11 files.
11 files found.
IM000000.BMP. 624 points.
IM000001.BMP. 637 points.
IM000002.BMP. 622 points.
IM000003.BMP. 612 points.
IM000004.BMP. 610 points.
IM000005.BMP. 627 points.
IM000006.BMP. 605 points.
IM000007.BMP. 614 points.
IM000008.BMP. 620 points.
IM000009.BMP. 626 points.
IM000009.BMP. 626 points.
IM000010.BMP. 638 points.
REST0000.BMP DELETED.
REST0001.BMP DELETED.
REST0002.BMP DELETED.
REST0003.BMP DELETED.
REST0004.BMP DELETED.
REST0005.BMP DELETED.
REST0006.BMP DELETED.
REST0007.BMP DELETED.
REST0008.BMP DELETED.
REST0009.BMP DELETED.
REST0010.BMP DELETED.
```

5. Important issues.

- For perfect operation the program must be located in the following directory: ‘`C:\Jordi\C\Subpixel`’. To install it in a different location it must be compiled. Contact me for details.

- Be sure that all files in the directory where the program is located are **NOT** Read-only. The program saves the preferences in a file called `Subpixel.cfg`. If this file is read-only the program cannot save the preferences and will show an error message. For security, there is a copy of the `Subpixel.cfg` file called `Secure-SubPixel.cfg`. If the normal file is corrupted, just delete it and rename `Secure-SubPixel.cfg` to `Subpixel.cfg`.

- Be sure that the images are in grey-scale (8 bits color depth). RGB (16, 24, or 32 bits color depth), monochrome or other formats are not supported, as well as compressed BMP. The program could try to load these images, but will result in strange results. The program may also hang up.

- This basic documentation help won’t be displayed if the document is in use by other program, such as Word.

A.4 Data analysis: `ANALYSIS3.EXE`

Jordi Soriano, September 2002.

(This text can be edited and modified using any editor capable of reading RTF formats, such as Word. Some elements, such as colors in tables are only visible when this document is opened using Word)

BASIC DOCUMENTATION FOR THE EXPERIMENT ANALYSIS.

1. Scope of the program.

This program is the core of the analysis of the experiments. Once the images have been processed and the interfaces extracted, we launch this program to calculate all the important magnitudes for the analysis of data: *rms* width, power spectrum, and spatial correlations. The program also includes extra options to perform detail analysis of data, such as local velocities. In addition, the program includes data preprocessing tools to eliminate overhangs and to equispace data to a number of points power of two.

Other features include the visualization of the evolution of the interfaces, the possibility of showing the original experimental images as a movie, and the possibility to compare the images with the recognized contour.

2. Basic functions in the main window.

In the main window we specify the input data files and the desired calculus. It gives as well information about the files being processed and the calculus that the program is performing.

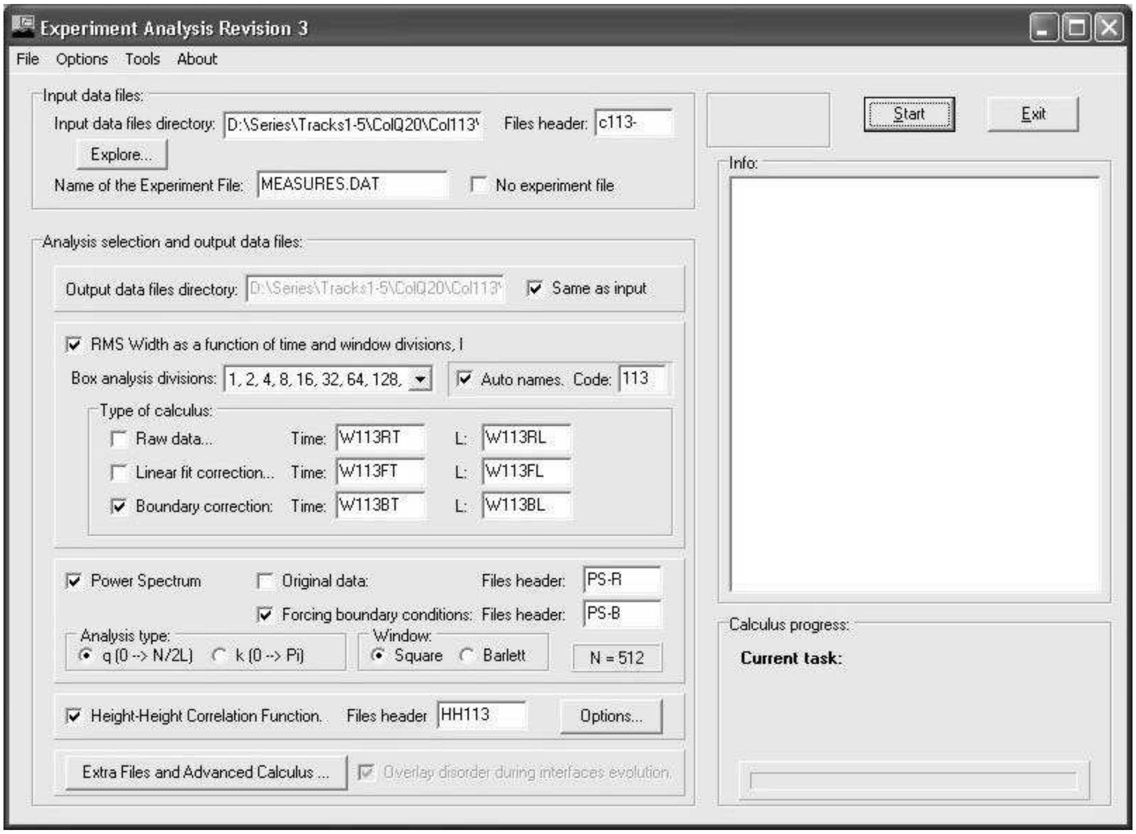

Input data files:
Input data files directory: D:\Series\Tracks1-5\ColQ20\Col113
Files header: c113-
Name of the Experiment File: MEASURES.DAT
☐ No experiment file

Analysis selection and output data files:
Output data files directory: D:\Series\Tracks1-5\ColQ20\Col113
☑ Same as input

☑ RMS Width as a function of time and window divisions, l
Box analysis divisions: 1, 2, 4, 8, 16, 32, 64, 128,
☑ Auto names. Code: 113
Type of calculus:
☐ Raw data... Time: W113RT L: W113RL
☐ Linear fit correction... Time: W113FT L: W113FL
☑ Boundary correction: Time: W113BT L: W113BL

☑ Power Spectrum
☐ Original data: Files header: PS-R
☑ Forcing boundary conditions: Files header: PS-B
Analysis type: ● q (0 --> N/2L) ○ k (0 --> Pi)
Window: ● Square ○ Barlett
N = 512

☑ Height-Height Correlation Function. Files header HH113

☑ Overlay disorder during interfaces evolution.

Info:

Calculus progress:
Current task:

2.A. Input data files

Here we specify the directory where the files containing the interfaces profiles are stored. The **experiment file** is also expected to be found in the same directory. Pressing the **Explore** button allows to inspect the hard disk to find data files more easily. In this case, once the directory is found you have to press **Select directory and close** to return to the main window. The field **input data files directory** will be updated.

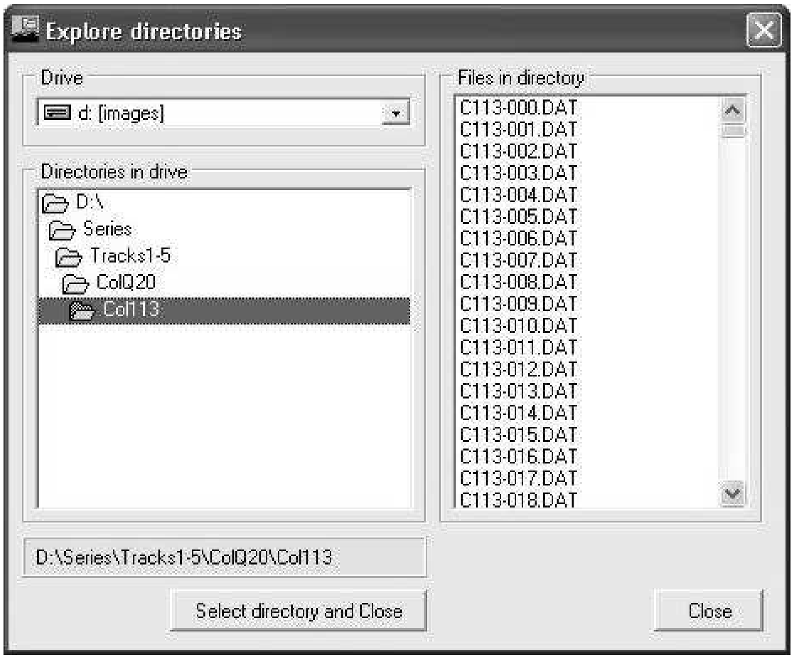

Drive: d: [images]

D:\Series\Tracks1-5\ColQ20\Col113

In the field **files header** we specify the header name of the data files. All the experimental data files have a code that identifies the experiment. Usually this code is the same as the one selected for output data files during the analysis of the images. This code identifies the experiment and it is of the style `*###`, where `*` is an alphanumerical value and ### a group of digits. After the symbol ‘-’ there is the image code, a 3-digit group that identifies the image.

Important: The full name of the input data files must have 8 characters (+ 4 for the ‘.DAT’), with no more than 5 characters in the header. An example is `C023-001.DAT`. Moreover, **the program expects that the data files are in two columns (x values in the first column and y=h(x) values in the second), and comma delimited.** A sample of a typical data file is:

```
192.776132, 14.086589
192.405052, 14.086589
192.405052, 13.720703
192.033972, 13.720703
191.662892, 13.720703
191.662892, 13.354818
191.291812, 13.354818
190.920732, 13.354818
190.920732, 12.988932
190.549652, 12.988932
190.178571, 12.988932
189.807491, 12.988932
189.807491, 12.623047
```

In the field **Name of the experiment file**: we specify the name of the experiment file. All the experiments carried out with the PCVision board and the associated VisualBasic application **Cameras Control** (after June '99) have an associated experiment file. In this file all the relevant information of the experiment is stored. This file contains a header delimited by two lines that contains the character #. This header contains general information about the experiment, such as experiment code, the experimental parameters, and the resolution. After the header there is a list that contains the camera used, the image number, and the capture time. An example of this file is shown below:

```
##################################################
-- AUTOMATIC ACQUISITION EXPERIMENT --
  Images expected: 200
  Duration of the experiment: 6600 s
  Capture type: logarithmic in time
--------------------------------------
Experiment date: 11/04/2000
Experiment time: 10:33:52
Images header name:  IM
Images directory:  c:\IMAGES\Col116\
Info files directory:  c:\IMAGES\Col116\
Experiment code: Col116
Experiment geometry: rectangular
Cell type: sizeable cell
           (upper injection + torical ring)
Plates manufacturer and date: 2CI, November '99
Other plates information:
    Length: 56 cm.
    Code: COL99-20.2 (1.5 mm)
    Orientation: Only one available
    Plate fixing method: Removable stick glue
    Spacers disorder-glass: Yes
    Injection type: Upper glass (two holes)
                    50 ml syringe.
    Upper glass: 2 cm thick
Experiment parameters: b=0.36 mm; Q=20 ml/h; W=190 mm
Images calibration:
  Camera 0:
    width_pixels=768; width_mm=281
    height_pixels=574; height_mm=213
  Camera 1:
    width_pixels=768; width_mm=281
    height_pixels=574; height_mm=213
Author: Jordi Soriano
Notes:

##################################################

0, 0,  0.00
0, 1,  1.10
0, 2,  1.43
0, 3,  1.71
0, 4,  2.03
0, 5,  2.31
0, 6,  2.64
0, 7,  3.52
0, 8,  3.79
0, 9,  4.07
0, 10,  4.95
0, 11,  5.28
0, 12,  5.55
0, 13,  5.93
0, 14,  6.26
0, 15,  6.59
0, 16,  6.87
0, 17,  7.20
0, 18,  8.35
```

```
0, 19,  8.68
0, 20,  9.01
```

In some cases there is no experiment file associated to the experiment (for example in the experiments carried out before June ’99, or experiments that come from other acquisition applications). If this is the situation, click the check box named **No experiment file**. The program will extract the image number from the data file name and will use this value instead of the time for all calculations. If you keep this checkbox unchecked and there is no experiment file, the program will prompt you to create one, and will contain only the header. You will have to add the columns of camera type, image number, and capture time manually.

The experiment file also accepts a format of two columns instead of three, the first containing the image number and the second the capture time. Usually the information about the camera used is not necessary, so I recommend to use directly two columns if you have to create an experiment file. You can use Origin or Excel to create the list. In the Origin, for example, create a worksheet with two columns and fill the columns with the image numbers and capture times. Then export the worksheet, with **neither column names nor column labels**, and with the separator “,SPACE”. Then, with any text editor you can create a single file that will contain the header and the list of data.

2.B. Analysis selection and Output data files

- Output data files: Here we specify which calculations we want to perform and the directory where the new output files will be stored.

Check the box labeled **Same as Input** to save the new data files in the same directory as the input data files. This option is strongly recommended to store all input and output data files in the same directory.

The different boxes indicate which calculus we want to perform. These calculus are the following:

- Mean width as a function of time and system size L:

It is defined as $w(l, t) = (< (h(x, t) - < h(t) >)^2 >_{x, i})^{1/2}$, where l is the window size, $< h >$ the main height, and $< >_{x, i}$ the average over x in a given window, and the average over all possible origins i of a given window l. Because we need to study w as a function of time and window size, we will have a couple of output files for every kind of special data processing selected. The output files formats are:

a) Mean width as a function of time:

capture time	w for l=L/N_1	w for l=L/N_2	w for l=L/N_3	…	w for l=L/N_m	< h > for l=L
t_0 (first image)						
t_1						
…						
t_k (last image)						

Important: For completeness, we save the mean height for l=L in the last column.

N_i goes from 1 to 256 in powers of two if we specify this option in the **Box Analysis Division** checkbox. It is also possible also to select only N=1.

Example of output file:

In this example w(t) has been studied for a set of 200 images (8 shown) and with l=L/N_i, N_i=1 … 256.

```
0.00, 0.171795, 0.173453, 0.156275, 0.139860, 0.130091, 0.122705, 0.110960, 0.088115, 0.050121, 9.4501420
```

```
0.82, 0.133524, 0.075388, 0.070525, 0.060459, 0.050604, 0.044589, 0.033859, 0.023997, 0.013962, 9.6380780
1.15, 0.117457, 0.099634, 0.091534, 0.078743, 0.071608, 0.060027, 0.046576, 0.033027, 0.016468, 9.7038220
1.76, 0.233355, 0.222712, 0.208309, 0.161421, 0.124036, 0.095624, 0.072546, 0.049457, 0.027925, 10.145459
2.03, 0.273934, 0.253246, 0.233311, 0.177930, 0.133392, 0.103082, 0.076452, 0.052351, 0.029357, 10.517794
2.91, 0.319856, 0.294293, 0.276244, 0.216096, 0.167876, 0.128321, 0.089266, 0.057575, 0.028641, 11.416057
3.24, 0.378087, 0.345025, 0.327512, 0.254684, 0.199997, 0.160490, 0.104947, 0.060166, 0.027209, 11.745501
3.51, 0.427809, 0.398369, 0.383521, 0.309730, 0.255274, 0.210477, 0.146259, 0.087939, 0.040097, 12.071358
```

b) Mean width as a function of window size *l*:

l = L / N_i	w(*l*) for t_0	w(*l*) for t_1	w(*l*) for t_2	…	w(*l*) for the last image, t_k .
(Label) L	(Label) IM0	(Label) IM1	(Label) IM2		(Label) IMk
L / N_1					
L / N_2					
…					
L / N_m					

Important: the first line of the output file contains labels to make easier to identify each image.

Example of output file:

This example corresponds to the same experiment as the previous example. w(t) has been studied for a set of 200 images (5 shown) and with *l*=L/N_i, N_i=1 … 256.

```
L,           IM0,      IM1,       IM2,       IM3,       IM4,       IM5
169.583618, 0.171795, 0.133524, 0.117457, 0.233355, 0.273934, 0.319856
84.6258760, 0.173453, 0.075388, 0.099634, 0.222712, 0.253246, 0.294293
42.1470050, 0.156275, 0.070525, 0.091534, 0.208309, 0.233311, 0.276244
20.9075690, 0.139860, 0.060459, 0.078743, 0.161421, 0.177930, 0.216096
10.2878520, 0.130091, 0.050604, 0.071608, 0.124036, 0.133392, 0.167876
4.97799300, 0.122705, 0.044589, 0.060027, 0.095624, 0.103082, 0.128321
2.32306300, 0.110960, 0.033859, 0.046576, 0.072546, 0.076452, 0.089266
0.99559900, 0.088115, 0.023997, 0.033027, 0.049457, 0.052351, 0.057575
0.33186600, 0.050121, 0.013962, 0.016468, 0.027925, 0.029357, 0.028641
```

(some spaces have been added to show the file structure clearer)

c) The different types of analysis:

- Raw data: Performs the calculus of w(l,t) without any modification to the input data files. The only modification is the treatment of overhangs (if present) and data interpolation (if desired).

- Linear fit correction: Performs the calculus of w(l,t) eliminating the average slope of the interface by subtracting the line obtained from a linear fit of the data. Other possible modifications to data include overhangs treatment (if present) and data interpolation (if desired).

- Boundary correction: Performs the calculus of w(l,t) forcing periodic boundary conditions, i.e. subtracting the line that connects the two ends of the interface. Other possible modifications to data include overhangs treatment (if present) and data interpolation (if desired).

The analysis that is more commonly performed in the experiments of roughening is the **Boundary correction**.

It is very convenient to check the **Autonames** checkbox. It allows to create automatic names of the output files using the header code of the input data files.

- Power spectrum:

It is defined as $S(k,t) = |h(k,t)*h(-k,t)|$, where $h(k,t) = (1/N)^{1/2}$? $[(h(x,t) - <h>)\cdot e^{ikx}]$, where < h > is the main height. The power spectrum is computed using a FFT algorithm (routine FOUR1 of the Numerical Recipes). For its computation it is necessary to have a number of points power of 2. For this reason data are linearly interpolated. The final number of points N can be selected in **Options / Program and calculus preferences / Calculus Option** of the main menu. I recommend a value of N as close as possible to the actual resolution of the experiment. For example, in the experiments of roughening we have about 500 pixels in the lateral direction, so the best choice is N=512.

In the main window, a panel in the right-bottom corner of the power spectrum box indicates which is the current value of N that will be used for data interpolation.

The power spectrum can be calculated using raw data directly (i.e., original data interpolated and corrected from overhangs) and data with forced periodic boundary conditions (i.e., data interpolated, corrected from overhangs, and with the line that connects the two ends subtracted). In the former case the power spectrum is affected by an artificial overall slope -2, which is eliminated in the latter case.

Apart from the kind of data that we want to use to calculate the power spectrum, we can decide if we want the wave number in dimensionless units, i.e. from 0 to ? , or in physical units, i.e. from 0 to N/2L, with L/N ⁇ ? being the sampling interval. Usually in the analysis of the experimental results it is more convenient to use physical units, which allows identifying directly over the spectrum different characteristic length scales.

Another option that has been added for completeness is the possibility of using a **different window** instead of the usual rectangular one. I have added the Barlett (triangle) window. It is used to force periodic boundary conditions by multiplying the original data by a function that is zero at the ends of the interface, 1 in the middle, and increases linearly from 0 to 1 in the rest (see Numerical Recipes for details). Because we usually force periodic boundary conditions by subtracting the line that connects the two ends of the interface, this option has not been used in general. However, raw data with Barlett window give similar results as the data with forced periodic boundary conditions and rectangular window.

Because the input data are N real data points, the power spectrum returns N/2 data points. The output format of the file that contains the calculus of *S (k, t)* is a file with two columns. The first column contains the values of k (from 0 to ? or from 0 to N/2L), and the second column the power spectrum. An example of output file is the next:

```
0.000000, 0.000000
0.005897, 762.819641
0.011794, 73.366890
0.017690, 9.923923
0.023587, 11.492601
0.029484, 56.040554
0.035381, 14.898949
0.041278, 69.518608
0.047174, 73.591179
0.053071, 2.935197
0.058968, 1.992087
0.064865, 8.946370
0.070762, 26.899002
0.076658, 24.083315
0.082555, 6.451737
0.088452, 13.599674
0.094349, 1.141571
0.100246, 34.144005
0.106142, 0.050928
0.112039, 31.240074
0.117936, 50.339798
0.123833, 25.850023
0.129730, 6.958723
```

```
0.135626, 34.711468
0.141523, 0.642989
0.147420, 51.234097
0.153317, 10.414542
0.159213, 28.395399
0.165110, 8.320187
0.171007, 9.764891
```

In this example, L=169.58 mm and N=512. ? ?? ?0.331 mm. The first value of the left column is 1/L, the second 2/L, and so on. Only 30 points are shown.

- Height-Height correlation function:

It is defined as $C(d) = [< (h(x+d) - h(x))^2 >_x]^{1/2}$. It allows to determine the growth exponents and the roughness exponents in a different way. In the main window you may specify the header of the output files. If the checkbox **Autonames** is checked, an automatic name is selected, containing the labels ‘`HH`’ plus the code of the experiment (for example `HH115`). The rest of the file name will be completed depending on the analysis you want. Click the **options** button to access a new window where the details of the calculation are specified. In this window you will find the definition of the height-height correlation function, a short description of the output files, and two checkboxes where you select the different output files that you are interested to create: using raw data or forcing periodic boundary conditions. Two output files will be created in both cases: As a function of time and as a function of *d*. The program automatically adds the labels ‘-d’ and ‘-t’ to differentiate the two files. For example, a full name of the output files would be `HH115R-d.DAT` and `HH115R-t.DAT`.

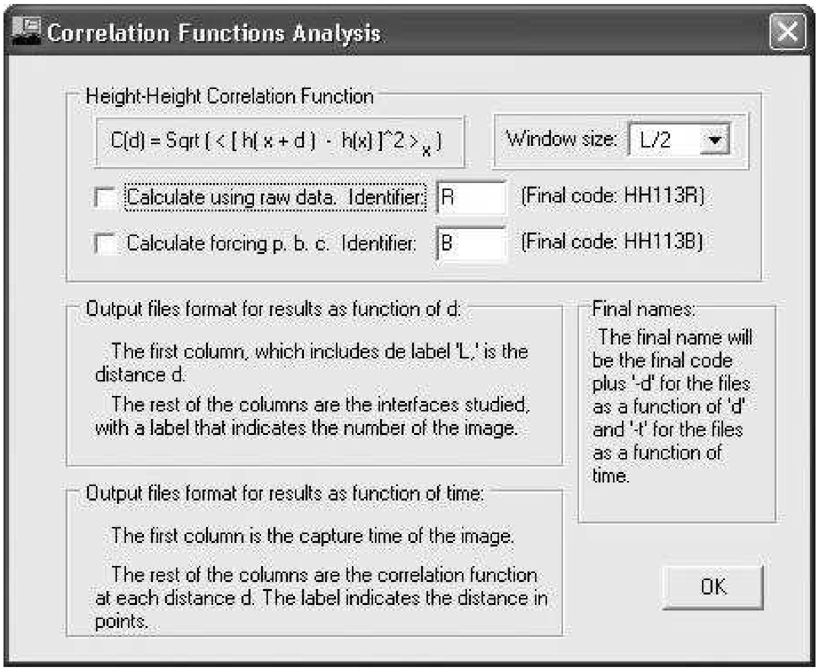

Correlation Functions Analysis

Height-Height Correlation Function

C(d) = Sqrt (< [h(x + d) - h(x)]^2 >$_x$)

Window size: L/2

☐ Calculate using raw data. Identifier: R (Final code: HH113R)

☐ Calculate forcing p. b. c. Identifier: B (Final code: HH113B)

Output files format for results as function of d:

The first column, which includes de label 'L,' is the distance d.

The rest of the columns are the interfaces studied, with a label that indicates the number of the image.

Final names:

The final name will be the final code plus '-d' for the files as a function of 'd' and '-t' for the files as a function of time.

Output files format for results as function of time:

The first column is the capture time of the image.

The rest of the columns are the correlation function at each distance d. The label indicates the distance in points.

The option labeled **Window size** allows defining the size of the window in calculation of the correlation function. The maximum value is L/2, and the minimum L/8. The range of *d* is from L/N to L/(Np), where p=2, 4, or 8. N is the number of points after interpolation. N is the same for all calculations, so if N was selected to N=512 for the computation of the power spectrum, the same value will be used for the rest of the calculations. Usually the window size used is L/2. However, in some cases it is interesting to improve statistics by reducing the window size. Notice that in this case we will have less values of *d*.

The output files formats are:

a) Height-height correlation function as a function of time:

capture time	C(d) for d=L/(Np)	C(d) for d=2L/(Np)	…	C(d) for d=L/p
t_0 (first image)				
t_1				
…				
t_l (last image)				

Example of output file:

In this example C(d) has been studied for a set of 200 images (the first 5 shown) and with a window size L/2. Raw data are analyzed with N=512. Only the first 8 values of C(d) of the 256 total are presented. L=169.252 mm. The experiment analyzed is the same as previous examples.

```
0.000000, 0.000000, 0.146426, 0.146426, 0.153402, 0.160075, 0.156774, 0.158433, 0.172649
0.820000, 0.000000, 0.135288, 0.133341, 0.142810, 0.148201, 0.146426, 0.155097, 0.156774
1.150000, 0.000000, 0.102268, 0.116604, 0.121005, 0.116604, 0.116604, 0.121005, 0.125252
1.760000, 0.000000, 0.155097, 0.151688, 0.171127, 0.168044, 0.171127, 0.185779, 0.177134
2.030000, 0.000000, 0.155097, 0.140967, 0.155097, 0.155097, 0.158433, 0.164902, 0.168044
```

b) Height-height correlation function as a function of window size *d*:

d = L / (Np)	C(d) for t_0	C(d) for t_1	C(d) for t_2	…	C(d for the last image, t_l .
(Label) L	(Label) IM0	(Label) IM1	(Label) IM2		(Label) Im'l'
L / (Np)					
2L / (Np)					
…					
L / p					

Important: the first line of the output file contains labels to make easier to identify each image.

Example of output file:

This corresponds to the same experiment as the previous example. C(d) has been studied for a set of 200 images (5 shown). The first 8 values of d are presented, as well as the last one. N=512 and the window size L/2. L=169.252 mm.

```
L,         IM0,      IM1,      IM2,      IM3,      IM4,      IM5
0.000000, 0.000000, 0.000000, 0.000000, 0.000000, 0.000000, 0.000000
0.331866, 0.146426, 0.135288, 0.102268, 0.155097, 0.155097, 0.121005
0.663733, 0.146426, 0.133341, 0.116604, 0.151688, 0.140967, 0.144629
0.995599, 0.153402, 0.142810, 0.121005, 0.171127, 0.155097, 0.161700
1.327465, 0.160075, 0.148201, 0.116604, 0.168044, 0.155097, 0.168044
1.659331, 0.156774, 0.146426, 0.116604, 0.171127, 0.158433, 0.178604
1.991198, 0.158433, 0.155097, 0.121005, 0.185779, 0.164902, 0.185779
2.323064, 0.172649, 0.156774, 0.125252, 0.177134, 0.168044, 0.195383
...
84.625897, 0.271541, 0.205811, 0.178603, 0.359396, 0.437488, 0.533855
```

(some spaces has been added to show the file structure clearer)

2.C. Extra files and advanced calculus.

There are several other possible analysis which are useful to characterize the experiments. However, **most of the possible analysis are designed specifically for experiments of interfacial roughening**. By clicking to the button labeled **Extra files and advanced calculus** a new window opens. The extra files and the advanced calculus are the following:

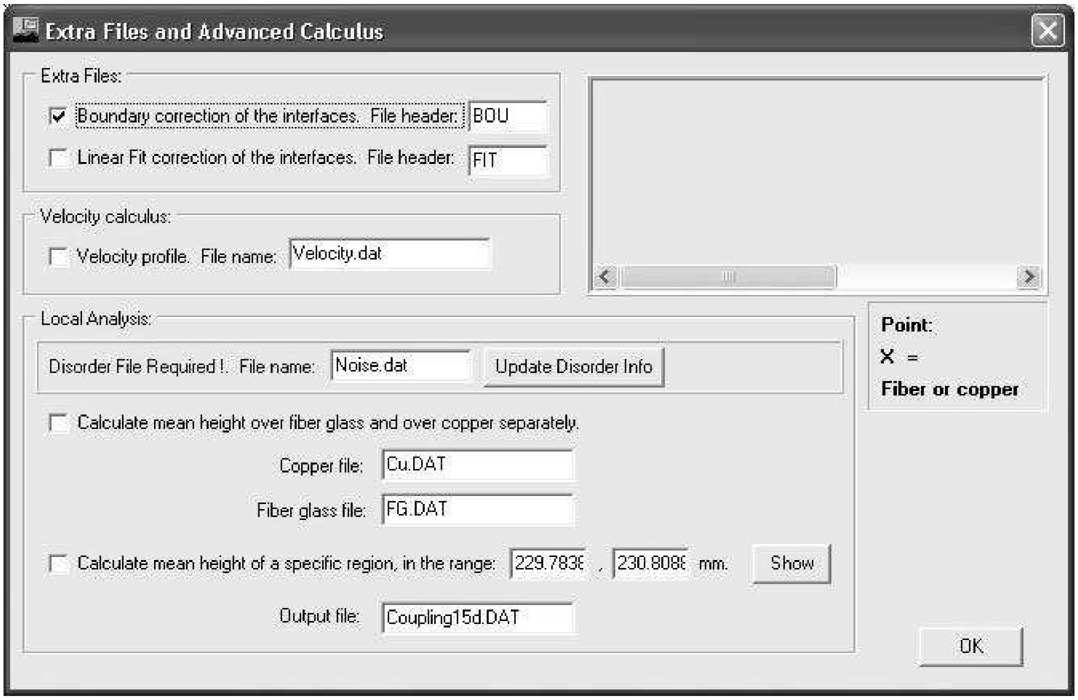
Extra Files and Advanced Calculus

Extra Files:
☑ Boundary correction of the interfaces. File header: BOU
☐ Linear Fit correction of the interfaces. File header: FIT

Velocity calculus:
☐ Velocity profile. File name: Velocity.dat

Local Analysis:
Disorder File Required !. File name: Noise.dat
☐ Calculate mean height over fiber glass and over copper separately.
Copper file: Cu.DAT
Fiber glass file: FG.DAT
☐ Calculate mean height of a specific region, in the range: 229.783 , 230.808 mm.
Output file: Coupling15d.DAT

Point:
X =
Fiber or copper

- Extra files:

Checking the different checkboxes available allows saving in different files the interface profiles that result from imposing a linear fit or a periodic boundary correction on the original data. The new data files will contain N points, where N is the value selected for interpolation. It is necessary to specify the header name for the output files. If we select, for example, `BOU` and `FIT` as header names for these files, the output files and the corrections implemented will be:

- Original file:
  470 points, overhangs, ordered from X_{max} to X_{min}. Name `C115-0010.DAT`.

- Extra files:
  N points (power of 2), no overhangs, ordered from X_{min} to X_{max}.
    Linear fir correction: Name `FIT00010.DAT`
    Periodic boundary conditions: Name `BOU00010.DAT`

These files will be created only if we calculate the mean width for these specific type of corrections (i.e., the corresponding checkboxes in the main window are checked).

Note: If you are also interested in saving the modified data resulting from raw data (i.e, with only overhangs corrections, data order, and interpolation) you have to check the checkbox labeled **Save the new data in files** present in the options window **Options / Program and calculus preferences / Calculus Option** of the main menu.

- Velocity calculus:

This option calculates and saves the velocity profile for the experiment. In addition, if the program can extract from the experiment file the set of experimental parameters, it is possible to write the velocity in ml/h, which is useful to compare the 2-D velocity (measured over the images) with the volumetric injection rate given by the pump.

The name of the output file is specified in the corresponding edit box (notice that it must contain the full file name, for example `VELOCITY.DAT`. The output format is:

capture time	Mean height: H=<h>	Velocity: dH/dt	Volumetric velocity: A·b·dH/dt
t_0 (first image)			
t_1			
…			
t_k (last image)			

A and **b** are the cell width and gap spacing respectively (extracted from the experiment file). To be sure that the conversion to the volumetric injection rate has the proper units, the program will consider that time is in s and the input data files are mm. The program will also consider a geometric correction that comes from the height of the copper obstacles (0.06 mm) and the occupation factor (0.35).

If the data that you want to process do not correspond to the specific experiments of roughening, this file is not useful in general. Moreover, you can extract easily the velocity profile by performing the derivative of the function H(t) using any data analysis program.

- Local analysis:

This set of options allow to perform a detailed investigation of the behaviour track by track. These analysis are essential to characterize the behavior when there is anomalous scaling.

The program will use the raw data for these analysis after interpolation them to N points (usually 512) and performing all necessary corrections (overhangs elimination and data order).

These analysis require the presence of the **Disorder file**. This file contains the information about the spatial distribution of the copper tracks in a given disorder realization. This file must contain a number of points N equal to the number of points used for interpolation (typically N=512), and the position occupied by copper tracks must contain the value `+1`, while the position occupied by the fiberglass substrate must contain the value `-1`. In addition, the disorder file and data file must coincide in X. An example of a partial noise file compared with a data file is shown below:

Noise file	Data file
0.0000, -1	0.0000, 132.267578
0.3319, -1	0.3319, 132.267578
0.6637, -1	0.6637, 132.267578
0.9956, -1	0.9956, 131.901688
1.3275, -1	1.3275, 131.901688
1.6593, -1	1.6593, 131.901688
1.9912, -1	1.9912, 131.901688
2.3231, -1	2.3231, 131.901688
2.6549, -1	2.6549, 131.901688
2.9868, -1	2.9868, 131.901688

3.3187, -1	3.3187, 131.901688
3.6505, -1	3.6505, 132.267578
3.9824, -1	3.9824, 132.267578
4.3143, -1	4.3143, 132.633469
4.6461, -1	4.6461, 133.365234
4.9780, 1	4.9780, 133.731125
5.3099, 1	5.3099, 139.951172
5.6417, 1	5.6417, 139.951172
5.9736, 1	5.9736, 140.317062
6.3055, 1	6.3055, 140.317062
6.6373, -1	6.6373, 140.317062
6.9692, -1	6.9692, 139.951172
7.3011, -1	7.3011, 139.951172
7.6329, -1	7.6329, 139.951172
7.9648, 1	7.9648, 140.317062
8.2967, 1	8.2967, 140.317062
8.6285, 1	8.6285, 140.317062
8.9604, 1	8.9604, 140.317062

(For clarity, the regions that correspond to copper tracks are marked in grey.)

There is no technique to extract the disorder file from a given disorder configuration. The best choice is to do it manually using Origin and a data file (equispaced and corrected) that contains an interface well developed, which allows to identify clearly the regions with copper tracks and fiberglass substrate. Then assign +1 to the regions of copper and -1 to the regions of fiberglass substrate. Finally, export the worksheet to a new file (named for example `DISORDER.DAT`) to the same directory as the data files.

If you have the noise file, press **Update Disorder Info** to load it. Once loaded, the different calculus are available. Just check the desired checkboxes to perform the calculus. It is possible to determine the **mean height of the interface as a function of time for copper tracks and fiberglass substrate separately**. Then the program will average out the result on different tracks and will save the final results in the specified output file. If you want to determine the mean height as a function of time in a single track, use the checkbox labeled **Calculate mean height of a specific region**. You should specify the region of interest. It is useful in this case to click over the diagram that represents the disorder. Notice that moving the mouse over the diagram activates a box below the diagram that indicates the place you are pointing to, its value of X and if it belongs to copper tracks or to fiberglass substrate. Left click on the diagram to set the starting value of the region of interest. Right click to set the ending value. In addition, you can click the button **Show** to draw two red lines that indicate over the disorder pattern the selected points.

All the files that correspond to a detailed analysis track by track have the same format of the output files. It is simply:

capture time	Mean height for Cu, FG, or selected region
t_0 (first image)	
t_1	
…	
t_k (last image)	

Finally, in the main window there is a checkbox in the group of local analysis labeled **Overlay disorder during interfaces evolution**. When the disorder is available and has been loaded (by clicking **Update disorder info** in the window for the extra calculus) this checkbox is available. Checking it overlays the disorder pattern in the window that shows the evolution of the interfaces (see later), which is useful to understand better the evolution of the experiment. If the information about the disorder pattern is not loaded or could not be found, this checkbox is inaccessible. By default, when the program starts this checkbox is disabled until you update the noise info.

2.C. Other relevant information

Once you have selected all the calculus you want to perform press the **Start** button. All the analysis will be performed automatically, and the program will inform you about all relevant information concerning the analysis, both in the info window and in message boxes if necessary.

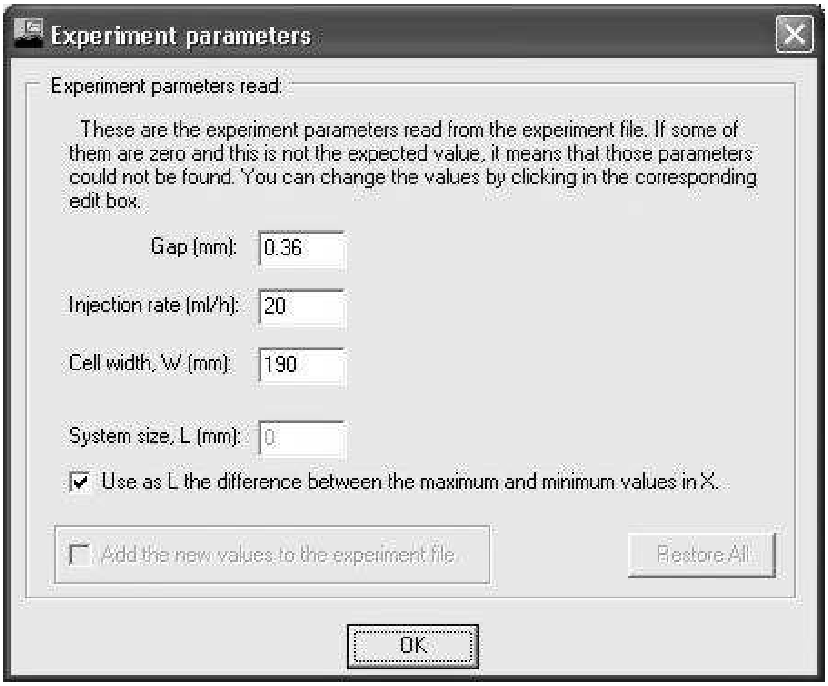

Experiment parmeters read:

These are the experiment parameters read from the experiment file. If some of them are zero and this is not the expected value, it means that those parameters could not be found. You can change the values by clicking in the corresponding edit box.

Gap (mm): 0.36

Injection rate (ml/h): 20

Cell width, W (mm): 190

System size, L (mm): 0

☑ Use as L the difference between the maximum and minimum values in X.

☐ Add the new values to the experiment file

The program will first check the input files (data + experiment file). Once the files are read, a message box will appear showing the information that could be extracted from the experiment file. Just press OK if you don't want to make any change. Then, the program will test files concordance, i.e. if all the images captured in the experiment have a corresponding data file. Usually some data files could not

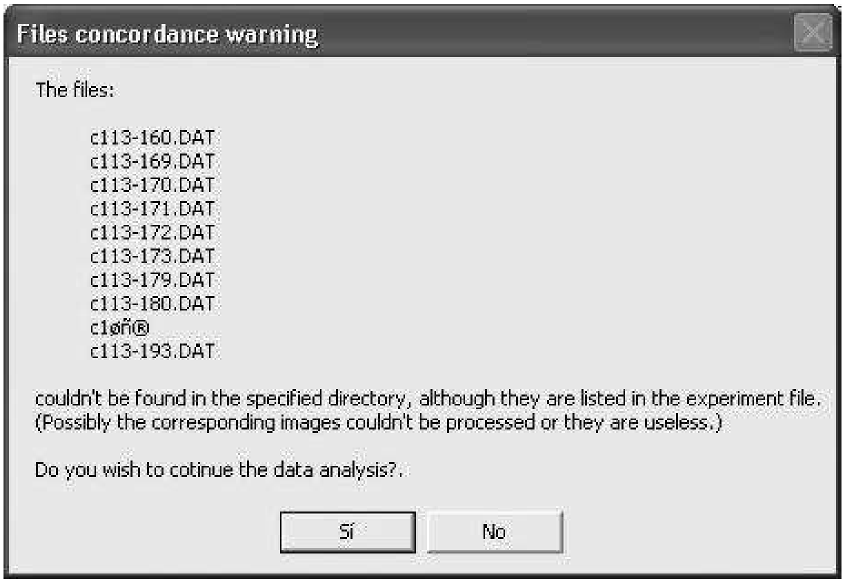

The files:

```
c113-160.DAT
c113-169.DAT
c113-170.DAT
c113-171.DAT
c113-172.DAT
c113-173.DAT
c113-179.DAT
c113-180.DAT
c1øñ®
c113-193.DAT
```

couldn't be found in the specified directory, although they are listed in the experiment file.
(Possibly the corresponding images couldn't be processed or they are useless.)

Do you wish to cotinue the data analysis?.

be created (e.g. because the interface could not be resolved or because the image was useless), which will result on a warning message from the program. A message box will be displayed with the list of the files that the program would expect to find. Just click YES to continue the analysis, or NO to stop it. After testing files concordance the program will start all calculus.

The calculus cannot be stopped. You will have to wait until they finish to close the program or to make any changes. A panel in the bottom-right corner of the main window will inform you about all the tasks that the program is performing. Other relevant information about the analysis will be shown in the Info window.

To exit the program press **Exit**. All the information about the status of the checkboxes and the text of the edit boxes will be saved. Next time the program is started, it will load the information saved last time.

3. Options and other features through the main menu.

In the menu bar there are the following items:

1. File / Load Data File.

This options allows opening a data file for inspection. When you select this item the program will prompt you for the name of the file. Just select the desired file and open it. This tool is useful for inspecting output files or to check the format of some input data files.

2. File / Exit.

Exits the program and saves all the contents of the edit boxes, as well as the status of the check boxes in the `Analysis.cfg` file. When you restart the application, this file will be read and all contents updated.

2. Options / Program and Calculus Preferences.

Here we select many different options of the program. The different options are grouped in three tab sheets:

- Interfaces evolution window:

Here we specify if we want to show the evolution of the interfaces when input data files are read. Just enable the corresponding check box.

The **rescale method** tells the program how the window where the interfaces are displayed will be rescaled. If it is selected **rescale proportionally respect to an aspect ratio**, when we resize the interfaces window the final size will be readjusted proportionally to the specified aspect ratio. This is very useful if we want to show the interfaces with the same aspect ratio as the real images. You should specify which is the aspect ratio. For convenience, you must introduce a value for x and a value for y (could be, for example, the size of the images in mm). Select **resize arbitrarily** if you are not interested in keeping an specific aspect ratio.

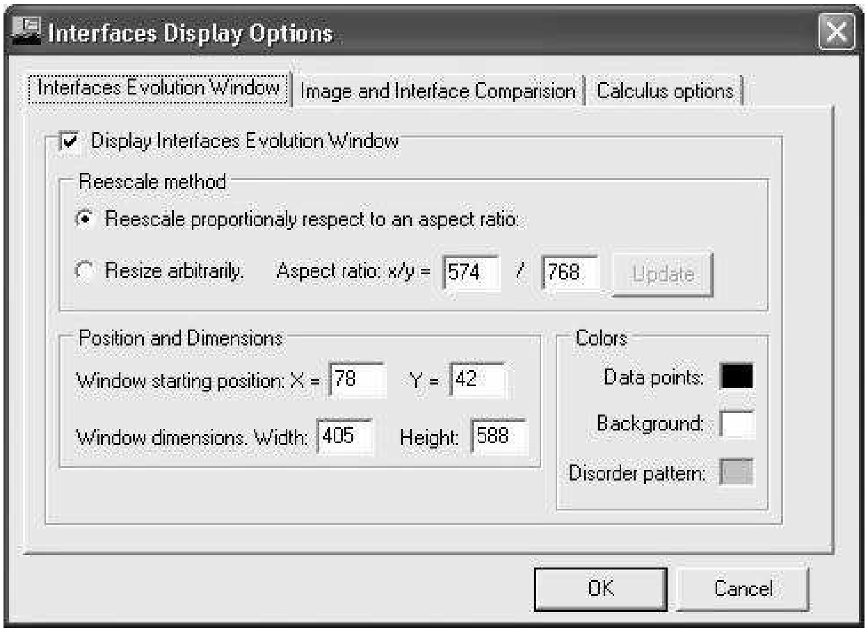

☑ Display Interfaces Evolution Window

Reescale method

● Reescale proportionaly respect to an aspect ratio:

○ Resize arbitrarily. Aspect ratio: x/y = 574 / 768

Position and Dimensions

Window starting position: X = 78 Y = 42

Window dimensions. Width: 405 Height: 588

Colors

Data points: ■

Background: □

Disorder pattern: ▨

In the **position and dimensions** box we specify the position and size of the interfaces window respect to the main window. Usually it is done by moving and resizing the windows using the mouse, but is has been introduced here in order to recover a convenient size if the window has become too large and cannot be reduced again. Notice that if the rescale method is respect to an aspect ratio, the values of width and height will be adjusted automatically to this aspect ratio.

Finally, you can specify the color that you want to display the interfaces, the background, and the disorder pattern (if present and loaded). Just double click on the different colors to set the new ones.

- Image and Interface comparison:

An interesting tool of the program (accessible in the menu through **Tools / Compare digitized data and original images**) allows to show the images of the experiment, display them as a movie and compare the recognized contours with the original images. The options that you specify in this tab sheet are related to this tool.

You have to specify if the units of the input files are pixels or mm. In the first case no calibration is needed. In the second case you must indicate the calibration of data in order to be possible overlay the interface over the images. In addition, you have to specify if the interface have to drawn as if the front was advancing from left to right (this is the case of the experiments on roughening) or as if it was advancing from bottom to top.

- Calculus options:

Here we specify some options that affect the calculus itself.

Data pre-processing is necessary to check for the existence of overhangs in the system. We also specify if the data have to be interpolated or not. You have different options. The most commonly used is the first, i.e. data are interpolated and if there is overhangs, the value of Y used will be the highest. The rest of the options are for data that won't be interpolated. You can select to average out different values of Y if there are multivaluations or just take the most advanced point. Finally, you can keep data without any modification. In this case, some results cannot be reliable. You can save the new, modified data in new files. Just check the corresponding check box. You must specify a header name for the output files, e.g. `MOD`. If the name of an input data file is `C115-0010.DAT`, the corresponding modified data file would be `MOD00010.DAT`.

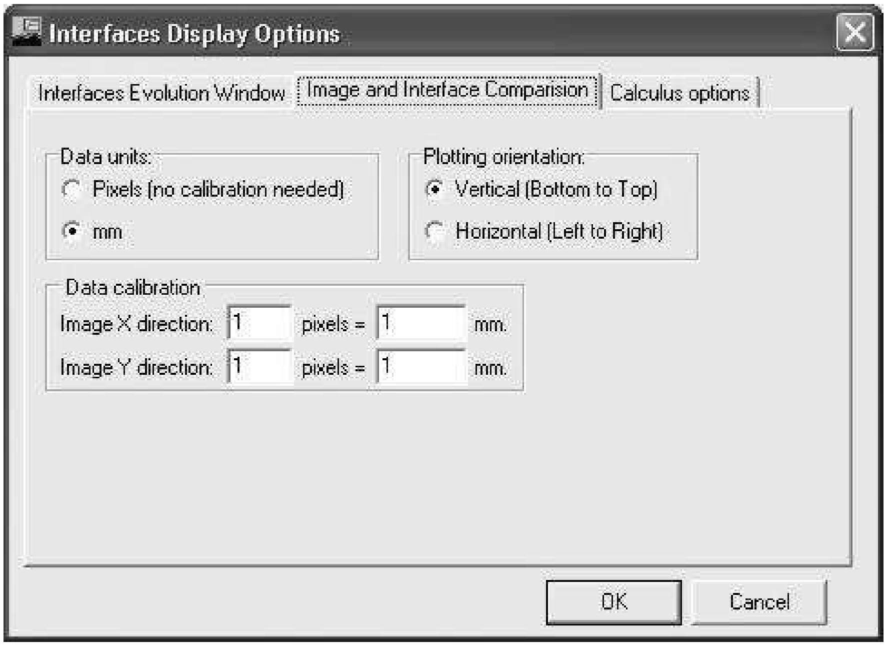

Interfaces Display Options

Interfaces Evolution Window | Image and Interface Comparision | Calculus options

Data units:
- ○ Pixels (no calibration needed)
- ● mm

Plotting orientation:
- ● Vertical (Bottom to Top)
- ○ Horizontal (Left to Right)

Data calibration
- Image X direction: 1 pixels = 1 mm.
- Image Y direction: 1 pixels = 1 mm.

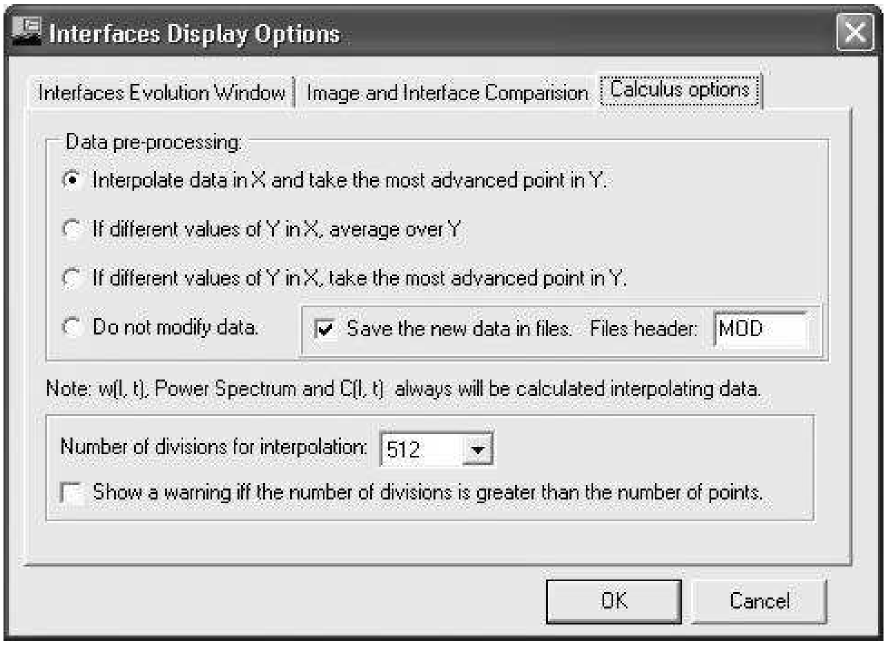

Interfaces Display Options

Interfaces Evolution Window | Image and Interface Comparision | Calculus options

Data pre-processing:
- ● Interpolate data in X and take the most advanced point in Y.
- ○ If different values of Y in X, average over Y
- ○ If different values of Y in X, take the most advanced point in Y.
- ○ Do not modify data.
- ☑ Save the new data in files. Files header: MOD

Note: w(l, t), Power Spectrum and C(l, t) always will be calculated interpolating data.

Number of divisions for interpolation: 512

☐ Show a warning iff the number of divisions is greater than the number of points.

Please notice that **the power spectrum will always be evaluated interpolation data**.

The final option is the number of points to be used for interpolation. Just select the number you want in the pop up edit box. N=512 has been the value used in the experiments of roughening, because it is the closest value (power of 2) to the original lateral number of pixels (about 500). Finally, you may check the box at the bottom of the tab sheet if you want to show a warning when the number of points of interpolated data is larger than the original data points, which introduces a larger artificial resolution. Usually this option is disabled.

3. Tools / Compare digitized data and original images.

The scope of this tool is to visualize the images that has been obtained from the experiment either image by image or as a movie, and compare them with the recognized contour that is the input data files of all the analysis. **The images must be in BMP format** (TIFF is not supported). Use the TIFFConverter if necessary to convert all TIFF images to BMP. An error message will appear if you try to load any other format.

To load a single picture, press **Load picture**. To load a sequence of numbered pictures click the **load** (yellow) button. You should indicate the first picture you want to load (for example `IM000000.BMP`). The program will then load all movies until it finds the end of the list. Once the pictures are loaded, you can use the navigation buttons to **play** the sequence as a movie (blue arrow button), to pause (blue bars button), to **advance one** (green short right arrow), to **advance back one** (green short left arrow), to **go to the end** (green long right arrow), and to **go to the beginning** (green long right arrow). In addition you can use the **magnifying glass buttons** to enlarge or reduce the pictures.

Finally, to overlay a data file over an image, click the **Load Data** button and select the file. The interface will be drawn over the image. You can change the color of the plotted data by clicking the **Change color** button. You can load as many files as you want over the same picture. Press the **Clear overlay** to clear all plots.

At this moment there is no a tool to load a picture and the corresponding data file at the same time.

Press the button **Close** to return to the main window.

4. About / About Analysis.

Shows the number of the current version of the application, as well as the date of the first running version and the last update.

4. About / Basic Documentation.

Shows this file.

4. Related programs.

The following programs perform useful calculus or analysis that are an extension of this application:

- **`CORRECT.exe`**: Located in `C:\Jordi\C\Correct`. Allows modifying the data files correspoding to an experiment in order to correct possible errors made during the recognition of the interface contours. For example, if we have made an error setting up the calibration, it is very unconvenient to run again the image analysis program and retrieve again all the contours. It is better to multiply by a factor the two columns of all data files.

- **`WTCorrected.exe`**: Located in `C:\Jordi\C\W-T Corrected`. Performs the correction of the intrinsic width $w(l, t_0)$ for an experiment. Given the correction of t_0 and the file that contains the results of $w(l, t)$, the program calculates the subtracted width $W(l, t) = (w(l, t)^2 – w(l, t_0)^2)^{1/2}$ for each window size. The output file will be similar in structure to the original, but with $t - t_0$ in the first column and *W/l, t*) in the rest.

- **`SLOPES.exe`**: Located in `C:\Jordi\C\Slopes`. Performs the calculus of the average slopes as a function of time, <? h> and <? ^{2}h>$^{1/2}$, which allows an alternative way for calculating the exponent ?* in the experiments of anomalous scaling.The program also performs the analysis of the interfaces using the max-min method, which allows an alternative way to determine roughness exponents.

- **`HISTO.exe`**: Located in `C:\Jordi\C\HistoSlopes`. Gets the statistical distribution of height differences, averaged out over all the images after saturation. See the program for information about the output files.

- **`ROUGHNESS.exe`**: Located in `C:\Jordi\C\Rough Exponent`. Performs the average of the power spectrum over all experiments with the same experimental parameters. By specifying the location of the different experiments and the time correction for each experiment, the program reads all data and averages out the power spectra that corresponds to the same time. Then, new output files are created containing the power spectrum averaged. The program can also determine the value of the roughness exponent ? , showing its temporal evolution.

- **`COLLAPSE.exe`**: Located in `C:\Jordi\C\Collapse`. Performs the Y and the X-Y collapses of the power spectra at different times, which is essential to get the complete set of scaling exponents that characterizes the anomalous scaling. This program uses as input data the averaged power spectra obtained from the `ROUGHNESS.exe` program. The output data files are the power spectra collapsed as well as a text file that contains the information of the final set of scaling exponents.

Note: the last two programs are very complex in use and require some training.

5. Important issues.

- For perfect operation the program must be located in the following directory: ‘`C:\Jordi\C\Analysis Revised`’. To install it in a different location it must be compiled. Contact me for details.

- Be sure that all files in the directory where the program is located are **NOT** Read-only. The program saves the preferences in a file called `Analysis.cfg`. If this file is read-only the program cannot save the preferences and will show an error message.

- **Very important**: Sometimes we will be interested in re-analyzing some experiments, so we will overwrite the existing output files. To make sure that this won’t cause any problem, be sure that **all output files are not read-only**. This may take place when saving data on a CD and then copying these data again to a hard disk. Data recorded on a CD is set automatically to read-only, so make sure that you return all files to read-and-write if you want to re-analyze data. The program will become unstable if it cannot overwrite a file, and non-desired behavior could take place. The program may also hangs up.

- This basic documentation help won’t be displayed if the document is in use by other program, such as Word.

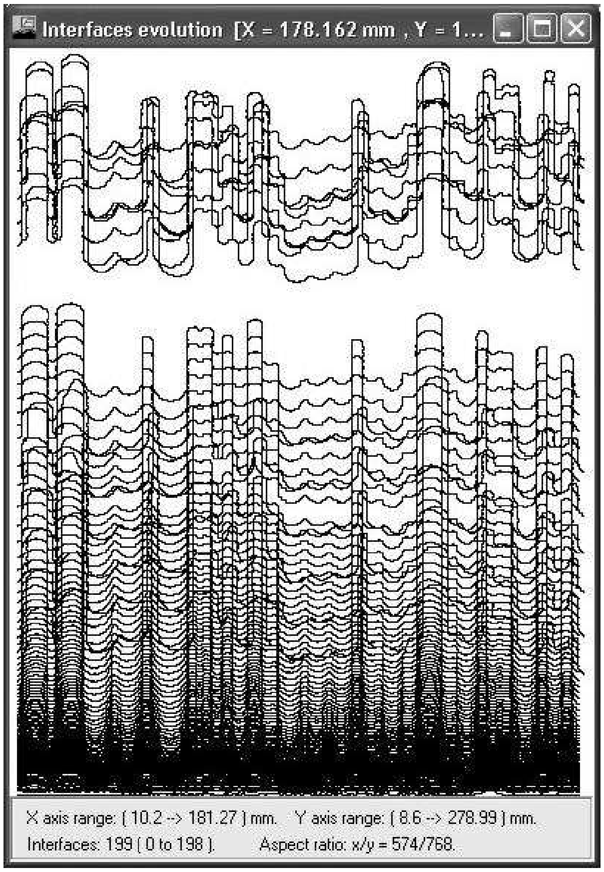

X axis range: [10.2 --> 181.27] mm.   Y axis range: [8.6 --> 278.99] mm.
Interfaces: 199 [0 to 198].   Aspect ratio: x/y = 574/768.

Appendix B

Programming with PCVision and PCVisionPlus frame grabbers

The programming of the image acquisition system for our experiments have become as important as the design of the experimental setup, and an enormous investment of time. To reflect this effort and to provide the basic documentation for future users, I have included in this Appendix the basic documentation of the software tools dedicated to the capture of images.

Jordi Soriano, December 2002.

(This text can be edited and modified using any editor capable of reading RTF formats, such as Word)

IMAGES ACQUSITION SOFTWARE.

A. Introduction.

I have developed different software tools to monitor the experiments of interfacial roughening. We have used a PCVsion frame grabber and two JAI CVM10 progressive scan CCD cameras. The frame grabber and cameras allow pictures to be taken at a rate that varies from 3 frames/s (when the capture is directly to hard disk) to 25 frames/s (when the capture is sequential and all frames are stored in memory).

I have used two languages for the programming task, VisualBasic and C++. The former has been used for manual and low rate acquisitions, while the latter has been oriented to high speed captures or captures synchronized with other devices. Although the libraries and programming structure are very different in VBasic and C++, the functions to control the cameras and frame grabber are rather similar in structure, and it is not very difficult to change from one to another using the specifications of the manual. In addition, the code that I have developed is very useful as an example for creating new applications or to improve the existing.

The libraries and tools served by the manufacturer to control the frame grabber are constantly updated and improved. I have used the ITEX libraries, version 4.1. However, since the appearance of the PCVisionPlus board, these libraries have been replaced by the IFC libraries, version 5.1 and higher. For this reason, my programs for PCVision and PCVisionPlus boards use different libraries. The next table summarizes these ideas

Board and camera	Frame rate (imag/s)	Programming libraries	Software	Associated experiments
PCVision JAI M10	Màx. 25	ITEX 4.1	Cameras Control (VBasic) Cameras C++ (C++)	Roughening and avalanches
PCVisionPlus JAI M40	60, 120, 240	IFC 5.2	Cameras Mireia (C++)	Viscoelastic fluids

The programs Cameras Control and Cameras C++ have been the software tools used to monitor the experiments of interfacial roughening. The Cameras Control has been the most used application and its basic functions will be explained in the next sections. To introduce the programs, the next diagram shows schematically how they work and the different kinds of acquisition options.

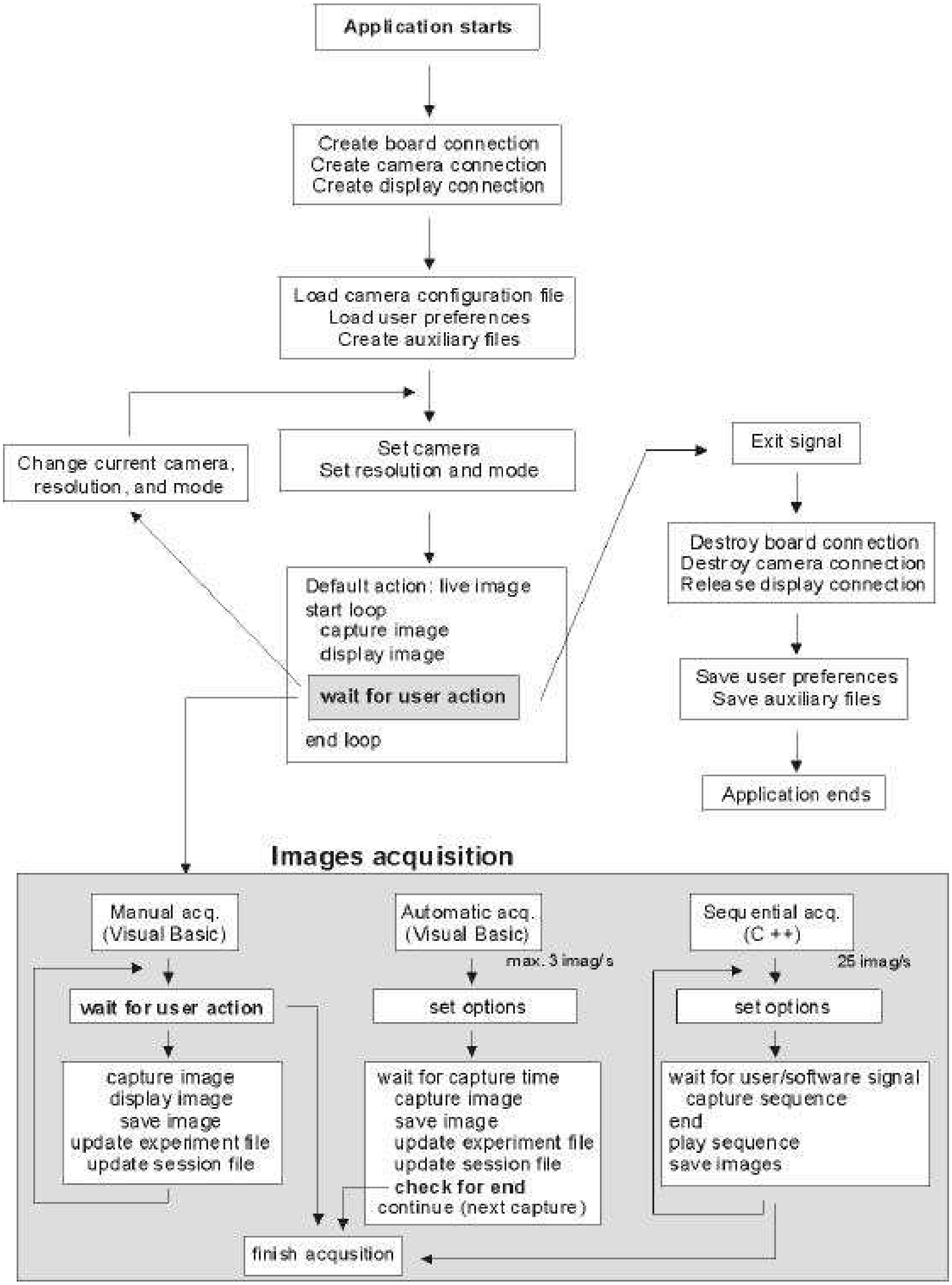

B. Cameras Control (VisualBasic).

This program controls two cameras, named 0 and 1, and saves captured images to disk. The images are captured using either manual acquisition or automatic acquisition. The latter allows linear or log acquisition and automatic camera change, so that the program can control a full experiment without the supervision of the user. In addition the program creates output files that contain information about the images acquired and capture times. If you need sequential acquisition, please use the program in C++.

Camera 0 ready.

Camera 0 (768 x 574 PLL)

(No acquisition mode)

Important issues:

- The *Itex Message Console* window remains opened after exiting the program. You should close it manually. (It closes automatically only when no images were captured).

- Do not run more than one Cameras Control at once. The *Itex Message Console* will show a warning in one of the programs and general errors will appear.

- Do not close the *Itex Message Console* while the main program is still running. This action will force the main program to be closed and some files could be lost.

- The program is fully multitasking. It can support at the same time 5 other programs (Corel, Origin, Word, Photoshop…). Do not abuse, especially when the program is saving images at very high rate (automatic acquisition with log captures in time). It is recommended to leave the program running alone until the delay between two consecutive pictures is at least 10 s.